U C L

Bayesian Networks for the Multi-Risk Assessment of Road Infrastructure

Pierre Gehl

Department of Civil, Environmental and Geomatic Engineering

EPICentre - Earthquake and People Interaction Centre

Submitted to University College London for the degree of Doctor of Philosophy

March 2017

Supervisor:
Prof. Dina D'Ayala

Declaration of Authorship

I, Pierre Gehl, declare that this thesis titled, 'Bayesian Networks for the Multi-Risk Assessment of Road Infrastructure' and the work presented in it are my own. I confirm that:

- This work was done wholly or mainly while in candidature for a research degree at this University.
- Where any part of this thesis has previously been submitted for a degree or any other qualification at this University or any other institution, this has been clearly stated.
- Where I have consulted the published work of others, this is always clearly attributed.
- Where I have quoted from the work of others, the source is always given. With the exception of such quotations, this thesis is entirely my own work.
- I have acknowledged all main sources of help.
- Where the thesis is based on work done by myself jointly with others, I have made clear exactly what was done by others and what I have contributed myself.

Signed: *Original document signed on March 20th 2017*

Date: *March 20th 2017*

U C L

Abstract

Department of Civil, Environmental and Geomatic Engineering

Bayesian Networks for the Multi-Risk Assessment of Road Infrastructure

by Pierre GEHL

The purpose of this study is to develop a methodological framework for the multi-risk assessment of road infrastructure systems. Since the network performance is directly linked to the functional states of its physical elements, most efforts are devoted to the derivation of fragility functions for bridges exposed to potential earthquake, flood and ground failure events. Thus, a harmonization effort is required in order to reconcile fragility models and damage scales from different hazard types.

The proposed framework starts with the inventory of the various hazard-specific damaging mechanisms or failure modes that may affect each bridge component (e.g. piers, deck, bearings). Component fragility curves are then derived for each of these component failure modes, while corresponding functional consequences are proposed in a component-level damage-functionality matrix, thanks to an expert-based survey. Functionality-consistent failure modes at the bridge level are then assembled for specific configurations of component damage states. Finally, the development of a Bayesian Network approach enables the robust and efficient derivation of system fragility functions that (i) directly provide probabilities of reaching functionality losses and (ii) account for multiple types of hazard loadings and multi-risk interactions.

At the network scale, a fully probabilistic approach is adopted in order to integrate multi-risk interactions at both hazard and fragility levels. A temporal dimension is integrated to account for joint independent hazard events, while the hazard-harmonized fragility models are able to capture cascading failures. The quantification of extreme events cannot be achieved by conventional sampling methods, and therefore the inference ability of Bayesian Networks is investigated as an alternative. Elaborate Bayesian Network formulations based on the identification of link sets are benchmarked, thus demonstrating the current computational difficulties to treat large and complex systems.

Acknowledgements

Firstly, I would like to express my sincere gratitude to my advisor Prof. Dina D'Ayala, whose indefectible support and enlightened advice were instrumental in the completion of this thesis. She was always by my side, selflessly pushing me to thoroughly explore the implications of my developments and to disseminate my results to the risk management community. Repeatedly, her experience and immense knowledge have rescued me from technical dead-ends and improved my understanding of the subject.

I would also like to thank the various academic staff members at UCL that I had the chance to meet and collaborate with, especially Prof. Tao Cheng for agreeing to supervise some of my work, Prof. Tiziana Rossetto for her warm welcome in the EPICentre group, Prof. Richard Chandler for his kind assistance on statistical models, and Dr. Carmine Galasso for his willingness to help me on many occasions.

A significant part of this thesis could not have been achieved without the support of Prof. Paolo Franchin and Dr. Francesco Cavalieri, who were kind enough to welcome me to University La Sapienza in Rome for a short yet very productive research exchange. I still have fond memories of my stay in Italy and I am very grateful for that.

This thesis has also been made possible thanks to BRGM, which agreed to my two-year leave-of-absence and supported the PhD tuition costs. I am very grateful to Dr. Evelyne Foerster, Dr. Gilles Grandjean and Bouc Olivier for their consistent support, especially regarding the administrative issues that kept occurring along the way. While writing these lines, I have a special thought for Prof. Hormoz Modaressi and Dr. John Douglas, my former mentors at BRGM, who kept insisting – and rightly so – that I enrolled for a PhD program.

I also thank my department colleagues and friends at UCL, who showed me so much of London and its hidden gems: 'cultural exchanges' on Friday nights were a fine way to briefly escape the challenges of academic research. I am also grateful to my friends in France, especially in Orléans, who were always happy to have me back and motivate me whenever I felt the need to rest from the hectic London lifestyle.

Last but not least, I would like to express special thanks to my family: my parents and my brother have always supported me throughout this PhD and my life in general. They have actively encouraged me to embark on this journey, and I know how much this represents for them.

Contents

List of Figures

List of Tables

Abbreviations

BN	**B**ayesian **N**etwork
Co	**Co**st of repair operations
CPT	**C**onditional **P**robability **T**able
DS	**D**amage **S**tate
Du	**Du**ration of repair operations
EDP	**E**ngineering **D**emand **P**arameter
FL	**F**unctional **L**oss
FLI	**F**unctional **L**oss during **I**ntervention
GMPE	**G**round **M**otion **P**rediction **E**quation
IM	**I**ntensity **M**easure
MCS	**M**inimum **C**ut **S**et
MECE	**M**utually **E**xclusive and **C**ollectively **E**xhaustive
MLS	**M**inimum **L**ink **S**et
PGA	**P**eak **G**round **A**cceleration
PGV	**P**eak **G**round **V**elocity
RC	**R**einforced **C**oncrete
SA	**S**pectral **A**cceleration

Chapter 1

Introduction

1.1 Background

The risk assessment of critical infrastructure exposed to natural disasters has been a growing concern over the past years, especially since the occurrence of catastrophic events such as the Tohoku earthquake or the Canterbury earthquake sequence in 2011. Most catastrophic disasters have been shown to result from unforeseen combinations of adverse events or cascading effects, which exceed the loading levels for which infrastructure systems have been designed. These observations reveal the need for a robust method for the risk assessment of infrastructure systems, with an emphasis on the prediction of high impact low probability events.

However, the risk assessment of critical infrastructure systems is hindered by a series of factors that have to be accounted for:

- Cascading events are a common cause for infrastructure failures. They may consist of cascading hazards (i.e. one hazard event that is triggered by another one) or cascading failures (i.e. a localised failure occurring on a single element and propagating through the whole system).
- The risk assessment of an infrastructure system exposed to multiple hazard types usually requires a wide range of hazard and fragility models, which use hardly reconcilable intensity measures and damage scales.

- Infrastructure loss has consequences that go well beyond the direct repair costs or the casualties it induces. The computation of the downtime and the associated economic losses is therefore of key importance: in addition to the system performance, it is also useful to track which physical elements have failed, in order to estimate the severity and the duration of repair operations.

- Most infrastructure systems are interconnected, so that they are often referred to as a 'system of systems'. Therefore the consideration of interdependencies between systems is necessary in order to account for the beneficial or detrimental effects of this interconnection.

- The interdependence between infrastructure elements and their respective contribution to the system performance lead to a solution space with a very high dimensionality (i.e. number of potential outcomes corresponding to specific combinations of element failures). The use of Monte Carlo simulations enable the approximation of the probabilistic distribution of the system losses, however the exploration of rare events requires more efficient algorithms.

Some of these conceptual difficulties have been recognised and addressed by recent studies during the last years [Pitilakis et al., 2014], although there remains a need to assess the reliability of these systems, both at the component level (i.e. through probabilistic vulnerability models) and at the system level (i.e. evaluation of the system performance or serviceability through network analysis). In this context, the FP7 INFRARISK project [O'Brien and the INFRARISK Consortium, 2013–2016] aims at developing a stress test framework to assess the coupled impacts of natural hazards on interdependent infrastructure networks, while focusing on low-probability high-consequence events. This thesis has been carried out with the objective of providing results that are directly usable and consistent with the INFRARISK framework, especially with respect to the harmonization of fragility models and damage scales in a multi-hazard context.

1.2 Scope and Aims of Research

The scope of this study is concentrated on the multi-risk assessment of road infrastructure: while most of the work presented here is focused on seismic risk, the impact of

other hazard types (i.e. floods and ground failures) is also considered in order to account for multi-hazard interactions. Such hazard events may be considered either as independent events that have a concomitant occurrence or as triggered events that are generated by the same source.

While a road infrastructure may be broken down into a wide range of physical elements (e.g. road segments, bridges, tunnels, earthworks, etc.), this study specifically addresses the case of highway RC bridges. Such elements are considered to be critical assets, due to both their exposition to natural hazards and the crucial influence they have on the network's performance. Bridges are complex structural systems where the various components are likely to experience a wide range of damage mechanisms, depending on the type of hazard loadings they are subjected to. Therefore they make for a suitable test subject, on which to apply the various tools and methods that are presented here. Finally, the choice of highway bridges is motivated by the criticality of some highways networks across Europe, which are identified as being part of the core TEN-T network [European Union, 2013].

Within this context, the main objective of this thesis is to address some of the conceptual challenges that are raised by the multi-risk assessment of infrastructure systems. More specifically, the use of original modelling approaches such as Bayesian Networks is investigated as an alternative to simulation-based methods such as Monte Carlo sampling, in order to successfully quantify the probability of occurrence of rare events. It is then anticipated that the proposed framework will be able to provide technical solutions to the issues at hand, through the application of the Bayesian Network method at two levels:

- At the element level (i.e. bridge), Bayesian Networks are developed in order to assemble hazard-specific component fragility curves, thus enabling the quantification of system failure modes that are consistent in term of induced functionality losses for all hazard types. This step presents the twofold merit of (i) directly providing harmonized functional losses and (ii) accounting for cumulated damages in the case of joint hazard events.
- At the infrastructure level (i.e. road network), Bayesian Networks are used to quantify the probability of exceedance of system losses, starting from the definition of multiple hazard source events. The aim is to explore the ability of

Bayesian analyses to treat multi-risk problems and to discover extreme and potentially catastrophic events, which may be overlooked by more classical sampling techniques.

Finally, the core of the thesis is devoted to the development of an original methodological framework, which is intended to be applied to any type of infrastructure and any hazard, provided that the relevant physical models are specified. On the other hand, the bridge and network examples that are used in the different chapters do not necessarily correspond to real-life infrastructure objects: the difficulty to access the huge amount of sensitive data that is required for infrastructure risk studies constitutes a significant limitation, which is avoided here by assuming hypothetical yet realistic values for some of the parameters. This assumption then provides a total control over the input variables, which is a desirable feature when performing a sensitivity analysis of the potential sources of uncertainty, which is the focus of the final part of the thesis.

1.3 Outline of Thesis

Chapter 2 starts with a literature review of the three main technical concepts that are involved in the proposed framework, namely (i) fragility analysis of bridges, (ii) infrastructure risk assessment and (iii) multi-risk analysis. The current gaps and shortcomings that may prevent a robust analysis are then identified. Finally, the proposed framework based on Bayesian Networks is detailed with respect to the various levels of analysis, i.e. from the network system to the structural components, and the methodology underlying the study is presented in detail.

At the bridge level, Chapter 3 makes the inventory of the various component failure modes that have been found in the literature or following post-disaster surveys, for all three hazard types considered (i.e. earthquakes, floods and ground failures). Since the severity levels of the different damage scales prove to be inconsistent, each component damage state is associated with loss measures, such as functional loss or repair duration, which enable the harmonization of the different failure modes. The quantification of functionality losses is made possible by the probabilistic treatment of an expert-based survey among infrastructure managers.

For each of the component damage states that have been previously identified, Chapter 4 aims at deriving specific fragility functions. In the case of seismic hazard, component fragility curves are analytically derived through finite element simulations, while simplified fragility assessment methods are also benchmarked. The state of knowledge for the fragility curve derivation for floods and ground failures does not yet permit the application of robust analytical methods, therefore empirical or expert-based fragility functions existing in literature are reviewed and proposed in some cases.

Parallel to the hazard-specific component fragility curves, Chapter 5 presents the Bayesian Network method that is proposed for the derivation of system fragility curves that predict consistent levels of functionality losses. The merits of this approach are demonstrated through two applications, namely (i) the derivation of harmonized multi-hazard fragility functions and (ii) the derivation of probabilistic functionality curves that directly express the probability of exceeding some functional losses given the hazard intensity.

Then, Chapter 6 conducts a review of the various sources of uncertainties that are involved in the multi-risk analysis of infrastructure systems, as well as the possible tools that can be used to propagate and visualise these uncertainties. Examples of uncertainty quantification are then developed, with specific attention to the epistemic uncertainties due to the choices of GMPEs and bridge fragility models.

At the network level, Chapter 7 presents the Bayesian Network method for the performance assessment of spatially distributed systems, with the double objective of facilitating the propagation of uncertainties and identifying the probability of occurrence of extreme events. Various Bayesian Network formulations are benchmarked with respect to their ability to efficiently model large and complex systems, while hybrid methods, based on simulation results and simplified Bayesian Networks, are shown to yield promising prospects. This approach is demonstrated with an application of the Bayesian Network method to a small-scale network in the case of multiple hazards.

Finally, Chapter 8 summarizes the main findings of the thesis and concludes by recommending future directions of investigation.

Chapter 2

Background and Proposed Framework

2.1 Literature Review

The aim of this literature review is to identify existing works on the three main technical concepts that are necessary to perform the multi-risk assessment of road infrastructure, namely (i) fragility analysis of bridges, (ii) infrastructure risk assessment and (iii) multi-risk analysis. Based on the available literature references, current technical gaps and shortcomings are then identified.

2.1.1 Fragility Functions for Bridges

This section details the state-of-the-art for the derivation of fragility functions for bridges, which is an essential component for the subsequent infrastructure risk assessment. Fragility derivation methods are mostly presented in the context of seismic risk, due to the availability of more advanced studies in this field. While a very large body of literature exists for the derivation and interpretation of fragility functions for different assets, the discussion here will be confined primarily to works applicable to bridges.

2.1.1.1 General Principles

Over the past decades, fragility functions have become a widespread probabilistic tool for the seismic vulnerability assessment of a given structural system [Calvi et al., 2006]. They are based on a set of prerequisites, which include the following [Negulescu and Gehl, 2013]:

- an Intensity Measure (IM) that represents the hazard loading applied to the structure. It is usually a ground-motion parameter such as Peak Ground Acceleration (PGA) or Spectral Acceleration (SA) at a period of interest.
- a damage scale that comprises a set of discrete Damage States (DS). The damage states are bounded by limit states or damage levels, which usually correspond to a given threshold in the potential values of a given engineering demand parameter (EDP).
- a functional form linking the probability of reaching or exceeding a damage state as a function of the selected IM. For instance, if a cumulative lognormal distribution is adopted, then the distribution parameters (i.e. mean α and standard deviation β) represent the fragility parameters, with α indicating the IM value that corresponds to the 50% chance of damage exceedance, and β representing the dispersion of the fragility curve (see Figure 2.1).

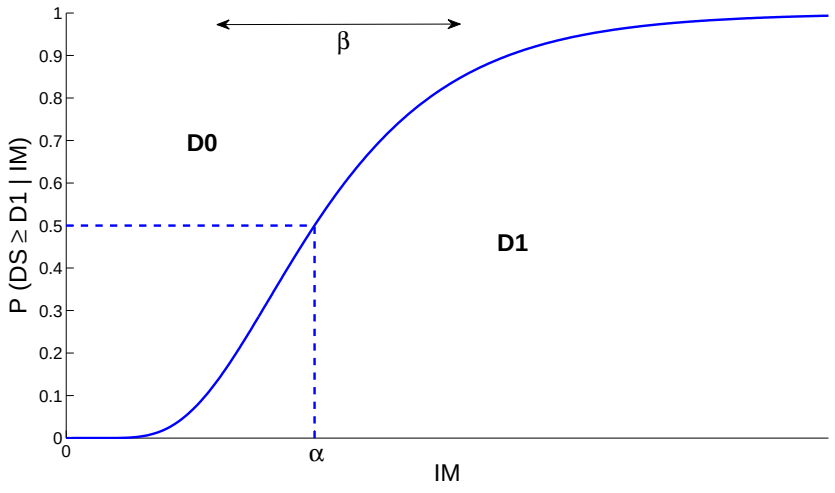

FIGURE 2.1: Fragility curve for damage level 1, showing the probability of reaching or exceeding damage state D1.

The mathematical expression of a fragility curve can then be written as a conditional probability, where the aforementioned log-normal assumption enables the variable log IM to be represented within a standard normal cumulative distribution function ϕ, with log representing the natural logarithm:

$$\mathrm{P}\left(\mathrm{DS} \geq ds|\mathrm{IM}\right) = \phi\left(\frac{\log \mathrm{IM} - \log \alpha}{\beta}\right) \tag{2.1}$$

Fragility curves are a key element of the Performance-Based Earthquake Engineering (PBEE) framework [Krawinkler, 1999]: the standard deviation β is directly linked to the various uncertainties that are contained in the prediction of DS given IM. These uncertainties are usually classified as *aleatory* or *epistemic* [Kennedy et al., 1980], i.e. respectively related to the inherent variability of the process or the lack of knowledge. For instance, an important aspect is that just knowing the IM alone does not provide sufficient information for predicting the damage state, therefore most of the dispersion is associated with the 'predicting power' of the IM with respect to the damage state. It is then possible to decompose the total dispersion into specific uncertainty sources, i.e. whether they are linked to the loading demand or the structural capacity [Bradley, 2010, D'Ayala et al., 2014a, Wen et al., 2003]:

- β_c, the standard-deviation representing the uncertainties in the capacity of the studied structure (e.g. modelling uncertainties, variability in the mechanical or geometrical properties).
- β_d, the standard-deviation representing the uncertainty in the seismic demand, e.g. the record-to-record variability.
- β_{DS}, the standard-deviation that is linked to the probabilistic EDP threshold identifying the damage level. It is related to the empirical nature of EDP in trying to quantify damage. For instance, $\beta_{\mathrm{DS}} = 0.4$ is recommended by HAZUS [FEMA, 2003] in the case of buildings. β_{DS} can also be estimated by compiling field data or conducting surveys with engineers or inspectors in order to obtain a distribution of the EDP threshold for a given damage state [Nielson, 2005].

If the uncertainties are assumed to be independent, which is mostly the case for common structural systems, all the aforementioned standard-deviations can then be combined in

order to obtain the total dispersion of the fragility model, which is expressed as [D'Ayala et al., 2014a]:

$$\beta = \sqrt{\beta_c^2 + \beta_d^2 + \beta_{\mathrm{DS}}^2} \tag{2.2}$$

The specific choice of IM, damage scale, functional form and uncertainty approach provide a base for the classification of fragility functions. Proposed approaches to determine or describe each of the above elements are discussed in turn.

a. Derivation Methods

Fragility curves are derived through regression models that use various sources of data points. Empirical fragility curves are mainly based on post-earthquake field observations, where the observed damage states are associated to the ground motion levels that have been recorded in the vicinity [Basoz et al., 1999, Elnashai et al., 2004, Shinozuka et al., 2000]. While the empirical approach results from direct observations, this method still presents some shortcomings, such as the difficulty to obtain accurate ground motion parameters next to the studied site, or the presence of data gaps for higher seismic intensity levels.

In the case of scarce data, expert judgement may be needed: a panel of experts in the adequate technical field can be interviewed in order to propose a mean and a dispersion for a given fragility function. Each expert judgement can then be weighted, depending on the level of experience of the expert or the trust they place in their own opinion [Jaiswal et al., 2013, Porter et al., 2007].

Alternatively, analytical fragility curves are based on numerical models of the studied structures, thus enabling the computation of the structural response for an extended range of ground motions. For instance, Mander [1999] has derived fragility curves with a static capacity spectrum approach, while introducing additional variability in the mechanical properties of the models. With the increase in computing capacity and the development of more robust finite element codes, non-linear dynamic analyses with a large set of ground motion records have also become more popular, whether they are carried out via Monte-Carlo sampling [Nielson and DesRoches, 2007, Shinozuka et al., 2000], or Incremental Dynamic Analysis [Vamvastikos and Cornell, 2002]. Even

though the analytical approach enables to perform sensitivity tests on various input parameters, the use of numerical models may also introduce biases with respect to the actual structural response or additional modelling uncertainties, especially in the non-linear range where not all physical phenomena can be accounted for.

Finally, hybrid fragility curves [Kappos et al., 2006] can also be derived in order to calibrate analytical results with some posterior post-earthquake observations [Singhal and Kiremidjian, 1998] or with in-situ measurements [Michel et al., 2010], through a Bayesian updating process. Jaiswal et al. [2011] have used Bayesian updating to compute the posterior distribution of collapse fragility using post-earthquake field observations, where the prior fragility curves are either based on expert judgement or estimated with the EMS'98 [Grünthal, 1998] vulnerability classes.

The estimation of the fragility parameters is achieved by performing a regression over the set of data points. Two distinct approaches can be identified in the literature and common practice. First, Cornell et al. [2002] and Baker [2007] present the so-called 'regression on a cloud', where a least-square regression is performed on the [IM-EDP] points, while assuming the following model:

$$\log \mathrm{EDP} = a \cdot \log \mathrm{IM} + b + \epsilon \tag{2.3}$$

where a and b represent regression parameters, and ϵ represents the regression residuals.

The response residuals of the regression are then computed, and β_ϵ denotes the standard deviation of the residuals. After selecting a given damage threshold EDP_{th}, the fragility parameters (median α and standard-deviation β of the distribution detailed in Equation 2.1) can then be expressed as:

$$\begin{cases} \alpha = \exp\left(\frac{\log \mathrm{EDP}_{th} - b}{a}\right) \\ \beta = \frac{\beta_\epsilon}{a} \end{cases} \tag{2.4}$$

This approach is based on the actual EDP values in the data set and it has proven to be rather stable, even with a reduced amount of points [Gehl et al., 2015]. However, it appears that, in the case of a multi-state structure, the estimated standard-deviation stays the same for all damage levels. While this constraint may be desired to avoid the

overlapping of successive fragility curves, it constitutes also an over-simplification of the problem, since it assumes that the β parameter is constant for all damage states, with is not necessarily the case for highly non-linear structures [D'Ayala, 2005].

On the other hand, the maximum likelihood approach proposed by Shinozuka et al. [2000] directly translates the EDPs into the corresponding DSs: for a fragility curve with a given damage level, the vector of DSs is then comprised of binary values (1 if damaged, 0 if not). The fragility parameters α and β are then estimated so that they maximize the following likelihood function:

$$L(\alpha, \beta) = \prod_{i=1}^{n} [\mathrm{P}_i(\alpha, \beta)]^{x_i} \cdot [1 - \mathrm{P}_i(\alpha, \beta)]^{1-x_i} \tag{2.5}$$

where $\mathrm{P}_i(\alpha, \beta)$ is the probability of reaching damage, n is the number of data points and x_i is a binary variable (1 if damage is reached, 0 if not).

Even though this approach is more suitable for the derivation of empirical functions (i.e. due to the use of discrete damage states), it has also been applied to analytical results in previous studies [Baker, 2015, Gehl et al., 2013a, Zentner, 2007]. The main reason for this is that the maximum likelihood model only requires a clear dichotomy between 'damage' and 'no damage' regardless of the actual EDP values. Therefore it can be applied to cases where the numerical model fails to accurately describe the response after the damage has occurred (e.g. derivation of collapse fragility curves). As a result, only a linear elastic model is required in order to estimate the fragility curve associated with the yielding limit of a given structural component. It should be noted that the maximum likelihood approach applied to a lognormal distribution is only a special case of the more generic concept of Generalized Linear Model (GLM) regression, which has been applied to seismic fragility models [Ioannou et al., 2012] (see details in Appendix B).

b. Selection of Intensity Measures

The selection of the IM is a key step in the derivation of fragility curves, since an informative IM can reduce the standard-deviation of the probability distribution, thus delivering a sharper prediction of the damage states. In the case of seismic risk, due the inherent properties of a ground-motion record, the hazard loading is only imperfectly

represented by any single ground motion parameter while the rest of the unaccounted parameters is usually considered as aleatory uncertainty (i.e. record-to-record variability). Therefore the objective is to find an IM that provides the highest correlation possible to the structural response.

Several criteria are proposed by Padgett et al. [2008b] in order to assess the 'adequacy' of a given IM, such as efficiency, sufficiency, practicality, proficiency and hazard computability.

The **efficiency** of an IM can be quantified by the standard error of the residual of the prediction of the EDP given IM, through the following power law:

$$\log \hat{\mathrm{EDP}} = a \cdot \log \mathrm{IM} + b + \epsilon \tag{2.6}$$

where the residual ϵ is assumed to have a normal distribution with standard deviation β_ϵ, which is used as the efficiency measure.

The slope parameter in Equation 2.6 may also be used to quantify the **practicality** of an IM, which measures the strength of the correlation between the IM and the demand parameter. The larger the slope parameter a, the more practical the IM.

On the other hand, **proficiency** is a composite measure of efficiency and practicality, which is based on the modified dispersion ξ of the regression in Equation 2.6 (a lower ξ means a higher proficiency):

$$\xi = \frac{\beta_\epsilon}{a} \tag{2.7}$$

Moreover, an IM is considered as **sufficient** if the residuals ϵ are statistically independent from the characteristics (e.g. magnitude, type of fault rupture, depth and epicentral distance) of the earthquake that generated each ground motion. A qualitative way to check sufficiency is to plot the residuals with respect to some earthquake measures and to check whether a trend can be observed [Padgett et al., 2008b]. A quantitative method to compare the sufficiency of two IMs is proposed by Jayaler et al. [2012], who have introduced a relative sufficiency index. The additional quantity of information I provided by an IM_2 with respect to a reference IM_1 is expressed as:

$$I\left(\text{EDP}|\text{IM}_2|\text{IM}_1\right) = \int \log_2 \frac{p\left(\text{EDP}|\text{IM}_2\left(\ddot{x}_g\right)\right)}{p\left(\text{EDP}|\text{IM}_1\left(\ddot{x}_g\right)\right)} \cdot p\left(\ddot{x}_g\right) \cdot \mathrm{d}\ddot{x}_g \tag{2.8}$$

where $\ddot{x}_g$ represents a possible acceleration time-history used in the fragility analysis, with $p\left(\ddot{x}_g\right)$ its probability of occurrence, given the location of the studied site and the seismotectonic context. A base 2 logarithm is used in the equation, so that the results may be seen as bits of information.

The final quality indicator for an IM is the **computability**, which describes the ability to accurately characterise the IM at the site of interest. This measure is usually linked to the availability of GMPEs for the given IM, which may be used to qualitatively estimate robustness of the uncertainty structure of the prediction models.

For a given structural system, an efficient and sufficient ground motion parameter is usually SA at the period corresponding to the first mode of vibration. It has also been found that the addition of a second parameter (e.g. SA at a higher period) generates a vector-valued fragility function (i.e. fragility surface) that has a lower dispersion than a scalar-based fragility curve [Gehl et al., 2013a, Seyedi et al., 2010]. Using the Akaike information criterion, it can be shown that the accounting for a second IM is statistically relevant. In the case of bridge portofolios (i.e. bridge classes incorporating variability in the geometric configuration and the modelling properties), however, Padgett et al. [2008b] have shown that PGA should be preferred: the choice of PGA as IM is motivated by the various types of bridges (i.e. with different modal periods) that may compose a given infrastructure network and the need for a common IM, for comparison purposes for instance. In the case of a single bridge, spectral quantities such as SA could still be the IM of choice: specific computations of the efficiency or sufficiency indices should be carried out as a part of the fragility estimation process.

c. Damage Scales

A set of fragility curves has to be associated with a damage scale that describes the different physical states that the structural system can reach: such a scale usually ranges from the elastic/linear state to complete damage or collapse. A damage state represents the configuration in which a structural system or component is found. It can be viewed as an interval that is bounded by two successive limit states (see example in Figure 2.2).

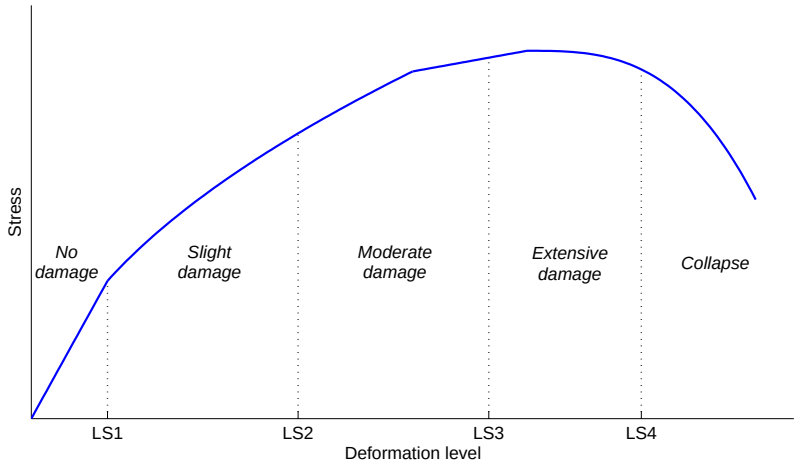

FIGURE 2.2: Example of a damage scale based on the level of deformation sustained by a structural element. The LS_i values represent the limit states.

In the case of bridge systems exposed to seismic hazard, several damage scales have been proposed in previous studies [Cardone, 2014, FEMA, 2003, Nielson, 2005]. They are usually built in a way that the consistency between the component damage states is ensured: for instance, two different component types have equivalent damage states in terms of severity, so that the system damage state can directly be estimated from the states of the component. While this approach has proven to be very convenient to derive system fragility curves, it lacks information on the specific impact of each component damage state on the structural system. As a result, the correlation between local and global damage states is not straightforward in the case of bridges, due to existence of multiple types of structural components, with subtantially different responses.

Other hazard types do not present so well constrained damage scales, since most of the fragility models that address a specific damage mechanism due to ground failure or flood loadings only consider a single damage state, i.e. the failure of the component [ALA, 2005]. In the case of subsidence in embankments or backfill soils, some damage scales based on the extent of vertical settlement may be used [Werner et al., 2006], while the damage to pier foundations due to scour can be represented by the scour depth with respect to the bridge footing [Pearson et al., 2002].

The link between damage scales and bridge functionality is often neglected, even though such information is vital to quantify the performance of the road network after the disrupting event. Still, in the case of bridges exposed to seismic hazard, some studies address the issue of functionality, such as the REDARS methodology [Werner et al.,

2006] or the HAZUS model [FEMA, 2003]. These loss model propose bridge closure percentages and restoration times for the global damage states that are defined by their respective damage scale.

2.1.1.2 Repositories of Fragility Functions for Earthquakes

One of the key results of the FP7 SYNER-G project [Pitilakis and the SYNER-G Consortium, 2009–2013] consists in the collection and review of fragility functions for critical infrastructure components. More specifically, fragility functions of road and railway bridges have been critically appraised and stored in a Fragility Function Manager Tool [Silva et al., 2014, Tsionis and Fardis, 2014]. The tool proposes a taxonomy for the different bridge typologies, based on a dozen of parameters, such as material, superstructure type, deck type, pier-to-deck connection, dimension, pier type, seismic design or regularity. Other classifications have been defined, such as the one by HAZUS [FEMA, 2003], including the following prescriptive parameters:

- Geographic area: California, Non-California;
- Construction year: 1900, < 1975, > 1975, < 1990, > 1990;
- Design: Seismic, Conventional;
- Description: Major bridge (> 150 m), Single span, Single-/Multi-column bent, Box girder, Simple support, Continuous concrete, Prestressed concrete, Continuous steel.

Other taxonomies can also be found in the studies by Nielson [2005] or Basoz and Kiremidjian [1996]. The bridge typology strongly influences the type of components that comprise the bridge system. In the present study it is proposed to focus on multi-span RC girder bridges, with either simply-supported or continuous decks, which represent the most widely used typology for highway bridges in Europe [Cardone, 2014].

The SYNER-G database of bridge fragility functions is particularly useful in this context. It contains 373 curves for various typologies, extracted from around 30 literature references. The distribution of the fragility derivation methods is detailed in Figure 2.3: it can be noticed that dynamic non-linear analyses are the most common way to derive

fragility curves, while PGA still remains by far the IM of choice. The reason for the low proportion of empirical fragility curves for bridges may lie in the lack of focus on infrastructure components during post-earthquake surveys (at least until recently), as well as the limited number of bridges damaged by an earthquake in any given event when compared to buildings, and hence the difficulty of building a robust statistical model based on observations.

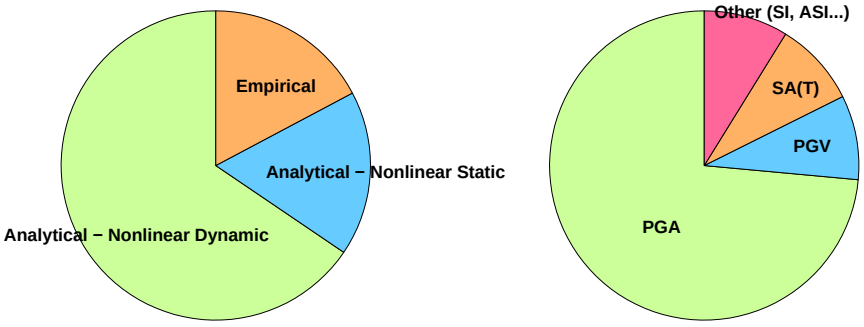

FIGURE 2.3: Proportion of derivation methods (left) and selected IMs (right) among the references considered in the SYNER-G database.

According to Crowley et al. [2011], RC bridges represent the vast majority of the studied typologies, 76% of them consisting of bearing-isolated pier-deck connections, the rest of them forming a monolithic pier-deck block. In the case of decks supported by bearings, a further distinction has to be made between independent deck spans (i.e. bearings allowing translational movement between two deck spans) and continuous decks (i.e. bearings mainly allowing free rotation between the pier and the deck).

It is also possible to identify the geographical area for which the bridge fragility functions have been derived, as shown in Figure 2.4. The apparent high proportion of European fragility curves should be moderated by the fact that most of these curves have been derived during the SYNER-G project and are extracted from a single reference [Tsionis and Fardis, 2014]. On the contrary, U.S. fragility curves are found in a variety of references, thus covering a larger range of typologies and derivation methods. Some studies have considered bridges from very different locations, such as United States and

Greece or Japan: they are usually the outcomes of the empirical treatment of various recent earthquake events (e.g. 1994 Northridge and 1995 Kobe earthquakes).

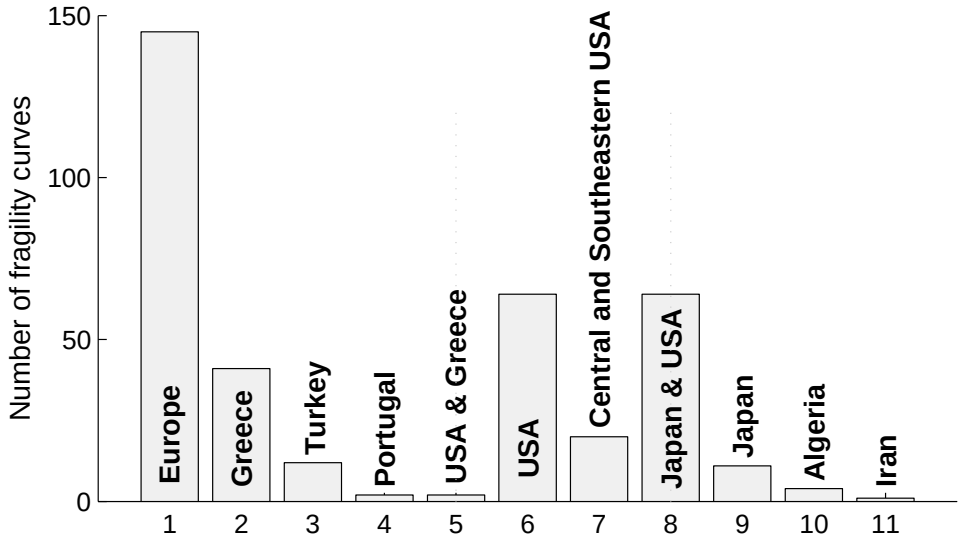

FIGURE 2.4: Geographical areas of applicability for the fragility curves contained in the SYNER-G database.

The review by Tsionis and Fardis [2014] proposes also a comparative analysis of the respective merits of non-linear static and dynamic analyses, confirming the ability of non-linear dynamic analyses to account for the contribution of higher modes and for the ground-motion variability, while pushover-based fragility curves are usually derived with an arbitrary standard deviation. Another key aspect is the distinction between fragility curves derived for a single bridge or for a class of bridges: the aforementioned bridge taxonomies are then useful in the latter case, in order to define a variable space from which a set of mechanical or geometrical properties can be sampled [Padgett and DesRoches, 2007]. In order to optimize the number of analyses on the different bridge models, parametrized fragility curves can then be derived, where the evolution of the fragility parameters as a function of the model variables is represented on a response surface [De Felice and Giannini, 2010, Park and Towashiraporn, 2014].

The analytical derivation of fragility curves has first been limited to the study of bridge piers as the most vulnerable components. For instance, Franchin et al. [2008] have simply compared distributions of ductility demand and ductility capacity in order to quantify the probability of pier failures. Other studies [Karim and Yamazaki, 2001, Kibboua et al., 2011, Kim and Feng, 2003] have only considered the damage to bridge piers when

conducting non-linear dynamic analyses, which presents the merit of requiring only one damage scale with one type of EDP (e.g. column curvature or drift).

The study by Nielson [2005] has considered nine bridge classes in the Central and South-eastern United States for the derivation of analytical fragility curves, using non-linear time-history analyses. Probabilistic seismic demand models are derived for all bridge components, while system-level fragility curves for global damage states are assembled through joint probability distributions that account for the correlation between bridge components. This robust fragility analysis demonstrates the contribution of components other than piers to the global fragility of bridges. The same approach, using similar bridge models with component- and system-level fragility curves, has then been used by Aygün et al. [2010], Nielson and DesRoches [2007], Padgett and DesRoches [2008] for various applications.

These fragility curves have also led to more elaborate models that account for some of the following issues:

- Fragility curves can be derived on a retrofitted bridge model in order to quantify the effect of different retrofit measures on the vulnerability of the bridge. This enables to estimate which specific measure is adequate for a given bridge typology or a given damage state [Padgett and DesRoches, 2009].
- The effect of the skew angle on the fragility curves has been studied by Avsar et al. [2011], where an increase in the mean of the fragility curve is observed for skew angles higher that 30°.
- Spatial variability in the seismic loading for large span bridges may have a detrimental impact on the fragility curves, depending on the soil heterogeneity and the wave propagation velocity that can induce a loss of coherence in the input signal [Lupoi et al., 2005, Saxena et al., 2000].
- Temporal fragility curves can assess the vulnerability over the lifetime of the bridge, accounting for effects such as corrosion [Ghosh and Padgett, 2010], flood scour or cumulated seismic loadings [Franchin and Pinto, 2009].

Tsionis and Fardis [2014] have proposed a method for fast fragility analysis of regular bridges with a reduced set of parameters such as the deck-pier connection type and

the bridge geometry (e.g. pier height, span length). This approach follows the design procedures of Eurocode 2 [CEN, 2004a] or Eurocode 8 [CEN, 2004b], based on the level of seismic design. As a result, significant efforts are still needed to assess the fragility of bridges with low design levels, prior to the application of Eurocodes.

Simplified analytical methods have also been used, as the one proposed by Paulotto et al. [2007]: it is based on the use of substitute linear models and response spectra, while the hysteretic energy dissipation is simulated by an increased damping ratio. The damping ratios for individual members (i.e. beams and columns) are averaged and weighted with the elastic energy dissipated in each member, in order to compute the modal damping ratios for the system. The substitute linear structure is obtained by evaluating the secant stiffness corresponding to the ductility ratio of each element. Finally, the method is applied to RC bridge piers, while the deck is assumed to remain linear elastic. A similar approach has been proposed by Peloso and Pavese [2008], namely the 'Secant Modes Superposition': it relies on the same iteration steps, i.e. updating the secant stiffness of the members and using an over-damped response spectrum in order to obtain the member displacements at the modal level, which are then recombined. Starting from a target displacement profile, an equivalent modal analysis is conducted with the updated stiffness matrix at each iteration until convergence is reached. However, few examples of the application of this approach to systematic structural analysis have been found.

Sadan et al. [2013] have developed the concept of direct displacement-based seismic assessment (DDBA) of bridges, which is based on the direct displacement-based design (DDBD) method by Priestley et al. [2007]. Key differences in the DDBA compared to the DDBD are summarized in the following steps:

- Acquisition of structural information, e.g. for piers, in terms of moment-curvature and force-displacement curves and shear failure capacity.
- Derivation of the deformed shape of the structure for the target displacement (i.e. corresponding to the deformation of the *a priori* critical element at a given performance limit state): the equivalent modal shapes are estimated with the secant stiffness matrix via an iteration process, referred to as 'Iterative Eigenvalue Analysis' (IEA).

- Computation of equivalent SDOF system properties, namely the total base shear capacity and the effective stiffness and damping ratio.
- Assessment of the bridge by comparing the displacement capacity with the demand spectrum, using a reduction factor in order to account for over-damping.

However, in Sadan et al. [2013], DDBA is only applied to continuous decks that are pinned to bridge piers or supported by bearings. Using a set of regular and irregular bridge configurations, comparisons are conducted between DDBA, IDA and standard response spectrum analysis, showing a good performance of DDBA, especially in the case of bearing-supported decks.

Cardone [2014] has extended the DDBA to the case of independent bearing-supported deck spans. For each performance limit state, performance displacement profiles (PDPs) are defined based on the first component that reaches the limit state (see example in Figure 2.5): the procedure for the PDP estimation is assessed through different approaches, especially the displacement adaptive pushover (DAP) [Antoniou and Pinho, 2004] and the effective modal analysis (EMA). The latter approach is actually the one that is described by Sadan et al. [2013], i.e. the iterative eigenvalue analysis. Finally, an inverse adaptive capacity spectrum approach [Cardone et al., 2011] is used in order to find the PGA value of a given design spectrum that corresponds to the performance point of the equivalent SDOF system. Assuming a arbitrary value for the standard deviation (i.e. $\beta = 0.6$), Cardone et al. [2011] also show that this approach can be used to derive fragility curves for the different performance limit states.

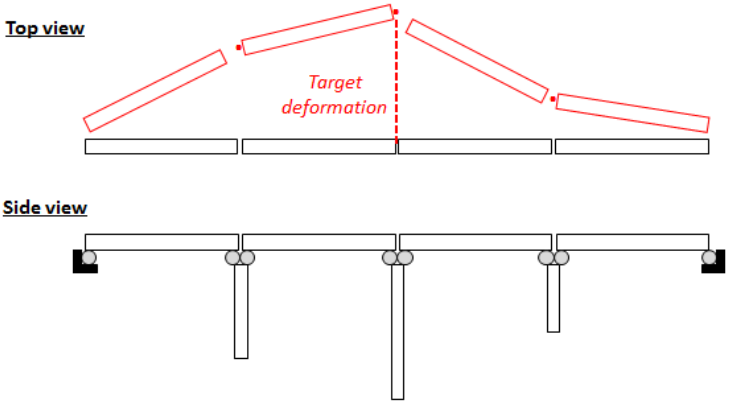

FIGURE 2.5: Illustration of a performance displacement profile (deformed shape in red).

More recently, Franchin et al. [2016] have developed a procedure for the automated and fast generation of bridge fragility curves, based on the knowledge of a few structural parameters (e.g. geometry, pier type, material strength, etc.) that are fed into a Bayesian belief network. In the proposed application, the content of the Bayesian network (e.g. conditional probability tables) is acquired through the analysis of an Italian bridge database [Borzi et al., 2016].

2.1.1.3 Fragility Functions for Ground Failures

In the present study, ground failure hazard refers to all phenomena that are related to large permanent deformations of the soil, such as subsidence, lateral spreading or slope failure. Such mechanisms are usally triggered or facilitated by heavy rainfall (i.e. raise of water table) or earthquake ground motion. There is no ready-to-use fragility model for a global bridge system exposed to ground failure: this is mostly due to the nature of the hazard loading, which can take many forms as opposed to seismic ground motions. As shown by Pitilakis et al. [2011], who have compiled the most up-to-date fragility functions for buildings and structures exposed to ground failure, a wide range of models exist for road segments along slopes or embankments, but none of the developed methods have been applied to bridges.

However, there are available methods to quantify the occurrence of two of the most common manifestations of ground failure hazard, namely slope failure and subsidence/settlement. Ground failure is usually considered as a cascading hazard, in the sense that it may be triggered by a seismic ground motion while heavy rainfall with saturation of the soil with water is an aggravating factor. For this reason, fragility functions for ground failure are mostly expressed with respect to a seismic intensity measure (e.g. PGA) [Saygili and Rathje, 2009].

Regarding slope failure, analytical methods may be distinguished between finite element models and simplified approaches, such as the rigid block model [Newmark, 1965]. The latter method may be applied to different types of landslides: in the case of shallow planar landslides, an infinite slope model may be adopted in order to perform the stability analysis of the rigid block, as proposed by Jibson et al. [2000]. Then, the probabilistic relations between the permanent ground deformation and the PGA applied to the slope enable the derivation of fragility curves for different levels of soil deformation [Bray and

Travasarou, 2007]. In the case of deep-seated rotational landslides, a circular slip surface is usually proposed in order to minimize the factor of safety of the slope [Sarma, 1975]. For a given PGA level, the probability of slope failure can then be derived by considering uncertainties on the soil parameters, using for instance a mean-value First-Order Second-Moment method as proposed by Wu [2015].

On the other hand, finite element analysis of the supporting soil is a popular approach in the case of subsidence/settlement. For instance, Argyroudis and Kaynia [2014] have modelled the backfill soil of a bridge abutment with a vertical retaining wall and they have applied ground-motion time histories at the basis of the soil-structure system in order to quantify the permanent strain of the supporting soil. Thus, once some deformation thresholds have been defined, these data points can be used to derive fragility curves for the subsidence of bridge abutment backfill soil, for various heights and EC8 soil types.

2.1.1.4 Fragility Functions for Floods

The HAZUS Flood Model [FEMA, 2005] discusses very briefly the vulnerability of bridges, since there is no available bridge damage database from which to extract valuable information. Therefore the HAZUS model focuses on the vulnerability of bridge foundations, while ignoring potential damage to the superstructure. For a few predefined return periods of flood events, failure probabilities due to scour are then proposed, for different values of scour potential rating (i.e. scour vulnerability index). Such probability tables are similar to Damage Probability Matrices, which cannot be really be compared to more elaborate models such as fragility curves. Moreover, it appears, for other assets, that the HAZUS model advocates the use of damage functions expressing a damage percentage as a function of water depth, instead of probabilistic fragility functions.

However, recent catastrophic flood events have resulted in the collapse or the damage of numerous bridges, thus providing valuable information for the derivation of empirical fragility curves. For instance, Padgett et al. [2008a] have collected damage data from 44 bridges exposed to either storm surge, wind, debris impact or inundation, following the 2005 Katrina hurricane. An analytical approach is also developed by Kameshwar and Padgett [2014], where meta-models are built in order to represent the bridge response

under the effects of hurricanes. A logistic regression model is then derived, enabling the expression of the fragility with respect to surge elevation and wave height.

While a few references propose fragility curves for bridges exposed to scour [Alipour et al., 2012, Tanasić et al., 2013], the importance of the waterway conditions and configurations in the evaluation of scour usually limits the derivation of scour fragility curves to specific single case-studies, until realistic representations of typologies of $\{bridge - waterway\}$ systems can be produced. Therefore the modeller can refer to the HEC-18 guidelines [Richardson and Davis, 1995] in order to quantify scour depth, for any type of bridge and waterway configurations. Moreover, the HYRISK methodology [Pearson et al., 2002] proposes to separate the bridge condition from the waterway configuration by providing tabulated probabilities of scour failure based on a scour vulnerability grade (i.e. linked to the susceptibility of the bridge to scour) and an overtopping frequency (i.e. directly linked to the waterway adequacy).

2.1.2 Infrastructure Risk Assessment

Infrastructure constitute the backbone of increasingly connected and interdependent societies, therefore the risk assessment of infrastructure systems has emerged has a key aspect for the resilience analysis of communities. The development of procedures for infrastructure risk assessment has been the object of growing interest over the past few years, as shown by the following studies and projects:

- In the United States, the HAZUS methodology has developed a framework for the vulnerability assessment of various assets, with respect to earthquakes [FEMA, 2003] and floods [FEMA, 2005]. Fragility models are developed for all elements at risk composing the infrastructure systems, such as utility lifelines or transportation networks. These developments have been implemented in risk assessment tools such as HAZUS-MH and MAEViz. The MAEViz model is focused on consequence-based risk assessment, with decision-support tools that enable to compare socio-economic losses resulting from physical failures (e.g. bridge closure or pipeline rupture).

- The FP6 Risk-UE project [Mouroux et al., 2004] is concentrated on the seismic risk analysis of seven cities in Southern and Eastern Europe. Most of the work

is devoted to the vulnerability of buildings, however a section of the project has tackled the issue of critical lifelines: some fragility models are proposed for the lifeline components, even though no framework for network analysis is provided.

- The FP7 SYNER-G project [Pitilakis and the SYNER-G Consortium, 2009–2013] has led to the development of a method for the systemic analysis of interdependent infrastructures (i.e. system of systems) exposed to seismic hazard, using a scenario-based approach. To this end, various fragility models have been reviewed and implemented for all elements at risk, in order to generate failure events and compute the system's performance with connectivity or serviceability level approaches.

While the final objective is usually the quantification of the system's performance based on the exposure of the components to various hazard loadings, the high number of possible damage scenarios across all interdependent components constitutes the main computational hurdle in the case of a probabilistic analysis. Several approaches have been proposed in the past, as detailed below.

2.1.2.1 Simulation-based Methods

Monte-Carlo simulations consist in the sampling of random realisations of the various input variables and the estimation of the final risk metric for each run, thus enabling the derivation of a probability distribution for the quantity of interest. This framework is fairly straightforward to implement and it has the ability to treat any types of systems, without any needs for analytical solutions. Therefore Monte-Carlo simulations are a popular way to assess the reliability of systems, especially in the case of spatially distributed infrastructure systems that are exposed to seismic hazard. For instance, Adachi and Ellingwood [2008] have used Monte Carlo sampling to quantify the serviceability of a water supply system subjected to a single earthquake scenario. The functionality of a water system facility is a combination of the physical failure of the facility, the presence of a backup power system and the failure of the supporting electrical system, thus accounting for the interdependency between water and electrical supply systems. A similar Monte-Carlo-based approach has been implemented by Dueñas Osorio et al. [2007], who provide probabilities of the connectivity loss of interdependent water and power distribution networks. The loss probabilities are computed for various earthquake scenarios

that are representative of increasing return period events. Wang and Au [2009] have also used Monte Carlo simulations to quantify the water supply reliability under seismic risk. Local and global performance indicators such as the Damage Consequence Index or the Upgrade Benefit Index are introduced in order to identify critical components within the system.

While most studies focus on utility networks (e.g. water supply systems or electric power networks), the simulation of transportation networks has also been the object of some developments. For instance, a simulation approach for the seismic risk analysis of highway systems has been proposed by Werner et al. [2000]. The authors use four simulation modules (i.e. hazard, component, system and transportation cost) that are coupled in order to quantify expected monetary losses and increased travel times for different durations of infrastructure exposure. Goretti and Sarli [2006] have also used Monte-Carlo simulations to assess the connectivity and serviceability of road networks after an earthquake. Functional interactions with the built environment are taken into account through short-term (i.e. connectivity between strategic buildings and damaged areas) and long-term (modification of network demand due to displaced population) objectives, while a physical interaction is also considered due to the potential blockage of roads from to collapsed buildings.

In Europe, the FP7 SYNER-G project has led to the creation of an Object-Oriented Framework for Infrastructure Modeling and Simulation (OOFIMS) [Franchin and Cavalieri, 2013]. This tool aims at addressing the issue of a 'system of systems' exposed to seismic hazard.

The object-oriented approach presents the merit of organizing each considered system (i.e. built area, utility systems, transportation system and health-care system) with a set of classes, attributes and methods, thus grouping components with similar features (see Figure 2.6). The simulation framework is designed in a way that a probabilistic sampling is performed at various levels:

- earthquake events (i.e. epicentre location and magnitude) are sampled from given seismogenetic areas;
- spatially correlated ground motion fields are sampled from the GMPE uncertainties;

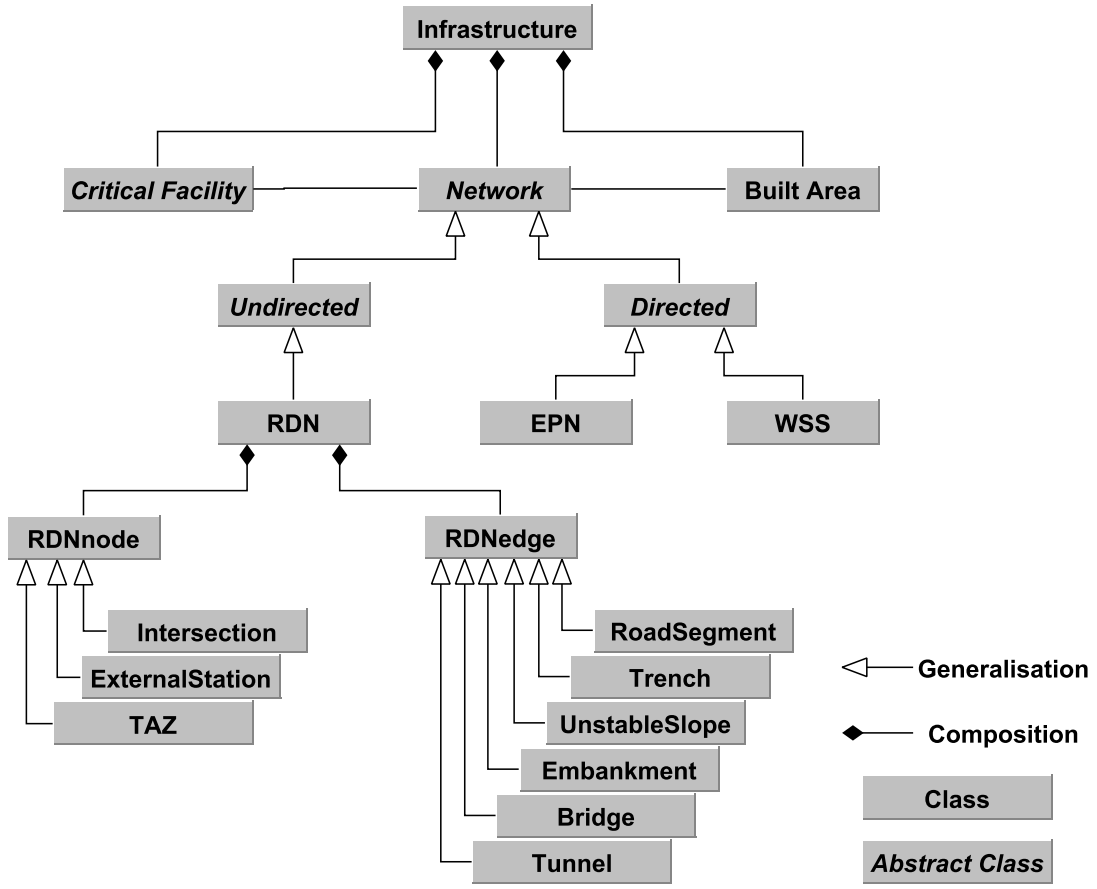

FIGURE 2.6: Details of the object-oriented structure of the road network (RDN) class in OOFIMS, adapted from Modaressi et al. [2014]. EPN stands for electric power network, WSS for water supply system and TAZ for traffic analysis zone.

- component damage states are sampled from the dispersion in the fragility curves.

Based on the component damage states, functional losses are then derived and various simulations methods may be applied, depending on the type of systems, in order to compute the distribution of system performance indicators. An option is available to apply importance sampling instead of plain Monte-Carlo sampling, in order to improve the convergence of the loss distributions. The OOFIMS tool has been successfully applied to the seismic risk assessment of the road network of the city of Thessaloniki in Greece [Argyroudis et al., 2015] and the gas network in the L'Aquila area in Italy [Esposito et al., 2015].

2.1.2.2 System Reliability Methods

As opposed to simulation-based methods, other approaches focus on the investigation of the system's structure and topology, in order to extract some rules that directly provide the system's response from the components' states. Any system may be represented as a graph, where the logical relations between the various elements and events may be explicated (see glossary in Appendix A).

First, a fault-tree [NRC, 1981] is a logic graph, where a set of basic events (i.e. component failures) is assembled through Boolean gates (e.g. AND or OR gates) in order to represent their impact on the failure event of the system (e.g. loss of connectivity or functionality), referred to as the top event. As stated by Bensi et al. [2011], a fault tree is specifically designed to identify the potential causes of a given system failure mode, therefore a single fault tree is usually insufficient to account for all possible failure modes of the system. Due to their visual nature, fault trees are preferentially used for qualitative analyses, although it is possible to build a quantitative framework by assembling the component failure probabilities according to the rules of the Boolean gates. A fault tree can also be represented as a reliability block diagram, which enables to visualize the system's topology and the relations between the components, and between virtual source and sink nodes (see Figure 2.7).

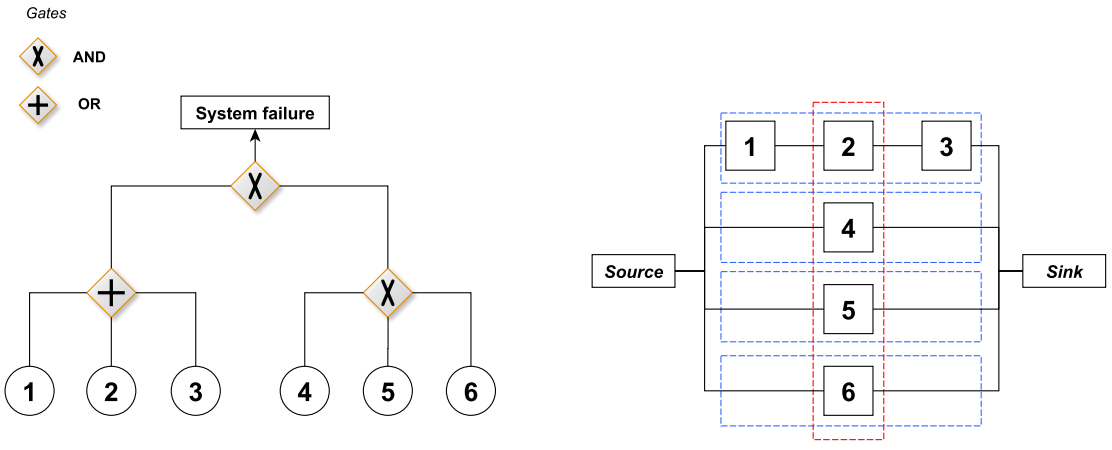

FIGURE 2.7: Example of a fault tree for a virtual system (left) and its corresponding reliability block diagram (right). The dotted lines represent the outline of the MLSs (in blue) and MCSs (in red), as explained in the text. For clarity purposes, the MCSs $\{1, 4, 5, 6\}$ and $\{3, 4, 5, 6\}$ are not represented.

Within a fault tree, it is possible to decompose the system into sub-systems with specific properties (see example in Figure 2.7):

- A *minimal link set* (MLS) is the smallest set of components whose joint survival induces system survival. It corresponds to a series sub-system.
- A *minimal cut set* (MCS) is the smallest set of components whose joint failure induces system failure. It corresponds to a parallel sub-system.

Fault-tree analyses have been used in multiple studies for the reliability assessment of engineered structures. They are often useful to incorporate different types of failure mechanisms at the component level, thus leaving the possibility to account for various hazard types. For instance, in the case of bridges, loading events such as scour, overloading, fire, corrosion, collisions, earthquakes or floods can be assessed throughout the life cycle of the bridge, along with their reliability indices [Davis-McDaniel, 2011, LeBeau and Wadia-Fascetti, 2000, Zhu, 2008]. The location of the MCSs within the fault tree can then be used to identify the most critical events that are likely to lead to bridge failure.

Another application of the fault-tree analysis lies in its ability to identify which components are the most likely to lead to the system failure. This enables to evaluate all possbile component failure combinations within the fault tree, each of these configurations being associated with a given repair cost or recovery time. Therefore, even if the system has a given functionality state, the specific way it has failed is a key information to evaluate the severity of the repairs. This approach has been applied by Porter and Ramer [2012] to a data centre submitted to an earthquake, thus enabling the computation of the downtime duration. Ferrario and Zio [2014] have also proposed a new framework, referred to as a 'goal-tree success-tree': it is based on the same concept as fault trees, except that the top event represents the ability of the system to fulfil its function, and that the basics event represent all the components that are required by the system to operate. This approach is applied to a power plant facility subjected to an earthquake, while each component failure is associated with a recovery time.

The formalisation of the system reliability with respect to the component failures has been achieved by Song and Kang [2007] and Kang et al. [2008], which introduce the matrix-based system reliability method: in this framework, the probability of the system being in a given state results from the matrix product of a matrix of component configurations and a vector of component damage probabilities. The main advantage of

this approach is its computational simplicity, since the probabilities can be estimated with matrix-based operations. In the case of large or complex systems, the size of the matrices can also be reduced by considering sub-systems and adopting a multi-scale approach [Der Kiureghian and Song, 2008]. When the components are statistically dependent, it is possible to assume conditional independence between component events given a set of random variables, which represent 'environmental dependence' or 'common source effects' [Kang et al., 2008]. This system reliability approach has been applied to the seismic vulnerability assessment of various engineered systems, such as:

- A highway network composed of vulnerable bridges [Kang et al., 2008], linking different cities to a hospital. By defining the bridge failures as basic MECE (i.e. mutually exclusive and collectively exhaustive) events, various measures for the system event can be introduced (e.g. disconnection between a city and the hospital, number of failed bridges, disconnection between a county and the hospital...).
- A bridge structure [Song and Kang, 2009], where the component failures represent the basic events. The damage state of the bridge system can then be estimated, based on the component fragility curves. Other measures are also explored, such as the number of failed components as a function of the seismic IM.
- A truss structure [Song and Kang, 2009], composed of a set of perfectly brittle members. By using a global damage state criterion such as the number of failed members, the system failure probability can then be assembled. In the case that one member has failed, the load distribution across the structure is updated and new component events are introduced for the surviving members.
- A network of electrical substations [Der Kiureghian and Song, 2008], where a multi-scale approach is applied in order to decompose the substations into a set of sub-systems of electrical components.

Finally, Bensi et al. [2011] have detailed the application of Bayesian networks to the seismic risk assessment of infrastructure systems. Modelling techniques are proposed in order to generate Gaussian random fields (i.e. to account for the spatial correlation of the ground motion field) and to assess the system performance as a function of the components' performance. Two illustrative examples are described, namely the connectivity of a transportation network and of a high-speed rail system.

The discrete nature of the Bayesian variables is well adapted to the discrete damage states that are usually used for structural systems. However, variables such as seismic IMs or sampled structural properties, which are usually forming the root nodes, have an inherent continuous distribution, thus requiring a discretization process. The Bayesian updating of probabilities can be carried out within a forward or a backward analysis: due to the application of Bayes' theorem, backward analysis (i.e. inference) constitutes a characteristic feature of the Bayesian framework. However, for large systems, the computation of the CPTs for a node with many parent variables can become intractable: to this end, a careful definition of the structure of the Bayesian network or the application of efficient inference algorithms are key steps in the probabilistic assessment of the system.

While Bayesian networks have become a popular tool among transportation network managers for the health monitoring (e.g. fatigue, corrosion) or the life-cycle analysis of bridges [Wang, 2012, Wang et al., 2010], their application to the progressive failure of structural systems subjected to extreme loading such as earthquakes is less common. Mahadevan et al. [2001] have proposed an approach for the reliability reassessment of structural systems with Bayesian networks, accounting for multiple failure sequences as well as for the correlation between the component damage states: the method is applied to structural systems of bars and trusses in parallel or in series, where conditional failure probabilities are updated depending on the state of the other components and the load redistribution. This study shows the benefits of using a Bayesian network when a backward analysis is performed, i.e. the estimation of the component failure probabilities when evidence is provided at the system level. In order to reduce the number of damage configurations, algorithms such as branch and bound or truncated enumeration are recommended to discard insignificant (i.e. low probability) failure sequences.

Bayesian networks have also been used by Banazadeh and Fereshtehnejad [2011] for the identification of the different failure mechanisms of steel moment frames. Failure modes are defined as the sequence of plastic hinges that form across the frame until the collapse of the structure. The Bayesian network formulation enables also the introduction of basic random variables (i.e. root nodes), such as record-to-record variability or modelling parameters, with the possibility to track the effect of specific configurations on the occurrence of failure modes.

2.1.3 Multi-Risk Analysis

While the aforementioned studies provide a clear framework for the analysis of critical infrastructure, one could argue that they are mainly focused on single risk analyses. Due to the inter-dependencies between systems and the large spatial extent covered by most lifelines, it is necessary to consider a multi-risk framework, where cascading or coincidental events may lead to unforeseen system failures [Paté-Cornell, 2012]. Also, the inclusion of various hazard types and damaging mechanisms may result in harmonization issues at the level of fragility models and their interpretation in terms of physical or functional damages.

2.1.3.1 Multi-Hazard Frameworks

The FP7 MATRIX project [Zschau and the MATRIX Consortium, 2010–2013] has focused on the hazards that are the most likely to affect Europe, namely earthquakes, landslides, volcanoes, tsunamis, wild fires, storms and fluvial and coastal floods. A distinction is made between the following frameworks:

- Single-type risk assessment, where losses are estimated for a single independent hazard type.
- Multi-type risk assessment, which may result from the occurrence of multiple hazard types, in the following configurations:
  - simultaneous (and possibly independent) events occurring in the same area and time window;
  - cascading events, where a given hazard event may trigger a secondary hazard event.

In the case of independent single risks, the use of probabilistic risk curves is advocated by the MATRIX project, since these enable a straightforward combination and comparison of the considered risk levels. The combination of the aggregated risk that is associated with a given area is performed, thanks to the independence assumption of the considered hazards. The comparison of two independent risks can then be performed for a given return period: the median of the loss distribution curves for the selected return period

can be compared with some significance statistical tests, in order to check whether the differences between the potential losses induced by different hazards are notable or not. Such an exercise is directly aimed at facilitating the decision-making process that is involved in the resource allocation for risk mitigation.

When multiple hazards are considered, interactions have to be taken into account at both the hazard (i.e. cascading hazard events) and the consequence levels (i.e. cascading failure events): whether hazard events are considered as simultaneous or triggered, the aggregation of the total losses usually requires fragility models that are able to account for the joint loading of two or more hazard types (see Figure 2.8) [Marzocchi et al., 2012]. Finally, a combination of event- and fault-tree formulations is often employed in order to ensure an exhaustive exploration of all possible cascading scenarios.

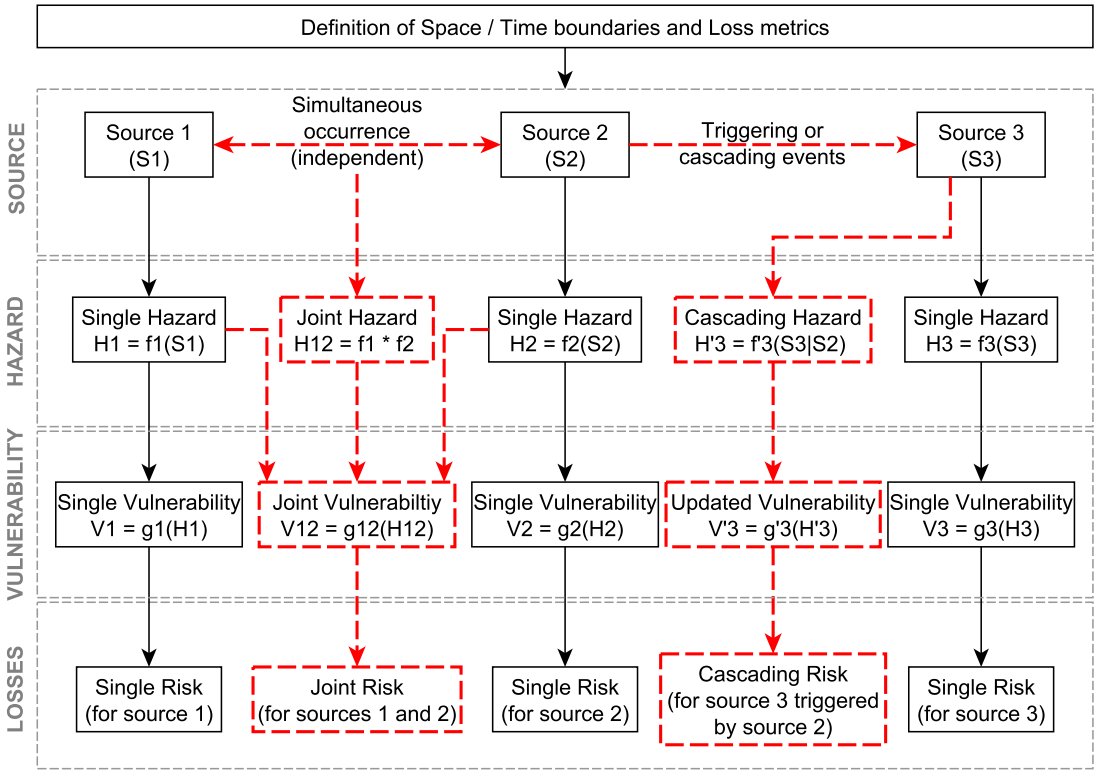

FIGURE 2.8: Multi-risk assessment framework proposed by Marzocchi et al. [2012], for joint independent hazards (sources 1 and 2) and cascading hazards (source 2 triggering source 3).

The MATRIX framework has been applied by Mignan et al. [2014], who define a virtual city exposed to generic types of hazards (e.g. earthquakes, volcanoes, tsunamis, technological accidents, etc.). A dynamic multi-risk process is implemented through

the sequential Monte Carlo Method, which enables the generation of coinciding or cascading events while accounting for time-variant vulnerability and exposure. Different assumptions are tested (e.g. interactions between hazard events, updating of exposure or fragility models, etc.), so that the comparison of the annual probabilities of occurrence of aggregated losses highlights the risk migration that is induced by the multi-risk interactions.

Independently, Selva [2013] has proposed a probabilistic framework for the statistical treatment of multi-risk interactions. Functional forms are introduced for the quantification of all types of interactions (i.e. in terms of hazard, exposure and fragility), while various risk factors are defined in order to identify the different types of contributions from the multiple hazards. The concept of the time window, during which the effects of multiple hazards are still present on a given asset, is recognised as a key parameter of multi-risk analyses.

It should be noted that the aforementioned studies focus on single or independent assets (e.g. a built area or a given facility), while multi-risk assessment in the context of infrastructure systems remains poorly investigated. An attempt in this direction has been made by Gehl et al. [2013c], who study the impact of combined hazard events from a volcanic eruption on Mt Cameroon on various infrastructure systems. These issues are also studied in the FP7 INFRARISK project [O'Brien and the INFRARISK Consortium, 2013–2016], which aims at proposing a stress-test strategy for transportation networks subjected to earthquake, flood and landslide hazards.

2.1.3.2 Multi-Hazard Fragility Functions

Apart from the generation of multi-hazard events, multi-risk interactions have also to be considered at the fragility level, in order to account for the damages that are potentially accumulated from joint or subsequent hazard loadings. Such effects cannot be taken into account by the combination of single-hazard fragility curves, since some hazard loadings will have the effect of altering the state of the structural system and its structural response to subsequent loading, as shown in Figure 2.8.

One of the first of these models is the one developed by Lee and Rosowsky [2006], who consider the combined effect of snow and earthquake loadings on woodframe buildings.

Parametric seismic fragility curves are derived for different values of snow load on the rooftop, thus resulting in a fragility surface expressing the probability of failure with respect to seismic intensity and snow load. Similar considerations are investigated by Zuccaro et al. [2008], who propose vulnerability models that account for cumulated damages during volcanic eruptions. More specifically, the effect of volcanic ash load on the rooftop is quantified with respect to earthquakes and pyroclastic flows: no fragility curves are developed, but load multiplier coefficients or updated vulnerability classes are proposed as inputs to damage probability matrices.

In the case of bridges, the combined effects of scour and earthquakes have become a popular subject in the last few years. For instance, through vibration monitoring on an Italian roadway bridge, Foti and Sabia [2011] have demonstrated the impact of scour on the dynamic response of the structure. It is shown that modal identification may be used as a powerful tool to locate and monitor the evolution of scour at bridge piers. On the other hand, Prasad and Banerjee [2013] have used non-linear time-history analyses to compute fragility curves for RC bridge piers subjected to various levels of scour: the results are presented as a response surface, which shows the evolution of the fragility median with respect to the scour depth and the diameter of the equivalent foundation pile. Alipour et al. [2012] have also used non-linear bridge models to derive parametric fragility curves for various scour depths. The probability of failure due to the combined effects of scour and earthquakes during the design lifetime of the bridge can then be quantified: it is represented as a joint probability density function of scour depth and PGA, which can be compared with the maximum acceptable probability of failure given by design codes in order to obtain scour load-modification factors.

A final example of multi-hazard fragility analysis is the study by Kafali [2008], who considers the fragility of an offshore platform subjected to both wind and wave loadings. The wind drag force acting on the deck structure and the wave force acting on the platform's column are both included in the equation of motion of a single-degree-of-freedom system. A reliability analysis on the quasi-static response of the system enables then the derivation of the probability distribution of failure.

2.2 Methodology

This section analyses the potential shortcomings of the state-of-the-art with respect to the objectives of the thesis. As a result, a methodological framework is proposed and exposed in the last part of this Chapter.

2.2.1 Gaps and Key Issues

Regarding the derivation of seismic fragility curves for bridges, the literature review has identified a wide range of approaches and studies, which demonstrate the significant technical developments that have contributed to this topic. However, a majority of the proposed models mainly focus on the fragility of bridge piers, while the contribution from the other components (e.g. bearings, abutments, etc.) might be neglected: this is not a trivial point, since it has been observed that piers do not fail that often [Nielson and DesRoches, 2004], and if they do, they are expected to yield by design. In this context, Nielson [2005] has made use of a joint probabilistic seismic demand model to account for multiple component damage states, while system reliability methods such as the one by Song and Kang [2009] enable the formalisation of the derivation of system fragility curves. Such techniques remain however to be systematically applied to wider scale real-life problems.

On the other hand, existing global damage scales for seismically induced failures focus on the qualitative description of the state of each component type for each damage grade. These damage scales are designed to be consistent in terms of damage severity across all component types, however there is usually little justification or evidence to support this point. Moreover, the translation of these global damage states into functionality losses remains unclear, even though such loss metrics constitute critical inputs to the system evaluation models that are needed to quantify indirect consequences. Some references [FEMA, 2003] propose restoration curves or traffic disruption models based on the physical damage of bridges: however one can argue that the damage to a given component might lead to a much shorter repair time than another, while both component damage states correspond to the same global damage grade in current approaches.

If ground failure and flood hazards are added in the context of a multi-risk analysis, the harmonization of the fragility models between the different hazard types is hindered by several issues, which are overlooked by the literature:

- There are usually conceptual differences in the respective definitions of fragility curves between hazard types (e.g. probabilistic models versus vulnerability functions). In the case of ground failure or floods, the actual fragility curves are rather scarce and they are derived through a variety of approaches.
- The main obstacle resides in the different damage scales that are used across all hazard types, thus making it difficult to reconcile the consequences in a harmonized multi-risk framework. While earthquake damage scales tend to be specified through global damage scales, ground failures or floods usually apply loading on localized areas of the bridge, thus contributing to the failure of specific components.
- Multi-risk interactions must be taken into account at the fragility level as well. However current fragility models that consider cumulated damage from joint hazard loadings are very scarce, the most common interaction being the combined effect of scour and earthquake.

In terms of seismic risk assessment to infrastructure systems, simulation-based methods have been the object of significant developments in the last decade, thus allowing the derivation of probabilistic loss curves for a wide range of system performance indicators. These methods have proven to be very efficient for the prediction of average risk levels, however the quantification of low-probability high-consequence events remains difficult due to the nature of the sampling techniques used. On the other hand, non-simulation methods, such as Bayesian Networks or other system reliability methods, are able to explore all possible configurations of the system, thus providing exact probabilities of occurrence of potentially catastrophic events. However, such approaches usually suffer from computational issues when addressing real-life complex systems.

Finally, it appears that multi-risk frameworks have been successfully developed for single assets or independent elements (i.e. built areas), while infrastructure systems have not been addressed from this angle yet. This seems quite paradoxical, since spatially distributed infrastructure are precisely the type of assets that are potentially exposed to a

wide range of hazards, while a failure at a given location might be able to propagate over the whole infrastructure. The harmonization of uncertainty sources from various hazard types constitutes also a challenge in order to provide a robust multi-risk assessment approach that accounts for possible interactions between hazards.

2.2.2 Summary of Proposed Framework

In view of the current difficulties to reconcile damage events from different hazard types, a methodological framework for the multi-risk assessment of infrastructure systems is developed, with the specific aim of harmonizing the fragility models for various hazard types. At the bridge level, the proposed approach starts from the observation that the specific effects of various hazard loadings have to be assessed at the local level, in order to ensure that all failure modes are accounted for. The different component damage states can then be reconciled by considering their effects on the bridge functionality instead of using solely the definition of the physical states. If harmonized multi-hazard fragility functions can be generated, the multi-risk assessment of a road network becomes straightforward, provided that the hazard events are properly specified in terms of spatial and temporal dimensions.

Hence the procedure that is presented in this thesis can be summarised in the following steps (see Figure 2.9):

- The infrastructure system (e.g. road network) is decomposed into its physical elements (e.g. bridges), which are in turn decomposed into structural components (e.g. piers, bearings, etc.). This choice is motivated by the need to treat the road infrastructure as a system (i.e. the network) of sub-systems (i.e. the physical elements), as opposed to conventional frameworks that consider the vulnerability of physical elements on a more global scale. The present work is focused on bridges and their decomposition into structural components, however a similar appraoch is applicable to other elements such as tunnels or embankments.

- For each component, the failure modes that are specific to each type of hazard loading are identified, based on the analysis of post-disaster reports or existing damage scales (i.e. Chapter 3). As discussed in the previous sections, the various types of structural components and hazard loadings may lead to a wide range

of damage mechanisms, which all have to be accounted for in the context of a multi-risk analysis.

- For each component failure mode previously identified, specific loss metrics (e.g. repair duration, functional loss, etc.) are proposed through an expert-based survey, in order to quantify the consequences in terms of functionality (i.e. Chapter 3). The novelty of this step lies in the identification of the functional losses induced by specific component failure modes, which has the effect of greatly refining the loss assessment and harmonizing the potential contribution from each hazard loading.

- In parallel, for each of the component failure modes, hazard-specific fragility curves are derived at the component level. This step is necessary in order to quantify the probability of occurrence of each component failure mode. It has to be component- and hazard-specific, since fragility derivation methods and related assumptions vary greatly between the different hazard types (i.e. Chapter 4).

- The knowledge of the functionality losses associated with each component failure mode enables then the creation of a hazard-harmonized damage scale, which contains system failure modes that are consistent in terms of functionality (i.e. Chapter 5). The identification of these system failure modes in a multi-hazard context enables the definition of top events at the bridge level that may be triggered by the occurrence of hazard-specific component failure modes, thus ensuring the harmonization between the various hazard loadings considered.

- For each of the system failure modes previously identified, hazard-harmonized fragility curves are assembled at the system level, based on the relevant component fragility curves (i.e. Chapter 5). Bayesian Networks are investigated as a modular and efficient probabilistic tool with respect to the matrix-based system reliability approach. Thanks to the Bayesian Networks, system fragility curves (i.e. probability of occurrence of system failure modes) are assembled from the probabilities given by the hazard-specific component fragility curves, while accounting for the statistical dependence between the damage events.

- Uncertainty sources are identified throughout the process, so that they can be propagated into the final loss estimations (i.e. Chapter 6). This step is mostly dedicated to the quantification of uncertainties related to the choice of possible models (i.e. epistemic uncertainties), for ground-motion prediction equations or

fragility curves. The objective is to show how the uncertainty sources may influence the global risk assessment, depending on various levels of knowledge of the studied area.

- Finally, the hazard-harmonized fragility functions can be used to compute the probabilistic distributions of losses at the infrastructure level, in a multi-risk context (i.e. Chapter 7). Conventional methods such as Monte Carlo sampling may be used to obtain an estimate of the loss distrubtion, however the use of Bayesian Networks as an alternative to simulation-based methods is also investigated. Issues of computability due to the size and the complexity of the infrastructure are discussed, in order to design a simplified Baysian Network that may be used for the quick updating of loss probabilities (i.e. towards a decision support system).

2.3 Conclusion

While the literature review has shown that infrastructure risk assessment has recently benefited from significant research efforts, it appears that current multi-risk frameworks have not been designed to adress the issue of infrastructure systems such as road networks, which comprise numerous types of interdependent elements.

Therefore an original method is presented in the present work, where physical elements such as bridges are decomposed into their structural components, so that the impact of each hazard loading on each component may be properly modelled and taken into account. The definition of a damage scale in terms of functional losses presents the double merit of harmonizing the respective contributions from various hazard types and providing loss metrics that are directly usable in the performance assessment of the road network.

The construction of a Bayesian Network that represents the interactions between potential damage events in the bridge system constitutes an innovative way to derive system fragility functions that are expressed with respect to multiple intensity measures. Finally, a similar Bayesian framework will also be applied at the network level, for which size limitations and potential solutions in terms of computational load are discussed.

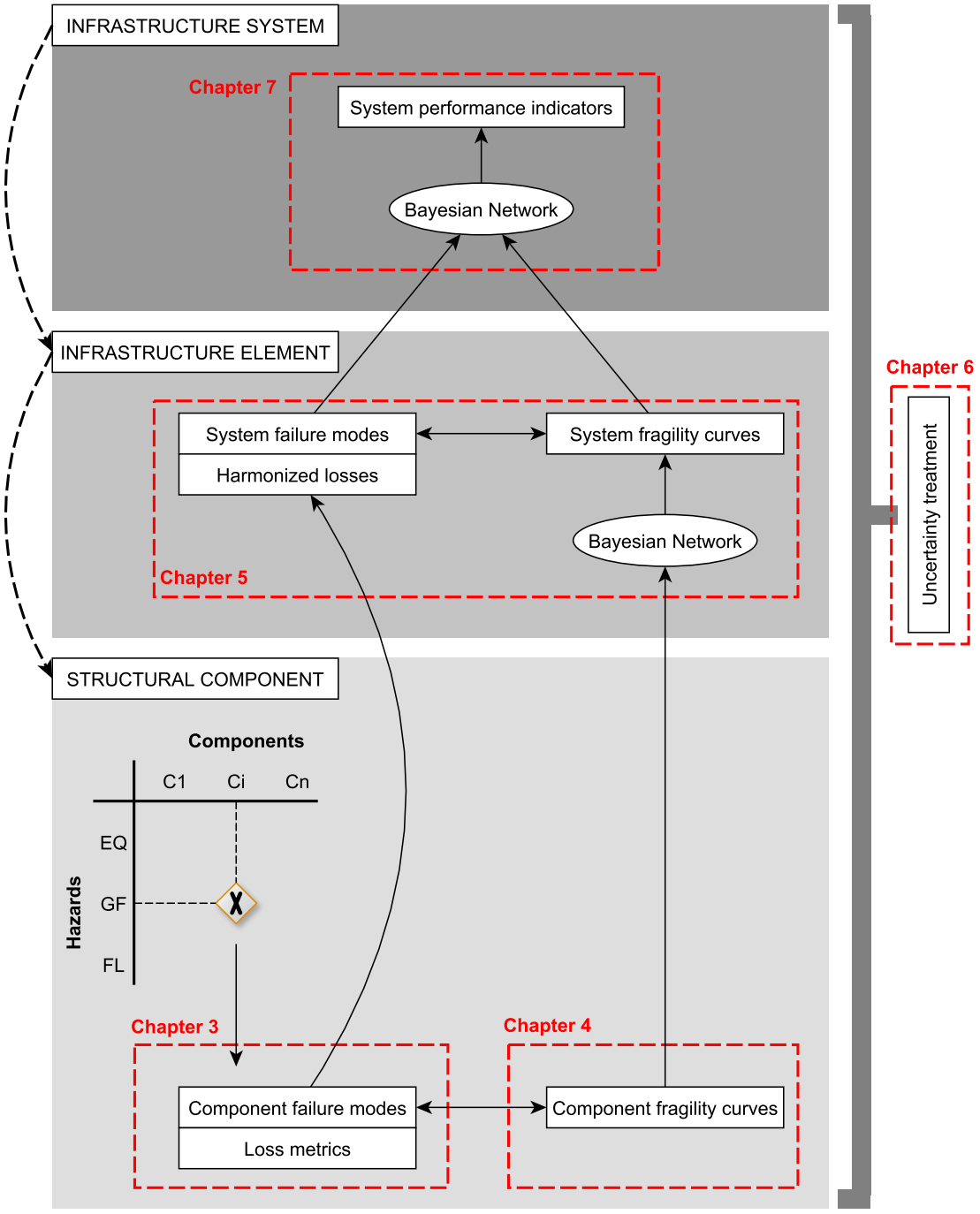

FIGURE 2.9: Summary of the proposed method for the multi-risk assessment of road infrastructure.

Chapter 3

Bridge Failure Modes and their Functional Consequences

3.1 Introduction

This chapter is dedicated to the first step of the proposed framework, which consists in identifying the bridge damage states at the component level. The main objective is to account for all possible failure modes from different hazard types and to associate them with induced losses and functional consequences, in order to facilitate the harmonization of the fragility curves in the later steps.

Section 3.2 presents the most common components that are found in highway bridges, along with a description of their role within the system and a summary of their structural features. The starting point of this inventory is the bridge taxonomy [Silva et al., 2014] that has been defined in the frame of the SYNER-G project.

For each of these components, Section 3.3 classifies the most common damage states or failure modes that are found for each type of hazard loading. This inventory is based on a literature review and an account of past damaging events, leading to a failure modes matrix for each combination of component and hazard type.

Finally, Section 3.4 establishes an association between each component failure mode and a set of loss metrics. The adopted method relies on an expert-based survey, which leads to probabilistic functionality curves given the component damage state: measures

such as the duration and cost of repair operations and the functional losses (e.g. speed reduction or lane closure) are essential to harmonize the impact from all hazard types and to quantify the performance on the road infrastructure.

3.2 General Description of Bridges

The following paragraphs describe the main components that usually comprise a bridge system. As it will be shown in the next sub-sections, the geometry and the structural characteristics of a given bridge heavily influence the component types that need to be considered. Within the frame of the INFRARISK project, the considered case-study areas are located in Europe and especially along the Italian highway network. Therefore this section focuses on bridge types that are consistent with the inventory of these areas, i.e. mostly RC multi-span bridges with simply-supported decks.

3.2.1 Typological Classification

One of the key results of the FP7 SYNER-G project consists in the collection and review of seismic fragility functions for critical infrastructure components. More specifically, fragility functions for road and railway bridges have been critically appraised and stored in a Fragility Function Manager Tool [Silva et al., 2014].

The tool proposes a taxonomy for the different bridge typologies, based on a dozen of parameters, such as material, superstructure type, deck type, pier-to-deck connection, dimension, pier type, seismic design or regularity. This taxonomy is inspired by the classifications that have been defined in previous classifications [Basoz and Kiremidjian, 1996, FEMA, 2003, Nielson, 2005]. The SYNER-G taxonomy comprises the following parameters:

- **Material 1 (MM1):** Concrete (C), Masonry (M), Steel (S), Iron (I), Wood (W), Mixed (MX)
- **Material 2 (MM2):** Reinforced concrete (RC), Post-tensioned or Pre-stressed reinforced concrete (PC), Unreinforced masonry (URM), Reinforced masonry (RM), etc.

- **Type of superstructure (TD1):** Girder bridge (Gb), Arch bridge (Ab), Suspension bridge (Spb), Slab Bridge (Sb)
- **Type of deck (TD2):** Solid slab (Ss), Slab with voids (Sv), Box girder (B), Modern arch bridge (MA), Ancient arch bridge (AA)
- **Deck characteristics (DC):** Width of the deck
- **Deck structural system (DSS):** Simply Supported (SSu), Continuous (Co)
- **Pier to deck connection (PDC):** Not Isolated – monolithic (NIs), Isolated – through bearings (Is)
- **Type of pier column (TC1):** Single-column Pier (ScP), Multi-column Pier (McP)
- **Number of columns for pier (NP)**
- **Type of section of the pier (TS1):** Cylindrical (Cy), Rectangular (R), Oblong (Ob), Wall-type (W)
- **Type of section of the pier (TS2):** Solid (So), Hollow (Ho)
- **Height of the pier (HP)**
- **Spans (Sp):** Single span (Ssp), Multi spans (Ms)
- **Spans characteristics (SC):** Number of Spans (NS), Span Length (SL)
- **Type of connection to the abutments (TCa):** Free (F), Monolithic (M), Isolated – through bearings or isolators (Isl)
- **Bridge configuration (BC):** Regular (R), Semi-regular (SR), Irregular (IR)
- **Level of seismicity (LS):** No seismic design – design for gravity loads only (NSD), Seismic design (SD)

The above taxonomy has been specifically designed for seismic hazard, so that bridges may be classified according to these parameters and potentially associated with a given typology with a known response behaviour represented by existing fragility functions. In the case of other hazard types, fragility developments are usually case-specific, due to the numerous parameters that have to be accounted for. For instance, the fragility

to fluvial floods and induced scour is heavily influenced by the shape of the channel, the material in the stream bed, the position of the piers, the foundations, etc. [Richardson and Davis, 1995]. A refined topography model and knowledge of the surrounding soil and its interaction with foundations are also required to assess the susceptibility of the bridge system to ground failure, since such characteristics are required to feed modelling tools.

3.2.2 Description of Bridge Components

A bridge typology is strongly influenced by the type of components that comprise the bridge system. It is proposed here to focus on multi-span RC girder bridges, with either simply-supported or continuous decks, which represent the most widely used typology for highway bridges in Europe.

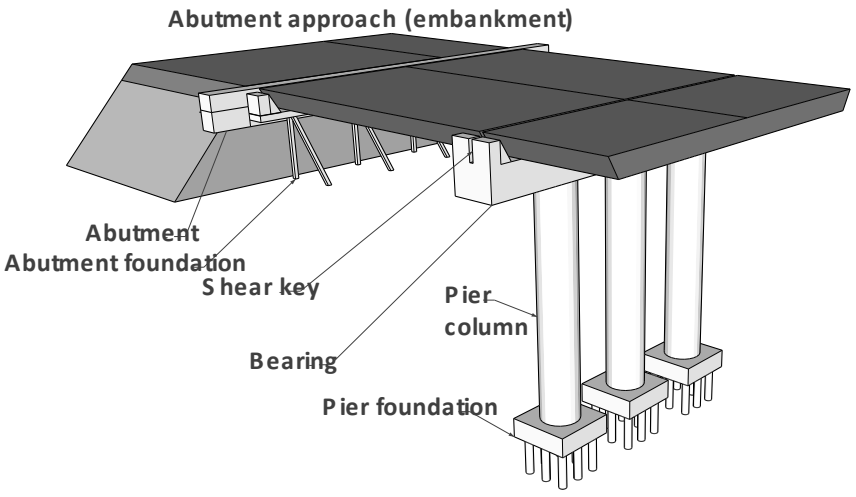

FIGURE 3.1: Sketch of a half-bridge system and its components.

Such bridge types usually include the following components (see Figure 3.1):

- **Piers:** single-/multi-column bents, rectangular or cylindrical columns;
- **Deck:** continuous or simply supported, slab, steel girder, concrete girder, concrete box girder;

- **Abutments:** seat-type abutment supported by a single / double row of RC piles or by a wall;
- **Bearings:** fixed / expansion bearings, bolted / unbolted neoprene pads, elastomeric pad and dowel bearings, steel pendulum bearings, sliding/roller bearings;
- **Pier foundations:** deep or shallow foundations, pile or spread footings, drilled or driven piles;
- **Shear Keys:** interior or exterior shear keys;
- **Expansion joints:** small or large movement joints;
- **Energy dissipating systems**, in retrofitted cases (e.g. viscous dampers or isolators).

3.2.2.1 Piers

Two main characteristics of the piers are the number of columns and the shape of the columns. The number of columns per pier has a significant effect on the seismic response of piers, as it influences whether a flexural or a shear failure mechanism should be considered. Shear failure of piers is estimated by comparing the shear capacity with the yield capacity associated to flexural behaviour. The occurrence of one of the two mechanisms depends strongly on the nature of the connection of the pier system to the deck: it is especially true in the case of transverse loading, where the value and location of the maximum bending moment can significantly vary depending on the pier-deck configuration, as shown by Figure 3.2 [Cardone, 2014]. Smaller flexural moments due to the connection of the pier cap to the deck might then favour the shear failure as the main damage mechanism, since the distribution of the shear demand along the pier remains similar whatever the connection conditions at the pier cap.

Finally, the shape of the pier columns has a strong impact on the flow-structure interactions in the case of a flood, especially for the computation of the scour level. An additional classification may be made on whether the piers are equipped with scour countermeasures or not. The main scour protection methods consist in the application of riprap material or the construction of collars around the base of the bridge piers.

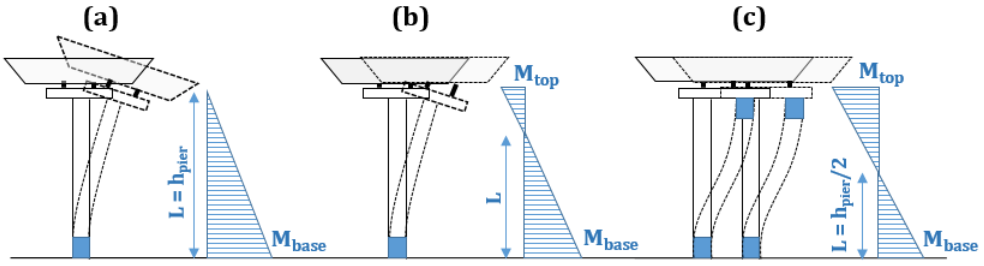

FIGURE 3.2: Typical flexural length L for (a) Cantilever pier with torsionally free deck; (b) Cantilever pier with torsionally constrained deck; (c) Double bending piers (adapted from Cardone [2014]).

3.2.2.2 Abutments

Seat-type abutments are specifically presented here, because they represent the most widely used abutment type in Italian highway bridges, according to Cardone [2014]. The study by Nielson [2005] presents four types of seat-type abutments, depending on the configuration of the supporting piles and walls (see figure 3.3):

- Gravity-type: the bridge seat consists of a wall that is connected to the ground through a footing, while a full height back wall is used to retain the backfill soil.
- U-type: it is similar to the gravity-type abutment, except that the back wall has a U-shape in order to laterally restrain the backfill soil.
- Spill-through-type: the back wall is not continuous all the way to the ground, and the seat is supported by buttress walls.
- Pile bent-type: it is similar to the spill-through abutment, except that the buttress walls are replaced by RC piles.

While the primary purpose of abutments is to ensure the support of vertical loads, they also have to withstand horizontal loading, whether it results from traffic loads or from seismic actions. In the case of longitudinal loading, two types of behaviours can be identified. When the bridge deck is pulling away from the abutment (extension), the resistance is only provided by the RC piles or walls (active resistance, if the deck is connected rather than just seating on the abutment). If the bridge deck is pushing towards the abutment and the deck-abutment gap is closed (compression), the backfill soil starts

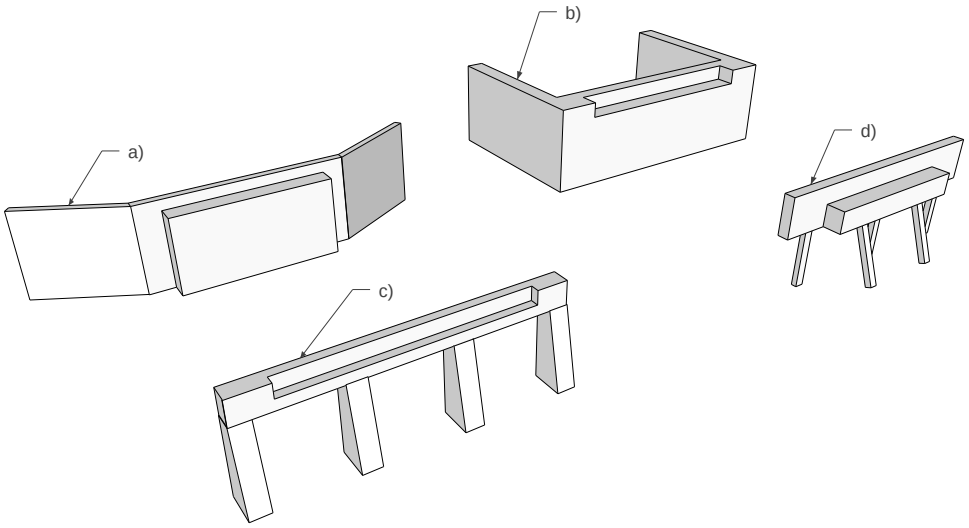

FIGURE 3.3: Schematic view of common abutment types: a) Gravity-type b) U-type c) Spill through-type d) Pile bent-type, adapted from Nielson [2005].

to provide some resistance, along with the RC pile/walls (passive resistance). Therefore the displacement – force relationship of an abutment system usually consists of an asymmetrical curve, where both passive and active mechanisms are described, depending on whether the system is in compression or extension (see Figure 3.4). Dissipating devices, such as dampers, might also be put at the interface between deck and abutment in order to control this movement: hence this parameter is very important for mitigation provisions.

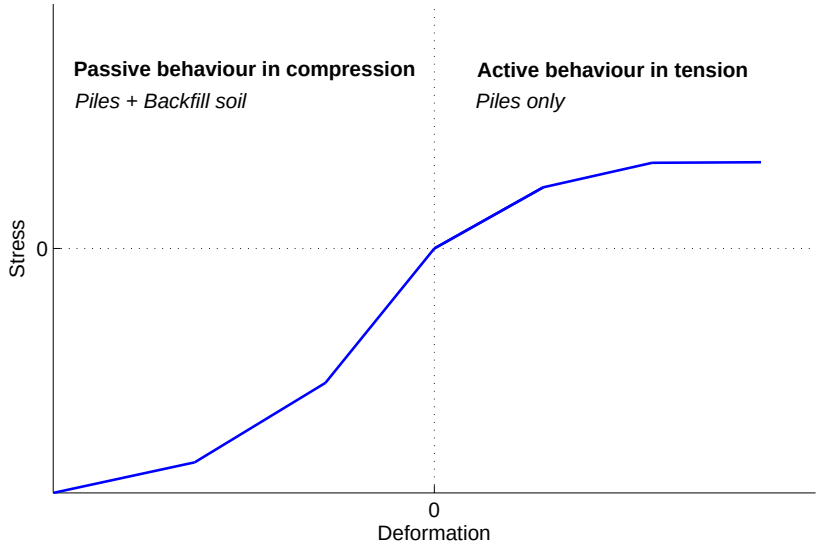

FIGURE 3.4: Illustration of the passive and active behaviours in an abutment.

In the case of transverse loading, the lateral walls are usually not sufficient to make the backfill soil contribute to the horizontal resistance and it can be assumed that the pile bents, if present, provide most of the resistance (active behaviour). Shear keys can also be added between the abutment and the deck in order to restrain some of the lateral movements.

3.2.2.3 Shear Keys

Shear keys are RC blocks that are usually present at abutments in order to prevent excessive lateral displacement of the deck. They are usually used as restraints under non-seismic conditions or moderate earthquakes. However, in the case of large earthquakes, they should act as sacrificial elements in order to prevent the damage of more critical components such as abutment walls. According to CALTRANS [2000], shear keys can be classified according to their aspect ratio $\alpha = h/d$ (see Figure 3.5):

- $\alpha < 0.5$: sliding shear friction model;
- $0.5 \leq \alpha < 1.0$: strut-and-tie model;
- $\alpha \geq 1.0$: flexural / moment resistance model.

An additional distinction can also be on the location of the shear keys, i.e. whether they are located on the extremity or on the inside of the transversal deck section (exterior and interior shear keys, respectively).

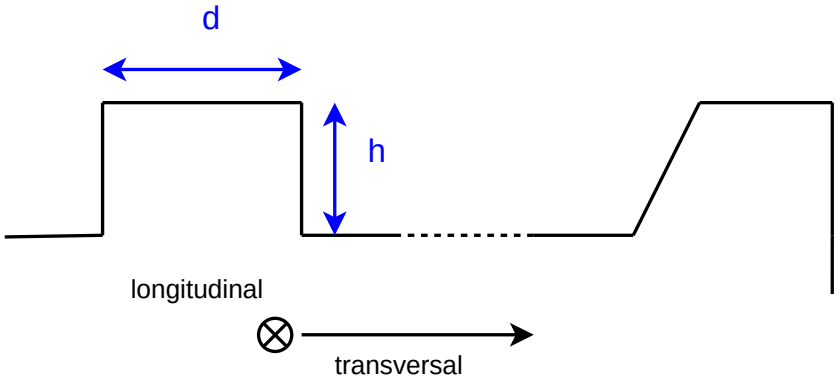

FIGURE 3.5: Schematic view of interior (left) and exterior (right) shear keys.

3.2.2.4 Bearings

Bridge bearings can be classified depending on the type of movement they allow [Nielson, 2005], i.e. fixed or expansion bearings. Only rotations are allowed with fixed bearings, while both rotations and translations – to a certain extent – are permitted with expansion bearings.

Steel bearings can cover many shapes and designs, among which the most common are:

- **Pinned bearings:** they only allow rotations and they are usually composed of a cylindrical steel pin between the pier cap and the deck superstructure, allowing free rotations (see Figure 3.6).

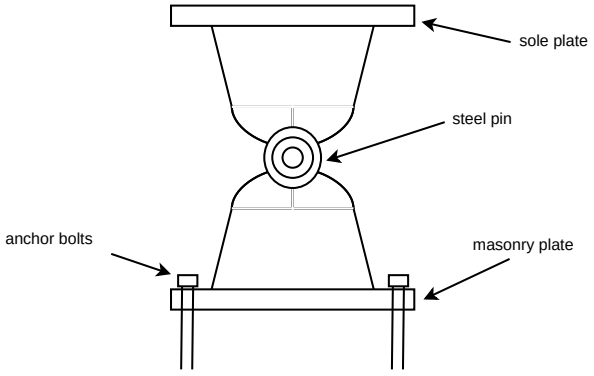

FIGURE 3.6: Schematic view of a pinned bearing.

- **Rocker bearings:** sometimes referred to as steel pendulum bearings, they allow only rotations if they are pinned, and only one-dimensional translations otherwise (see Figure 3.7). They are also referred to as high-type bearings, as opposed to sliding bearings (low-types).

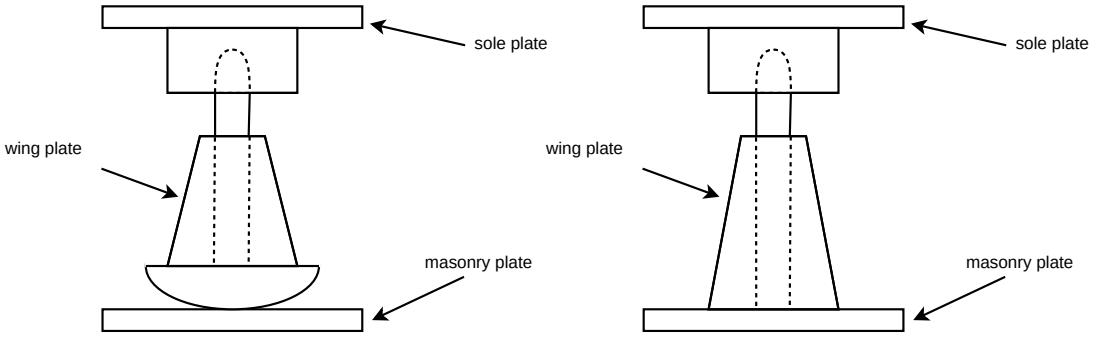

FIGURE 3.7: Schematic view of an expansion rocker bearing (left) and a pinned rocker bearing (right).

- **Roller bearings:** they allow one-dimensional translations, but no rotational movements. They are composed of one or several steel cylinders than can roll when the bearing takes up forces from the superstructure (see Figure 3.8).

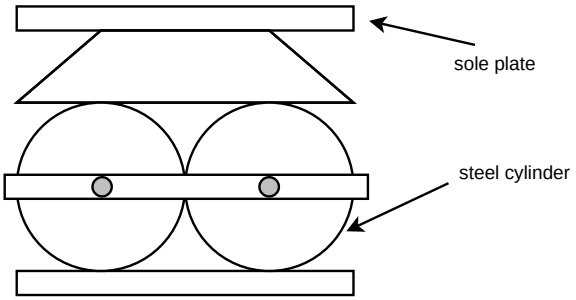

FIGURE 3.8: Schematic view of a roller bearing.

- **Sliding bearings:** expansion sliding bearings allow one dimensional translations, but no rotational movements, while the fixed version allows for rotation while restricting translations. They are the simplest form of bearing, since they are mainly comprised of the sole and masonry plates. The sliding plate is usually made of another material, like stainless steel or bronze to ease up the sliding. Expansion bearings are usually found with a guide plate that is bolted to the masonry plate in order to limit the translation to one direction (see Figure 3.9).

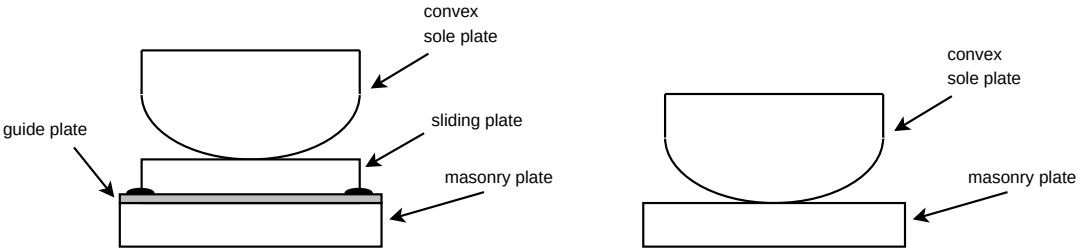

FIGURE 3.9: Schematic view of an expansion sliding bearing (left) and a fixed sliding bearing (right).

Apart from steel bearings, elastomeric pad bearings are also a common alternative, and expansion bearings of this type can allow bi-dimensional translations (in both longitudinal and transversal directions), as well as rotational movements. Elastomeric pads can be either bolted or unbolted to the sole plate: their respective damage mechanism will then differ, as explained in Figure 3.10.

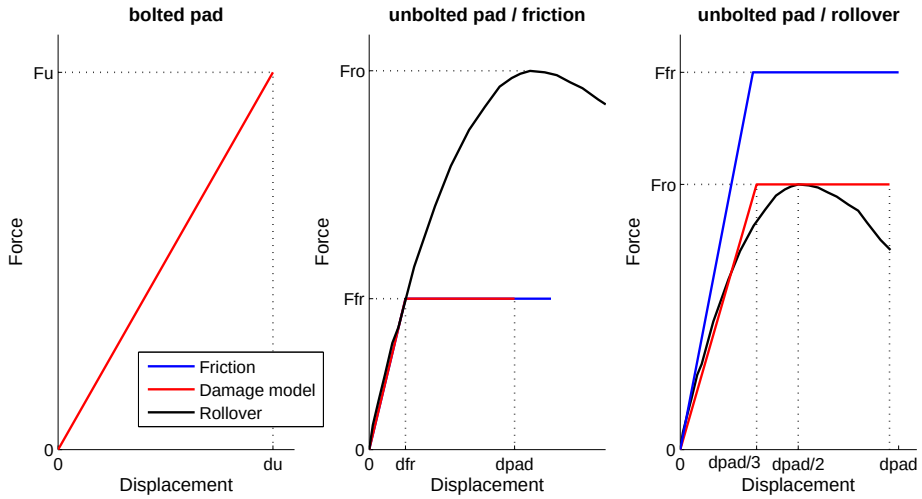

FIGURE 3.10: Possible failure mechanisms for neoprene pads: (a) bolted – rubber shear failure (b) unbolted – slipping, if low axial load and thin pad (c) unbolted – rollover, if high axial load and thick pad (adapted from Cardone [2014].

3.2.2.5 Pier Foundations

Pier foundations typically consist of a footing (i.e. pile cap) that is supported by a buried group of piles, while other types of foundations are simply comprised of a single drilled or driven pile. The foundation type plays a significant role in the seismic response of the whole bridge, since it ensures the transfer of inertial forces and determines the nature of soil-structure interactions. However, pile foundations are usually over-designed due to the difficulty to inspect structural damages on buried elements. As a result, the piles may be modelled as linear elastic components.

In terms of flood-induced scour or ground failures, the foundation depth is an essential characteristic. For instance, in the case of deep foundations, there is usually a portion of the pile length that is not designed to support the pier, so that it can be excavated to a certain extent without endangering the stability of the bridge (i.e. the deeper portion of the pile is still providing enough support).

3.2.2.6 Deck

The deck superstructure can either be made of reinforced concrete or steel, or composite materials. Deck spans are usually supported by steel girders or a box-girder system. For shorter span lengths, slab decks can also be found: they are assembled from precast prestressed concrete sections. Finally, a major typological feature that determines the

global behaviour of the bridge is whether the deck is simply supported or continuous (no free rotations of the pier-deck connections).

3.2.2.7 Energy Dissipation Systems

Existing bridges may be retrofitted through the application of energy dissipation systems at the interface between the pier cap and the deck. These devices can consist of friction dampers, viscous dampers or active dampers, but the objective remains the same, i.e. generating large hysteresis cycles in order to reduce the amount of inertial forces, while staying within the specified range of deformations.

3.3 Identification of Component Failure Modes

As observed in Chapter 2, each of the aforementioned bridge components is potentially vulnerable to various types of hazard loadings: therefore these local damage mechanisms (i.e. component failure modes) need to be identified and organized for each of the hazard types considered (i.e. earthquake, ground failure and flood). The possible damage states that correspond to each component are identified with a literature review, before being reviewed and summarized in a multi-hazard table of component failure modes.

3.3.1 Component Failure Modes from Earthquakes

This section reviews some of the recent studies that describe damage states and corresponding limit values for various bridge components exposed to seismic hazard.

3.3.1.1 HAZUS Technical Manual for Earthquakes [FEMA, 2003]

In the HAZUS framework [FEMA, 2003], the following damage states are identified for bridges, which are defined at global level but include clear reference to specific components and relate them also to repair needs. The HAZUS damage scale contains five damage states, with DS1 representing the Intact/No damage State:

- DS2 (Slight/minor damage): Minor cracking and spalling at the abutment piles, cracks in shear keys at abutments, minor spalling and cracks at hinges, minor

spalling at the columns (damage requires no more than cosmetic repair) or minor cracking to the deck.

- DS3 (Moderate damage): Any column experiencing moderate (shear cracks) cracking and spalling (column structurally still sound), moderate movement of the abutment (< 2 inches), extensive cracking and spalling of shear keys, any connection having cracked shear keys or bent bolts, keeper bar failure without unseating, rocker bearing failure or moderate settlement of the approach.

- DS4 (Extensive damage): Any column degrading without collapse – shear failure - (column structurally unsafe), significant residual movement at connections, or major settlement of the approach, vertical offset of the abutment, differential settlement at connections, shear key failure at abutments.

- DS5 (Complete damage): Any column collapsing and connection losing all bearing support, which may lead to imminent deck collapse, tilting of substructure due to foundation failure.

3.3.1.2 Study by Nielson [2005]

Nielson [2005] had proposed another damage scale, for which a qualitative description of each of the four damage states at the component-level is provided in Table 3.1.

TABLE 3.1: Description of proposed limit states for bridge components, from Nielson [2005].

Component	Slight	Moderate	Extensive	Complete
Steel bearings	Generation of cracks in the concrete pier	Severe deformation of anchor bolts	Complete fracture of the bolts (toppling or sliding of bearings)	Unseating
Elastomeric bearings	Noticeable deformation	Possible deck realignment and dowel fracture	Necessary girder retention and deck realignment	Unseating
Columns (piers)	Yielding	Cracking	Spalling	Reinforcement buckling
Abutments	Half of first yielding point	First yielding point	Ultimate deformation	Twice the ultimate deformation

A set of prescriptive limit states for different bridge components is also specified (see Table 3.2): the way these values are chosen is based on prescriptions by an analyst (i.e.

performance objectives), with the necessity to define these prescriptions at levels that would be noticeable during a physical inspection of the bridge.

TABLE 3.2: Quantitative limit states for bridge components, from Nielson [2005]. 'High' and 'Low' refer to the height of the bearing profile.

Component	Slight	Moderate	Extensive	Complete
Concrete column (curvature ductility)	1.0	1.58	3.22	6.84
High - steel fixed bearing – long. [mm]	6	20	40	255
High - steel fixed bearing – trans. [mm]	6	20	40	255
High - steel rocker bearing – long. [mm]	50	100	150	255
High - steel rocker bearing – trans. [mm]	6	20	40	255
Low - steel fixed bearing – long. [mm]	6	20	40	255
Low - steel fixed bearing – trans. [mm]	6	20	40	255
Low - steel sliding bearing – long. [mm]	50	100	150	255
Low - steel sliding bearing – trans. [mm]	6	20	40	255
Elastomeric fixed bearing – long. [mm]	30	100	150	255
Elastomeric fixed bearing – trans. [mm]	30	100	150	255
Elastomeric expansion bearing – long. [mm]	30	100	150	255
Elastomeric expansion bearing – trans. [mm]	30	100	150	255
Abutment – active [mm]	4	8	25	50
Abutment – trans. [mm]	4	8	25	50

The limit states are specified with absolute values, which are based on the characteristics of specific bridges (e.g. width of the column cross-section, dimensions of the pie cap, etc.). In the case of columns, the use of curvature ductility (i.e. yield curvature is defined as the curvature corresponding to the yielding of the first reinforcement bar) as the damage measure is a way to ensure that the proposed limit states may be used for other bridge geometries. On the other hand, limit states for bearings or abutments are entirely based on specific geomtries, therefore they should be applied with caution to other bridge types.

In addition to these presciptive limit states, Nielson [2005] has also used a more subjective approach, where the outcome of a survey conducted on bridge inspectors and operators has been analysed in order to quantify so-called descriptive damage states. Both prescriptive and descriptive values are then fed into a Bayesian updating process, which enables the derivation of limit state distributions (i.e. updating of the presciptive limit states based on the data points provided by the expert survey). This step leads to the quantification of a standard deviation β_{DS}, which represents the uncertainty associated with the definition of the damage state threshold.

3.3.1.3 SYNER-G Project [Crowley et al., 2011, Tsionis and Fardis, 2014]

The FP7 SYNER-G project (2009-2013) proposes a review of existing fragility curves for roadway and railway bridges. The available fragility functions are harmonized according to two damage states, i.e. yielding and near collapse.

Damage measures have been defined for piers and elastomeric bearings only. Damage to piers is assessed based on the value of peak chord rotation demand at the member end (at the yield and near collapse damage states), and member peak shear force demand (at the near collapse damage state).

Regarding bearings, shear strain deformation and unseating are adopted as criteria for the near collapse damage state. Experimental data [Bousias et al., 1990] suggest an ultimate shear deformation of $\gamma = 156\%$. Unseating occurs when, in any direction, the displacement of the deck relative to the pier exceeds half of the bearing length.

The review of available fragility functions in the literature has enabled to compare the different existing limit states for piers and elastomeric bearings (see Table 3.3 and Table 3.4 respectively). A large variability is observed between the different proposed limit states: some references propose absolute drift values, while others use measures that are relative to yield curvature or rotation. These values depend greatly on the pier type and the definition that is given to the damage states, thus generating epistemic uncertainty on the estimation of the limit state value, as discussed later.

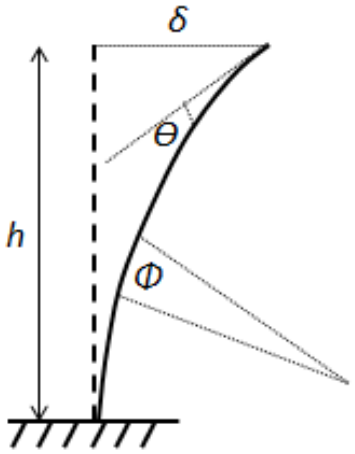

FIGURE 3.11: Deflection of a cantilever beam and associated measures (δ represents the top displacement, θ the rotation and Φ the curvature), which are taken at the most critical location of the beam.

TABLE 3.3: Review of proposed limit states for bridge piers, from Tsionis and Fardis [2014]: the various EDPs used are defined in Figure 3.11.

EDP	Reference	Slight	Moderate	Extensive	Complete
Drift ratio δ/h	Banerjee and Shinozuka [2008]	1.0%	2.5%	5.0%	7.5%
	Kim and Shinozuka [2004]	0.7%	1.5%	2.5%	5.0%
	Li et al. [2012]	1.5%	2.6%	4.3%	6.9%
	Yi et al. [2007]	0.7%	1.5%	2.5%	5.0%
Curvature Φ	Avsar et al. [2011]	Φ_y	-	-	Φ_u
	Cardone et al. [2011]	Φ_y	$0.5\Phi_u$	-	Φ_u
	Choi et al. [2004]	Φ_y	$2.0\Phi_y$	$4.0\Phi_y$	$7.0\Phi_y$
	Jeong and Elnashai [2007]	Φ_y	-	-	-
	Nielson and DesRoches [2007]	$1.3\Phi_y$	$2.1\Phi_y$	$3.5\Phi_y$	$5.2\Phi_y$
	Padgett and DesRoches [2009]	$9.4\Phi_y$	$17.7\Phi_y$	$26.1\Phi_y$	$30.2\Phi_y$
	Zhang et al. [2008]	Φ_y	$2.0\Phi_y$	$4.0\Phi_y$	$7.0\Phi_y$
Rotation Θ	Qi´ang et al. [2012]	Θ_y	$2.0\Theta_y$	$6.0\Theta_y$	$11.0\Theta_y$
	Saxena et al. [2000]	Θ_y	$2.0\Theta_y$	$6.0\Theta_y$	$11.0\Theta_y$
	Shinozuka et al. [2000]	Θ_y	-	$2.0\Theta_y$	-
	Yi et al. [2007]	Θ_y	$1.3\Theta_y$	$2.6\Theta_y$	-
Displacement δ	Monti and Nistico [2002]	$0.5\delta_u$	-	$0.7\delta_u$	δ_u

TABLE 3.4: Review of proposed limit states for bridge bearings, from Tsionis and Fardis [2014]. When two values are present, the left one corresponds to fixed bearings, and the right one to expansion bearings.

EDP	Reference	Slight	Moderate	Extensive	Complete
Shear deformation of elastomeric bearings	Moschonas et al. [2009]	20%	150%	200%	500%
	Zhang et al. [2008]	100%	150%	200%	250%
Displacement δ [mm]	Choi et al. [2004]	1/–	6/50	20/100	40/150
	Ghosh and Padgett [2010]	6/37	20/104	40/136	187/187

As seen in Table 3.3 and Figure 3.11, the limit states for piers may be based on a wide range of EDPs. Drift ratios are expressed as absolute values: such limit states are very dependent on the detailing of the pier section and on its initial stiffness and ductile capacity, which make these values quite specific to the type of piers studied. Rotation and curvature metrics, on the other hand, are based on yield values that are usually defined by the yielding of the first reinforcement bar within the pier [Nielson, 2005]. Therefore such measures may have a wider application to different types of piers; even though some disparities may observed for heavier damage states (e.g. 30 times vs 5 times the yield curvature for complete damage), thus highlighting the influence of the pier's ductile capacity on its seismic behaviour. Finally, it should be noted that displacement- or drift-based EDPs may also be useful for the estimation of shear failure, while rotation or curvature metrics constitute the most reliable indicators for flexural failure.

3.3.1.4 Study by Cardone [2014]

In conducting a direct displacement-based seismic assessment of Italian bridges [Cardone, 2014], the following performance levels (PL) are proposed by the author, also providing reference to functional consequences:

- **PL1**: Very limited structural damage has occurred. The structure retains nearly all of its pre-earthquake strength and stiffness, and although some minor structural repairs may be appropriate, these generally do not require any traffic interruption.
- **PL2**: Significant damage to some structural elements has occurred but large margin against partial or global collapse still remains. Although the damaged structure is not at imminent collapse risk, it would be prudent to implement structural repairs. This may require traffic interruptions or the installation of temporary bracing systems. The overall risk of life-threatening injury as a result of structural damage is expected to be low.
- **PL3**: Severe damage to some structural elements has occurred but some margin against either partial or global collapse still remains. The structure may be technically repairable but costs would be very high and the closure of the bridge for a long time is inevitable. Injuries may occur during the earthquake; however, the overall risk of life-threatening injury as a result of structural damage is expected to be low.
- **PL4**: The structure continues to support gravity loads but retains no margin against collapse. Extensive structural damage has occurred that potentially implies significant degradation in the stiffness and strength of the lateral-force resisting system and large permanent lateral deformations. Aftershock could induce structural collapse. Significant risk of injury exists and the structure may not be technically repairable.

According to Cardone [2014], the deformation limit states for each of the bridge components (see Table 3.5) are consistent with each other: it is assumed that one component reaching a given damage state corresponds to the equivalent performance level of the bridge system. This is further explained in the following:

Piers:

Damage states for piers depend on the expected collapse mechanism: either ductile collapse mechanism due to the formation of plastic hinges, or brittle shear failure. In the case of flexural failure, the pier top yield and ultimate displacements, respectively d_y and d_u, can be estimated by assuming an elastic perfectly plastic moment-curvature relationship. If shear failure is possible, the displacement d_{sh} is set to correspond to the intersection between the flexural behaviour of the pier and its shear strength (see Figure 3.12).

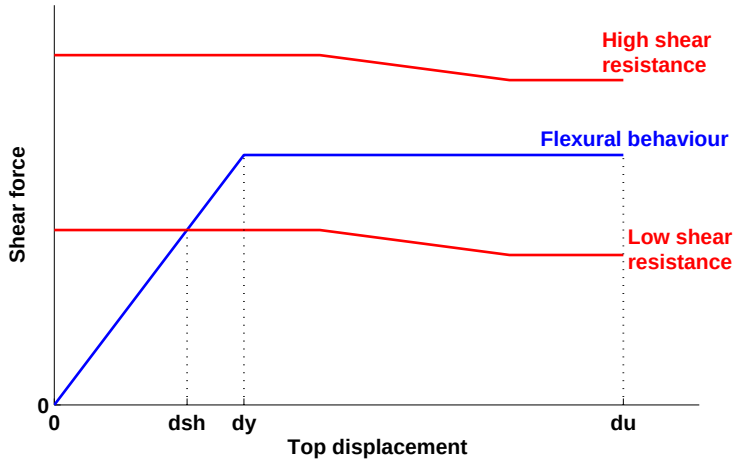

FIGURE 3.12: Possible failure modes for piers and corresponding limit values, according to Cardone [2014].

Abutments:

The emphasis is put here on the longitudinal response of seat-type abutments on piles, which represent a typical abutment type in Italian bridges. The behaviour of the abutment depends on the gap between the deck extremity and the abutment back-wall. Until the gap is closed, the deck's inertia forces are mainly soliciting the bearings. After gap closure, the deck is in direct contact with the abutment back-wall and can mobilize the passive backfill pressure. Therefore the following damage states can be defined for the deck-abutment subsystem:

- **DS1:** deck longitudinal displacement is equal to d_{gap} (gap width, usually ranging from 20 to 50 mm in Italian highway bridges), which corresponds to joint closure.

- **DS2:** deck longitudinal displacement is equal to $d_{y,ab}$, which corresponds to the attainment of the passive resistance of the backfill soil. Typical values of $d_{y,ab}$ range from 80 to 120 mm.
- **DS3:** deck longitudinal displacement is equal to $d_{y,ab} + 2/3(d_{u,ab} - d_{y,ab})$, where $d_{u,ab}$ corresponds to the ultimate displacement of the abutment-backfill system. Experimental studies by Stewart et al. [2007] propose $d_{u,ab} = d_{gap} + 0.10h_w$, where h_w is the back-wall height.
- **DS4:** deck longitudinal displacement is equal to $d_{u,ab}$.

Shear keys:

Shear keys located at the abutments of bridges are generally designed to provide transverse restraint to the deck during service load and moderate earthquakes. In the case of strong earthquakes, shear keys are designed as sacrificial elements to protect abutment walls and piles from damage. This implies that the shear keys should break off before damage occurs in piles and abutment walls. Two damage states are proposed:

- **DS1:** deck displacement in the transverse direction is equal to $d_{gap,t}$, corresponding to joint closure.
- **DS3:** deck displacement in the transverse direction is equal to $d_{u,sk}$, corresponding to shear key failure, either by sliding shear mechanism or by strut-and-tie mechanism.

Fixed bearings:

Fixed bearings that are based on steel hinges or dowel steel bars experience an elastic behaviour until collapse, which is characterized by either attainment of shear strength or premature failure of anchor bolts:

- **DS2:** displacement is equal to d_{fix} (ratio between shear strength and elastic stiffness), corresponding to the collapse of the device or of the anchor bolts.
- **DS3:** displacement is equal to $d_{fix} + 2/3(d_{uns} - d_{fix})$, where d_{uns} is the displacement corresponding to deck unseating from pier cap or lintels.

- **DS4:** displacement is equal to d_{uns}.

Pendulum, sliding or roller bearings:

The cyclic behaviour of these bearings is governed by the frictional resistance between sliding/rolling surfaces. These types of bearings are not designed to absorb seismic displacements and their displacement capacity is generally quite low. Sometimes, sliding and roller bearings present a stopper, after reaching their displacement capacity, to prevent deck unseating. On the other hand, pendulum bearings may be subjected to vertical instability. The following damage states are then proposed for sliding and roller bearings:

- **DS1:** displacement is equal to d_{max}, corresponding to the displacement capacity of the bearing under non-seismic conditions (traffic loads, temperature changes, shrinkage, creep, impact forces, etc.).
- **DS2:** displacement is equal to $d_{max} + 1/3(d_{uns} - d_{max})$, where d_{uns} is the displacement corresponding to deck unseating from pier cap or lintels.
- **DS3:** displacement is equal to $d_{max} + 2/3(d_{uns} - d_{max})$, where d_{uns} is the displacement corresponding to deck unseating from pier cap or lintels.
- **DS4:** displacement is equal to d_{uns}.

For pendulum bearings, the proposed damage states are:

- **DS1:** displacement is equal to d_{max}, corresponding to the displacement capacity of the bearing under non-seismic conditions (traffic loads, temperature changes, shrinkage, creep, impact forces, etc.).
- **DS2:** displacement is equal to d_{lim}, where d_{lim} is the horizontal displacement corresponding to vertical instability (e.g. $50 - 60\%$ of the effective height of the pendulum).
- **DS3:** displacement is equal to $d_{lim} + 1/3(d_{uns} - d_{lim})$, where d_{uns} is the displacement corresponding to deck unseating from pier cap or lintels.
- **DS4:** displacement is equal to d_{uns}.

Neoprene pads:

Neoprene bearings exhibit a visco-elastic behaviour and can experience different failure mechanisms: rubber shear failure for bolted neoprene pads; slipping between neoprene and concrete surfaces, and roll-over mechanism for unbolted neoprene pads.

Bolted neoprene pads exhibit a linear visco-elastic behaviour up to shear strains of the order of $200 - 300\%$, usually. Therefore, the proposed limit states are expressed as a function of the shear strain amplitude of rubber.

Unbolted neoprene pads with small rubber thickness and/or low load pressure usually experience a slipping failure mechanism. Beside large residual displacements, slipping can also produce damage to bearings, through tearing of rubber, distortion of steel reinforcement and heating generated by sliding. A linear visco-elastic behaviour followed by a pure friction behaviour is expected for such a mechanism. Therefore the proposed limit states are the following:

- **DS1:** displacement is equal to d_{fr}, corresponding to the attainment of the friction resistance.
- **DS2:** displacement is equal to $d_{fr}+1/3(d_{pad}-d_{fr})$ where d_{pad} is the pad dimension in the motion direction.
- **DS3:** displacement is equal to d_{pad}.
- **DS4:** displacement is equal to d_{uns}.

The roll-over mechanism may occur with unbolted neoprene pads with large rubber thickness and/or high load pressure: the free edges of the bearing rotate and the originally vertical surfaces of each side come in contact with horizontal surfaces at both top and bottom. Then, horizontal displacement beyond this point can only be achieved by slipping. It is assumed that the peak horizontal force associated with a roll-over mechanism is attained for a displacement of the order of $d_{pad}/2$. Therefore the proposed limit states are the following:

- **DS1:** displacement is equal to $d_{pad}/3$.
- **DS2:** displacement is equal to $d_{pad}/2$.

- **DS3:** displacement is equal to d_{pad}.
- **DS4:** displacement is equal to d_{uns}.

TABLE 3.5: Proposed global limit states for bridges and corresponding component damage states, from Cardone [2014].

Component	Failure mode	DS1	DS2
Piers	Flexural	d_y	$d_y + 1/2(d_u - d_y)$
	Shear	-	-
Abutment		$d_{gap,l}$	$d_{y,ab}$
Shear keys		$d_{gap,t}$	-
Fixed bearings		-	d_{fix}
Steel pendulum		d_{max}	d_{lim}
Sliding bearings		d_{max}	$d_{max} + 1/3(d_{uns} - d_{max})$
Neoprene (unbolted)	Friction/slipping	d_{fr}	$d_{fr} + 1/3(d_{pad} - d_{fr})$
	Roll-over	$d_{pad}/3$	$d_{pad}/2$
Neoprene (bolted)		$d_{\gamma=150\%}$	$d_{\gamma=200\%}$
Component	Failure mode	DS3	DS4
Piers	Flexural	$d_y + 2/3(d_u - d_y)$	d_u
	Shear	d_{sh}	$1.1d_{sh}$
Abutment		$d_{y,ab} + 2/3(d_{u,ab} - d_{y,ab})$	$d_{u,abs}$
Shear keys		$d_{u,sk}$	-
Fixed bearings		$d_{fix} + 2/3(d_{uns} - d_{fix})$	d_{uns}
Steel pendulum		$d_{lim} + 1/3(d_{uns} - d_{lim})$	d_{uns}
Sliding bearings		$d_{max} + 2/3(d_{uns} - d_{max})$	d_{uns}
Neoprene (unbolted)	Friction/slipping	d_{pad}	d_{uns}
	Roll-over	d_{pad}	d_{uns}
Neoprene (bolted)		$d_{\gamma=300\%}$	d_{uns}

3.3.2 Component Failure Modes from Ground Failures

Information on the failure of bridges due to ground failures is rather scarce: most bridge piers are designed with deep footings and foundations, which prevents the immediate failure of piers due to shallow ground deformations.

However, in the case of deep landslides or slope failures that generate ground displacement below the depth of the pier footing, it is then possible to witness significant differential displacements at the deck level. One famous example is the Peace River suspension bridge in Canada, which collapsed in 1957 due to a deep landslide that occurred beneath the bridge abutment, at the level of the shale bedrock.

A more common failure mode involves the bridge abutment: when the backfill soil behind the abutment has not been well compacted during the construction phase, earthquake shaking can induce substantial differential settlements and pavement damage on the

approach to the abutment. However, abutment backfill subsidence does not result in very extensive damage. This phenomenon is known as the highway 'bump' [Helwany et al., 2007, Puppala et al., 2009] and is mainly due to the difference in foundation quality between the abutment and the approach slab, with the bridge system usually experiencing considerably less vertical settlement than the adjacent pavement. Werner et al. [2006] propose a damage scale based on the extent of approach-fill settlement in inches:

- **No damage:** settlement < 1 inch, no repairs needed.
- **Slight damage:** settlement between 1 and 6 inches, repair consists of mud jacking (coring holes and pumping in grout) and then ramping up.
- **Moderate damage:** settlement > 6 inches, temporary repairs involve building up a ramp, and permanent repairs can be done during off hours (assuming only small-moderate settlement and no fault rupture).

Another common damage mode is the impact of debris that may have been generated by an upstream landslide, with the potential to damage the piers and the deck or to obstruct the water channel. On the other hand, several examples of earthquake-induced liquefaction leading to bridge damage have been mentioned by Dickenson et al. [2002] and Bartlett [2014], such as the 1964 Alaska, 1964 Niigata, 1989 Loma Prieta, 1991 Costa Rica or 1995 Kobe earthquakes: most of the identified failure modes consist in the deformation of bridge embankments or the settlement or tilting of pile foundations, potentially leading to deck unseating in bridges with shallow foundations. The review by Bird and Bommer [2004] of the effect of earthquake-induced ground failures has described two main damage mechanisms: lateral spreading resulting to the failure of slopes or free face (e.g. at bridge abutments) or the vertical settlement of approach embankments. Finally, Dickenson et al. [2002] come up with the same conclusions (i.e. lateral spread on slopes and ground settlement at bridge approaches), even though some pile failure modes are also mentioned (e.g. buckling, plastic hinge or excessive rotation).

3.3.3 Component Failure Modes from Floods

This section reviews some of the recent studies that describe damage states and limit values for various bridge components exposed to flood hazard.

3.3.3.1 HAZUS Technical Manual for Floods FEMA [2005]

According to the HAZUS Flood Model [FEMA, 2005], bridges are not considered as highly vulnerable to inundation mechanisms. However, pier foundations can be strongly affected by erosion or scour and the bridge deck is also susceptible to be dislodged by the hydraulic pressure. Therefore the following failure modes can be considered:

- Scour on pier / abutment foundations: the impact on the overall bridge stability may be different whether the deck is simply supported or continuous. Most bridge failures occur with simple spans, therefore HAZUS recommends that the expected damage for continuous span bridges should be taken to be 25% of that for simple span bridges.
- Overtopping and hydraulic pressure applied on deck.

Scour vulnerability grades are defined for bridges from excellent to critical conditions, which depend on the current state of the foundations, the scour level or the existence of scour countermeasures [Pearson et al., 2002].

3.3.3.2 American Lifeline Alliance Report [ALA, 2005]

The American Lifeline Alliance report [ALA, 2005] on local road systems is based on the analysis of several case-studies. This has led to the identification of some of the most common failures modes for roadway bridges:

- Local scour at piers and abutments with and without permanent structural damage;
- Downcutting of streambeds, which may affect bridge abutments/piers and undercut culvert inlets and outlets;
- Washout of gravel low-water crossings;
- Deposition of bed load that restricts the hydraulic capacity of crossings;
- Debris accumulation that may contribute to backup of water and damage to adjacent properties;

- Shifting of bridge decks due to pressure of rising floodwaters;
- Shifting or migration of waterway channel alignment.

However, some of these damage mechanisms are mostly applicable to minor roads with low clearance crossings, and they are not really consistent with highway bridges, which are the main focus of this study.

3.3.3.3 Study by Lin [2012]

Lin [2012] has identified four main types of bridge failure modes due to scour:

- Vertical failure: it is mainly due to inadequate vertical bearing capacity of the soil and it can manifest through four different failure modes:
  - Undermining of footing base;
  - Penetration of friction pile;
  - Undermining of pile tip;
  - Buckling of pile.
- Lateral failure: it is due to the reduction of the lateral restraints of pier foundations, which may lead to three different failure modes:
  - Pushover failures of piers: significant scour depths reduce the lateral resistance capacity of the soil and the pier, which alters the pushover capacity of the bridge, while lateral loads due to water flow and accumulation of debris tend to increase;
  - Structural hinging of piles: it occurs when the transverse loads applied to the piers trigged excessive bending moments at the base of the piers;
  - Kick-out failures of foundations: if the scour excavates most of the depth of the pier foundations, the lateral loads may dislodge the foundations from the remaining soil cover. This failure mode is especially frequent in the case of shallow foundations.
- Torsional failure: it may occur when skewed flows (i.e. flows with an angle of attack) produce eccentric loads and lead to torsional deformation of piers and piles;

- Bridge deck failure: it occurs when the flow height reaches the deck level and washes out the deck (i.e. overtopping), especially in the case of simply-supported deck spans. It could be argued that this failure mode is more generic to fluvial flood and not limited to scour failure.

A summary of the different failure modes observed over 36 case-study bridges in New Zealand, United States and Canada is detailed in Table 3.6 [Lin, 2012].

TABLE 3.6: Review of failure modes of 36 scour failures, from Lin [2012].

Failure modes	Number	Percentage
Vertical failure	11	30%
Buckling	*2*	*5%*
Not identified	*9*	*25%*
Vertical failure	14	39%
Structural hinge	*5*	*14%*
Pushover failure	*4*	*11%*
Not identified	*5*	*14%*
Torsional failure	1	3%
Bridge deck failure	1	3%
Others	5	14%
Not identified	4	11%
Total	**36**	**100%**

3.3.3.4 Railway Bridge Failure during Flood in the UK and Ireland [Benn, 2012]

The study by Benn [2012] compiles historical events of railway bridge failures due to scour: 69 events have been recorded between 1845 and 2012 and they are summarized in Table 3.7.

TABLE 3.7: Failure classification of 69 water-related failures to railway structures, from Benn [2012].

Failure modes	Number	Percentage
Pier scour	23	34%
Abutment scour	14	20%
Floating debris	10	14%
Other debris	10	14%
Embankment scour	8	12%
Channel modification (e.g. dredging)	4	6%
Total	**69**	**100%**

3.3.4 Summary of Component Failure Modes

The previous sections have identified a wide range of potential failure modes for all bridge components and hazard types. Even though various studies propose different limit state values and different engineering demand parameters, the qualitative description of the damage states or failure modes is mostly comparable between the literature references that have been considered. Therefore the component failure modes that have been described above may be summarized and organised in Table 3.8, for all hazard types.

TABLE 3.8: Summary of the component failure modes identified for bridges.

ID	Component	Sub-type	Failure mode	Damage 'Severity'	Description
Earthquake hazard					
1	Pier	-	Bending	DS1	- Minor cracking/spalling - Yielding
				DS2	- Cracking/spalling (still structurally sound)
				DS3	- Column degrading without collapse (structurally unsafe)
				DS4	- Column collapsing - Reinforcement buckling
2	Pier	-	Shear	DS3	- Brittle shear failure
3	Pier	-	Tilting	DS4	- Tilting of substructure due to foundation failure
4	Abutment	-	Piles	DS1	- Minor cracking/spalling
				DS2	- First yielding point
				DS3	- Ultimate deformation - Vertical offset
5	Abutment	-	Backfill	DS1	- Gap closure
				DS2	- Passive resistance of backfill soil is reached
				DS4	- Ultimate displacement of the backfill system
6	Shear keys	-	Transverse loading	DS1	- Gap closure - Minor cracks

TABLE 3.8: (continued)

ID	Component	Sub-type	Failure mode	Damage 'Severity'	Description
				DS2	- Extensive cracking/spalling
				DS3	- Failure
				DS4	- Deck unseating
7	Bearing	Fixed	-	DS2	- Shear strength reached
				DS4	- Deck unseating
8	Bearing	Steel pendulum	-	DS1	- Bearing capacity under non-seismic conditions
				DS2	- Vertical instability
				DS4	- Deck unseating
9	Bearing	Sliding/ roller	-	DS1	- Bearing capacity under non-seismic conditions
				DS4	- Deck unseating
10	Bearing	Bolted neoprene	-	DS1	- 150% of rubber shear strain amplitude
				DS2	- 200% of rubber shear strain amplitude
				DS3	- 300% of rubber shear strain amplitude
				DS4	- Deck unseating
11	Bearing	Unbolted neoprene	Friction/ slipping	DS1	- Friction resistance is reached
				DS3	- Pad dimensions are reached
				DS4	- Deck unseating
12	Bearing	Unbolted neoprene	Rollover	DS1	- 1/3 of pad dimensions are reached
				DS2	- 1/2 of pad dimensions are reached
				DS3	- Pad dimensions are reached
				DS4	- Deck unseating

TABLE 3.8: (continued)

ID	Component	Sub-type	Failure mode	Damage 'Severity'	Description
13	Bearing	Elastomeric w/ dowels	-	DS1	- Noticeable deformation
				DS2	- Possible deck realignment and dowel fracture
				DS3	- Girder retention and deck realignment
				DS4	- Deck unseating
14	Deck	-	-	DS1	- Minor cracking - Curvature limits reached
				DS4	- Deck collapse
Ground failure hazard					
15	Foundations	-	Slope failure	-	- Differential displacements leading to deck collapse
16	Abutment approach	-	Subsidence/ settlement	-	- Settlement of soil under approach embankment
Flood hazard					
17	Pier foundations	-	Local scour	-	- Scour depth (below/ within/above footing)
18	Pier foundations	-	Streambed downcutting	-	- Piers are affected - Culverts are undercut
19	Abutment foundations	-	Local scour	-	- Scour depth (below/ within/above footing)
20	Abutment foundations	-	Streambed downcutting	-	- Abutments are affected - Culverts are undercut
21	Deck	-	Overtopping	-	- Shifting of deck due to hydraulic pressure
22	Waterway	-	Debris accumulation	-	- Reduction of flow capacity - Backup of water flow
23	Waterway	-	Channel	-	- Shifting/migration of

TABLE 3.8: (continued)

ID	Component	Sub-type	Failure mode	Damage 'Severity'	Description
			modification		waterway channel alignment

In Table 3.8, the field describing the damage 'severity' represents the global damage state (i.e. at the level of the bridge system) that is usually considered to be reached when the given component is damaged through the mentioned failure mode. This classification directly results from the analysis of the qualitative damage scales that have been defined for bridges in the literature. It appears that this information is mostly available for failure modes that are related to seismic hazard, while the current state of the art does not provide well-defined damage scales for ground failures or floods. Therefore it is necessary to harmonize the component damage states by considering functional consequences at the level of the bridge system. This step should lead to:

- the verification of the consistency of the seismic damage scale, by identifying component damage states that may induce disproportionate functional consequences;
- the definition of system failure modes for ground failures and floods, which may be use to create a consistent damage scale for these hazards.

3.4 Quantification of Functional Consequences

Once the physical damage states are defined and estimated through the application of fragility function curves, they need to be translated into functionality measures in order to properly estimate the effect of the damaged network elements on the global system performance, through the use of elaborate traffic models.

3.4.1 Loss Metrics

Functionality measures have to be useful for the subsequent network analysis, depending on the various global metrics that are studied, such as the amount of traffic, the additional delay, the travel distance between two locations or the possibility to conduct

emergency operations (e.g. Modaressi et al. [2014]). To this end, the following loss metrics are proposed to characterize the functional state of a given network element:

- **Functional Loss (FL):** loss of functionality induced by the damage to the element. It can have various effects on the normal operation conditions: reduction of the speed limit, closure of a proportion of lanes, reduction of the vertical load capacity. Speed limit and number of lanes are key parameters to estimate the flow capacity of a road section, which is an essential component of network analysis models. Finally, the reduction in load capacity can provide indications on the type of traffic that will be allowed through the road section (e.g. personal cars, trucks, emergency vehicles, etc.). These specific functionality measures are commonly used to quantify the flow capacity of a road segment in traffic analyses [Zhou and Taylor, 2014], and they present the merit of enabling the computation of both connectivity- or capacity-based performance indicators [Argyroudis et al., 2015].
- **Duration of intervention (Du):** the duration of the repair operations until the element is functional again.
- **Cost of intervention (Co):** the cost of the repair operations, generally expressed as a percentage of the replacement cost.
- **Functional Loss during Intervention (FLI):** the additional functional loss that is induced by the repair operations.

These four loss metrics will serve different purposes, namely (i) the quantification of the direct costs thanks to Co, (ii) the quantification of indirect costs (i.e. consequences of traffic disruption) thanks to FL and Du, and (iii) the elaboration of time-dependent restoration strategies thanks to FL, Du and FLI.

3.4.2 Expert-based Survey

In order to efficiently quantify these loss metrics, it is necessary to consider the physical damage states at the component level, since it has been seen that each component type has very specific failure mechanisms when exposed to different hazard types. Therefore

it is proposed to associate these loss metrics to each of the component failure modes summarized in Table 3.8.

To this end, it is proposed to build these loss metrics by using expert judgement. This decision is motivated by the lack of available empirical data in literature for infrastructure failure events, especially in the European context. Moreover, detailed accounts of failures are required, since the objective is to quantify the consequences of damaged components and not only the global state of the bridge: a thorough survey of past events has revealed that only extreme events (e.g. collapsed bridges) are accurately documented, while less severe events that may lead to modest traffic disruption do not get recorded [Middleton and Imhof, 2009]. Therefore these reasons have led to the adoption of an expert elicitation effort, due to its ability to produce information when empirical information is lacking.

Expert elicitation procedures have been the object of rigorous methodological developments throughout the last decade [Aspinall, 2006, 2010]: Cooke's rational method [Cooke, 1991] has been proven to be an efficient and mathematically sound way to reconcile apparently disparate experts' recommendations. It is based on the following steps:

1. All experts are invited to provide a best estimate and a credible interval (i.e. 5%-95% confidence bounds).
2. Seed questions are designed in order to rate the 'quality' of the experts. Two objective metrics can be defined: (i) calibration score, representing statistical accuracy; and (ii) information score, which represents the extent of the proposed interval compared to a reference uniform distribution.
3. Based on the experts' score, a weighting is applied to the various results.
4. The different intervals proposed by the experts are pooled (i.e. weighted average) in order to build a reconciled distribution of the variable that is investigated.

The main merit of Cooke's method resides in the integration of the uncertainties that are generated by the various experts' contributions, instead of reaching a poentially biased consensus. However great care should be taken when selecting the experts and assessing their contributions, which should be achieved by the seed questions.

Therefore a survey form has been sent to infrastructure managers and experts within the INFRARISK consortium, with the objective to quantify the four loss metrics that correspond to each component failure mode (see Appendix C. Three groups of experts have provided answers to the survey:

- Group 1 (three people). Five years of engineering experience on geotechnical works on transport networks, both design and contractual. Furthermore, relevant literature was consulted: Zezere et al. [2008], Klose [2015], Transport Research Board guidelines, etc.
- Group 2 (around a demi-dozen of people). Experts from various fields were solicited: geotechnical engineering, linear infrastructure, materials (pavements), structures (bridges), underground construction. They work in technical departments providing support to construction sites worldwide, from Australia or Chile to Canada, the United States or the United Kingdom. The range of experience of the different persons varies from a minimum of ten years to probably thirty or more.
- Group 3 (two people). About twenty years of experience in inspection, assessment and maintenance of infrastructure elements. Replies were solely based on own experience and expert judgement, without the use of any documentation or specific case studies assessed.

All groups of experts pointed out the difficulty to provide accurate answers for 'generic cases', since the loss metrics may vary greatly depending on the type of bridge (e.g. size, importance in the network, construction method, etc.). Another issue lies in the harmonization of the answers within each group, some proposed values varying greatly between the experts. Therefore all the answers are provided in the form of lower and upper bounds, in order to account for epistemic uncertainties. The results of the functionality loss assessment survey are summarized in Appendix D.

However, unlike what is recommended in Cooke's method, no seed questions have been submitted to the experts, thus preventing the use of weights in the answers. Unfortunately, this strong limitation is imposed by the modest amount of experts that have taken part in the study. An alternative approach could have consisted in weighting the

answers based on the experience and the size of each group, however the limited number of answers could not justify such a refinement. An extended group of experts could not be mobilised due to the difficulty to find experts whose knowledge spans all hazard types and the necessity to keep these developments within the project's consortium.

3.4.3 Derivation of Probabilistic Functionality Models

The intervals of functionality loss values proposed by the different groups of experts are reconciled by building a probabilistic functionality model for each type of loss metric. An empirical cumulative distribution function can be assembled for each component damage state, as shown in Figure 3.13, using equal weights. This construction corresponds to the 'pooling' step that has been mentioned in Cooke's method.

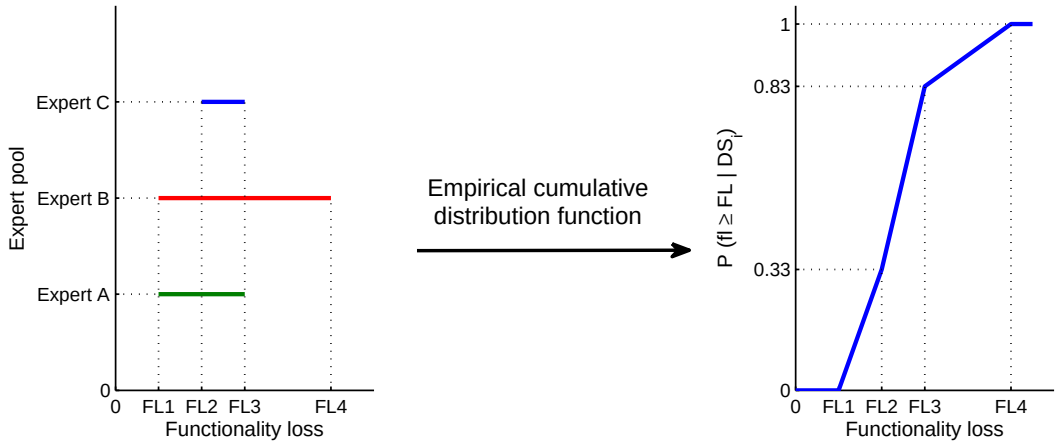

FIGURE 3.13: Construction of a probabilistic functionality model based on the expert-based survey, by assigning an equal weight to all experts' answers.

As illustrated in the hypothetical example in Figure 3.13, the pooling step may be summarised through the following steps:

- Three experts A, B and C propose an interval for the functionality loss induced by the occurrence of damage state DS_i to a given component.
- An empirical cumulative distribution function of the functionality loss is built by averaging the intervals provided by the experts and by converting them into a cumulative distribution function.

- For a given damage state DS_i, the induced functionality loss can then be obtained by sampling a standard uniform variable and reading the corresponding value on the X-axis of the curve.

These probabilistic functionality models can then be used to sample the functional losses that are induced by a given failure mode at the component level. However, the tables in Appendix D reveal that most of these failure modes can only be associated with one or two values, which is not sufficient to get a profile of the cumulative distribution function of losses with good resolution (i.e. most of the component-level functionality loss curves would be step functions, if plotted).

Therefore, for illustration purposes, it is proposed to build the probabilistic functionality loss models at the scale of the global damage states due to seismic risk. As explained in the previous section, most system-level damage scales for seismic risk are defined so that they are consistent across the various component damage states, e.g. a global damage state DS1 (i.e. slight or minor damage) is reached if at least one of the bridge components is in damage state DS1 (e.g. yielding of pier reinforcement, gap closure at bearings or abutments, etc.). The component failure modes in Table 3.8 follow the same logic in the way the damage states are enumerated from DS1 to DS4. Therefore, for a given global damage state, all corresponding component-level functionality loss metrics are assembled as shown in Figure 3.13. Hence, this assumption enables to build functionality models for global damage states DS1 to DS4, for each of the functionality loss metrics.

The choice to build functionality loss curves for global damage states (and not for component failure modes) is motivated by several points:

- More data on loss metrics are available, since all the component failure modes that are included in the given global damage state are considered. Therefore the functionality loss curves may be derived with a higher resolution.
- These global functionality loss models are more easily comparable to some of the loss values that are provided in the literature, since they are all based on global damage states.
- The derived functionality loss models may be used to check the consistency of the corresponding damage scale: a high dispersion in the cumulative distribution

function would imply that the global damage states are poorly constrained, thus demonstrating the necessity to work at the level of component failure modes in order to refine the functionality analysis.

The corresponding probabilistic functionality loss curves for seismic risk are presented in Figures 3.14 to 3.19.

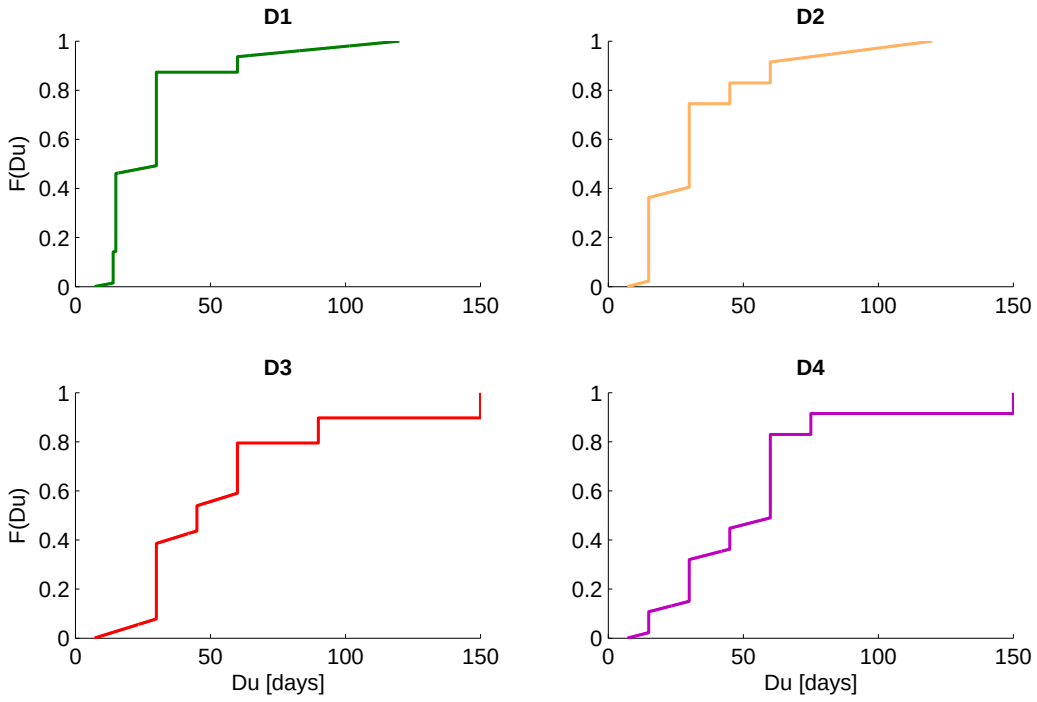

FIGURE 3.14: Duration of repair operations given seismic global damage states DS1 to DS4.

Except in the case of the repair duration and cost metrics, most of the functionality loss models are very coarse and some of them are even not computable (i.e. FLI for DS3 and DS4). This is due to the lack of sufficiently constrained data that have been gathered from the expert-based survey. Therefore these curves should be seen as a first attempt at developing the concept of functionality loss curves, while additional data should be used to better constrain the proposed models.

While comparing the functionality loss curves across damage states, it can also be observed that there is no clear difference between some damage states. For instance, the downtime durations due to DS3 and DS4 are almost identical, or the functional loss expressed in lane closure due to DS2 may be more severe than the one due to DS3. This exemplifies the limitations of the use of global damage states and global fragility

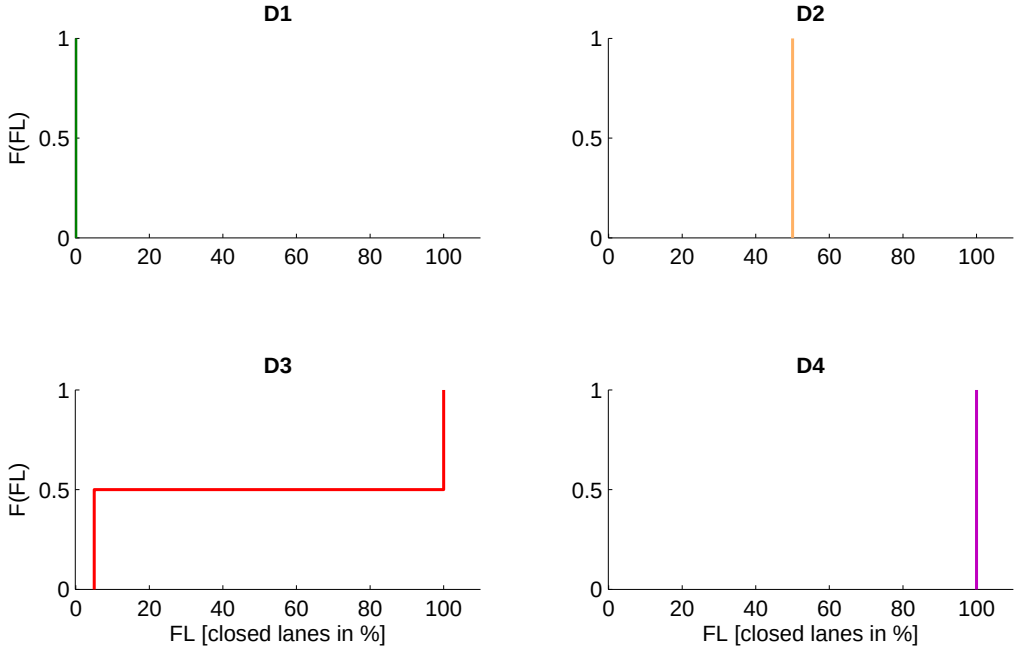

FIGURE 3.15: Functional loss (expressed in proportion of closed lanes) given seismic global damage states DS1 to DS4.

functions. While damage states may be structurally consistent between components, their respective failure or damage mechanisms may induce a wide range of functional consequences that do not necessarily remain consistent at the system level.

Finally, it should be noted that the functional loss models present some inconsistencies. When the bridge has reached damage states DS3 or DS4 (i.e. extensive damage or collapse), the speed reduction model in Figure 3.16 only shows a reduction of around 20%-25%, while the proportion of closed lanes is 100% according to Figure 3.15 (i.e. total closure of the bridge). Therefore some care should be taken when interpreting the proposed functionality models. The proportion of closed lanes appears to be the primary functional loss metric to considered, while the speed reduction may be seen as a secondary measure that can be used to update the speed limit of the remaining lanes. As a consequence, the influence of the speed reduction model is more significant for lighter damage states (i.e. DS1 and DS2) that do no require the closure of most lanes. One may also wonder whether the correlation between functional loss and repair duration is not lost when the component failure modes are directly agggegated into global damage states. In their present form, the functionality loss models may sample

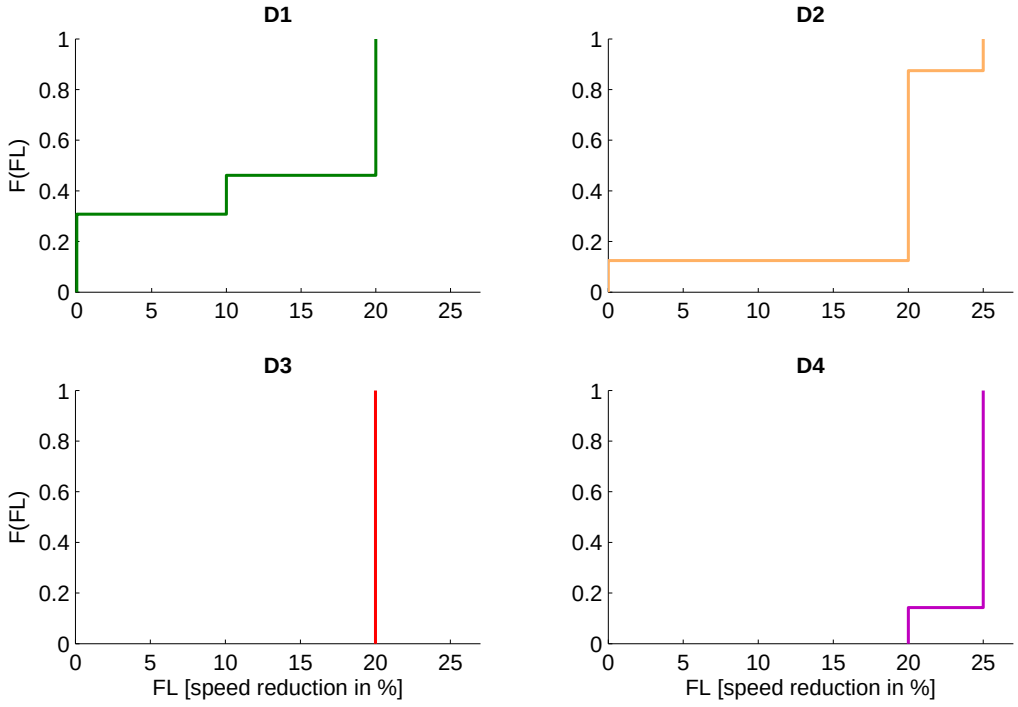

FIGURE 3.16: Functional loss (expressed in speed reduction) given seismic global damage states DS1 to DS4.

high functional losses with short repair times, which are not necessarily consistent with the initial outcomces of the expert-based survey.

Due to the aforementioned reasons, it is shown that the derived functionality loss models, which are based on global damage states, are neither accurate nor useful for a performance assessment of the road network. Therefore it is recommended to consider functionality losses for component-level events and to assess their joint probabilities of occurrence at the level of the bridge system, as it will demonstrated in Chapter 5.

3.4.4 Comparison with existing models

Even though the shortcomings of the previously-derived functionality loss curves have already been demostrated, it remains interesting to compare them with some functionality scales that are found in existing loss models. To this end, a literature review is conducted in order to extract functional loss values or downtime durations from past case-studies. In the case of bridges subjected to seismic risk, the following references provide information on the induced losses:

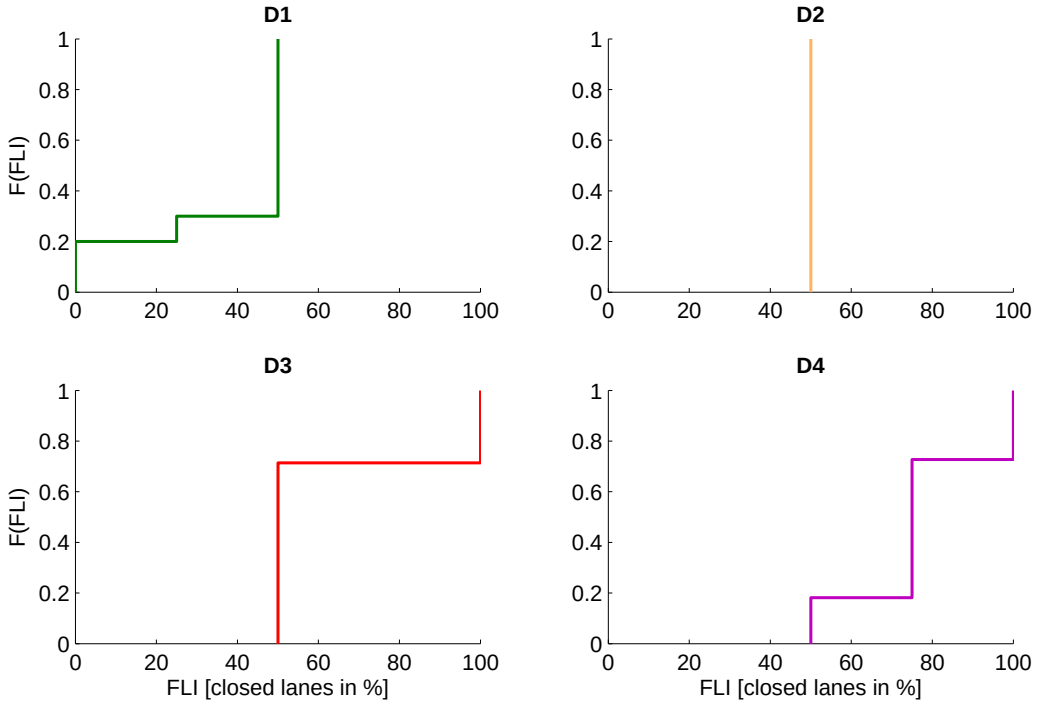

FIGURE 3.17: Functional loss during intervention (expressed in proportion of closed lanes) given seismic global damage states DS1 to DS4.

- Werner et al. [2006] propose values of traffic capacity, repair costs and durations for three damage states of bridge approach fill (i.e. three levels of soil subsidence), as summarized in Table 3.9.

TABLE 3.9: Functionality and repair model for damages to bridge approach fill, from Werner et al. [2006].

Damage state	Traffic capacity	Repair cost	Repair duration
D1 – settlement $\leq$ 1 inch	100%	0%	–
D2 – settlement $\leq$ 6 inch	0%	12%	1 day
D3 – settlement $>$ 6 inch	0%	55%	4 days

- In the framework of the SYNER-G project, the work from Argyroudis and Kaynia [2014] based on REDARS approach [Werner et al., 2006] provides functional losses in terms of lane closure for four global damage states at the system level, as summarised in Table 3.10.

- In the HAZUS recommendations [FEMA, 2003], restoration curves for highway bridges are proposed in order to show the evolution of functionality with time. However, the present approach, which is based on probabilistic functionality curves, is not compatible with deterministic restoration curves. Still, the HAZUS curves can provide two useful data points, which are summarised in Table 3.11:

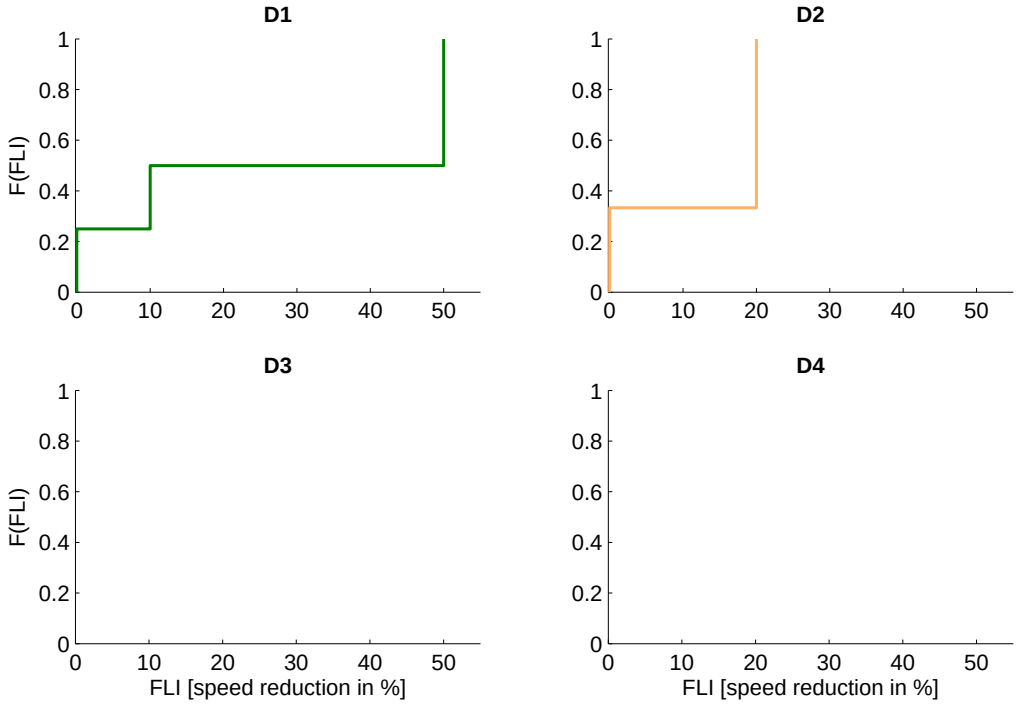

FIGURE 3.18: Functional loss during intervention (expressed in speed reduction) given seismic global damage states DS1 to DS4. No values are available for DS3 and DS4.

TABLE 3.10: Functionality levels for bridge systems, from Argyroudis and Kaynia [2014].

Damage state	Functional loss
D1	open
D2	partially open
D3	closed
D4	closed

– the remaining capacity immediately after the event gives the functional loss;

– the moment when the capacity is fully restored again gives the repair duration.

TABLE 3.11: Functionality and repair model for highway bridges, adapted from HAZUS [FEMA, 2003].

Damage state	Functional loss	Repair duration	Repair cost
D1	25%	1 day	1% – 3%
D2	70%	7 days	2% – 15%
D3	95%	130 days	10% – 40%
D4	100%	370 days	30% – 100%

These few data points from the considered literature references enable 'literature-based' functionality models to be built, by using the same technique as in Figure 3.13. Finally, a direct comparison can be made between the expert-based functionality models and the literature references (see Figures 3.20 to 3.23).

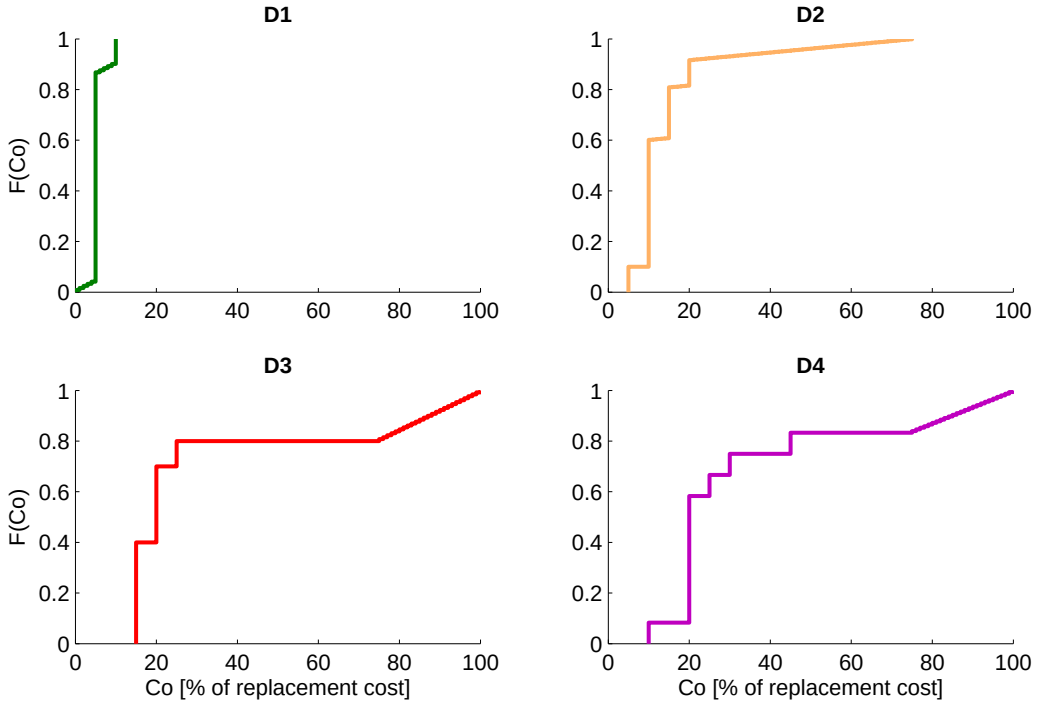

FIGURE 3.19: Cost of repair operations given seismic global damage states DS1 to DS4.

The insufficient number of data points and the coarseness of some of the functional models (e.g. step functions) make it very difficult to draw definite conclusions on the relevance of the proposed functional models. Still, most of the loss metrics are within the same range as the literature-based values, especially the cost model for global damage states in Figure 3.23. However, the repair duration model for global damage states in Figure 3.21 does not seem to be consistent with the values that have been extracted from the HAZUS restoration curves: the downtime duration appears to be overestimated for low damage states (DS1 and DS2) and underestimated for heavier damage (DS3 and DS4). This is partly due to the fact that the proposed duration model does not evolve much from DS1 to DS4, the values being stuck around 20-50 days. Globally, it appears that the proposed models tend to underestimate the losses for heavier damage states. This may constitute a limitation of the proposed approach, which is based on the individual component failure modes: the extensive damage or the global collapse of a bridge usually involves multiple components that are in a joint failed state, while the proposed approach considers that only one component may be damaged, thus leading to reduced losses or restoration times.

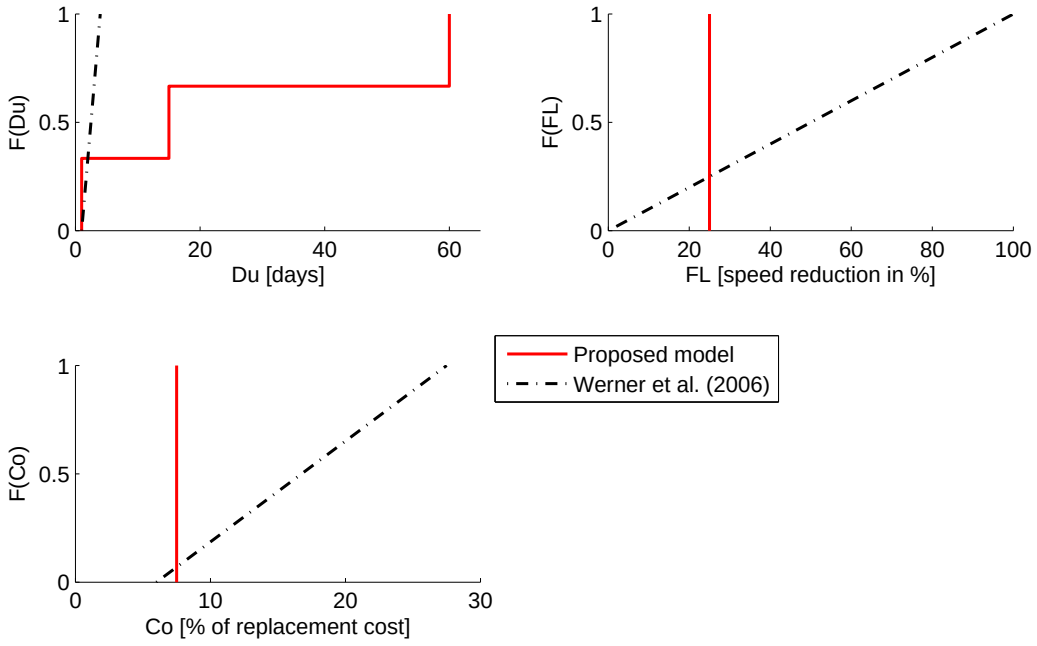

FIGURE 3.20: Comparison of the functionality models for subsidence of bridge approach fill (failure mode #16-DS1).

3.5 Conclusion

A general presentation of the most common structural components of bridges has led to the inventory of typical damage states for the identified components. These component damage states are based on potential failure modes that are specific to the type of hazard loading and the type of component. Table 3.8 has been assembled to summarise the component failure modes for earthquakes, ground failures and floods. A total of 23 failure modes, each having two or more damage states (i.e. 49 damage states in total), are described for 10 bridge components.

Since these component damage states are not always easily reconciled in terms of damage 'severity', functionality loss metrics are introduced in order to quantify their impact on the bridge system. To this end, the results of the expert-based survey have led to the development of probabilistic loss models at the component level. In the case of seismic hazard, the aggregation of functionality losses according to conventional damage scales has led to poorly constrained loss models, thus demonstrating the inaccuracy of global damage states at the system level. Moreover, the loss models proposed here should be

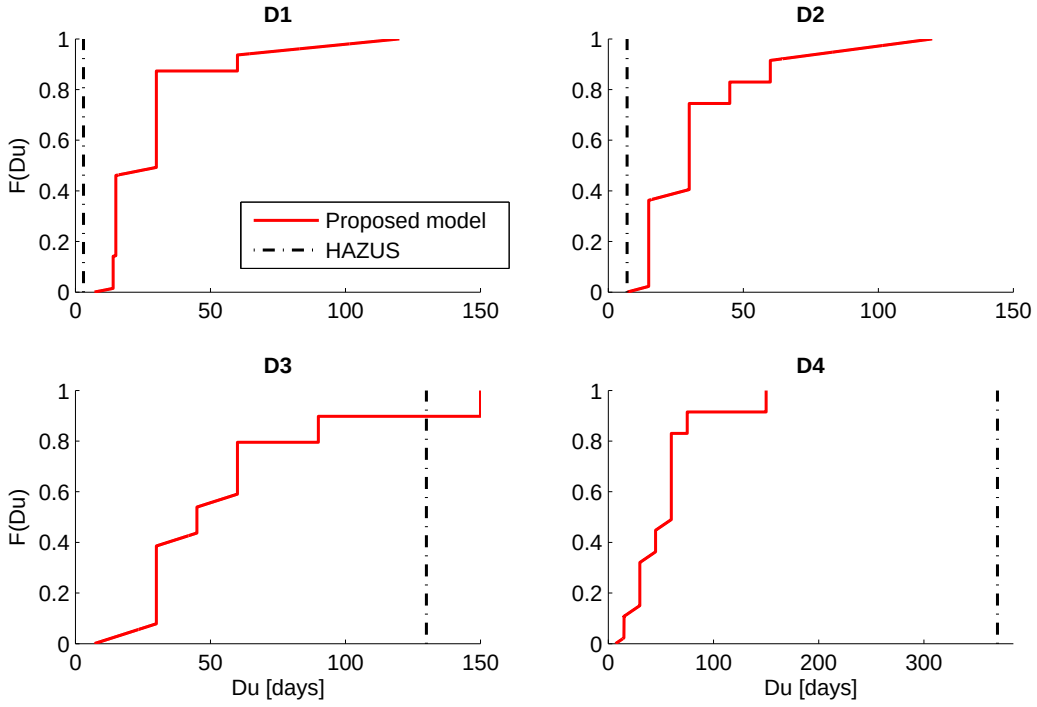

FIGURE 3.21: Comparison of the repair duration models for global damage states to bridges.

adopted with caution, due to the relatively small amount of data that has been gathered: further involvement of infrastructure managers is necessary to refine these models.

The identification of all component damage states constitutes the first step of the proposed method, while the probability of occurrence of theses damage events must then be quantified for the different hazard types. The derivation of theses component fragility curves will be the object of the next Chapter.

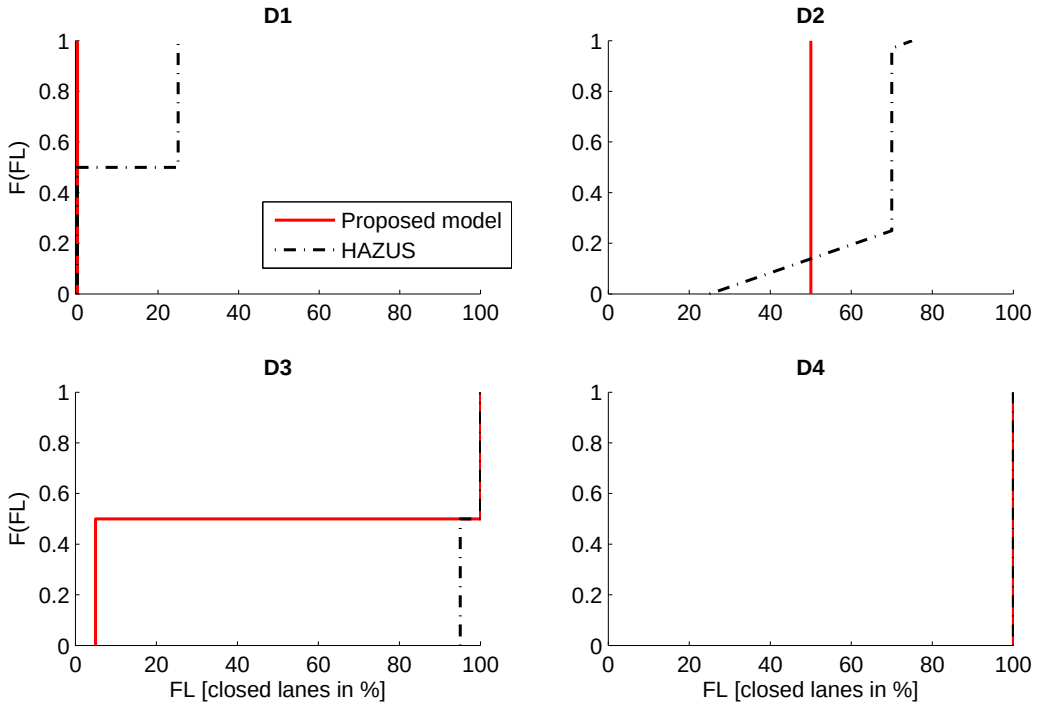

FIGURE 3.22: Comparison of the functional loss models for global damage states to bridges.

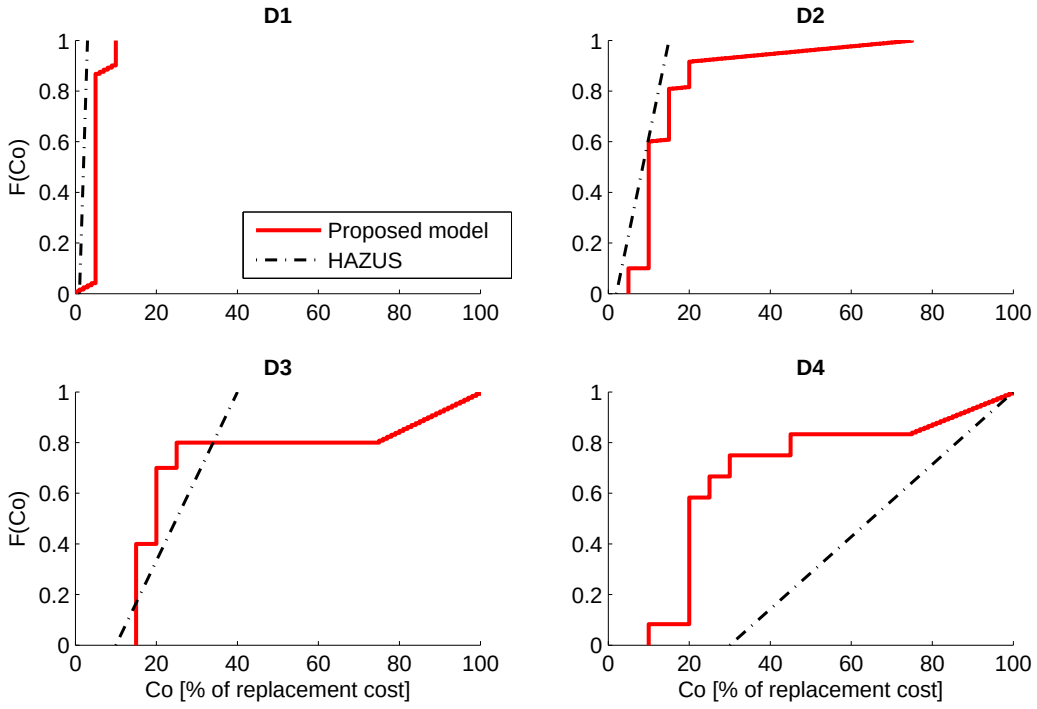

FIGURE 3.23: Comparison of the cost models for global damage states to bridges.

Chapter 4

Derivation of Hazard-specific Component Fragility Curves

4.1 Introduction

The vulnerability or the susceptibility of transport infrastructure elements to extreme loading scenarios, such as natural hazard events, can be quantified through fragility curves, which have become a popular tool, particularly in seismic risk analyses. These probabilistic tools may be applied to other hazard types such as ground failures or floods. Since a given infrastructure element usually comprises a wide range of structural or non-structural components, the same damage mechanism or engineering demand parameter usually cannot be applied to all components. The same rationale can also be developed for the different hazard types, which generate various types of loadings on each component. As a result, the component- and hazard-specific damage mechanisms that have been identified in Chapter 3 need to be associated with a set of component fragility functions, as shown in Figure 4.1.

The derivation of hazard-specific component fragility curves is demonstrated through a single bridge model, which is fully detailed in Section 4.2. A given bridge system is selected as the test-structure for the application of all fragility derivation methods. First, fragility curves for earthquake-induced damage are derived in Section 4.3, where non-linear dynamic analyses are performed on the finite element model of the bridge.

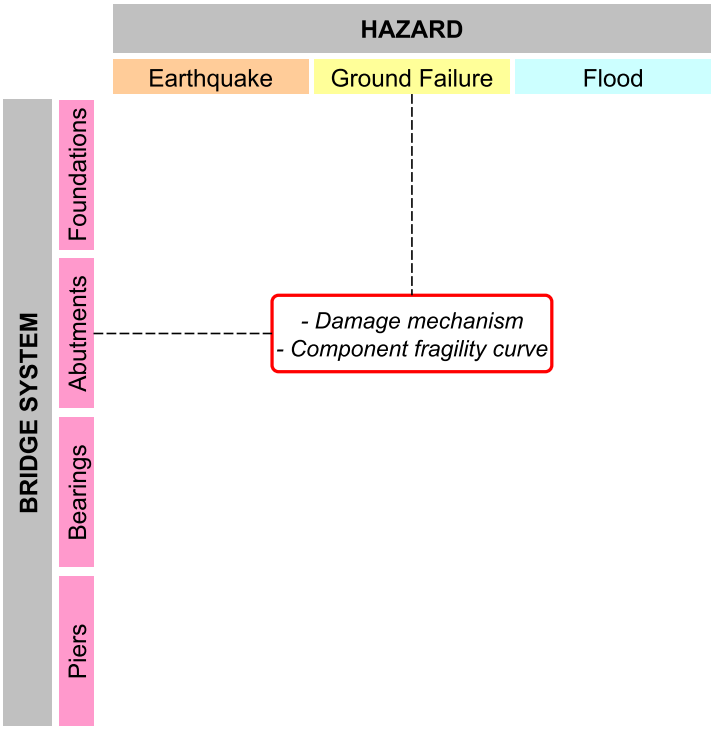

FIGURE 4.1: Decomposition of a bridge system into component types and related hazards. For each couple of hazard loadings and components, potential damage mechanism are identified and corresponding fragility curves are derived.

Fragility curves for ground failure are then presented in Section 4.4, where the probability of reaching circular slope failure at the abutments is quantified through the limit equilibrium approach. Available fragility curves for the subsidence of backfill soil are also discussed. Then, Section 4.5 details the adopted procedure for the derivation of fragility curves for flood-induced scour, while also existing models for deck unseating due to hydraulic pressure are considered. While the latter sections address the fragility assessment for various single hazard, Section 4.6 will consider potential cases of multi-risk interactions, which lead to the derivation of damage-dependent fragility functions. Finally, in the case of seismic hazard, Section 4.7 investigates the accuracy of simplified assessment methods such as DDBA for the prediction of component-level damage states, in an attempt to check whether such methods are applicable for a fast fragility assessment at a larger scale (i.e. road network comprised of dozens of bridges).

4.2 Proposed Bridge System

The model of a hypothetical yet realistic bridge is developed, assuming as reference for structural and geometrical properties the archetype bridge already studied by Nielson [2005]. It is a multi-span simply-supported concrete (MSSSC) bridge composed of two seat-type abutments and two piers with three cylindrical reinforced concrete columns. Deck displacement is restrained by elastomeric bearings (i.e. alternation of expansion and fixed devices) in the longitudinal direction. Several additional features have also been integrated to the original model [Nielson, 2005], in order to account for the effect of multiple hazards (see Figure 3.1):

- Shear keys have been added at the pier caps in order to model the constraints and determine the bridge response in the transversal direction.
- At each bridge extremity, an embankment approach is added in order to simulate the transition between the plain roadway segment and the bridge and to evaluate the effect of ground failure.
- Foundation elements have been added at the pier footings in order to properly model the effects of scour.

All other components follow the geometry of the MSSSC bridge described by Nielson [2005]. The deck consists of three independent spans that are supported by two piers, which are in turn composed of three RC cylindrical columns. The middle span has a length of 24.4 m, while end spans are 12.2 m long, thus resulting in a total bridge length of 48.8 m. The deck comprises a row of eight concrete girders across its width (i.e. 15 m): each of these girders is connected to the pier cap through an elastomeric bearing. Expansion and fixed bearings are alternating between each row in order to ensure a proper relative movement of the independent deck spans.

4.3 Fragility Curves for Earthquakes

As stated in the literature review in Chapter 2, a wide range of analytical methods and levels of analysis are available for the seismic fragility assessment of bridge systems.

This section is devoted to the definition of the model for seismic analyses. Moreover, the effect of previous damages due to potential floods is taken into account to derive damage-dependent fragility curves.

For the purpose of deriving the fragility curves, non-linear dynamic analyses on the bridge model are carried out with a set of selected records. The various assumptions that have been adopted for this approach are discussed in the following subsections.

4.3.1 Bridge Model for Seismic Analysis

The seismic inputs are successively applied to the bridge system along the longitudinal and transversal directions, in order to assess the fragility of the bridge for all axes of loading. In the longitudinal direction, ten components are considered (i.e. piers P1 and P2, abutments A1 and A2, fixed and expansion bearings B1 to B6), as well as in the transversal direction, except that the bearings are then replaced by the shear keys (i.e. Sh1 to Sh6), as shown in Figure 4.2.

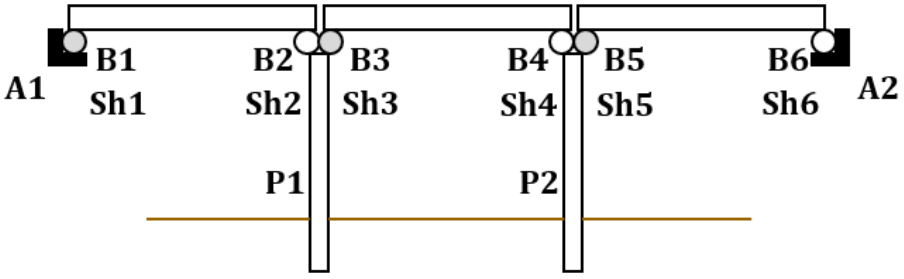

FIGURE 4.2: Bridge components considered in the seismic analysis. Grey circles represent fixed bearings, while empty ones are expansion bearings.

The MSSSC bridge has been modelled with the OpenSees platform [McKenna et al., 2000], using the same dimensions and constitutive models that are provided in Nielson [2005]. The following classes of elements have been used in OpenSees to model the various types of components.

4.3.1.1 Modelling of Piers

Beams and columns in the piers are modelled by `dispBeamColumn` elements, which follow a displacement-based formulation with a distributed plasticity along the whole length. The cyclic moment-curvature relation of the pier system (i.e. three columns and one

transverse beam) for both longitudinal and transversal loadings is represented in Figure 4.3.

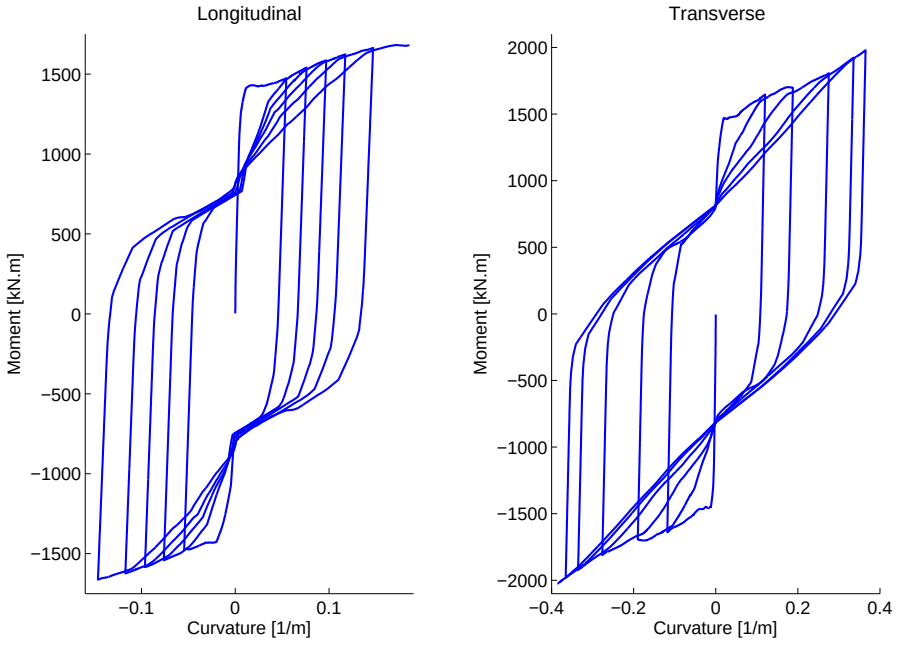

FIGURE 4.3: Moment-curvature cyclic response of piers in both loading directions.

4.3.1.2 Modelling of Bearings

Elastomeric bearings are modelled by `ZeroLength` spring elements: a parallel assembly of different constitutive laws is required in order to jointly model the Coulomb friction behaviour and the shear behaviour of the steel dowel that acts as a restraint. Expansion and fixed bearings are distinguished by the position of the steel dowel, which allows for more or less free movement, as shown in Figure 4.4. The weight of the deck has also an effect on the friction behaviour through the normal reaction, which induces a difference between the middle span and the end spans.

4.3.1.3 Modelling of Shear Keys

Additional shear keys are also added in order to account for the possibility of transversal movement of the deck spans. They are modelled according to a sliding friction shear mechanism. First, the deck slides on the pier cap according to a friction Coulomb law until the shear key is reached (i.e. gap closure). Then, the capacity of the shear key is

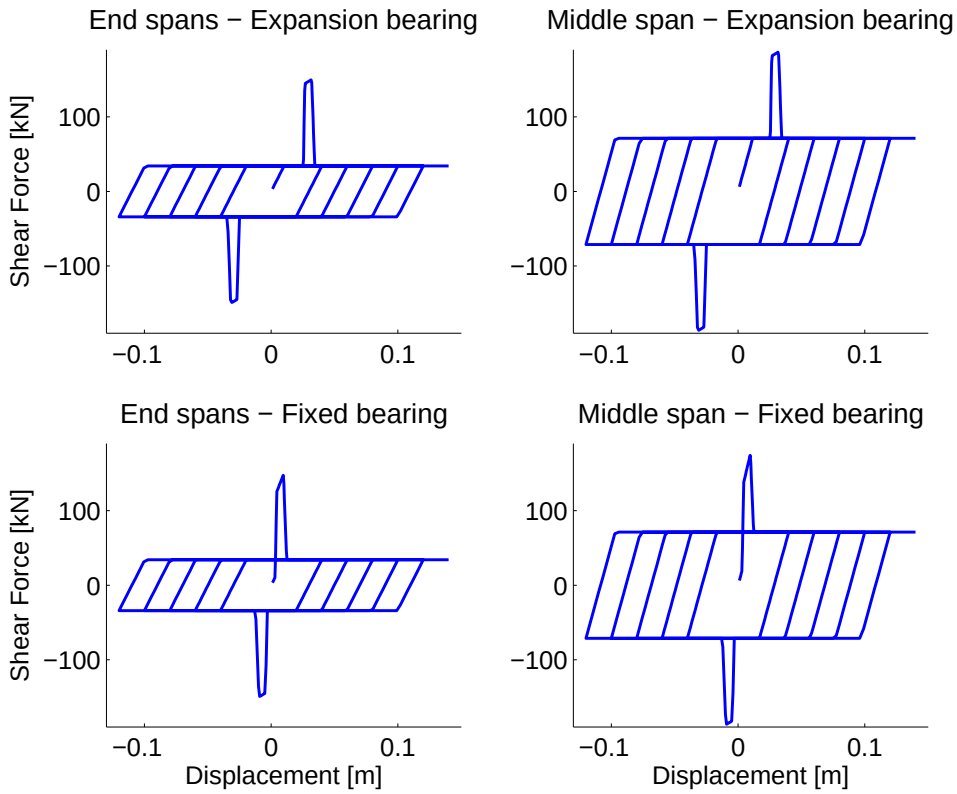

FIGURE 4.4: Cyclic response of bearings for all deck spans.

engaged until it ruptures through a shear mechanism. Once the shear key has failed, it is assumed that the deck keeps on moving freely until unseating. The assumed constitutive law for the shear keys is represented in Figure 4.5.

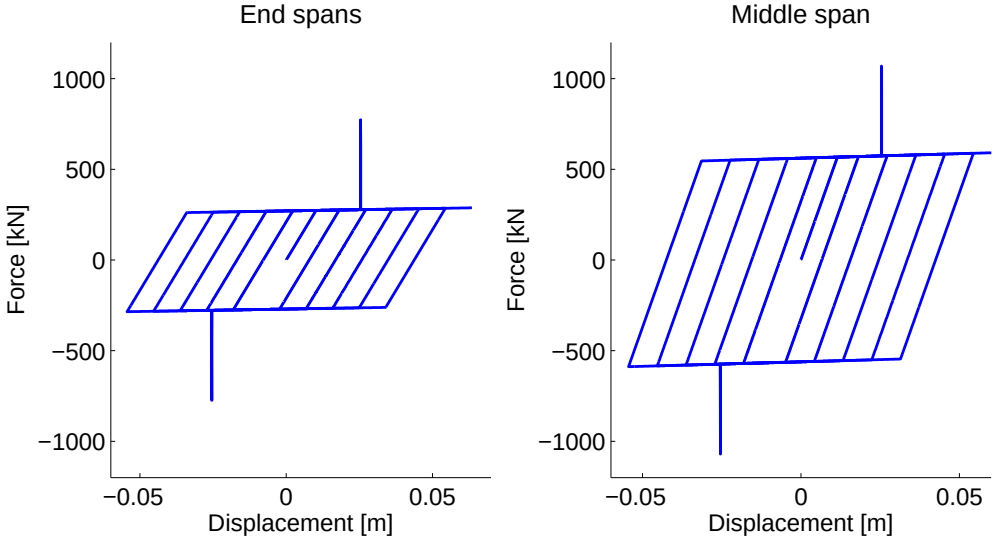

FIGURE 4.5: Force-displacement relationships for shear keys located at end and middle spans. The weight of the deck spans has a significant role on the friction behaviour.

4.3.1.4 Modelling of Abutments

Abutments are modelled by `ZeroLength` spring elements: a parallel assembly of different constitutive laws is required in order to jointly model the passive behaviour (i.e. compression of the backfill soil and resistance of the abutment piles) and the active behaviour (i.e. only the abutment piles are solicited when the abutment is in tension). This asymmetry of the initial stiffness and strength between the active and passive behaviour is highlighted in Figure 4.6.

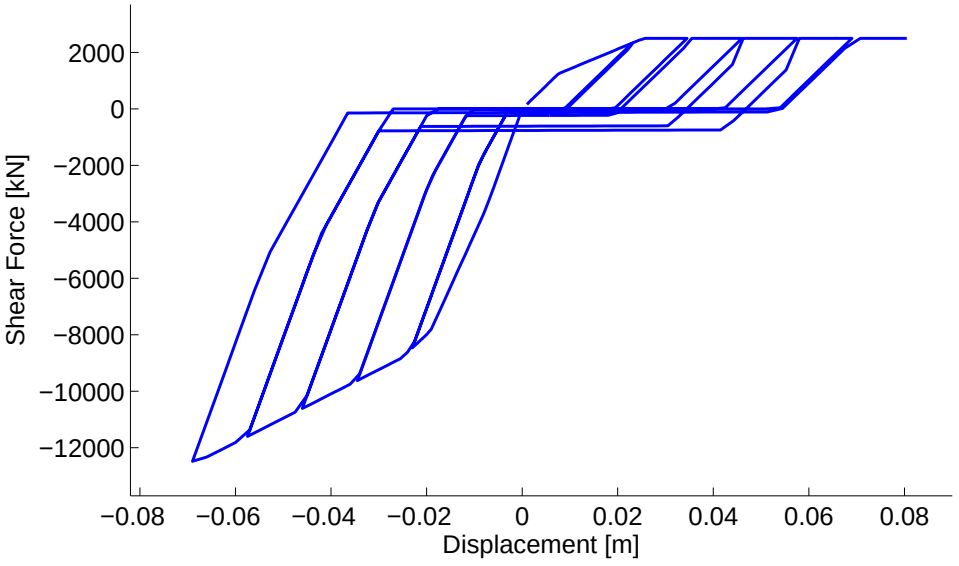

FIGURE 4.6: Cyclic response of abutments.

4.3.1.5 Modelling of Pier Foundations

Additional pier foundations are also explicitly modelled, unlike the assumption that has been adopted in the original model. Pier foundations are assumed to be anchored down to a depth of 8 m: the group of pile foundations, as described by Nielson [2005], is approximated by an equivalent elastic beam, which is connected to the ground through a set of Winkler p-y springs in order to model the soil resistance (see Figure 4.7).

A Winkler spring is located every 0.3 m between the altitudes 0 m and −8 m, in order to model the lateral resistance of the soil, as suggested by Prasad and Banerjee [2013]. Each spring is associated with a p-y curve expressing the soil resistance p at a depth h as a function of lateral pile deflection y:

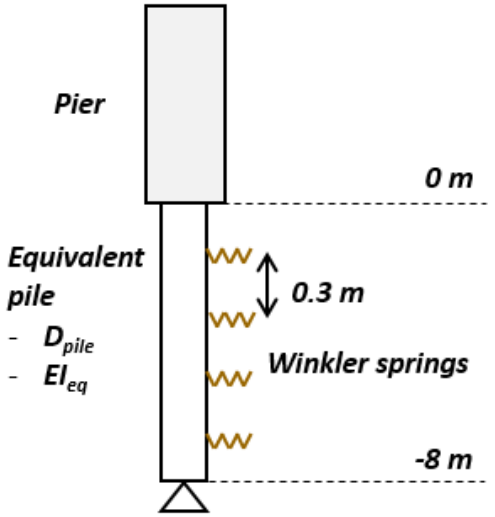

FIGURE 4.7: Schematic view of the equivalent pile foundations and the Winkler springs.

$$p\,(y) = A \cdot p_u \cdot \tanh\left(\frac{k \cdot h \cdot}{A \cdot p_u} \cdot y\right) \tag{4.1}$$

where A is a modification factor to account for cyclic and static loading ($A = 0.9$), k is the initial modulus of subgrade reaction ($k = 10\ 000$ kPa), obtained from API [2000]. The ultimate soil resistance p_u depends on the depth h, whether the foundations are deep or shallow:

$$p_u = \min\left[(C_1 \cdot h + C_2 \cdot D_{pile}) \cdot \gamma \cdot h \quad ; \quad C_3 \cdot D_{pile} \cdot \gamma \cdot h\right] \tag{4.2}$$

where C_1, C_2 and C_3 are coefficients that can be determined using the API [2000] guidelines ($C_1 = 1.9$; $C_2 = 2.65$; $C_3 = 28$), γ is the volumic mass of the soil, and D_{pile} is the equivalent diameter of the pile foundations.

Starting from a group of piles, an equivalent single pile has to be defined, as shown in Figure 4.7. The equivalent bending stiffness EI_{eq} for rocking motion can be computed according to Yin and Konagai [2001], which enables to access the equivalent diameter $D_{pile} = 1.1$ m. Finally, the p-y curves for the studied bridge model are computed for a few depths (see Figure 4.8).

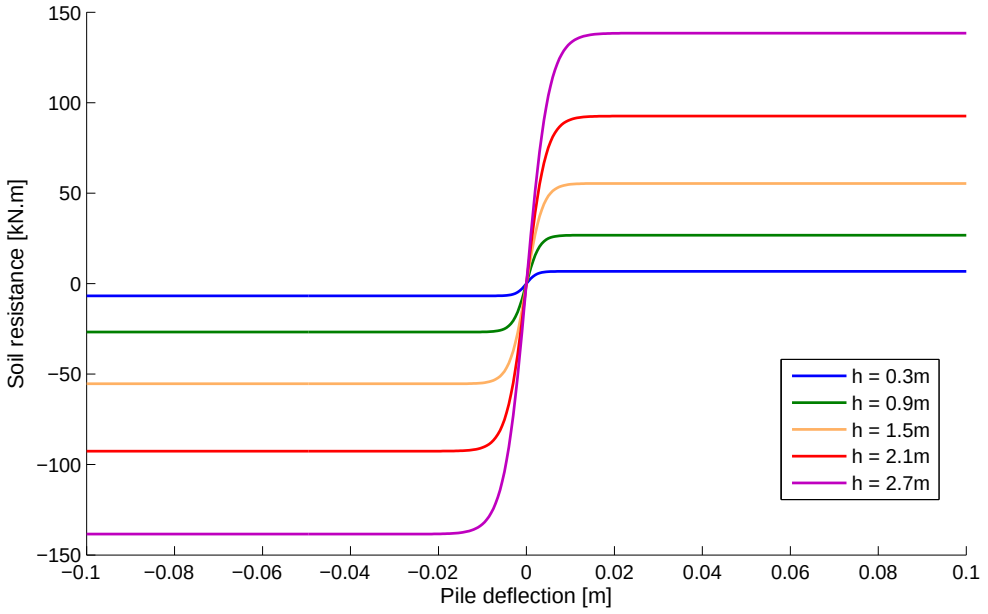

FIGURE 4.8: Force-deflection relations (p-y curves) for the soil surrounding the pile foundations, for different depths h.

4.3.1.6 Modelling of Deck

Deck spans are modelled by `elasticBeamColumn` elements: the deck is usually assumed to remain in the elastic range, due to its high rigidity with respect to bearings and piers. The whole deck width can be represented by a single linear element, since the movement of the deck span is transmitted to the whole width of the pier through rigid elements (i.e. common assumption).

4.3.2 Dynamic Properties

A modal analysis of the bridge system is performed, which results in a fundamental period of 0.64 s in the longitudinal direction, while the mode in the transversal direction is found for a period of 0.47 s: these period are in excellent agreement with the ones that have been computed by Nielson [2005], thus validating the dynamic properties of the bridge system in the elastic range. The deformed shapes for these modes are represented in Figure 4.9.

For validation purposes, the modal analysis has been carried out on the original model from Nielson [2005], without the addition of shear keys and the explicit modelling of pier

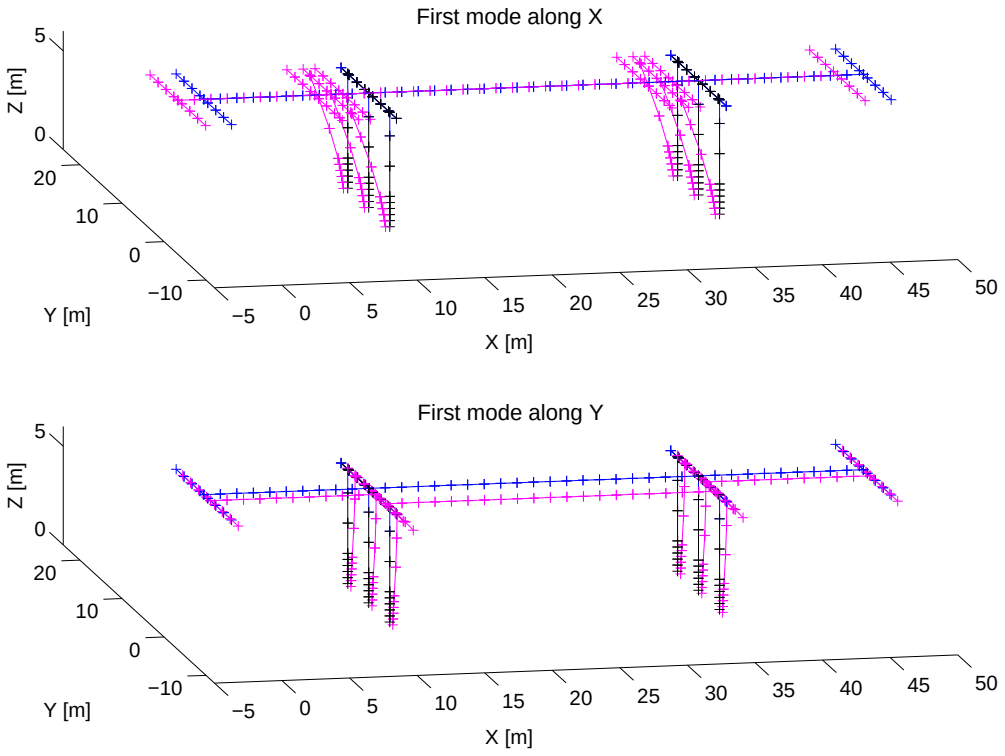

FIGURE 4.9: OpenSees finite element model of the MSSSC bridge. The pink lines represent the deformed shape of the bridge according to the first two vibration modes, thus allowing to visualize the zero-length springs that represent the bearings and abutments.

foundations. If these two features are added to the finite element model, the first mode is found at 0.67 s and the second one at 0.49 s: these modal values for the modified bridge are very close to the ones from the original model, while the slightly less stiff structure can be explained by the way the pier foundations are now modelled.

4.3.3 Seismic Input

The generation of the ground-motion suite follows the magnitude-distance criteria that are prescribed by Nielson [2005], in order to be consistent with the seismotectonic context of the area where the bridge has been modelled (i.e. Central Southern United States). Due to the constraints imposed on the ground motions as well as the large number of data points required by the fragility derivation method, the selection of natural records from European or worldwide databases [Ambraseys et al., 2004, PEER, 2010] would prove to be a very demanding task.

To this end, it is proposed to generate synthetic records using a stochastic procedure developed by Pousse et al. [2006], which is an extension of the method of Sabetta and Pugliese [1996]. This procedure is based on the definition of a magnitude, an epicentral distance and an EC8 soil class: using the criteria in Table 4.1 and proposed by Nielson [2005], 72 ground motions are then generated for each of the four selected soil classes (i.e. EC8 classes A to D), thus amounting to a total of 288 ground motions. In Gehl et al. [2015], it has been shown that several hundreds of ground motions are sufficient to achieve a satisfying estimation of the fragility parameters. The distribution of the PGA, SA(T_1) and SA(T_2) parameters, with $T_1 = 0.67$ s and $T_2 = 0.49$ s, is represented in Figure 4.10 for the generated ground motions.

TABLE 4.1: Magnitude-distance criteria for the selection of the ground motion suite [Nielson, 2005].

Epicentral distance [km]	Magnitude	Weighting
10	5.5	2
	6.5	2
20	5.5	1
	6.5	1
	7.5	2
50	5.5	1
	6.5	1
	7.5	1
100	7.5	1

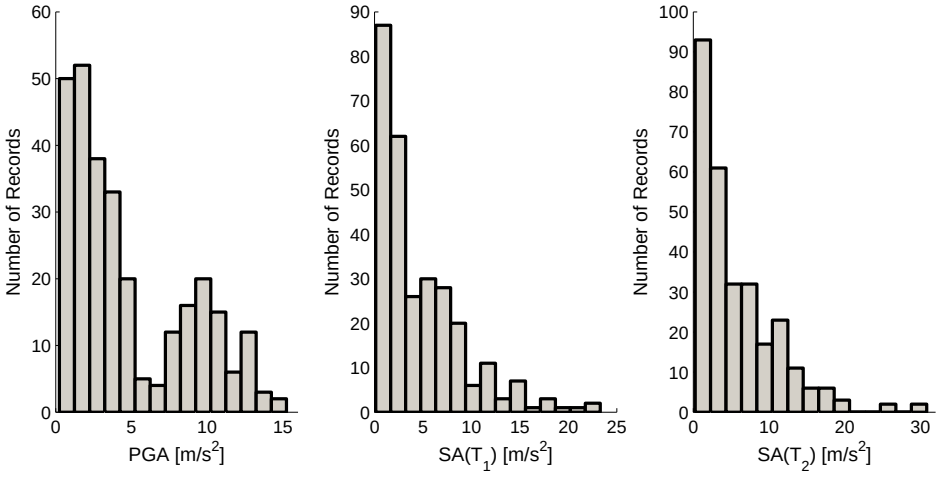

FIGURE 4.10: Distribution of the PGA, SA(T_1) and SA(T_2) parameters obtained from the generated records.

4.3.4 Derivation of Component Fragility Curves

Fragility curves for each component and for each loading direction (i.e. longitudinal and transversal) are then derived, using the following damage states (see Table 4.2):

- Piers: yielding (D1) and ultimate deformation (D2) of the columns;
- Abutments: yielding of the abutment piles in tension (D1), i.e. active behaviour;
- Bearings: restraint failure (D1) and deck unseating (D2);
- Shear keys: shear key failure (D1) and deck unseating (D2).

TABLE 4.2: Limit states for the component damage states. ϕ_y is the yield curvature corresponding to the yielding of the first steel reinforcement in the pier sections. The values for piers are based on Nielson [2005]. For the other components, the values are based on the constitute laws (yield points or unseating limits).

Components	EDP	Longitudinal direction		Transversal direction	
		D1	D2	D1	D2
Piers	Curvature	$1.29\phi_y$	$5.24\phi_y$	$1.29\phi_y$	$5.24\phi_y$
Abutments	Displacement	0.0192 m	–	0.0192 m	–
Fixed bearings	Displacement	0.0125 m	–	0.1866 m	–
Expansion bearings	Displacement	0.0345 m	0.1866 m	–	–
Shear keys	Displacement	–	–	0.0255 m	0.1866 m

The Generalized Linear Model regression with a probit link function (see Appendix B) is used to derive the seismic fragility curves, based on the components' responses from the 288 records applied to both directions. Such a regression model enables collapse states to be easily integrated. Moreover, the responses of some components (e.g. bearings) reveal significant threshold effects, which cannot be appropriately modelled by a cloud regression. The resulting fragility curves are presented in Figure 4.11.

A first analysis of the derived component fragility curves can lead to several observations:

- Due to the alternation of fixed and expansion bearings, the bridge is asymmetric along the longitudinal direction, a characteristic that is highlighted by the differences between the fragility curves (e.g. B2 versus B5, or B3 versus B4). Conversely, the bridge is symmetric along the transversal direction due to the use of identical the shear keys: as a result, the transversal fragility curves are the same for the components taken two-by-two (e.g. Sh1 versus Sh6, or Sh3 versus Sh4).

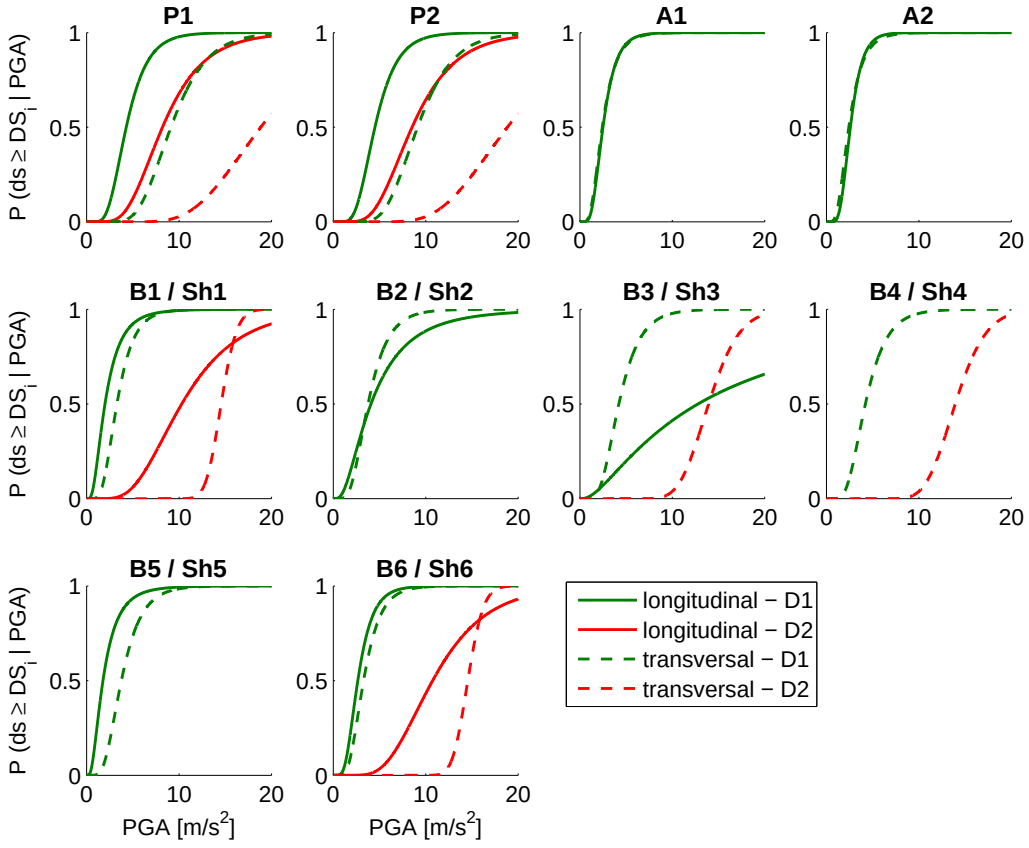

FIGURE 4.11: Fragility curves for the bridge components in both loading directions.

- In some cases, the fragility curve cannot be derived due to convergence issues of the GLM regression (e.g. damage state D2 of components B3 or B4): no data points have reached damage state D2 for these components, which may then be interpreted as components that are very unlikely to fail within this range of loading conditions. This issue constitutes both a drawback and a merit of the GLM regression: this statistical method tends to yield unstable values when data points are scarce, while the regression on a cloud would still be able to provide stable fragility estimates; however, it can be argued that the GLM regression prevents the modeller from using erroneous results, since the statistical model fails before proposing poorly constrained estimates.

- The component fragility curves enable the visualisation of the most vulnerable components within the bridge system: for instance, in the longitudinal direction, both piers tend to fail (damage state D2) before deck unseating is reached. However, for a given IM, the damage probabilities provided by the component fragility

curves must be considered as marginal probabilities, while the joint probabilities can only be assessed if the correlation matrix between component responses is estimated (see Figure 4.12) and system reliability methods are applied (see Chapter 5).

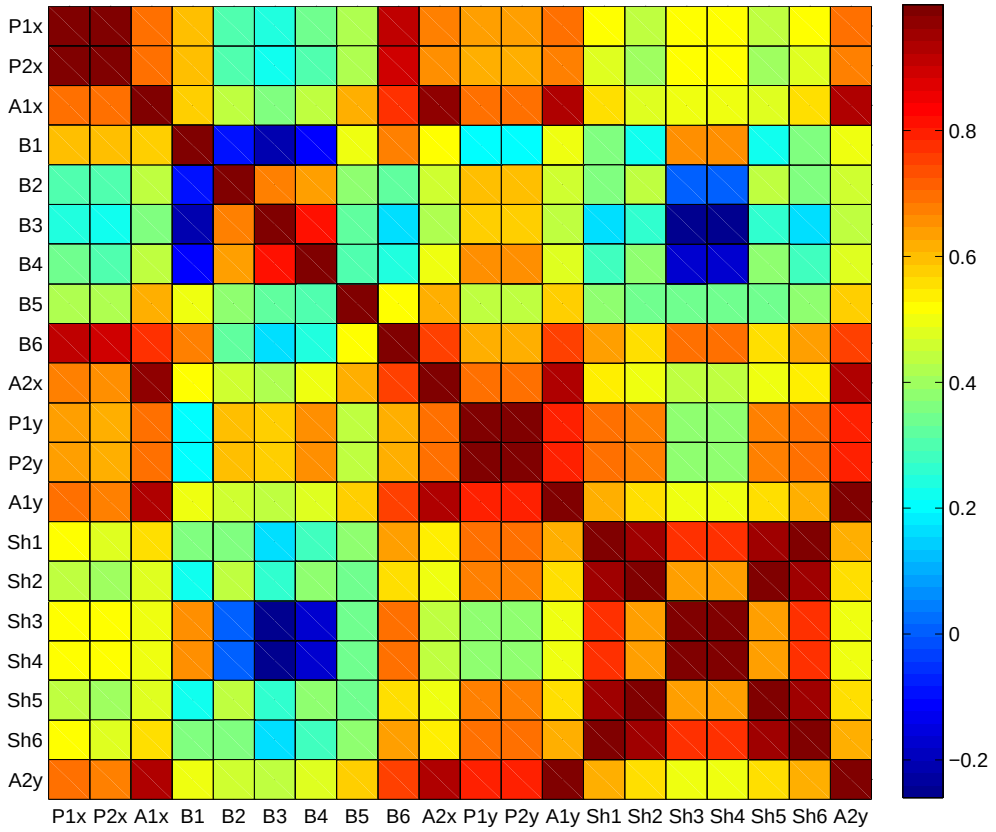

FIGURE 4.12: Correlation matrix of the component responses under seismic loading. The value of the correlation factors is given by the color map.

The correlation structure between the component responses is needed to quantify the probability of occurrence of the union or the intersection of given events, at the level of the bridge system. This statistical dependence is induced by the common cause failure that may be generated by the earthquake shaking, which is applied to all bridge components at once. Therefore, components that have a similar dynamic behaviour within the bridge system are highly correlated, such as the response of the two piers in the longitudinal direction (see Figure 4.12). Conversely, due the discontinuous deck spans in the studied bridge, some bearings on different locations of the bridge may move independently from one another, even when subjected to the same ground motion:

this is illustrated by the correlation matrix, which shows for instance that the response of bearing B1 is almost orthogonal – in terms of uncertainties – with the response of bearings B2 to B4 (i.e. correlation factor close to zero).

4.4 Fragility Curves for Ground Failures

This section describes the methods that have been adopted to derive fragility curves for component failure modes due to ground failures, as identified in Table 3.8.

4.4.1 Fragility Curves for Slope Failure (Failure Mode #15)

Slope failure may affect abutments, however the depth of the foundations of well-designed bridge abutments usually prevents superficial landslides from having an effect on the abutment itself. Still, in the case of deep-seated circular landslides that generate ground displacements below the depth of the abutment footing, it is possible to have significant differential displacements that may lead to bridge collapse. Hence circular slope failure is considered as the relevant failure mechanism for abutment foundations, characterized by a single damage state D1.

There is currently no fragility model available for bridge systems subjected to slope failure. The wide range of possible configurations regarding the bridge system and its soil environment makes it difficult to derive fragility functions that may be applied to a given typology. Therefore the derivation of fragility functions should be case-dependent, since a careful analysis of the bridge – soil configuration is usually required (e.g. soil conditions, near-surface geology, slope grade, position of foundations, etc.).

Slope fragility curves may then be developed for a given case-study, by using probabilistic slope stability analyses [Wu, 2013, 2015]. To this end, the factor of safety FS of potential sliding surfaces can be estimated with the limit equilibrium method (i.e. Bishop's simplified method). The surface is subdivided into a number n of vertical slices and the factor of safety FS is then expressed as the ratio of resisting versus destabilizing moments of all the slices (see Figure 4.13):

$$FS = \frac{\sum_{i=1}^{n} \frac{1}{F_\alpha} \cdot [c_i \cdot b_i + \tan\phi_i \cdot (W_i - u_i \cdot b_i)]}{\sum_{i=1}^{n} W_i \cdot \sin\theta_i + K_h \cdot W_i \cdot \frac{L_i}{R}} \tag{4.3}$$

where K_h is the horizontal seismic coefficient expressed as a function of PGA [Noda et al., 1975]:

$$K_h = \frac{1}{3} \cdot \left(\frac{\text{PGA}}{g} \right)^{1/3} \tag{4.4}$$

The factor F_α is expressed as:

$$F_\alpha = \cos\theta_i + \frac{\tan\phi_i \cdot \sin\theta_i}{FS} \tag{4.5}$$

Since the factor FS is present on both sides of the equations, a small iteration process is required in order to converge to the final FS value after a few steps.

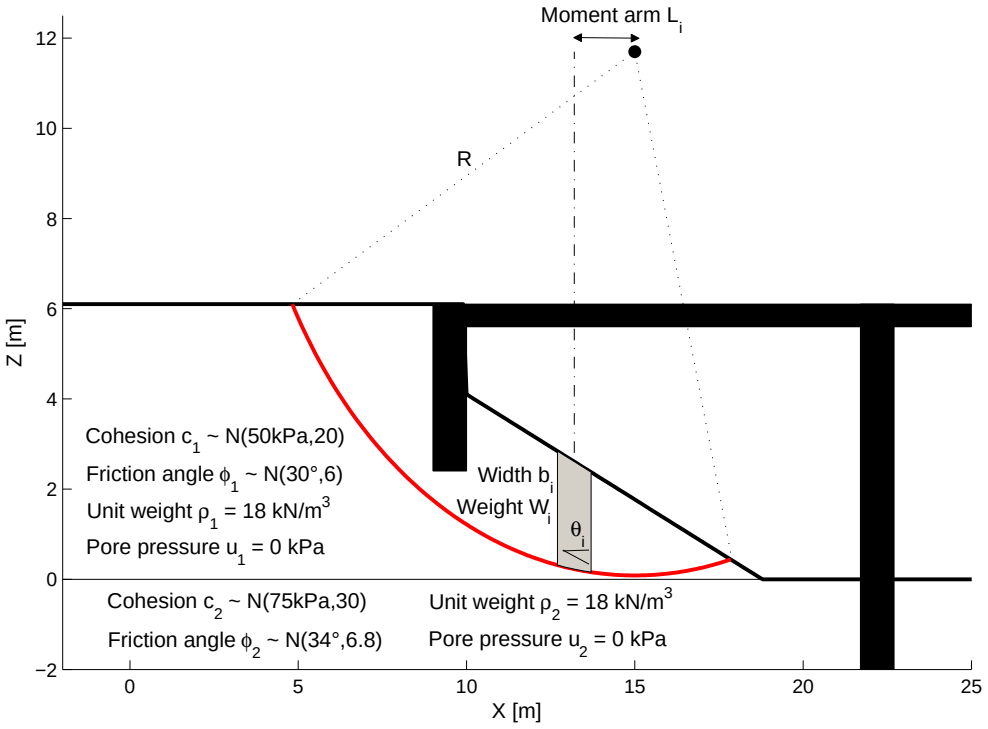

FIGURE 4.13: Slice equilibrium method for the estimation of the factor of safety for circular slope failure. The black shape is a simplified view of the studied bridge and its foundations.

Fragility functions for slope instability (D1) are then derived following the method proposed by Wu [2015]: for each increasing value of PGA, the reliability index of $\log FS > 0$ is estimated using a Mean-Value First-Order Second Moment (MFOSM) method:

$$\beta_{FS} = \frac{\log\mathrm{FS}\left(\mu_{X_i}\right)}{\sqrt{\sum_{i=1}^{n}\left(\frac{\partial \log\mathrm{FS}}{\partial X_i}\right)^2 \cdot \sigma^2\left[X_i\right] + 2\sum_{i,j=1}^{n}\left(\frac{\partial \log\mathrm{FS}}{\partial X_i}\right)\cdot\left(\frac{\partial \log\mathrm{FS}}{\partial X_j}\right)\cdot\rho\cdot\sigma\left[X_i\right]\cdot\sigma\left[X_j\right]}} \tag{4.6}$$

The partial derivative of $\log FS$ is approximated around its central value, by evaluating the slope between $\log FS$ at plus/minus one standard deviation. The input random variables X_i are the cohesion and friction angle of each soil layer, while a correlation factor of $\rho = -0.4$ is assumed between them [Wu, 2013]. The search algorithm for the probabilistic critical surfaces proposed by Hassan and Wolff [1999] is used in order to ensure that the minimum reliability index is found for each combination of the soil parameters and each proposed surface, based on the distribution of the factor of safety with respect to the value 1. An additional constraint is introduced by the location of the abutments foundations, since the critical surface is unlikely to generate any bridge failures if it intersects with the bridge abutment foundations. Therefore the critical surfaces that are found with the limit equilibrium method have to be deep enough, so that the ground displacement is unhindered by the abutments foundations, as it is shown in Figure 4.13. Finally, the reliability index is converted into the probability of failure P_f and the points [PGA ; P_f] are fitted into a fragility curve with a lognormal cumulative distribution function, through a straightforward optimization process that identifies the fragility paramters by minimizing the sum of squared errors with the discrete P_f points.

Using the soil parameters summarised in Figure 4.13, The fragility curve for the collapse of abutment foundations due to circular slope failure is derived and presented in Figure 4.14. The corresponding fragility parameters are the mean $\alpha = 12.62$ m/s^2 and the standard deviation $\beta = 1.03$.

4.4.2 Fragility Curves for Subsidence (Failure Mode #16)

The most common failure mode, i.e. the subsidence/settlement of the backfill soil, may be quantified by performing a finite element analysis in order to estimate the permanent strain of the supporting soil, when subjected to a ground motion time history at the base. Therefore an approach that is similar to the derivation of analytical fragility curves for embankments [Argyroudis and Kaynia, 2014, 2015] may be used. Moreover, fragility

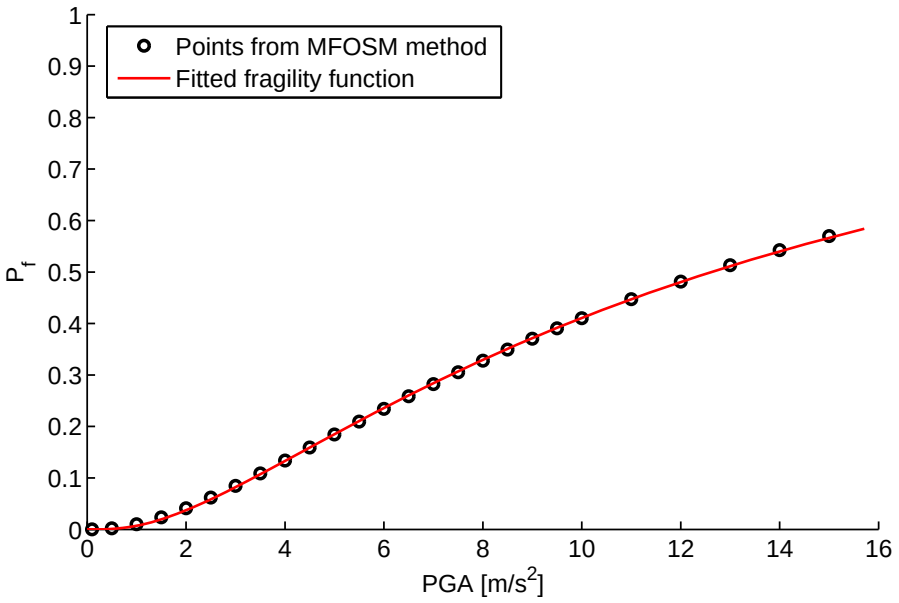

FIGURE 4.14: Derivation of the fragility curve for abutment foundations exposed to slope failure.

curves for the backfill of bridge abutments are proposed in Argyroudis and Kaynia [2014], for a bridge with a vertical retaining wall, with varying heights and EC8 soil types. The resulting fragility curves express the probability of exceeding three damage states as a function of PGA (i.e. earthquake-induced ground failure).

The proposed fragility curves for the subsidence of the bridge backfill soil are presented in Figure 4.15 while the corresponding fragility parameters are summarized in Table 4.3.

TABLE 4.3: Proposed fragility parameters (mean and standard deviation) for the subsidence of the bridge backfill soil, from Argyroudis and Kaynia [2014].

Damage states	α [m/s^2]	β
D1 - Subsidence $\geq$ 0.03 m	1.96	0.90
D2 - Subsidence $\geq$ 0.15 m	4.41	0.90
D3 - Subsidence $\geq$ 0.30 m	9.13	0.90

4.5 Fragility Curves for Floods

This section describes the methods that have been adopted to derive fragility curves for component failure modes due to fluvial floods.

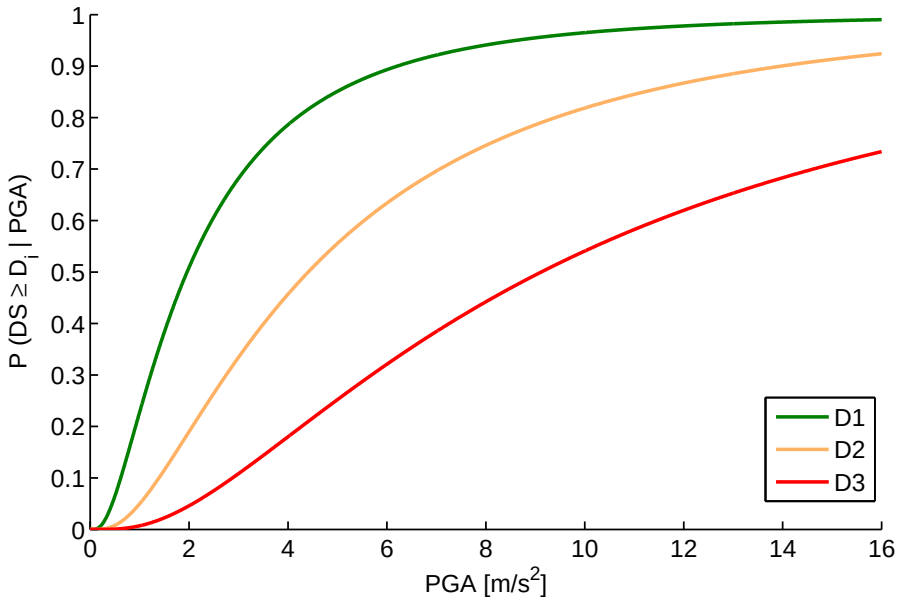

FIGURE 4.15: Proposed fragility curves (mean and standard deviation) for the subsidence of the bridge backfill soil, from Argyroudis and Kaynia [2014].

4.5.1 Fragility Curves for Scour (Failure Mode #17)

Fragility curves for bridges with respect to scour are less common than for seismic ground motion, however a few references are presented in Table 4.4.

TABLE 4.4: Available bridge fragility curves for flood hazard, in the case of scour.

Reference	Typology	Intensity Measure
Alipour et al. [2012]	Multi-span multi-column RC bridge	Scour depth
Tanasić et al. [2013]	Multi-span continuous RC bridge	Soil cover height at the pier
Pearson et al. [2002]	Generic bridges	Scour vulnerability grade and water height

The fragility curves proposed by Alipour et al. [2012] may not be seen as scour fragility curves per se, in the sense that they do not represent the direct bridge damage with respect to scour. Instead, scour depth is used as a modifying coefficient to adjust the parameters of the corresponding seismic fragility curve. Therefore this reference can be put to better use in the context of combined hazards (i.e. scour and earthquake).

Tanasić et al. [2013] have developed actual scour fragility curves that express the probability of bridge failure as a function of the height of ground that is still covering the pier foundations (i.e. the complement of the excavated scour depth). The bridge failure mode is explained by the degradation of the elastic and/or plastic soil parameters. This phenomenon can either induce:

- The sinking of the pier foundations, which in turn triggers a pier displacement, leading to kinematic mechanisms in the bridge.
- The degradation of the bearing capacity of the soil, until it is exceeded by the contact pressure load at the foundation.

The HYRISK methodology [Pearson et al., 2002] proposes a table of scour probability failures, which depend on (i) the scour vulnerability grade of the bridge and (ii) the water height (expressed as a dimensionless depth ratio, i.e. scour depth divided by foundation depth), as detailed in Table 4.5. The scour vulnerability grades may be qualitatively described by the scour level with respect to the foundation footings, as illustrated in Figure 4.16.

TABLE 4.5: Scour failure probability as a function of scour vulnerability grade and the dimensionless depth ratio [Pearson et al., 2002].

Scour vulnerability grade	Dimensionless depth ratio				
	$0.00 - 0.25$	$0.25 - 0.50$	$0.50 - 0.75$	$0.75 - 1.00$	> 1.00
0 (Bridge failure)	1.000	1.000	1.000	1.000	1.000
1 (Bridge closed)	1.000	1.000	1.000	1.000	1.000
2 (Extremely vulnerable)	0.250	0.400	0.550	0.700	0.880
3 (Unstable foundations)	0.140	0.200	0.300	0.450	0.650
4 (Stable, action required)	0.060	0.100	0.150	0.260	0.410
5 (Stable, limited life)	0.002	0.002	0.002	0.030	0.100
6 (Unassessed / Unknown)	0.100	0.150	0.225	0.355	0.530
7 (Countermeasure installed)	0.100	0.150	0.225	0.355	0.530
8 (Very good conditions)	0.002	0.002	0.002	0.010	0.050
9 (Excellent conditions)	0.002	0.002	0.002	0.002	0.010

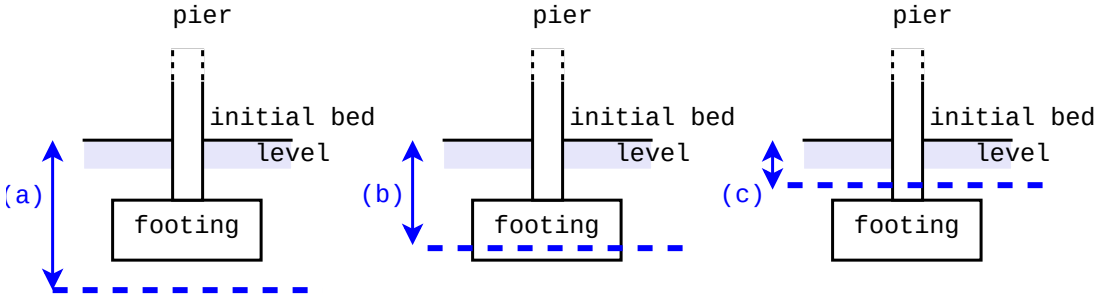

FIGURE 4.16: Scour levels with respect to bridge footing: (a) below footing (grades 2 and 3); (b) within limits of footing (grades 4 and 5); (c) above top of footing (grades 8 and 9).

No fragility curves for bridge failure due to debris accumulation (i.e. floating debris which are transported by the flood) are available. However, the detrimental effect of debris accumulation on the scour depth has been experimentally studied by Lagasse et al. [2010], for different shapes, sizes and porosity levels of debris masses. Regarding

analytical models and scour equations [Richardson and Davis, 1995], the effect of debris accumulation may be approximated by an increased effective pier diameter, especially if the debris mass is located at the water surface on a single circular pier [Melville and Dongol, 1992]. Other studies have also demonstrated that debris accumulation increase flow velocity and bed shear, thus leading to aggravated general scour [Diehl, 1997, Transportation Association of Canada, 2004].

In the present study, only local scour at piers is considered, since the general scour level (i.e. river bed degradation) is usually less significant than local scour [Barbetta et al., 2015]. Also, contraction scour may be neglected if we assume that there is no sudden change in the river bed cross-section. Empirical equations from HEC-18 [Richardson and Davis, 1995] are used to estimate the local scour depth y_s:

$$y_s = 2 \cdot K_1 \cdot K_2 \cdot K_3 \cdot K_4 \cdot y \cdot \left(\frac{D}{y}\right)^{0.65} \cdot F^{0.43} \tag{4.7}$$

where y represents the flow height, D is the pier width, F is the Froude number and the K_i parameters are corrective coefficients (see Table 4.6). The Froude number is expressed as:

$$F = \frac{v}{g \cdot y} \tag{4.8}$$

Since the Froude number is a function of both flow height and flow velocity, a way to keep the scour depth dependent on a single scalar IM is to combine these quantities into a new variable, such as the flow discharge Q. Assuming a rectangular river section, Q can be expressed as a function of velocity v and height y [Alipour et al., 2012], with river bed width b:

$$Q = b \cdot y \cdot v = \frac{b \cdot y}{n} \cdot \left(\frac{b \cdot y}{b + 2y}\right)^{2/3} \cdot S_0^{1/2} \tag{4.9}$$

where Manning's roughness coefficient n and slope grade S_0 are also specified in Table 4.6.

The input parameters in Table 4.6 are then sampled through a Monte Carlo scheme in order to generate 10 000 couples of values $[Q\ ;\ y_s]$, for different flow heights y. It is then

TABLE 4.6: Parameters used in the scour equations. Some of the probability distributions are taken from Alipour and Shafei [2012].

Variable	Description	Distribution	Value
K_1	Factor for pier nose shape	–	1
K_2	Factor for flow angle of attack	uniform	$[1; 1.5]$
K_3	Factor for bed condition	normal	$\mu = 1.1$; $\sigma = 0.055$
K_4	Factor for bed material size	–	1
n	Manning's roughness coefficient	lognormal	$\mu = 0.025$; $\sigma = 0.275$
S_0	Slope grade	lognormal	$\mu = 0.02$; $\sigma = 0.5$

possible to derive 'scour fragility curves' that express the probability of reaching a given scour depth with respect to flow discharge Q.

Three damage states have been defined, based on the effect the scour level has on the pier initial stiffness and the response of the bridge system under seismic loading (see Section 4.6):

- $y_s \geq 1$ m (D1): the first noticeable changes in the bridge's dynamic properties begin to appear;
- $y_s \geq 3.6$ m (D2): significant changes in the bridge response can be observed;
- $y_s \geq 5.1$ m (D3): the scour depth reaches almost the foundation length and it is assumed that the pier is not stable enough to support the bridge, as the moment capacity of the foundation is lost.

These parameters are very specific to the characteristics of the studied bridge. For instance, the limit states for scour depend directly on the type of foundations that is considered (i.e. deep or shallow), while the expression of the flow discharge Q as a function of flow height is only valid for this specific river section. Generic fragility curves for a set of bridges would require additional parameters representing various configurations of foundations and river sections.

The fragility curves and parameters for these three damage states are presented in Figure 4.17 and in Table 4.7, respectively.

4.5.2 Fragility Curves for Overtopping (Failure Mode #21)

It is assumed that the fluvial flood will affect mainly the interaction between the deck and the piers, by resulting in lateral pressure on the side of the deck. For simplicity,

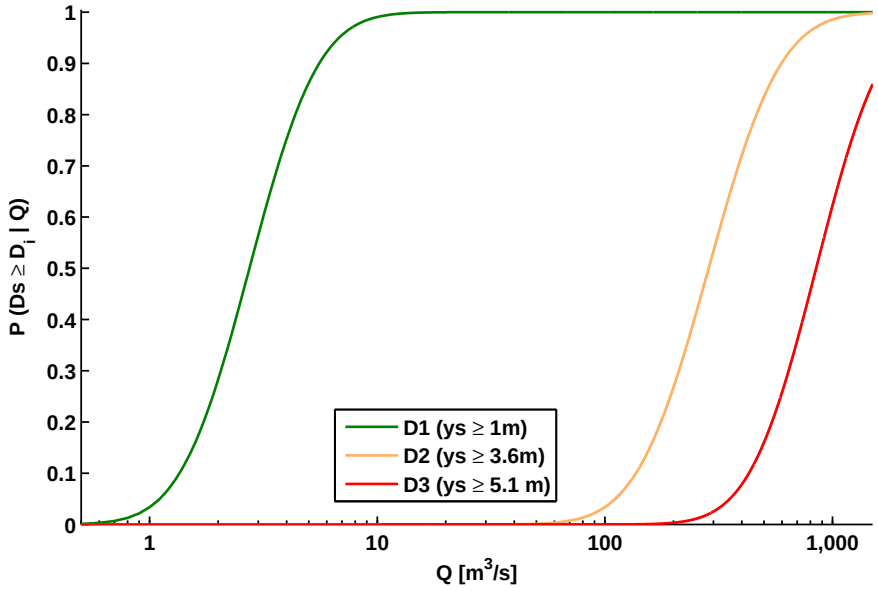

FIGURE 4.17: Fragility curves for pier foundations exposed to local scour.

TABLE 4.7: Fragility parameters (mean α and standard deviation β) for pier foundations exposed to local scour.

Damage states	α [m^3/s]	β
D1 - $y_s \geq 1$ m	2.7	0.55
D2 - $y_s \geq 3.6$ m	285.8	0.57
D3 - $y_s \geq 5.1$ m	847.6	0.53

two successive damage states can be considered. The failure of the shear keys (D1) and the unseating of the deck (D2). The aim is to obtain a fragility curve describing the probability of reaching these damage states with respect to a flood IM, which can be represented by water height or velocity or flow discharge). Although there is anecdotal evidence on the vulnerability of bridges due to hurricanes and storm surges [Kameshwar and Padgett, 2014, Padgett et al., 2008a], there is a dearth of data in literature to allow a robust quantification of the impact of fluvial floods on bridge superstructures.

Pending the empirical or analytical development of suitable fragility models, in the present application it is proposed to use the fragility curve from Kameshwar and Padgett [2014] for bridge failure due to storm surge. Through a logistic regression, the authors have built a logit function g representing deck unseating as a function of surge S, bridge height H_B and wave height H, as follows:

$$g\left(S,H,H_B\right) = -2.71 - 3.47 \cdot (H_B - S) + 1.59 \cdot H + 0.17 \cdot (H_B - S) - 0.22 \cdot (H_B - S)^2 + 0.05 \cdot H^2 \tag{4.10}$$

It is proposed here to set the coefficients related to wave height equal to 0, in order to represent the fluvial flood as a very rough approximation (i.e. removal of the wave effect in the equation). To determine the damage to shear keys (D1), a conservative assumption could consider failure as soon as the flow height reaches the top of the pier cap.

Although the aforementioned fragility models are expressed as a function of water height, it is proposed to convert this intensity measure into flow discharge Q in order to be consistent with the scour fragility curves (see Equation 4.9 in previous sub-section). The fragility curves and parameters for these two damage states are presented in Figure 4.18 and in Table 4.8, respectively.

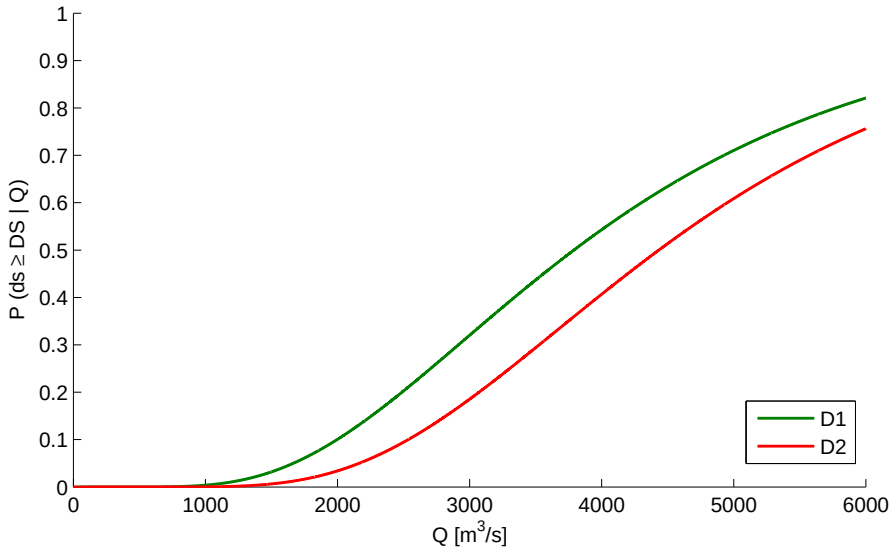

FIGURE 4.18: Fragility curves for the shear keys and deck spans exposed to fluvial flood.

TABLE 4.8: Fragility parameters (mean α and standard deviation β) for the shear keys and deck spans exposed to fluvial flood.

Damage states	α [m^3/s]	β
D1 - Shear key failure	3789.9	0.500
D2 - Deck unseating	4433.1	0.436

4.6 Cascading Effects from Different Hazards

Since one of the objectives of this study is the derivation of multi-hazard fragility functions, it is proposed to demonstrate the ability of the present framework to account for cumulated effects on the bridge system. Given the hazard types that are addressed in this work, the effect of concomitant earthquake and flood events on a given bridge is a known issue that has been addressed by several past studies [Alipour and Shafei, 2012, Guo et al., 2015, 2016]. By assuming a given time window during which the bridge is considered to be left unrepaired following a flood event, the cascading effects of fluvial flood or scour on the subsequent earthquake response can be quantified by the derivation of damage-dependent fragility curves.

Therefore different bridge models have to be developed, either by removing some Winkler springs (i.e. to model scour damage) or by removing the shear keys (i.e. to model damage due to fluvial flood): the successive steps of the proposed approach for the derivation of damage-dependent fragility curves in the case of flood and earthquake interactions are detailed in Figure 4.19.

In the present example, a total of six bridge configurations are considered, as shown in Table 4.9. Three discrete scour levels are defined, which correspond to the different scour damage states that are defined in Subsection 4.5.1; while the damage state D1* corresponds to the failure of shear keys due to hydraulic pressure, thus affecting the seismic behaviour along the transversal direction.

TABLE 4.9: Different bridge models considered to account for cumulated damage effects of flood and earthquake events. The * sign represents models that are only changing in the transversal direction.

Bridge configuration	Scour damage	Fluvial flood damage
1	D0	D0
2	D0	D1*
3	D1	D0
4	D1	D1*
5	D2	D0
6	D2	D1*

The thresholds for the different scour damage states described in subsection 4.5.1 are estimated by performing pushover analyses of the pier for different scour depths, as shown in Figure 4.20. Significant changes in the shape of the pushover curves are then used to select scour thresholds for which the scour damage states are defined. The

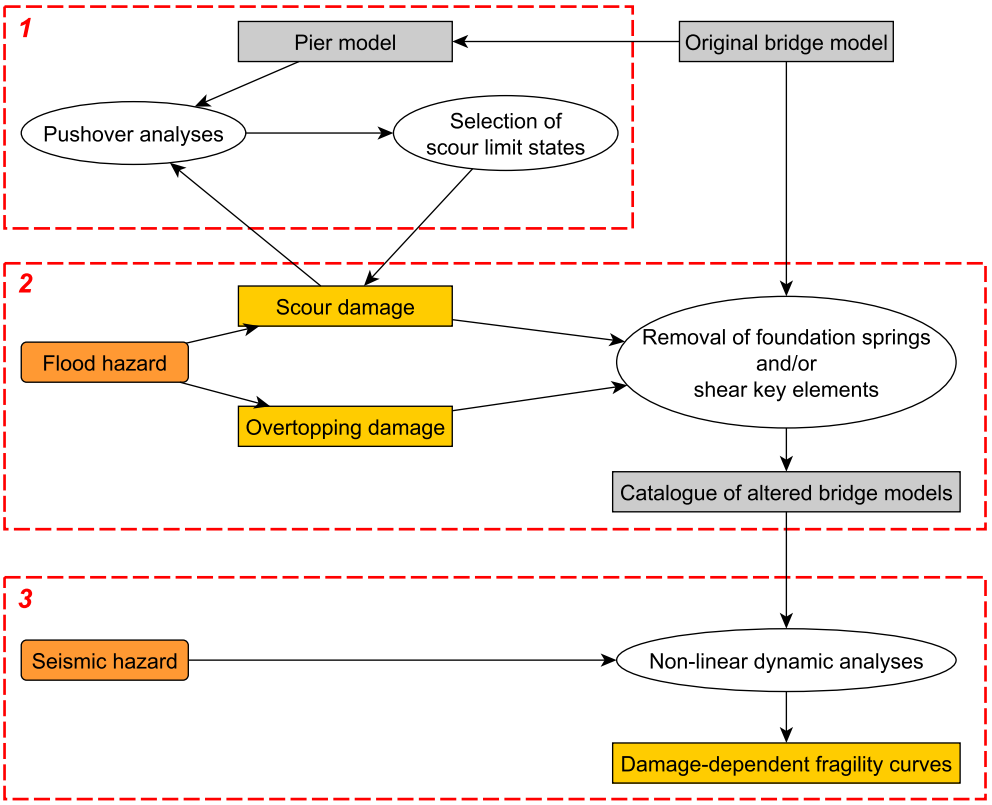

FIGURE 4.19: Proposed steps for the derivation of damage-dependent fragility curves: (1) selection of discrete scour levels based on the pushover analysis of bridge piers, (2) contruction of a dataset of 'damaged' bridge models and (3) derivation of seismic fragility curves for the altered models.

effect of scour can be clearly seen in the case of the pushover curves in the longitudinal direction: for levels of scour greater than 1 m the pier is affected by more severe stiffness degradation, while significant strength reduction is also observed for more than 3.6 m scour. Scour levels above 5.1 m do not guarantee the structural stability of the system, so that this value is considered as the limit state to assume pier collapse due to scour.

The seismic fragility curves are then derived for each scour damage state by uniformly sampling the scour depth that is bounded by two consecutive scour thresholds. The evolution of the mean parameters of the damage-dependent fragility curves is presented in Figure 4.21 for all bridge components.

The resulting fragility parameters in Figure 4.21 show that scour globally tends to raise the seismic vulnerability of shear keys, except for the ones that are in the middle of the bridge (i.e. Sh3 and Sh4). Regarding piers, the removal of Winkler springs relaxes the connection at the pier base, which has the effect of lowering bending moments and

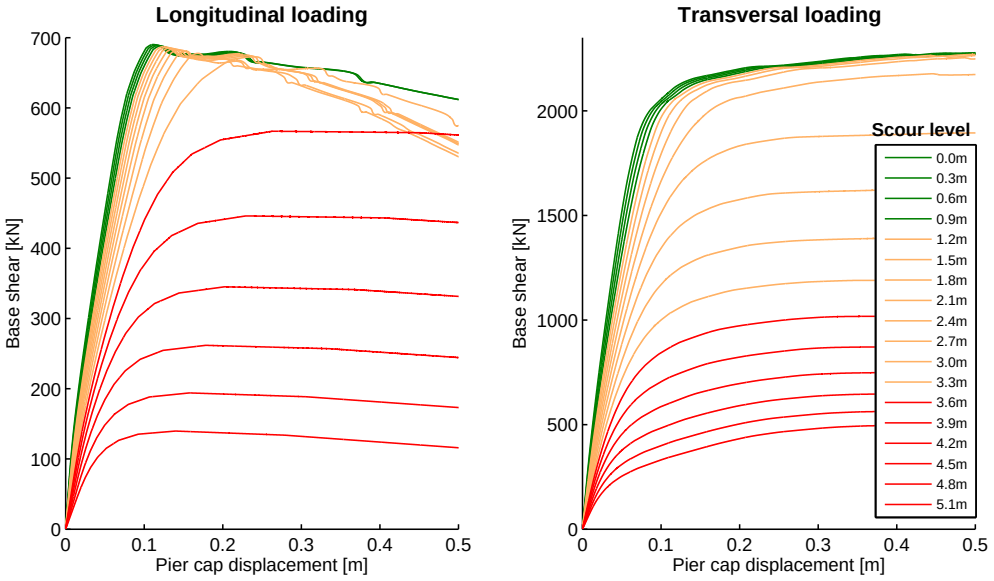

FIGURE 4.20: Pier pushover curves for different scour levels. Green lines represent less than 1 m scour (i.e. scour damage state D0), the yellow lines scour between 1 m and 3.6 m (i.e. scour damage state D1) and the red lines scour between 3.6 m and 5.1 m (i.e. scour damage state D2).

decreasing the failure probability for higher scour levels. Finally, the response of abutments seems to remain stable across the different scour depth. Similar observations have been made when fragility curves are computed for the components in the longitudinal direction. When shear keys are removed (i.e. fluvial flood D1), the seismic fragility slightly increases for lower damage states, while this effect becomes more significant for further damage states (i.e. the absence of restraints favours the occurrence of deck unseating).

It should be noted that a perfectly symmetric shape of the bridge and the river bed is assumed, so that the probabilities of reaching the different scour levels are equal at each pier location. Also, in order to limit the number of bridge configurations, it is assumed that the scour events have a joint occurrence across the different piers: this assumption tends to be conservative, since a bridge for which all pier foundations are subjected to scour will experience a more altered seismic response than a bridge for which only a portion of the piers are affected. The study of all possible configurations should still deserve dedicated effort in order to refine the global failure probabilities, but this is out of the scope of the present example.

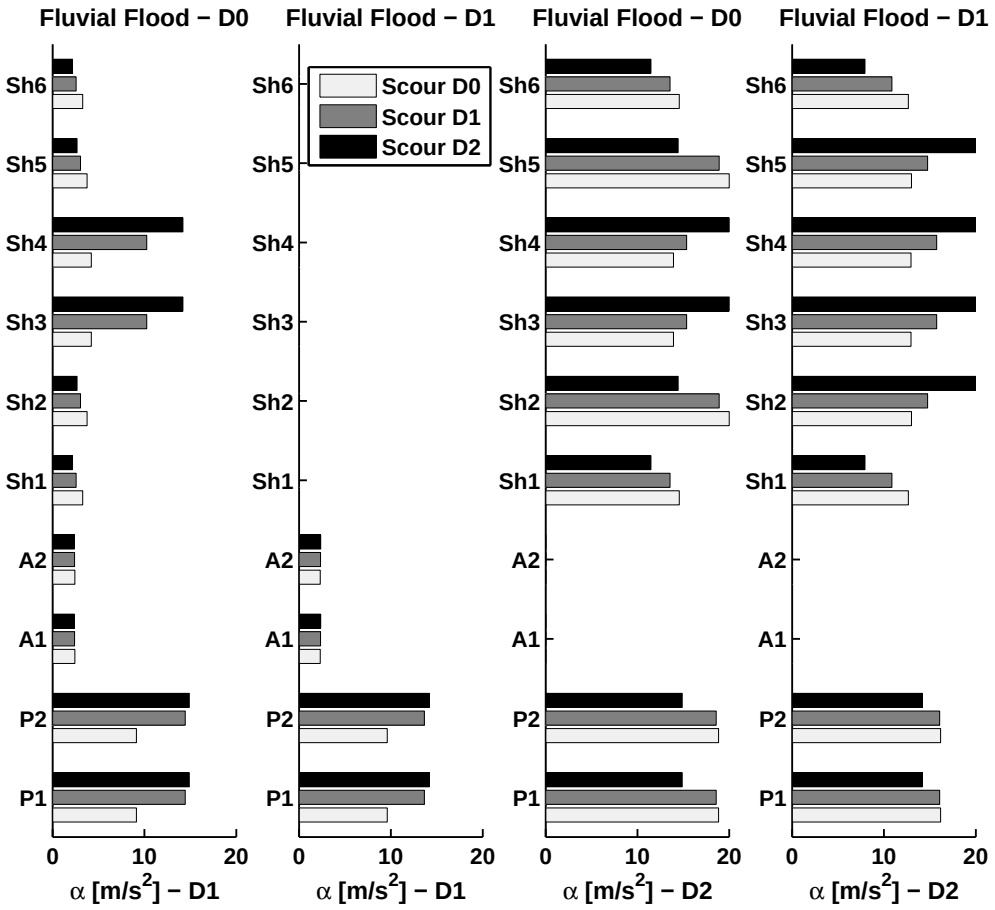

FIGURE 4.21: Evolution of the mean seismic fragility parameter α for both EQ damage states D1 and D2 and all components in the transversal direction, depending on the initial state of the bridge in terms of scour and fluvial flood damage.

4.7 Evaluation of Simplified Seismic Assessment Methods

The non-linear time-history analyses that have been conducted in Section 4.3 for the derivation of component fragility curves present the drawback of inducing long computation times and potential numerical convergence issues, especially when large bridges are considered. Therefore there is a need for an assessment procedure that yields accurate estimates while being simple enough for a systematic application to a large portfolio of bridges. Parallel to the non-linear displacement-based static methods, Sadan et al. [2013] and Cardone [2014] have introduced a direct displacement-based assessment (DDBA) procedure, which is a direct development of the displacement-based design approach by Priestley et al. [2007]. This method is based on the evaluation of the static capacity of an equivalent linearised bridge system (i.e. through the estimation of the secant stiffness

and the equivalent damping ratio) for a given target level of deformation of the bridge, referred to as Performance Displacement Profile (PDP) (see Figure 4.22).

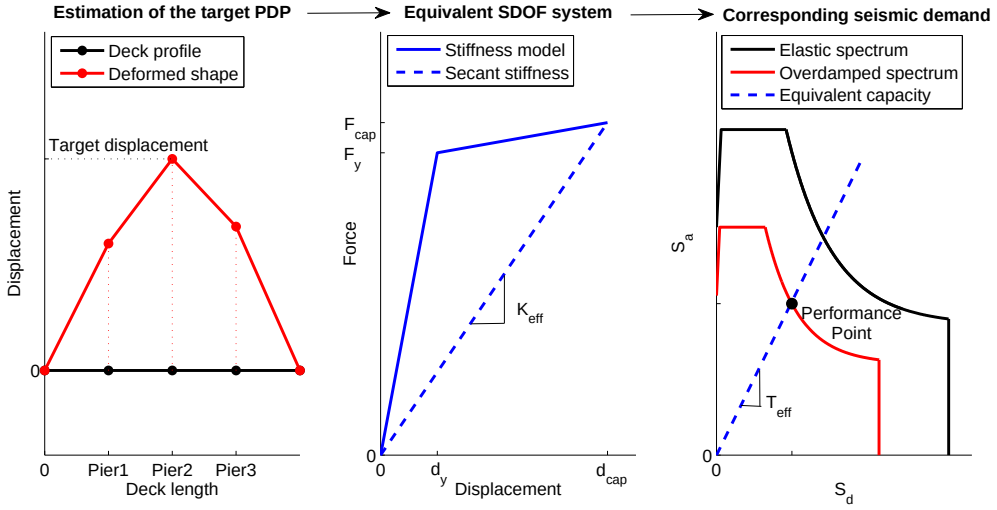

FIGURE 4.22: Main principles of the DDBA procedure.

The DDBA method only requires the definition of the capacity curves of the bridge components, a task that may be carried out without the use of a dedicated finite element model: the identification of the seismic demand corresponding to a given performance target may therefore be completed in a fraction of the time that would be required for non-linear dynamic analyses. However concerns have been raised on the accuracy of the DDBA when predicting structural responses for large non-linearities and for a variety of bridge systems, since comparisons have only been carried out for a limited number of bridge types [Cardone, 2014, Sadan et al., 2013].

Therefore the accuracy of the DDBA method is investigated for a set of bridge systems that represent distinct typologies, especially in terms of deck continuity and pier-to-deck connection. The DDBA and non-linear dynamic results are compared in terms of fragility curves at the component and system levels, since this measure has direct consequences on the damage assessment of the infrastructure components in the case of a risk analysis.

4.7.1 The Direct Displacement-Based Assessment Method

The DDBA is initiated by defining a target deformation level for a given bridge component (e.g. pier or bearing). An iteration procedure is then carried out to update

the modal properties of the structural system corresponding to the target deformation, by using the secant stiffness formulation. Cardone et al. [2011] have shown that the obtained displacement pattern of the bridge could be used to derive a fragility curve, if the target deformation is considered as a damage threshold: the input design demand spectrum is scaled and over-damped in order to account for the energy dissipation by the hysteretic cycles in the non-linear range, finally providing the intensity measure that corresponds to the target deformation. Updating the modal properties mainly serves the purpose of updating the equivalent properties of the single degree-of-freedom structure, in order to obtain response spectrum values. However, the following points could still be improved within the DDBA procedure:

- The standard-deviation of the median value of the fragility curve (i.e. dispersion) is arbitrarily chosen because a normalized design spectrum is used as input, rather than a suite of natural records.
- In order to estimate the spectrum scaling factor that will reach the target deformation, an inverse capacity spectrum method is used, where the coordinates of the performance point are derived from an equivalent single-degree-of-freedom approximation.
- Finally, while the DDBA iteration process starts from a target deformation level in order to estimate the corresponding intensity measure, the possibility to directly compute the bridge response from an input demand spectrum should be investigated.

Therefore it is proposed to use a set of natural ground motion records as input to the DDBA procedure, instead of a design demand spectrum: this modification enables to obtain a distribution of performance points for different levels of seismic intensity, thus accounting for the record-to-record variability. This variant of the DDBA procedure is named *EMA* (Effective Modal Analysis), and its main steps are defined in Figures 4.23 and 4.24.

It is observed that the main drawback of the *EMA* approach, as initially conceived, is the requirement to predefine a target deformation level (i.e. limit state) and to carry out the analysis for each component: for instance, in the case of a bridge system with

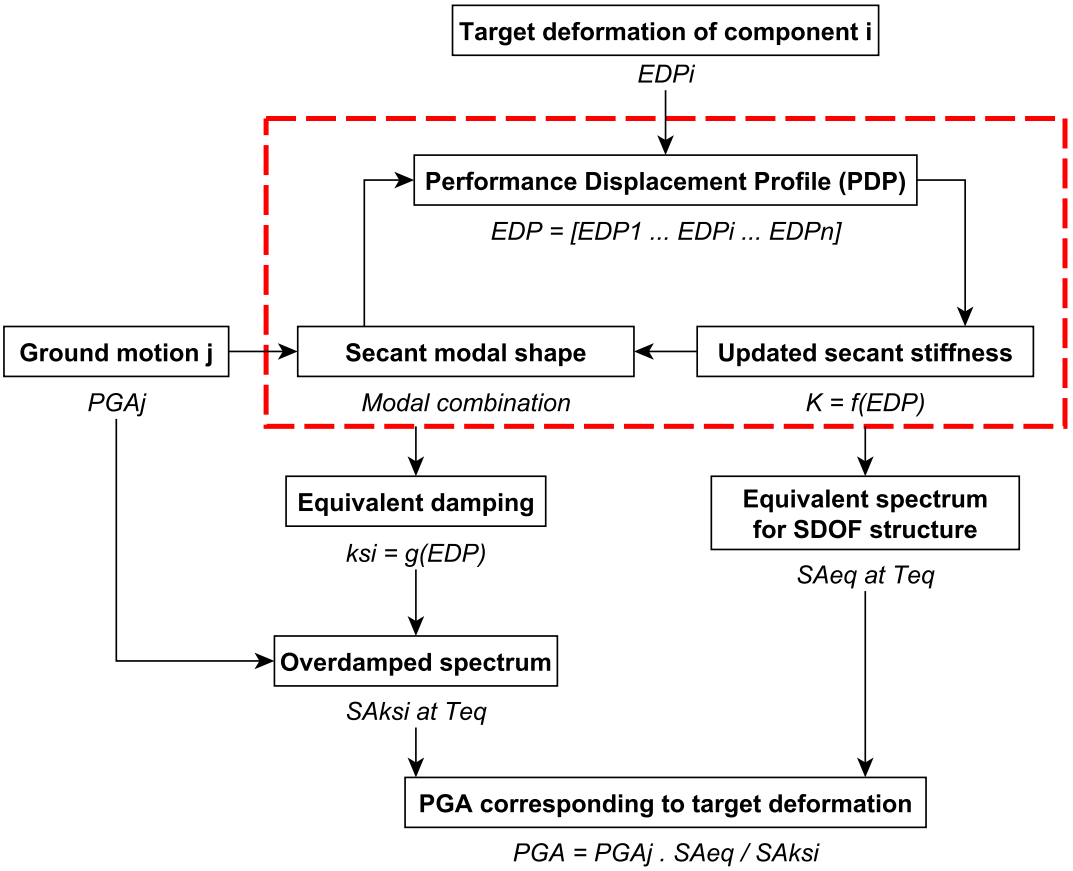

FIGURE 4.23: Main steps of the *EMA* approach for simplified seismic fragility assessment.

n components and m damage states each, a total of $n \cdot m$ *EMA* analyses will have to be performed in order to obtain the fragility parameters for all components. Moreover, the input records have to be scaled in order to match the seismic level that corresponds to the target deformation: a lot of care is usually required in the scaling process, so that the selected ground motions keep consistent properties (e.g. frequency content) over a given range of seismic intensity. Finally, the *EMA* approach is based on the estimation of equivalent properties (e.g. spectral coordinates of the performance point) of the single degree-of-freedom (SDOF) structure, so that it may be compared to the seismic demand spectrum: this approximation, present in the original DDBA approach, may also constitute a source of error.

Based on these observations, the EMA procedure is modified to obtain a more direct method: *dirEMA*, for direct Effective Modal Analysis (as shown in Figure 4.25). As opposed to the *EMA* approach, unscaled ground motion records are used as inputs in the *dirEMA* procedure, while the structural response is directly quantified as a result.

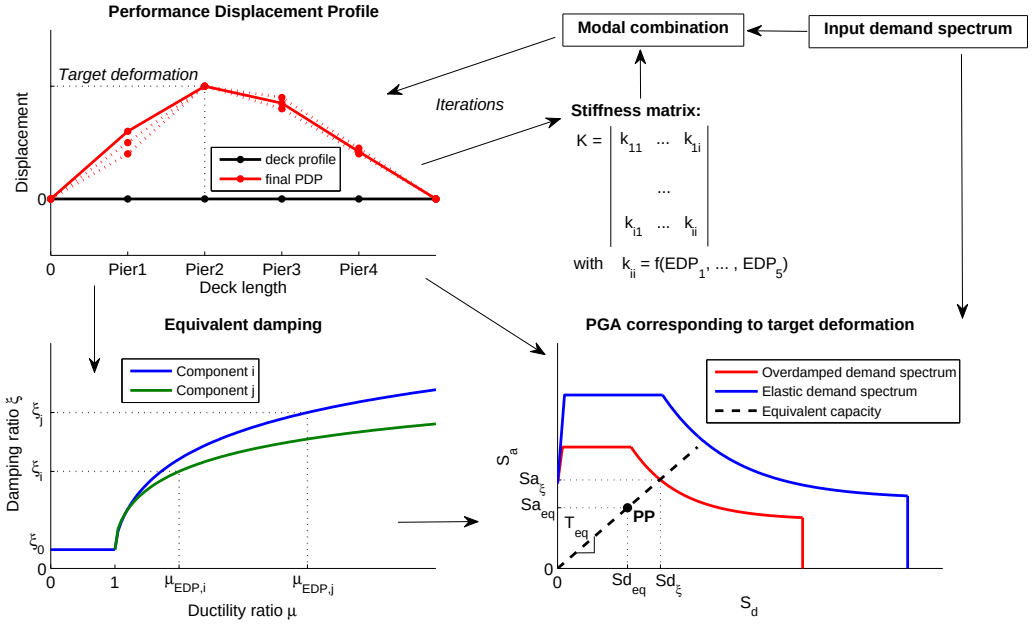

FIGURE 4.24: Physical illustration of the main steps in *EMA*.

This is achieved by reorganising the iteration cycle, which now includes the update of equivalent damping at each loop. Using this approach, all the component responses are obtained through only one run of the *dirEMA* algorithm and there is more flexibility in the choice of the input records, which can be either unscaled (e.g. 'cloud' analysis) or scaled (e.g. multi-stripe analysis or Incremental Dynamic Analysis).

Both *EMA* and *dirEMA* methods only require a limited amount of information in order to define the bridge system, i.e. the mass matrix, the connectivity between structural nodes, the constitutive model with hysteresis (i.e. in order to estimate equivalent damping) for each component and a set of acceleration time-histories. The outcome is then the structural response of the bridge components for a given ground motion if *dirEMA* is used, or the PGA level corresponding to the desired deformation level of a given component if *EMA* is used.

4.7.2 Definition of Bridge Typologies for Fragility Assessment

The simplified approaches that have been detailed in the previous sub-section may now be benchmarked for a selection of representative bridge types. The focus is put here on RC girder bridges that are typically found along road highways. A first distinction can be made regarding the deck, which can be either continuous or comprised of a set of

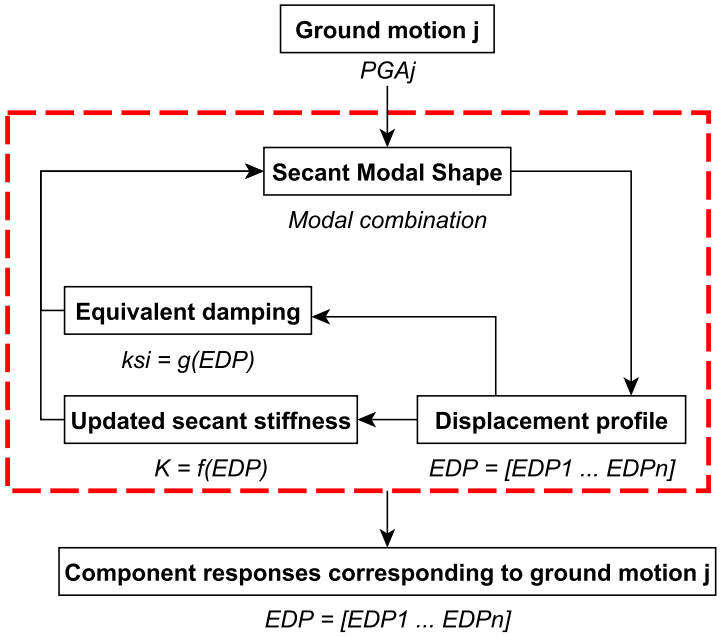

FIGURE 4.25: Main steps of the *dirEMA* approach for simplified seismic fragility assessment.

independent spans. Then, the deck can be connected to the pier cap through various bearing devices (i.e. simply-supported deck) or it can be directly connected to the pier (i.e. monolithic connection), thus preventing relative movement for all degrees of freedom. Finally, depending on the bridge configuration, the large rigidity of the deck in the longitudinal direction and the possibility (or not) of relative displacement between the deck and the piers, seismic analysis of the bridge in the longitudinal direction may be straightforward (i.e. only one degree-of-freedom), while the deformation of the deck in the transversal direction always allows relative displacements between the pier caps. As a result, five generic bridge layouts are proposed, as illustrated in Figure 4.26.

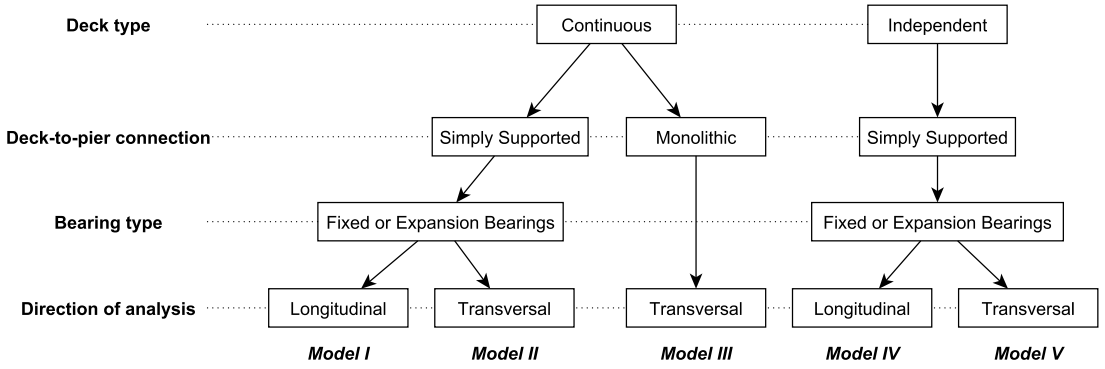

FIGURE 4.26: Bridge typologies considered in the benchmark study.

Variants of the five generic models are also developed, depending on the configuration of the expansion and fixed bearings (see Figure 4.27): this enables the sampling of a wide range of bridge layouts, from very rigid systems (i.e. only fixed bearings) to very flexible ones (i.e. only expansion bearings).

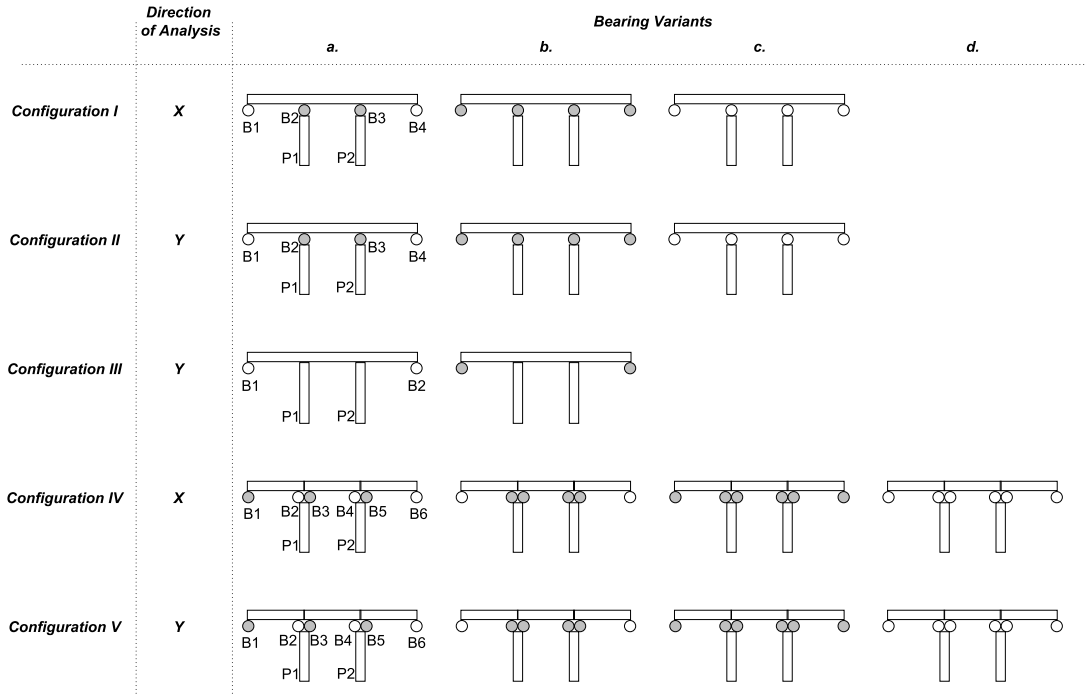

FIGURE 4.27: Layout of the bridge models considered in the study. White (respectively grey) circles represent expansion (resp. fixed) elastomeric bearings.

The mechanical properties and structural characteristics of the MSSSC girder bridge by Nielson [2005] have been used to define the five generic models, with the same RC pier and deck properties. Regarding the bearings, simplified stiffness models are proposed in order to facilitate the application of the *dirEMA* and *EMA* approaches: bilinear or trilinear models are used, in order to model the Coulomb friction law of the elastomeric bearings. In the case of fixed bearings, the stiffness model proposed by Cardone [2014] has been used, as shown in Figure 4.28. The equivalent bilinear stiffness model of the piers is obtained by fitting the pushover curve that has been derived through a non-linear static analysis on the OpenSees platform. Specific masses and kinematic conditions are added to the pier caps in order to simulate their behaviour when integrated to the bridge system.

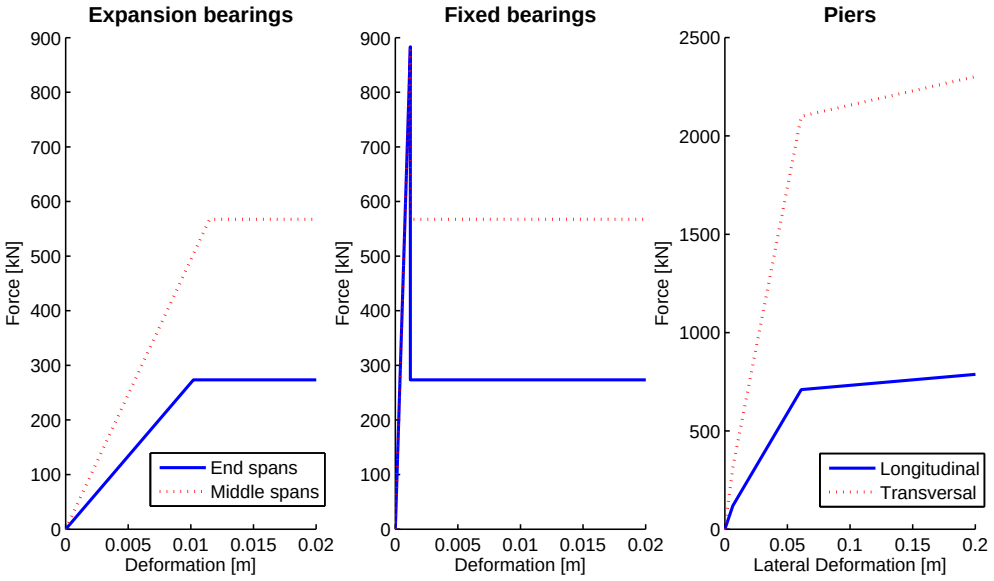

FIGURE 4.28: Stiffness models for expansion (left) and fixed (middle) bearings, and piers (right).

4.7.3 Secant Stiffness and Damping models

The execution of the *EMA* and *dirEMA* methods require the updating of the system's secant stiffness and damping ratio in the inelastic range. For each bridge component, a secant stiffness function with respect to the ductility ratio is easily derived from the models in Figure 4.28, by computing the ratio of the actual force that would be generated by the component in the non-linear range (i.e. according to the stiffness model) over the actual deformation of the component.

The initial damping ratio ζ_0 that is used in the elastic range has to be completed by another damping type ζ_{hys}, which represents the energy that is dissipated in the hysteretic cycles of the components, which are not accounted for by the secant stiffness model. The accurate estimation of hysteretic damping ζ_{hys} is an essential step, since it influences the level of the global damping and the amplitude of the structural response. Equations to determine ζ_{hys} have been proposed throughout various literature references and they can be distinguished between mainly analytical (equivalent damping) and empirical (substitute damping) methods.

According to the equivalent damping method by Jacobsen [1930], the additional viscous damping ζ_{hys} can be estimated by equating the energy of a viscously damped oscillator with the hysteretic energy of the non-linear oscillator for a steady state cycle at a given

ductility level [Judi et al., 2000]. Several studies [Blandon and Priestley, 2010] propose a review of equivalent damping relations, which are summarized in Table 4.10.

TABLE 4.10: Equivalent damping models for different types of structural elements, as a function of the ductility ratio μ. r represents the strain-hardening ratio, T is the effective period and the variables a, b, c, d and N represent some regression coefficients. α and β are parameters of Takeda's hysteretic model (i.e. coefficient of stiffness degradation and reloading curve).

Structural model	Equivalent damping
Perfectly-plastic bilinear [Rosenblueth and Herrera, 1964]	$\zeta_{hys} = \frac{2}{\pi} \cdot \frac{(1-r)\cdot(\mu-1)}{\mu - r\cdot\mu + r\cdot\mu^2}$
Takeda model [Gulkan and Sozen, 1974]	$\zeta_{hys} = 0.2 \cdot \left(1 - \frac{1}{\sqrt{\mu}}\right)$
Elastic and Coulomb slip elements [Iwan, 1980]	$\zeta_{hys} = 0.0587 \cdot (\mu - 1)^{0.371}$
Takeda model ($\alpha = 0.5$ and $\beta = 0$) [Kowalsky, 1994]	$\zeta_{hys} = \frac{1}{\pi} \cdot \left(1 - \frac{1-r}{\sqrt{\mu}} - r \cdot \sqrt{\mu}\right)$
Steel members [Priestley, 2003]	$\zeta_{hys} = \frac{1.5}{\mu\cdot\pi} \cdot (\mu - 1)$
Concrete frames [Priestley, 2003]	$\zeta_{hys} = \frac{1.2}{\pi} \cdot \left(1 - \frac{1}{\sqrt{\mu}}\right)$
Concrete columns and walls [Priestley, 2003]	$\zeta_{hys} = \frac{0.95}{\pi} \cdot \left(1 - \frac{1}{\sqrt{\mu}}\right)$
Hysteretic model [Blandon and Priestley, 2010]	$\zeta_{hys} = \frac{a}{\pi} \cdot \left(1 - \frac{1}{\mu^b}\right) \cdot \left(1 + \frac{1}{(T+c)^d}\right) \cdot \frac{1}{N}$

The method referred to as substitute damping, initially introduced by Gulkan and Sozen [1974] after a series of experimental and analytical studies, assumes that the ground motion energy that is input into a given structure corresponds to the one that is dissipated by an elastic system with viscous damping. Therefore, by equating the earthquake input energy with the dissipated viscous energy, the substitute damping, which includes both elastic and hysteretic damping, can be expressed as:

$$\zeta_{sub} = \zeta_0 + \zeta_{hys} = \frac{T_{sub} \cdot \int_0^t a_g(\tau) \cdot v(\tau) \cdot \mathrm{d}\tau}{4\pi \cdot \int_0^t v^2(\tau) \cdot \mathrm{d}\tau} \tag{4.11}$$

where T_{sub} is the effective period corresponding to the secant stiffness at maximum response, a_g is the ground motion acceleration, v is the relative velocity of the structure and t is the duration of the ground motion. It is then possible to apply this equation to

various structural components and to derive corresponding substitute viscous damping models.

First, in order to choose the most appropriate formulation for this study, a series of different elastic perfectly-plastic models are subjected to a set of ground motions (see selection in Section 4.3.3). The substitute viscous damping is then evaluated with Equation 4.11 for each input ground motion (see Figure 4.29 left), using the outputs of the OpenSees dynamic analyses. It is found that the results are stable for different configurations of the element's stiffness or yield strength. Therefore a regression of the form $\zeta_{hys} = a \cdot (\mu - 1)^2 + b \cdot (\mu - 1)$ is proposed, as used by Paulotto et al. [2007]. The substitute damping model can then be expressed as:

$$\zeta_{sub} = \zeta_0 + \zeta_{hys} = \zeta_0 - 0.00211 \cdot (\mu - 1)^2 + 0.0772 \cdot (\mu - 1) \tag{4.12}$$

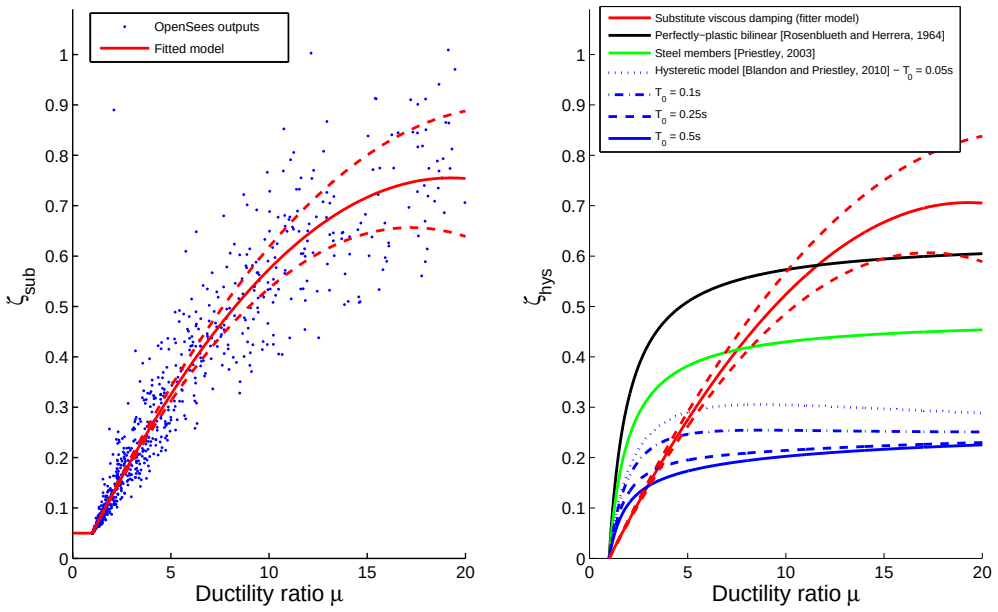

FIGURE 4.29: Left: Outputs of the OpenSees analyses and fitted model for the substitute viscous damping. Right: Comparison of the various damping models for perfectly-plastic bilinear components. Since the model from Blandon and Priestley [2010] is period-dependent, different sample periods are shown. The dotted red lines represent the 95% confidence bounds of the regression parameters.

The regression equation is compared with other equivalent damping models from the literature (see Figure 4.29 right). Overall, a good agreement on the general damping level can be found. However, the damping functions not do present the same shape: all

equivalent damping models seem to overestimate damping for small ductility ratios (i.e. in the range 1-10) and overestimate it for larger levels, as if the regressed equivalent damping models were not accounting for some physical characteristics of the structural element. To validate this, the response of a perfectly-plastic bilinear system is computed in OpenSees for the series of ground motions (see Subsection 4.3.3). The results are compared with the ones obtained with the EMA procedure. Table 4.11 compares the errors of the responses. The comparison between different damping models shows a significantly better performance of the substitute damping model, while the period-dependent model by Blandon and Priestley [2010] still yields more accurate results than the model by [Rosenblueth and Herrera, 1964].

TABLE 4.11: Performance of different damping models when applied to a perfectly-plastic bilinear element. SSE_{log} represents the sum of squared errors between the logarithm of the responses.

Damping model	SSE_{log}
Substitute viscous damping	0.0492
Bilinear model [Rosenblueth and Herrera, 1964]	0.0890
Steel members [Priestley, 2003]	0.0702
Hysteretic model [Blandon and Priestley, 2010]	0.0725

The better performance of the substitute damping may be due to the fact that this model has been empirically developed using the ground motion suite. It can also be observed from Figure 4.29 that the substitute damping curve crosses all the equivalent damping models for different ranges of ductility: this observation raises some interrogations on the validity range of the equivalent damping equations, since they seem to coincide with the substitute damping model, but only for narrow ranges of ductility. Finally, Table 4.11 shows that the choice of the hysteretic damping model is not critical for the EDP response, since the error rates remain within the same order of magnitude.

4.7.4 Derivation of Component Fragility Curves

Once that the modelling assumptions are specified, it is proposed to derive fragility curves at the component level, with either the simplified methods (i.e. *EMA* and *dirEMA*) or the non-linear dynamic analyses on a finite element model. Each of the bridge models from Figure 4.27 is subject to the same acceleration time-histories that are presented in Subsection 4.3.3. For each of the bridge components that are likely to

sustain any damage (i.e. RC piers, fixed and expansion bearings), the seismic response is recorded and compared to the limit state thresholds proposed by Nielson [2005] and summarized in Table 4.12. Only slight and moderate damage states are considered in this example, since most components have not reached further damage states under the selected range of ground motions (i.e. moderate seismicity): thus, due to the scarcity of data points for heavier damage states, stable estimates for the corresponding fragility parameters cannot be guaranteed.

TABLE 4.12: Median values for prescriptive limit states, as proposed by Nielson [2005].

Component	Slight	Moderate
Pier (longitudinal) – Curvature / Top Displacement [mm]	0.0039 / 52	0.0062 / 70
Pier (transversal) – Curvature / Top Displacement [mm]	0.0116 / 60	0.0183 / 74
Fixed elastomeric bearing – Deformation [mm]	30	100
Expansion elastomeric bearing – Deformation [mm]	30	100

The accuracy of the *EMA*- and *dirEMA*-derived component fragility curves can then be quantified with respect to the OpenSees results from non-linear dynamic analyses: while the direct comparison of both fragility parameters α and β does not necessarily provide a straightforward visualisation of the 'error rate', it is proposed instead to use the Kolmogorov-Smirnov (K-S) distance, which measures the largest absolute difference between two distribution functions (see Figure 4.30). This metric has previously been used by Gehl et al. [2015] for the comparison of fragility curves: it has the ability to directly express the maximal error in terms of probability of damage, which is a quantity that can be easily interpreted in practice. For instance, a K-S distance of 0.1 between two fragility means that, over the support of the probability distribution, the highest gap between the two probabilities of damage is 10%, which is deemed satisfactory given the uncertainties and assumptions at play.

A quick analysis of Figure 4.30 reveals the following points:

- Globally the performance of both *dirEMA* and *EMA* methods is not satisfying and many fragility curves result in a K-S distance that is superior to 0.5: in other words, for some PGA values, the difference between the approximate probability of damage and the OpenSees one is exceeding 0.5, which represents a non-negligible bias.

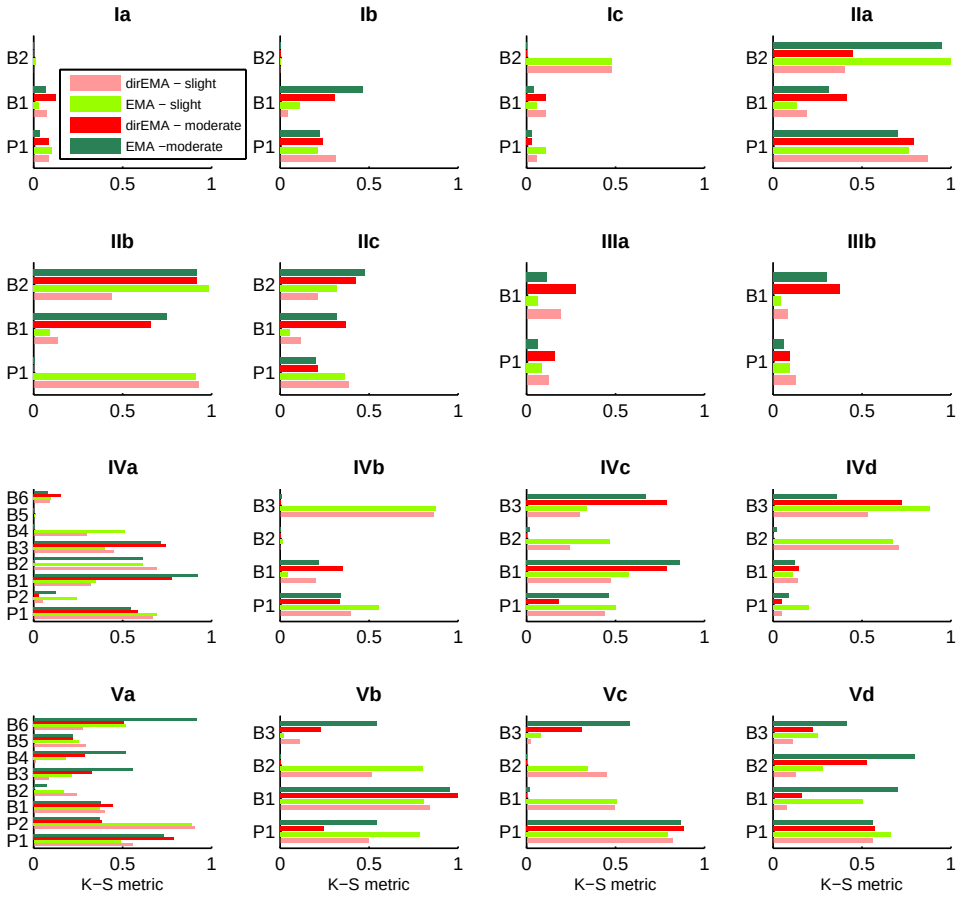

FIGURE 4.30: K-S distance between the OpenSees component fragility curves and the *dirEMA* (in red) and the *EMA* (in green) results, for the 16 bridge models (see Figure 4.27). Except for models IVa and Va, all bridges are symmetric and only half of the components are represented.

- While there is no overall significant difference between the performance of *dirEMA* and *EMA* methods, the *dirEMA* procedure seems to be slightly more accurate. This observation confirms that *dirEMA* could be used instead of *EMA*, since the former method is less time consuming than the latter while allowing the use of unscaled records.

- For simpler bridge models with lower numbers of in-series components (i.e. bearings), such as models I to III, the simplified approaches show reasonable accuracy. On the contrary, bridge models IV and V with simply-supported independent deck spans present the highest prediction errors, because components located towards

the middle of the bridge are less restrained and they are more influenced by the response of adjacent components.

- Bridge models with only expansion bearings appear to lead to more accurate results, due to their simpler stiffness model (i.e. bilinear curve), as opposed to fixed bearings.

Finally, it should be noted that the definition of the K-S distance yields an absolute measure, which proves difficult to interpret when trying to check whether the fragility curves are overestimating or underestimating the damage probabilities. However, it globally appears that the fragility mean α is slightly higher when applying the simplified approaches, i.e. an underestimation of damage occurrence with respect to non-linear dynamic analyses.

4.7.5 Discussion

Starting from the previously derived component fragility curves, fragility curves at the system level (see Figure 4.31) are derived by using the system reliability method developed by Song and Kang [2009]: it is assumed that the component damage states are consistent with each other, so that the system damage state (e.g. slight) occurs as soon as one of the components has reached such damage state (i.e. in-series system).

A first observation can be made on the satisfying performance of the *dirEMA* and *EMA* methods when considering the system fragility curves: it appears that the significant errors observed for the component fragility curves does not propagate to the same extent at the system level. This is explained by the various failure modes (i.e. individual component events) that may lead to a given system damage state: if some of the component fragility curves are inaccurately predicted but do not cause global system failures, their impact on the probability of damage at system level is dramatically reduced (i.e. because they are not the first to reach that damage state, the system damage state is not highly depedent on these components).

The simplified models perform especially well for the slight damage state, which can be expected as it relies mostly on elastic behaviour, while some biases start to appear at the moderate state: in general, both *dirEMA* and *EMA* approaches tend to provide

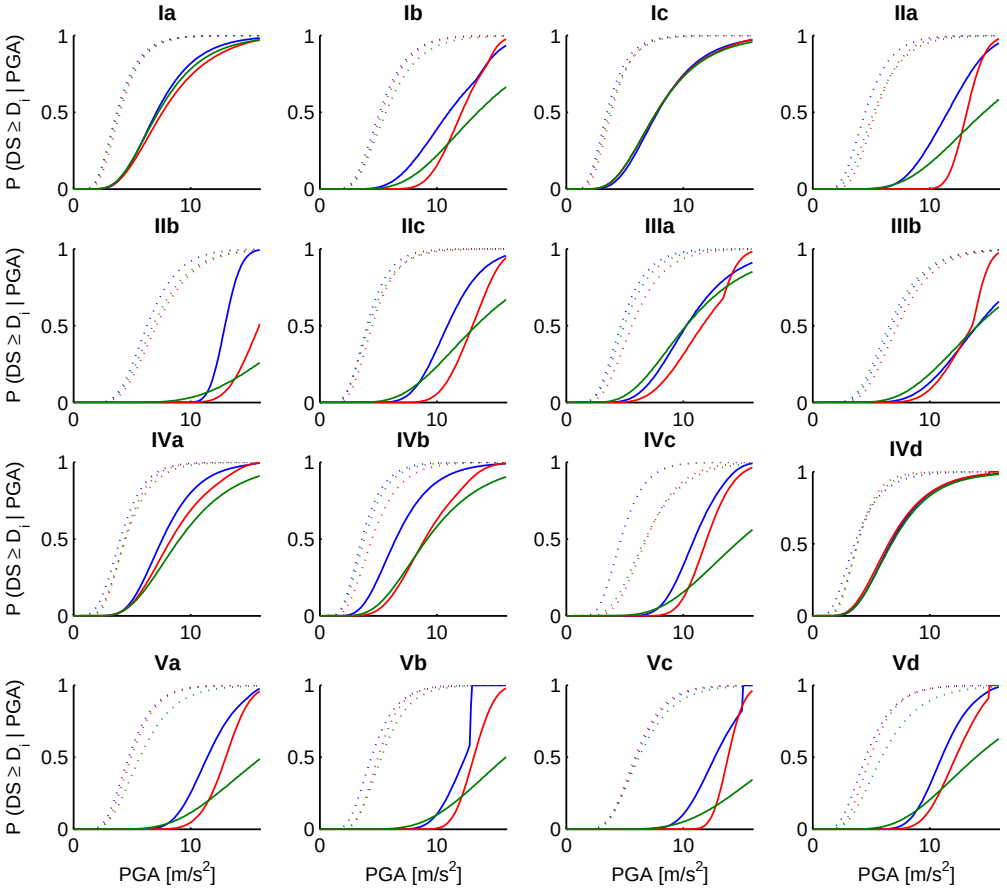

FIGURE 4.31: Fragility curves of the bridge system for slight (dotted lines) and moderate (solid lines) damage states. Curves derived from OpenSees, *dirEMA* and *EMA* are represented in blue, red and green respectively.

slightly non-conservative results. The performance of both simplified methods is roughly equivalent, even though the *dirEMA* approach seems to give slightly better predictions for the moderate damage state. However, it should be stressed that the two simplified methods are conceptually different in the way they make use of the input ground motions: the *dirEMA* procedure directly uses the dataset of records (i.e. same approach as the OpenSees analyses), while the *EMA* approach requires the scaling of each record for each limit states. This difference in the treatment of the record-to-record variability may also explain why the fragility curves developed through *dirEMA* tend to be closer to the OpenSees results. Finally, the models containing a high proportion of fixed bearings (e.g. Ib, IIb, IVb, IVc) generate the highest prediction errors, as opposed to expansion bearings that are associated with a simpler stiffness model.

To conclude, it has been shown that the use of natural ground motions as input to

the procedure of Cardone et al. [2011] is feasible in practice and that it leads to the quantification of the standard deviation β, instead of requiring the selection of an arbitrary value. A variant – *dirEMA* – of the DDBA method has also been proposed, where the structural response is directly estimated from an unscaled ground motion, through an iteration loop. An empirical comparison of the simplified approaches with non-linear dynamic analysis, for a variety of bridge models with different types of deck and pier-to-deck connections, leads to the following conclusions:

- The performance of the *dirEMA* procedure is globally equivalent to the *EMA* approach over the different bridge models, which enables to validate the use of *dirEMA* as a viable alternative to the more cumbersome *EMA* method.
- The use of the system reliability method for the assembly of the component fragility curves results in much smaller error rates at the system level, since some bridge components do not participate to the predominant failure mode.
- The accuracy of the simplified methods decreases when moderate damage states are considered: once a given level of ductility ratio is exceeded for a component, the estimation of the deformation in the non-linear range becomes more and more subject to modelling errors (e.g. equivalent damping, number of hysteretic cycles, etc.). However, moderate damage is usually difficult to predict as the system is in hybrid condition. Once significant damage is reached, it can be expected that differences may be lower, as they depend less on hysteretic behaviour and more on the failure of one dominant component and the way collapse is defined.
- The simplified approaches perform better when a reduced number of components are assembled in series, as opposed to models IV and V. Both *EMA* and *dirEMA* procedures tend to be less accurate when mainly fixed bearings are present: this observation is linked to the complexity of the stiffness and damping models that describe each component, which may be the source of initial errors in the estimation of the component's response. Therefore special care should be devoted to the definition of the component behaviour, especially regarding the selection of a relevant equivalent damping relation for each component type.
- The failure of the simplified approaches to accurately predict the specific response of individual components prevents the use of these methods in the present study,

where the derivation of component fragility curves and the identification of joint failure modes are essential steps. Therefore the use of non-linear time-history analyses is advocated for the derivation of seismic fragility curves in the rest of the study, even though they come at the cost of higher computational loads.

4.8 Conclusion

This Chapter has detailed the derivation of component fragility curves for the different hazard-specific failure modes. All computations have been applied to a generic bridge model, for which characteristics of the waterway and surrounding soil are assumed; the emphasis is put on the methodological developments, in order to provide relevant modelling tools for real-life applications.

It has been shown that the most accurate way to derive seismic fragility curves is to perform non-linear time-history analyses on a finite-element model. Simplified methods that are inspired from DDBA might provide accurate results for system-level fragility curves and specific bridge types (e.g. continuous decks): however these methods fail to deliver accurate component fragility curves, which are crucial elements within the proposed method. Moreover, the nature of some simplified approaches, such as *EMA*, prevents the computation of the correlation matrix between components: again, the correlation structure is required to determine the joint probability of occurrence of the damage events. Therefore the use of these simplified analysis approaches is not advisable in the present context, where the quantification of low-probability high-consequence events is one of the main objectives (i.e. the use of such simplified methods would generate large discrepancies, especially when damage events have to predicted around the tails of the fragility curves).

Regarding other hazard types, the concept of fragility is less advanced, which explains the scarcity of available analytical methods. Therefore the probability of soil subsidence is quantified through literature-based fragility curves, while static equilibrium equations are used to assess the probability of slope failure. On the other hand, fragility curves for scour are based on empirical equations for which the parameters are probabilistically sampled.

One of the challenges that has not been addressed is the multiplicity of fragility derivation methods for the different hazard types (see Figure 4.32). Some approaches include the variability of modelling parameters, while others account for the uncertainty on hazard loading (i.e. earthquakes), which hinders the harmonisation of all uncertainty sources. Such a standardisation is not always possible between the hazard types considered, since it would require models of equal 'quality' that may be used with sufficient data (e.g. similar 'completeness of empirical data or measurements for each hazard type), in order to propagate the same level of uncertainty through each fragility curve. However, the fact that each hazard type is treated within different fields, with different philosophies with respect to risk assessment, makes this harmonization a pending issue. If this harmonisation cannot be achieved, then there is the risk that some fragility curves will not account for all sources of uncertainty. As a result, the estimated loss distributions would lead to an over- or under-estimation of extreme events, which would be problematic when comparing losses between single hazard types.

Finally, once these component fragility curves have been derived, they must be assembled in order to compute joint occurrences of some damage events, with the ultimate goal of estimating functionality losses at the level of the bridge system: this further step will be the object of Chapter 5.

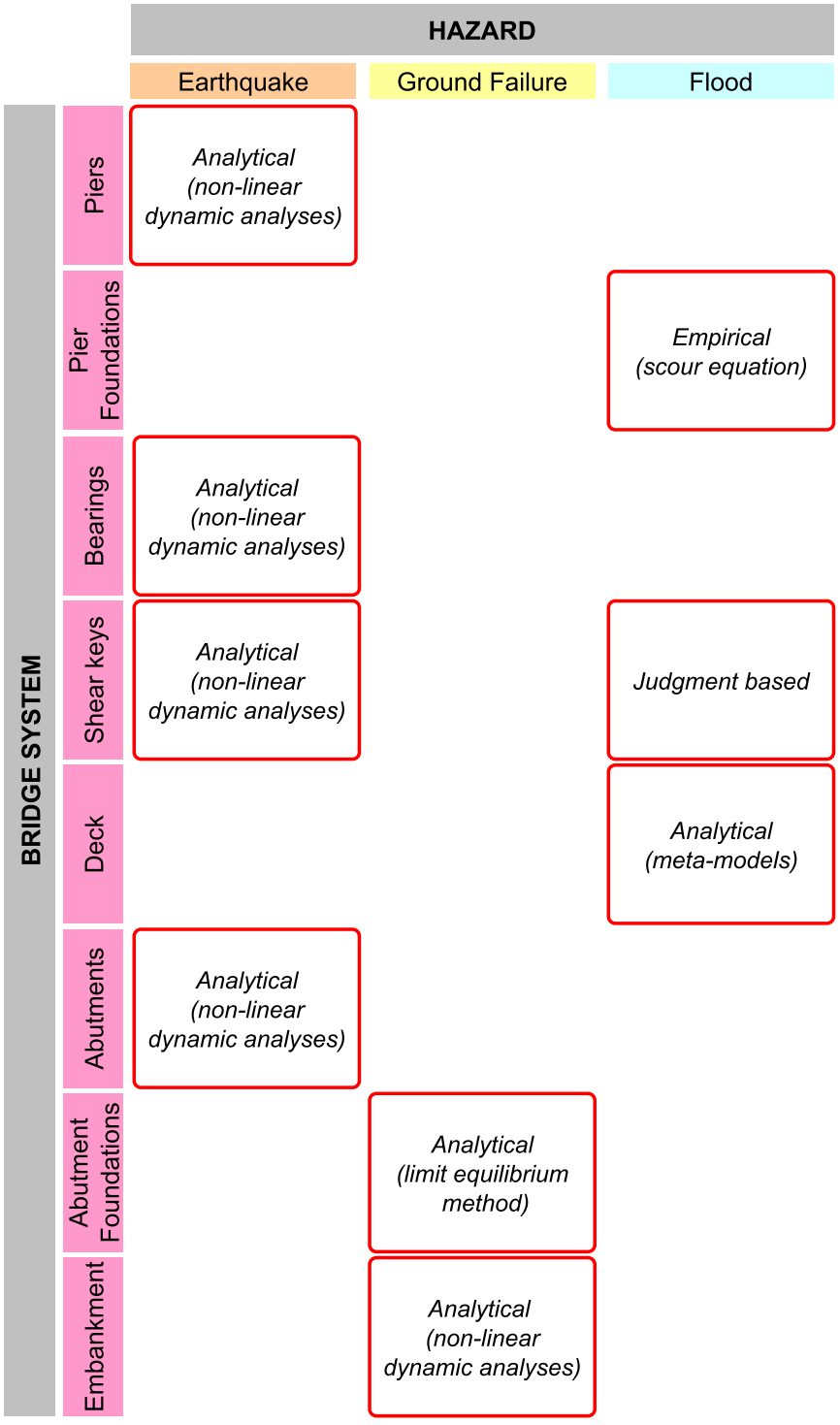

FIGURE 4.32: Summary of the fragility derivation methods considered for the combinations of components and hazards.

Chapter 5

Derivation of Hazard-harmonized System Fragility Curves

5.1 Introduction

Unlike residential buildings where the estimation of physical damage states is of paramount importance to predict potential losses of life, infrastructure elements of physical systems (e.g. bridges in a road network) are mainly characterized by the function they have to fulfil in order to ensure the system's performance [Modaressi et al., 2014]. Therefore fragility models for infrastructure objects should be directly linked to functionality states, so that accurate probabilistic assessments of the downtime or reduced functionality of infrastructure systems can be carried out. Moreover, since spatially distributed infrastructure systems such as road networks may be exposed to a variety of natural hazards [Deng et al., 2015], the direct reinterpretation of loss in terms of decreasing functionality levels allows for a harmonization of the potential impacts between multiple hazard types, without being hindered by the analysis of specific and often irreconcilable failure mechanisms. The critical role of the relationship between bridge damage and functionality loss has already been highlighted by Padgett and DesRoches [2007], who use the outcomes of a Web-based survey in the U.S. to define damage states in terms of restoration of functionality. In parallel, Mackie and Stojadinovic [2006] have used bridge column damage to identify the induced repair cost and loss of vertical load capacity, which are essential metrics for the post-earthquake evaluation of highway bridges.

To this end, the component fragility curves that have been derived for each hazard type and for each specific failure mechanism (Chapter 4) and the associated functionality losses (Chapter 3) are assembled in order to specify system failure modes. By relating different functionality levels to the various component damage states, the corresponding system fragility curves can then be assembled in order to express the probability of occurrence of specific failure modes that correspond to similar levels of functionality loss.

The quantification of the probability of failure of a given system may constitute a direct application of reliability analysis methods. Reliability engineering represents the field that studies dependability in the lifecycle management of a product, i.e. the ability of a system or component to function under given conditions for a specified period of time. Therefore reliability analysis has mainly emerged as a discipline in manufacturing industries (e.g. car industry), before being applied to civil engineering structures subjected to various loadings [Lemaire et al., 2005]. In the reliability theory, a system's or component's reliability is represented by a limit state function g, which is usually defined as the difference between the resistance R (i.e. capacity) and the load S (i.e. demand):

$$g(R,S) = R - S \tag{5.1}$$

Therefore the probability of failure P_f corresponds to the probability of the resistance R being exceeded by the load S (i.e. the component or the system enters the failure region defined by the limit state function):

$$P_f = \Pr(R \leq S) = \Pr[g(R,S) \leq 0] \tag{5.2}$$

If it is assumed that R and S follow a Gaussian distribution, the margin variable $Z = R - S$ is also Gaussian, with mean μ_Z and standard-deviation σ_Z [Benjamin and Cornell, 1970]. The probability of failure is then given by:

$$P_f = \Pr(Z \leq 0) = \Phi\left(-\frac{\mu_Z}{\sigma_Z}\right) \tag{5.3}$$

where Φ is the standard normal probability density function. Therefore the probability of failure is completely characterised by the factor $\beta_c = -\mu_Z/\sigma_Z$, which is called the reliability index.

In the case of system comprising a set of components, statistical tools such as reliability block diagrams or fault trees may be used to facilitate the calculation of the probability of failure of the whole system (see Subsection 2.1.2.2). More recently, matrix-based system reliability methods [Song and Kang, 2009] have proven their ability to tackle the problem at hand, especially regarding the issue of statistical dependence between components, as detailed in Section 5.2. However, their application to large structural systems with numerous components should be investigated in detail, in order to ensure that such approaches are suitable for the systematic analysis of a wide range of systems, especially in a multi-hazard context where more than one loading may be applied.

As an alternative, the Bayesian Network (BN) methodology, which has been introduced by Bensi et al. [2011] in the context of seismic risk, may be used in both the hazard and fragility assessment steps, thus potentially providing a seamless risk analysis framework (see Section 5.3). Siraj et al. [2015] have also introduced BNs for the fragility assessment of high-voltage transformers with respect to seismic risk, while accounting for various failure modes. However, although some BN formulations have been proposed for risk or fragility assessments, there are relatively few examples of their applications to real-world systems. Therefore Section 5.4 discusses the applicability of an efficient BN-based procedure for fragility assessment and its potential merits with respect to the matrix-based system reliability method.

Two applications are then presented in order to demonstrate the capabilities of the proposed BN approach. First, a fragility assessment is conducted on a bridge system that is exposed to multiple hazard events, namely earthquakes, ground failures and floods, thus taking advantage of the modularity of the method (see Section 5.5). While several studies have developed multi-hazard fragility functions for bridges, especially regarding the joint effect of scour and seismic hazard [Alipour et al., 2012, Prasad and Banerjee, 2013], it is anticipated that the proposed BN approach can provide a more generic framework with the possibility to integrate additional failure mechanisms and cumulated damage models. Secondly, Section 5.6 focuses on the fragility assessment of the same bridge system for single seismic hazard. The BN structure is slightly modified

in order to directly express the probabilistic distribution of functionality losses with respect to the seismic intensity, thus generating harmonized functionality curves.

5.2 The Matrix-based System Reliability Method

The matrix-based system reliability (MSR) method has been formalized by Song and Kang [2009] and Kang et al. [2008]. Its main principles constitute a robust framework for system failure analysis and hence they also represent the underlying assumptions of the BN application method developed here.

Specifically, it is assumed that for a system with n components, each component i has k_i states. The sample space is composed of $m = \prod_{i=1}^{n} k_i$ events $e_{j=1..m}$, *mutually exclusive and collectively exhaustive* (MECE). Therefore, a given system event can be associated with a vector $\mathbf{c}$ of length m, whose j^{th} element is a binary variable indicating whether the MECE event e_j is a part of the system event or not. Hence, if the probability p_j of the occurrence of e_j can be quantified, the probability of the system event E_{sys} can be directly expressed as a vector product, using the MECE property:

$$\mathrm{P}\left(\mathrm{E}_{sys}\right) = \sum_{j:e_j \subseteq \mathrm{E}_{sys}} p_j = \mathbf{c}^t \cdot \mathbf{p} \tag{5.4}$$

In the present context, the MSR method is applied to a structural system, which comprises components that are statistically dependent on each other, due to the common loading that is applied to them (e.g. acceleration time-history). To account for this condition Kang et al. [2008] have introduced a set of *common source random variables* (CSRVs), represented by vector $\mathbf{x}$, so that the component failures conditional on $\mathbf{x}$ are statistically independent, using the theorem of total probability. Equation 5.4 can be written as:

$$\mathrm{P}\left(\mathrm{E}_{sys}\right) = \int_{\mathbf{x}} \mathrm{P}(\mathrm{E}_{sys}|\mathbf{x}) \cdot \mathrm{f}(\mathbf{x}) \cdot d\mathbf{x} = \int_{\mathbf{x}} \mathbf{c}^t \cdot \mathbf{p}(\mathbf{x}) \cdot \mathrm{f}(\mathbf{x}) \cdot d\mathbf{x} \tag{5.5}$$

where $\mathrm{f}(\mathbf{x})$ is the joint probability density function of the CSRVs contained in vector $\mathbf{x}$.

Song and Kang [2009] have introduced a correlation model based on the Dunnett-Sobel class of variables [Dunnett and Sobel, 1955] **U** and **V**, which are used to rebuild the covariance matrix of the failure events. Using a reliability analysis for each component i, the component failure can be expressed as the condition $Z_i \leq -\beta_i$, where Z_i is a standard normal variable and β_i represents the component reliability index. Therefore the variable Z_i can be expressed as the following:

$$Z_i = \sqrt{1 - \sum_{j=1}^{k} r_{ij}^2} \cdot V_i + \sum_{j=1}^{k} r_{ij} \cdot U_j \tag{5.6}$$

where V_i and U_j are independent and identically distributed standard normal variables, k is the number of CSRVs that are required depending on the complexity of the problem and the correlation structure (i.e. the dimension of CSRV vector $\mathbf{x}$), and r_{il} is a Dunnett-Sobel coefficient that is used to emulate the correlation coefficient between variables Z_i and Z_l:

$$\rho_{il} = \sum_{j=1}^{k} r_{ij} \cdot r_{lj} \quad \text{if} \quad i \neq l \tag{5.7}$$

The coefficients r_{ij} can be found through an optimization routine, with the objective of minimizing the difference between the observed correlation matrix of the Z_i variables and the matrix assembled from the correlation coefficients estimated in Equation 5.7. Depending on the type of problem and the required accuracy level, either a single CSRV (i.e. $k = 1$) may be enough or several ones may be necessary in order to achieve a satisfying Dunnett-Sobel model: the effect of the Dunnett-Sobel fitting error on the system failure probability has been studied by Kang et al. [2012] for various system configurations.

Moreover, if the structural system is assumed to work in-series, as it is the case here, a system failure event is defined by the failure of at least one of n components. The corresponding system fragility curve can be expressed as the following, if lognormal-based fragility curves for component failures are used:

$$\mathrm{P}_{sys}\left(IM\right) = 1 - \int_{-\infty}^{\infty} \phi(x) \cdot \prod_{i=1}^{n} \left[1 - \Phi\left(\frac{\frac{\log IM - \log \alpha_i}{\beta_i} + r_{i1} \cdot x}{\sqrt{1 - r_{i1}^2}} \right) \right] \cdot \mathrm{d}x \tag{5.8}$$

where IM is the intensity measure (i.e. loading parameter), ϕ is the standard normal probability density function, Φ is the standard normal cumulative distribution function, r_{i1} is the Dunnett-Sobel coefficient (when the number of CRSVs $k = 1$) and α_i and β_i are the fragility parameters for component i (i.e. median and standard deviation of log). It should be noted that Equation 5.8 is valid for $k = 1$ and that the use of additional CSRVs would require the computation of double or triple integrals, and so on. The whole MSR procedure is available in a Matlab-based code [The MathWorks, 2013], namely the FERUM (Finite Element Reliability Using Matlab) toolbox [Der Kiureghian et al., 1999].

5.3 General Principles of Bayesian Network Modelling

As an alternative to the MSR method, a formulation of the problem with Bayesian Networks (BNs) is investigated, in order to verify the capabilities of this alternative in terms of computational efficiency and flexibility (i.e. ability to treat a wide range of systems). The BN theory has already been thoroughly detailed in the context of the seismic risk analysis of infrastructure systems [Bensi et al., 2011], where BNs are used to model spatially distributed seismic demand, as well as component and system performance. In the present study, the emphasis is put on the Bayesian graphs that are necessary to assess the fragility of structural systems such as bridges.

5.3.1 General Definitions

A BN takes the form of a *directed acyclic graph* (DAG), which comprises edges and nodes. Nodes are classified as *parents* or *children* depending on the direction of the edges. A node without any parents is referred to as a *root node* (see example in Figure 5.1).

Each node represents an event that may take different states (e.g. *survival* or *failure* for a node representing an infrastructure component). The probability of each state is given by a *conditional probability table* (CPT), which represents the probabilities given the states of the parents (see Table 5.1): in the case of a root node, the CPT becomes a table of marginal probabilities (e.g. assumed probability distribution for a given input variable). It can be noticed that the CPT grows exponentially with the number of parents, which usually generates computational issues when large BNs are solved.

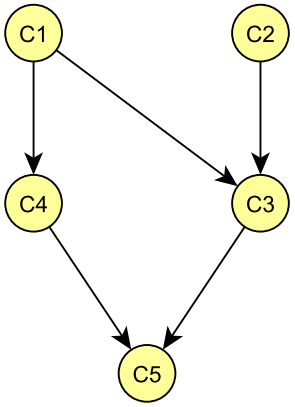

FIGURE 5.1: Example of a BN with 5 nodes (**C1** and **C2** are root nodes).

TABLE 5.1: Example of the CPT defining node **C3**, assuming binary states for **C1**, **C2** and **C3**.

C1	**C2**	**C3**	**CPT**
0	0	0	$Pr\,(\mathbf{C3}=0\vert\mathbf{C1}=0,\mathbf{C2}=0)$
1	0	0	$Pr\,(\mathbf{C3}=0\vert\mathbf{C1}=1,\mathbf{C2}=0)$
0	1	0	$Pr\,(\mathbf{C3}=0\vert\mathbf{C1}=0,\mathbf{C2}=1)$
1	1	0	$Pr\,(\mathbf{C3}=0\vert\mathbf{C1}=1,\mathbf{C2}=1)$
0	0	1	$Pr\,(\mathbf{C3}=1\vert\mathbf{C1}=0,\mathbf{C2}=0)$
1	0	1	$Pr\,(\mathbf{C3}=1\vert\mathbf{C1}=1,\mathbf{C2}=0)$
0	1	1	$Pr\,(\mathbf{C3}=1\vert\mathbf{C1}=0,\mathbf{C2}=1)$
1	1	1	$Pr\,(\mathbf{C3}=1\vert\mathbf{C1}=1,\mathbf{C2}=1)$

An *inference* is performed on the BN when one or more nodes are observed (i.e. *evidence* is entered by specifying a given state) and when the probabilities of the other nodes are updated. In the case of a forward analysis, evidence may be entered at the root nodes and the updated distributions can be estimated at the child nodes (e.g. distribution of infrastructure losses given the occurrence of some natural hazard events). Conversely, a backward analysis consists in the inference of the root nodes based on the observation of a given child node (e.g. updated distribution of the occurrence rate of some natural events given the observation of a given loss level).

5.3.2 The Junction-Tree Inference Algorithm

The junction-tree algorithm allows to perform an exact inference on the BN, which results in exact probability distributions at the nodes of interests. The algorithm is based on the following steps (see Figure 5.2), while the construction of a junction tree is demonstrated in Appendix F:

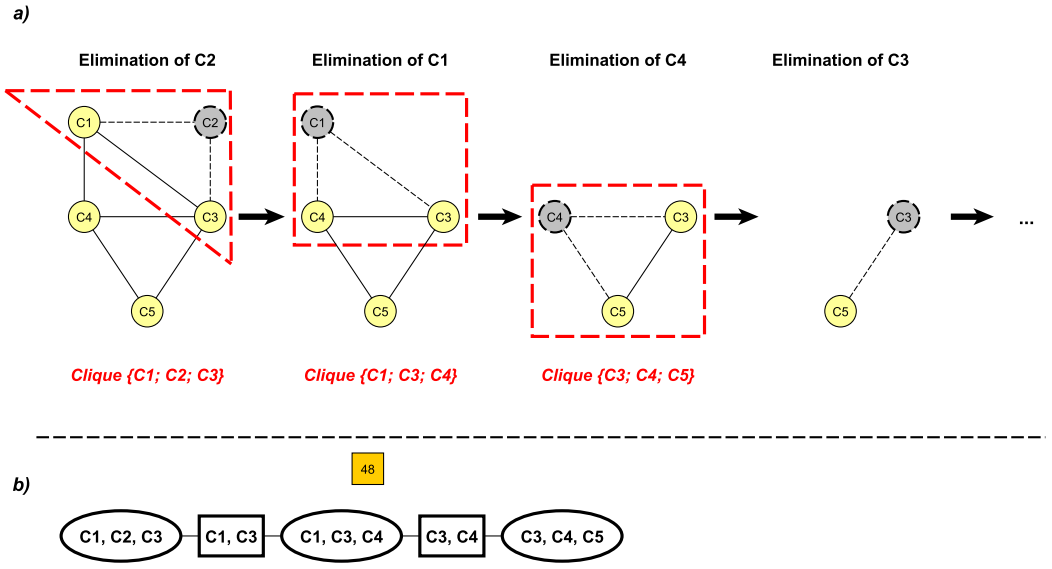

FIGURE 5.2: (a) Junction-tree algorithm applied to the BN example and (b) corresponding junction-tree containing the cliques.

1. Moralization of the BN: all edges are represented as undirected links, and all the parents of a same node are linked by a new undirected edge, if they were not previously linked.

2. The moral graph is used to successively remove nodes until the whole graph is eliminated.

3. When a given node is removed, its adjacent nodes are connected through additional undirected edges (i.e. fill-in edges), if they were not previously linked. Then a clique is formed by the eliminated node and all its adjacent nodes.

4. Another node is eliminated, and so on... A new clique is generated only if it is not a sub-group of previous cliques.

5. Once all nodes have been eliminated, all the successive cliques form the junction tree.

6. The potential (i.e. joint probabilities) of each clique needs to be computed. Once this operation is complete, the junction tree may be used for any inference of the BN.

It appears that the elimination order in the moral graph has a major influence on the computational load of the inference, since the early or late removal of some nodes

may generate non-optimal clique sizes, which may lead to an intractable number of probabilities to be evaluated. However, it has been shown that the determination of the optimal elimination order is an NP-hard problem [Franchin and Laura, 2014, Wen, 1990]. In practice, BN software such as the Bayes Net toolbox [Murphy, 2007] propose a partial optimization, whereby the next node that will generate either the least amount of fill-in edges or the smallest clique size is chosen: however, this method may still lead to elimination orders that lead to local optimal solutions only. Different elimination strategies have been studied by Kjaerulff [1990], depending on the topological structure of the BN.

5.4 Application of Bayesian Networks to the Reliability Assessment of Bridge Systems

This section describes the use of BNs to assemble component fragility curves into fragility functions at the system level. A comparative analysis is also proposed with respect to the matrix-based system reliability method.

5.4.1 Bayesian Network Structure

Define a BN that starts from the node(s) representing the hazard(s) loading and ends up with the node(s) representing the system event(s). The upstream part of the BN is composed of the following nodes (see Figure 5.3):

- root node(s) **IM** representing the hazard(s) loading applied to the n components;
- root node(s) $\mathbf{U_1}$ ... $\mathbf{U_k}$ representing the standard normal variables that are common to all components (k represents the number of CSRVs used to emulate the correlation structure), as introduced in Equation 5.6;
- root nodes $\mathbf{V_1}$ ... $\mathbf{V_n}$ representing the standard normal variables that are specific to each component (n represents the number of components in the system), as introduced in Equation 5.6;
- nodes $\mathbf{C_1}$ ... $\mathbf{C_n}$ representing the component failure events.

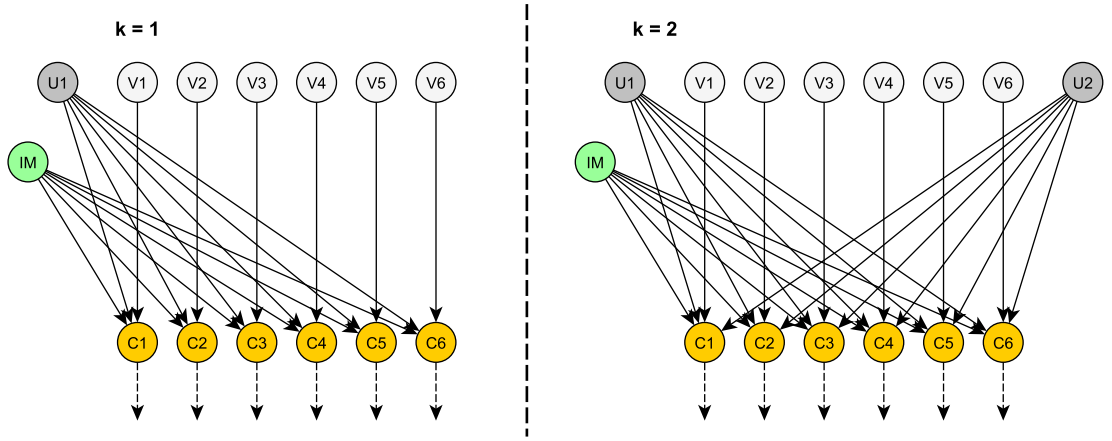

FIGURE 5.3: Bayesian Networks accounting for statistical dependence between component failures (one CSRV on the left, two CSRVs on the right), for a system with six in-series components.

As proposed in Bensi et al. [2011], Dunnett-Sobel classes can be modelled in BNs by creating root nodes (i.e. **U** and **V**) with a conditional probability table containing the discretised standard normal distribution. In the case that only one CSRV is needed, a component-event node $\mathbf{C_i}$ has three parent nodes, namely **IM**, $\mathbf{U_1}$ and $\mathbf{V_i}$. For each combination of sampled values $\{im; u_1; v_i\}$, the failure event of component i is expressed as the following condition:

$$\left(z_i = \sqrt{1 - r_i^2} \cdot v_i^2 + r_i \cdot u_1\right) \geq -\frac{\log im - \log \alpha_i}{\beta_i} \tag{5.9}$$

Using the corresponding probability density of values v_i and u_1, the final failure probability of component i can be calculated through Bayesian inference for any values of im.

The downstream part of the BN deals with the estimation of the system failure event, starting from the component events. Due to memory limitations in the size of the CPTs, a single system-level node **SYS** being the child of all component nodes (i.e. converging structure) is not recommended nor computationally realistic. A system with n components would result in a CPT of 2^{n+1} elements, assuming only binary states for the failure events. In the case of spatially distributed network systems, Bensi et al. Bensi et al. [2013] have introduced elaborate modeling strategies to build BNs based

on the identification of minimum link sets or cut sets. In the present study, however, the system considered is a single bridge structure that results from the assembly of structural components: it is expected that the definition of the system failure modes will result in much simpler formulations, which can be modelled through a few basic BN layouts, as detailed below. In practice, a bridge system may experience different system failures modes: it is likely that a given system failure mode is only related to a subset of components (e.g. only piers), while another system failure mode depends only on other types of components (e.g. superstructure elements). Then, each of these subsets of components corresponds to an in-series sub-system, for which a set of intermediate nodes can be defined in order to gradually reduce the number of parent nodes and the size of the CPTs, via two different strategies (see Figure 5.4):

- Layout 1: the component-event nodes are associated two by two, generating a layer of $n/2$ (or $[n-1]/2$ if n is an odd number) intermediate nodes $\mathbf{In_i}$. The nodes on this first layer are again linked two by two, and so on, until only two nodes are left to define the **SYS** node.

- Layout 2: the first two component-event nodes create a first intermediate node $\mathbf{In_1}$, which is in turn linked to the next component-event node in order to define another intermediate node $\mathbf{In_2}$, and so on, until there are no component-event nodes left. The last intermediate node then becomes the **SYS** node. This layout corresponds to a chain-like BN topology, which has been acknowledged as more computationally efficient than a converging structure [Bensi et al., 2013].

Multiple system failure modes for a given bridge are then assembled as shown on the left of Figure 5.5, which presents the case of a system with two failure modes, one being based on the state of the first three components, the other being based on the remaining components. This example shows the assembly of the two failure modes, which are in turn composed of a chain structure corresponding to the layout 2 of Figure 5.4. It is crucial to represent all possible system failure modes on the same BN structure, since this will enable the computation of the joint probability of occurrence of these failure modes, instead of only their respective marginal probability distribution. Finally, the **SYS** node assembles the different system failure modes into a unique indicator, which quantifies for instance the functional losses endured by the bridge system: the CPT

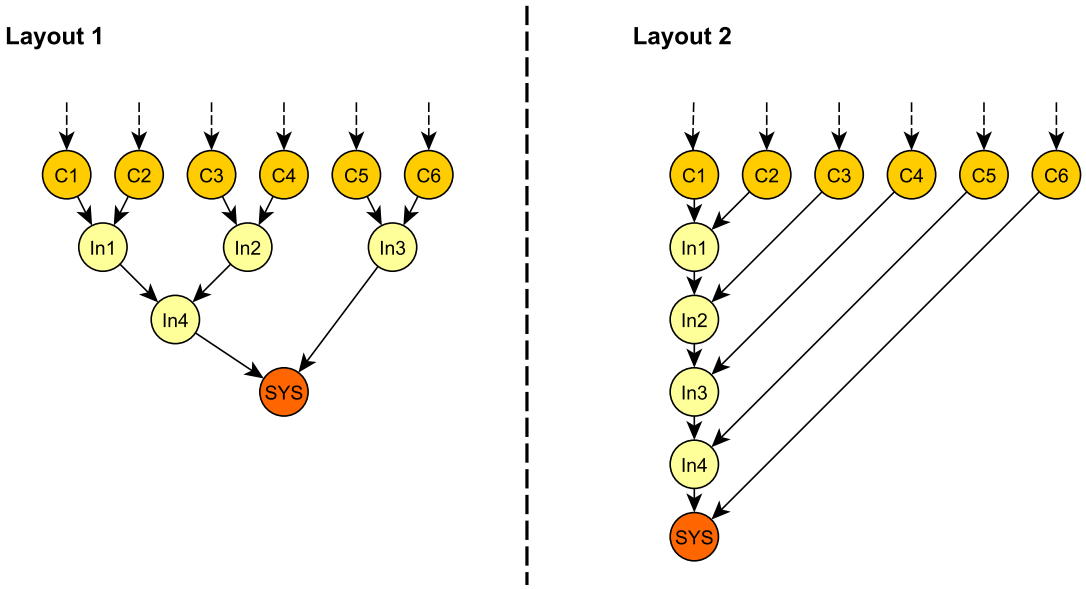

FIGURE 5.4: Two possible layouts for intermediate nodes, for a system with six in-series components. Each of the intermediate nodes represents an intermediate state of the partial combination of the components, in order to limit the computational load.

of this node may be built as a Boolean table representing the hierarchy or even the combination of the different failure modes in the case they have a joint occurrence. Its definition is entirely subjected to the modeller's definition of the system failure modes and their consequences in terms of induced functionality levels.

In the case where the bridge components may enter multiple damage states, each of these component damage states have to be considered as a potential contributor to one of the system failure modes. For instance, piers in a slight damage state may be part of a given failure mode (e.g. yielding of substructure elements), while piers a in collapse state may induce a different one (e.g. full failure of the bridge). Such a model is shown on the right of Figure 5.5, where intermediate component nodes with a binary output are inserted in order to decompose the states of the initial component nodes. Three states are assumed for each of the six components (i.e. 'intact','DS1' and 'DS2'), so that each $\mathbf{C_i}$ node generates two child nodes $\mathbf{C_{i1}}$ (i.e. with states 'intact' and 'D1/D2') and $\mathbf{C_{i2}}$ (i.e. with states 'intact/D1' and 'D2'). This intermediate step enables the treatment of each component damage state as individual contributors to the different system failure modes. It also has the merit of harmonizing the formulation of the various intermediate nodes, which can all be described with binary states.

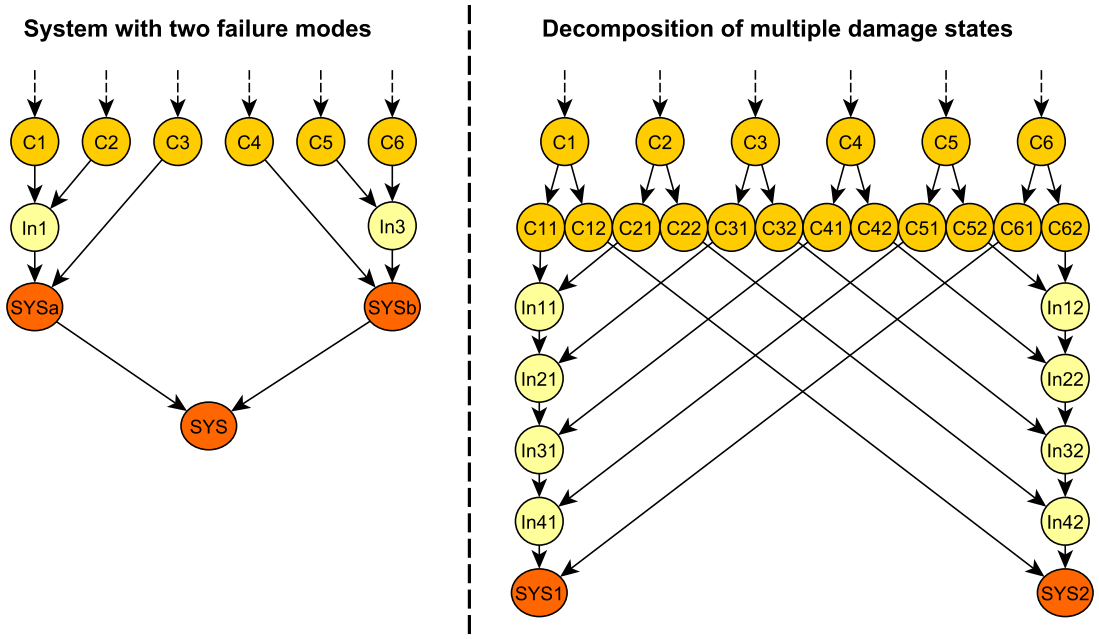

FIGURE 5.5: BN structure for components with multiple damage states (left), and BN structure for a system with two failure modes (right).

The simple non-exhaustive configurations developed above demonstrate the capabilities of the BN formulation, namely:

- the capacity to deal with a large number of components, especially through the use of intermediate nodes;
- the flexibility in the BN construction, which allows to account for multiple damage states and multiple system failure modes;
- the simultaneous computation of the joint probability of all failure modes, which can represent a significant gain in computation time.

As a result, the proposed BN procedure has been implemented into a Matlab-based code using the Bayes Net toolbox [Murphy, 2007]. The elementary configurations presented in Figures 5.3 to 5.5 can all be generated using straightforward algorithms: they may hence be used as bricks to automatically generate BNs for more complex systems, provided that the necessary input parameters are specified (i.e. number of components, correlation matrix between the component events, fragility parameters and damage states of the components, number of failure modes, component events for each failure mode, number of CSRVs). Currently, only up to two CSRVs have been implemented, mainly due to

the huge computational burden more CSRVs would represent, without a significant gain in accuracy: each time another CSRV is added, the size of the CPT of each $\mathbf{C_i}$ node is multiplied by the number of discrete states of the CSRV root node, which leads to an exponential increase in the CPT size. Moreover, the Bayes Net toolbox includes a junction-tree algorithm, which allows for exact inference of the events' probability.

The formulation and computation of such a BN, as it is implemented in the Bayes Net toolbox, are detailed in Appendix F.

5.4.2 Performance of the Bayesian Network Structure

The performance of the BN approach with respect to the MSR method is compared in terms of accuracy and computation time. To this end, a hypothetical system with n in-series components is designed and the system fragility curve is assembled for increasing values of n (up to 60). Different configurations are tested, by varying the number of CSRVs (i.e. one or two) or the BN layout (see Figure 5.4).

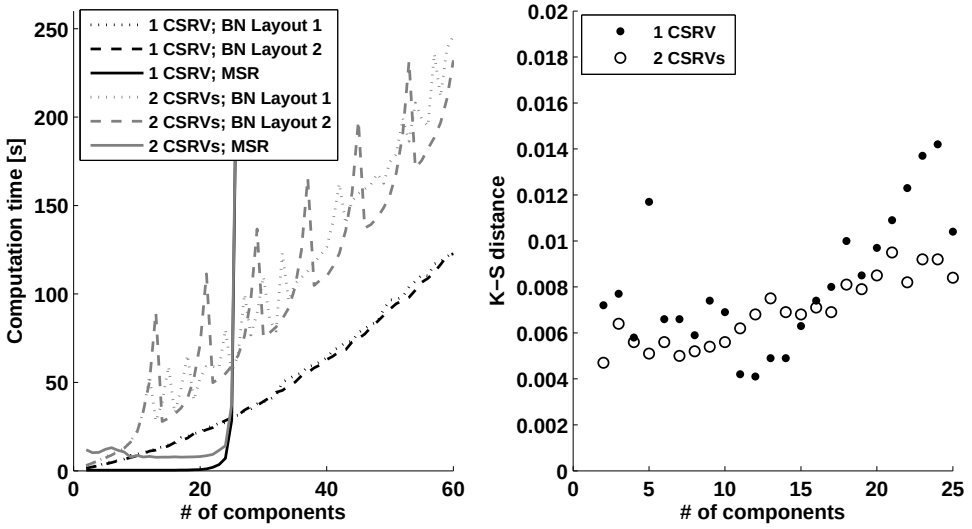

FIGURE 5.6: Computation time for various modelling strategies of a system with in-series components (left) and Kolmogorov-Smirnov distance between the BN- and the MSR-based system fragility curves (right).

The computation time is compared with the MSR method in Figure 5.6 left, using a personal computer with an Intel(R) Core(TM) i7 processor and 16 GB RAM. It can be seen that the computation time has almost a linear growth rate when the BN approach is used, even when 60 components are considered. The addition of a second CSRVs tends to

TABLE 5.2: For different system sizes, composition of the largest clique in terms of node types, and number of elements in the clique potential.

♯ of components	Nodes in largest clique	Size of potential
10	[9 **C**, 2 **U**, 1 **IM**]	369 664
11	[10 **C**, 2 **U**, 1 **IM**]	739 328
12	[11 **C**, 2 **U**, 1 **IM**]	1 478 656
13	[12 **C**, 2 **U**, 1 **IM**]	2 957 312
14	[9 **C**, 2 **U**, 1 **IM**]	369 664

double the computational load, even though the overall time remains reasonable. With two CSRVs, differences between the two BN layouts are also observed: layout 2 seems more efficient for most of the values of n, however there are periodic values where the computation time is dramatically increasing. Some details of the junction tree algorithm are presented in Table 5.2 for different numbers of components: it can be seen that the size of the largest clique potential is directly related to the computation time. As the number of component nodes included in the largest clique increases, the potential size is multiplied by the number of states of the extra component (i.e. binary states in the present case). For the system with 14 components, it appears that the elimination order is slightly different, leading to a final clique containing only 9 component nodes, as for the system with 10 components. This phenomenon is due to the fact that the junction-tree algorithm used in Bayes Net is not able to evaluate all possible elimination orders (i.e. an NP-hard problem [Wen, 1990]): a sequential ordering algorithm is used, which eliminates the node that generates the lightest clique weight and considers the minimum amount of added edges in case of tied nodes. Therefore, for some specific n values, the elimination algorithm may find non-optimal solutions that have the effect of lengthening the computation time. While the Bayes Net toolbox has been used here, other software might propose more elaborate elimination order algorithms, which may consider for instance 2 or 3 node elimination steps at a time: however such algorithms would come at the cost of heavir computations, without necessarily delivering the optimal elimination sequence.

Finally, it appears that the MSR method using the FERUM toolbox is at first insensitive to the number of components, until around 25 components: then, the computation time starts to exponentially increase until the program fails due to memory overflow. This issue is due to the manipulation of the event vector $\mathbf{c}$, which has to contain 2^n elements: it could be argued, however, that a multi-scale reliability analysis Der Kiureghian and

Song [2008] may be used in order to decompose the problem into a set of sub-systems.

One of the main drawbacks of the BN formulation is the CPTs that require the use of discrete variables: therefore continuous variables have to be discretized beforehand, while the level of resolution of the discretization will influence the size of the corresponding CPTs and, consequently, the computational load. In the present context, continuous variables V_i and U_j have been broken down into 19 discrete segments, in order to approximate the continuous standard normal distribution. System fragility curves derived from n in-series components are used to check the accuracy of the BN method with respect to the MSR approach, which is based on a more refined numerical estimation of the integral in Equation 5.8. To this end, arbitrary component fragility curves are built by randomly selecting means μ_i in the $[0.5; 5.0]$ m/s^2 interval and standard deviations σ_i in the $[0.3; 1.0]$ interval, while the elements in the correlation matrix are selected from the $[0.5; 0.95]$ range. These parameters have been chosen so that they represent the values that are generally used for seismic fragility curves: their actual values are not that essential for this hypothetical test, since the objective is to compare the computation time and the accuracy between the MSR method and the Bayesian formulation. System fragility curves are compared by using the Kolmogorov-Smirnov (K-S) distance as an accuracy indicator: this metric represents the maximum difference between two fragility curves over the whole range of IM.

The results of this accuracy test are displayed in Figure 5.6 right: they show that the K-S measure oscillates around 0.01, which represents a very satisfying level. Whether one or two CSRVs are used does not make a significant difference, even though the results with two CSRVs tend to be more stable. Finally, a slight increase of the K-S distance with the number of components can be observed, but the values remain reasonable even for a large number of components.

5.5 Application: Multi-risk Fragility Functions for a Bridge System

This section applies the BN framework to the multi-risk fragility analysis of the bridge system that has been introduced in Chapter 4, following the work by Gehl and D'Ayala [2015, 2016]. The component fragility curves that have been previously derived are

directly used here, while the corresponding fragility parameters are summarized in Appendix E.

5.5.1 Multi-Hazard Context

The considered bridge system is subjected to multiple loading mechanisms due to earthquake (EQ), ground failure (GF) and flood (FL) events. These three hazard events have been identified by Deng et al. [2015] as the main natural causes of bridge collapses in the United States in the 1990s. They have been chosen because they may affect a wide range of bridge components (see Tables 3.8 and 5.3) through various failure mechanisms:

- Earthquakes affect most of the structural components of the bridge: abutments, piers, bearings, shear keys. Deck unseating may occur if large enough deformations are recorded for either bearings or shear keys in the longitudinal and transversal directions, respectively.
- Fluvial floods are the source of hydraulic forces that may damage shear keys or even dislodge deck spans in extreme cases [Padgett et al., 2008a], while flood-induced scour may excavate pier foundations.
- Ground failures are likely to affect the approach embankment, as the difference in foundation depth and soil between the embankment and the bridge usually leads to vertical settlement [Puppala et al., 2009]. Deep-seated circular landslides may lead to the failure of abutment foundations.

TABLE 5.3: Bridge components and corresponding hazard types to which they are susceptible.

Component	EQ	FL	GF
Pier foundation		X	
Pier	X		
Bearing	X		
Deck		X	
Abutment foundation			X
Abutment	X		
Embankment			X
Shear key	X	X	

Using the event taxonomy proposed by Lee and Sternberg [2008], the three hazard types considered here offer the opportunity to analyse combined events, i.e. a single

event triggering multiple loading mechanisms such as an EQ event triggering a GF event, as well as subsequent events, i.e. unrelated single events triggered by different sources and possibly separated in time, such as a FL event followed by an EQ event. Therefore a flexible fragility model needs to be developed, where different hazard loading configurations can be taken into account, specifically:

- fragility to a single FL event;
- cumulated fragility to combined EQ and GF events;
- cumulated fragility to subsequent FL and EQ events (plus triggered GF event, if any).

In this multi-hazard context, the modularity of the BN approach can prove to be very useful to combine the hazard-specific damage probabilities for each component, so that multi-hazard system-level fragility functions can be derived.

5.5.2 Definition of system failure modes

According to the above discussions (see section 3.4), it is proposed to define a set of functionality loss levels and to associate them with specific system damage events, in order to identify the various damage configurations that may lead to similar consequences in terms of bridge closing time or repair operations.

These metrics represent the ultimate objective of the proposed BN approach, since they enable to evaluate the bridge performance in terms of functionality, regardless of the component damage event or sequence of hazard events that led to it. Therefore this framework is able to harmonize a system-level fragility function across multiple hazard types. Instead of speaking in terms of 'system damage states', which implies a clear hierarchy in the severity of the damage states, it is more appropriate to refer to 'system failure modes', which allows for consideration of either intersecting or disjoint sample spaces, as explained in the remainder of this section and as illustrated in Figure 5.7. In particular this approach decouples the direct correlation between severity of hazard event and magnitude of consequence, which is implicit in the damage state definition. Identifying different failure modes which may or may-not occur concurrently with different probability levels, allows to investigate the direct effect on functionality of low

probability events, with modest independent intensity, but high consequences. Therefore, based on simple considerations on the severity of each component damage state and on the corresponding functionality loss levels they might induce, a rationale is proposed here in order to identify homogeneous system failure modes:

- Failure mode F1 corresponds to slight damage only to approach embankments (D1), as such damage would not have a significant impact on the bridge functionality, even though repair operations would be eventually necessary. This failure mode may correspond to a functionality loss level FL1, implying slight repairs but no closing time;
- Failure mode F2 corresponds to minor structural damage to bridge components (i.e. the occurrence of any of piers, abutments, bearings and shear keys in damage state D1 due to earthquake, approach embankments in damage state D2 due to ground failure, damaged shear keys D1 due to fluvial flood). This class of failure mode may correspond to a functionality loss level FL2, implying moderate repairs with a short closing time;
- Failure mode F3 corresponds to a deck unseating event that induces long term closure of the bridge, even though temporary deck spans could be installed if the substructure components have not collapsed (i.e. deck unseating D2 due to fluvial flood, bearings and shear keys in damage state D2 due to earthquake). This failure mode may correspond to a functionality loss level FL3, implying extensive repairs with a prolonged closing time.
- Failure mode F4 corresponds to substructure components that have collapsed, thus inducing the total failure of the bridge system (i.e. piers and abutments in damage state D2 due to earthquake, scour damage state D3 at pier foundations, slope failure D1 beneath abutment foundations). This failure mode may correspond to a functionality loss level FL4, implying irreparable damage (e.g. full collapse of the bridge system).

These failure modes are summarized in Table 5.4, where all the in-series component damage events are detailed for each mode. They are also qualitatively represented as Venn diagrams in Figure 5.7 in order to demonstrate that they do not follow a clear hierarchy unlike regular damage states. The objective of such a representation is to

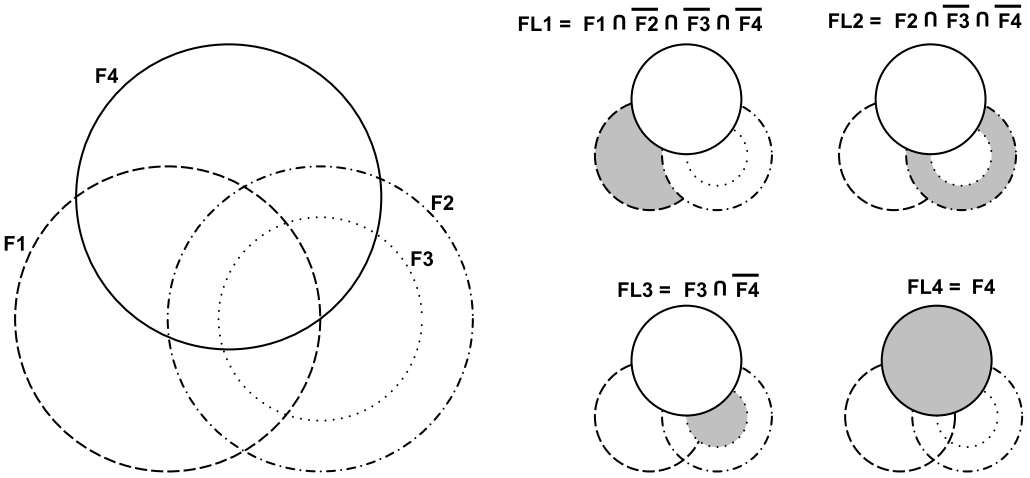

FIGURE 5.7: Venn diagrams qualitatively representing four failure modes and how they are assembled in order to specify the four functionality levels (grey area). F3 appears to be nested inside F2 because a quick analysis of the component failures leading to these failure modes reveals that the occurrence of F3 necessarily implies the occurrence of F2.

emphasize the difference between the failure modes F_i and functionality levels FL_i: a failure mode corresponds to a set of specfic events that have occurred within the system, while the functionality level is linked to the consequences of this failure mode. Since a low impact failure mode, such as F1, is very likely to occur whenever an heavier failure mode such as F2 is reached, the Venn diagrams are here to show how the functionality levels are computed in the case of disjoint or intersecting damage states. Corresponding functionality loss levels, on the other hand, show a gradation in the repair costs and closing time. Therefore it can be argued that, when two failure modes have a joint occurrence, the most severe functionality loss level is assumed (see right of Figure 5.7).

TABLE 5.4: Component damage states from the different hazard events leading to the four failure modes. For simplification purposes, only the component classes are displayed, and not the specific instances (e.g. only the component class bearing B is mentioned, to which six components belong in the actual model, while the number of them actually failing is not explicitly referred to). The x and y letters represent the component responses in the longitudinal and transversal directions, respectively. De represents the deck, Em the approach embankment, Pf the pier foundation and Af the abutment foundations.

Failure mode	FL	EQ	GF
F1	-	-	Em(D1)
F2	De(D1)	Px(D1), Py(D1), Ax(D1), B(D1), Sh(D1)	Em(D2)
F3	De(D2)	B(D2), Sh(D2)	-
F4	Pf(D3)	Px(D2), Py(D2)	Af(D1)

Finally, it should be noted that the proposed failure modes and functionality loss levels are mostly based on few literature references detailing usual causes of bridge failures

[Deng et al., 2015, Doll and Sieber, 2011, Lebbe et al., 2014] or post-disaster accounts [Elnashai et al., 2010]. Thanks to the expert-based survey aimed at quantifying functional consequences from component damage states (see section 3.4), this qualitative rationale may be refined in order to obtain estimate of the expected functionality losses, downtime durations or repair costs. Due the lack of sufficient data to derive accurate functionality loss models, a more qualitative approach is adopted here, where rough loss estimations are proposed for each failure mode for the sake of the demonstration. As a result, estimated bounds for functional consequence metrics are proposed in Table 5.5.

TABLE 5.5: Estimation of approximate loss metrics for the four failure modes identified, according to the INFRARISK expert-based survey. **Du** refers to duration of repair operations, **FL** to functional loss, **FLI** to functional loss during intervention and **Co** to cost of repairs.

Failure mode	Du	FL	FLI	Co
F1	-	-	-	-
F2	1-90 days	0% – 25% (speed)	0% – 10% (speed)	0% – 20%
F3	60-120 days	100% closed lanes	75% closed lanes	20%
F4	90-150 days	100% closed lanes	100% closed lanes	20% – 100%

Regarding failure mode 1 (i.e. slight subsidence of abutment approach), it is difficult to quantify the functional losses due to the very low damage extent: a 100% remaining functionality with very fast repair operations (e.g. less than a day) might be assumed.

5.5.3 Bayesian Inference for the Joint Derivation of System Fragility Functions

Once the component fragility curves and the system failure modes have been fully described, it is possible to build the corresponding BN by using the various algorithms described in section 5.4. A simplified graph of the BN is shown in Figure 5.8, where components are represented by their class, as explained in Table 5.4. The actual BN that has been solved with the Bayes Net toolbox contains each of the components of the bridge model and results in 64 nodes and 140 edges.

Numerical seismic analyses of the bridge system (i.e. non-linear time history analyses) enable to obtain a straightforward correlation matrix of the component responses, however this is not the case for floods and ground failures. It can however be assumed that flood- and earthquake-related failures are statistically independent, therefore a correlation factor of 0 is used between the damage events that are induced by different hazard

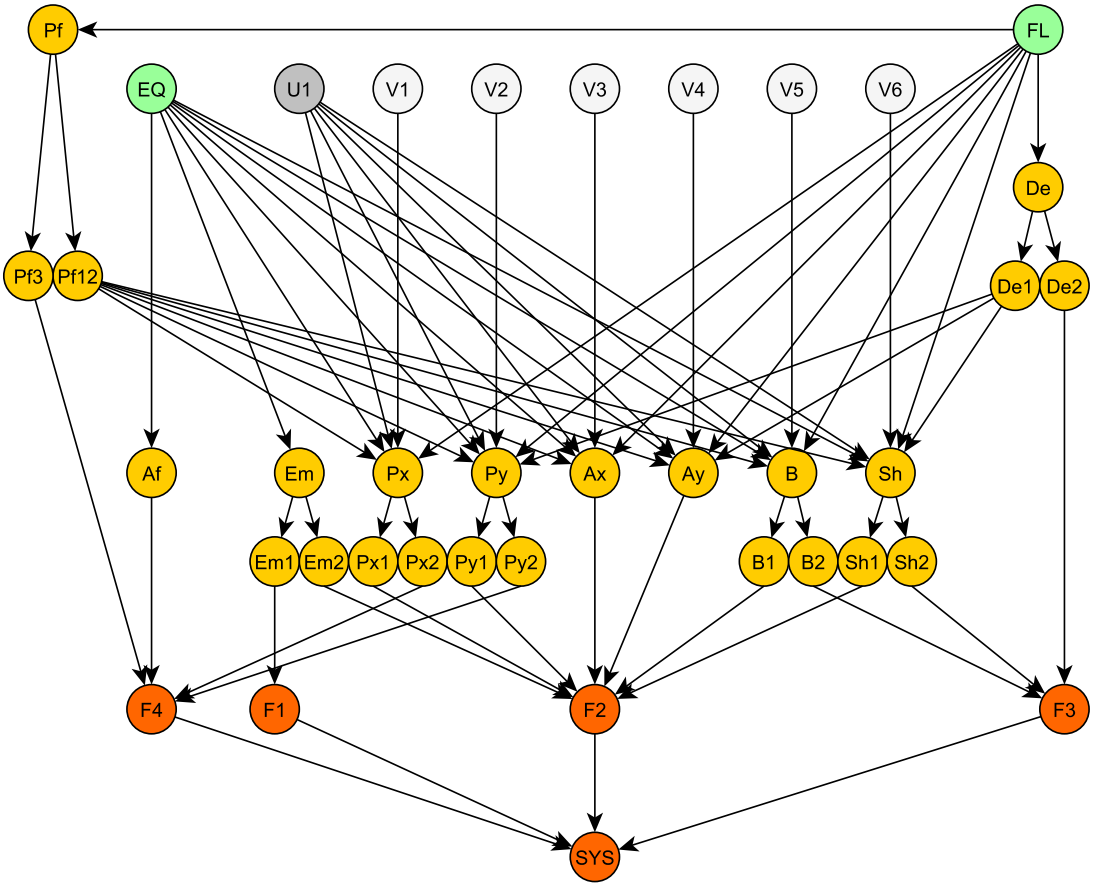

FIGURE 5.8: Global Bayesian Network for the bridge system exposed to seismic and flood loadings.

types. Therefore the correlation matrix is only built for earthquake-related events and it is assembled from 20 elements (i.e. 10 bridge components in each direction, longitudinal and transversal): the correlation values displayed in Figure 4.12 are used here for damage events of seismic origin. One limitation of the BN construction in Figure 5.8 is that the correlation coefficients r_i do not evolve with the different bridge configurations representing initial flood damage, since it may be expected that changes in the dynamic properties of the bridge system will alter the component responses and therefore the correlation matrix. However it has been observed that the changes are not significant for the present case-study: in cases for which the evolution of the correlation matrix would be too important to be neglected, additional BN nodes could still be added in order to represent the possible values of r_i.

In order to better explain the BN structure in Figure 5.8, the series of events leading to the 'deck unseating' failure mode F3 can be summarized as follows (see Figure 5.9):

- Deck unseating **F3** occurs if one of the bearings (or shear keys) exceeds a given deformation level (damage state D2) in the longitudinal (or transversal) direction (i.e. component events **B**2 or **Sh**2), or if the deck (i.e. component event **De**2) is directly upset by the fluvial flood (i.e. hazard event **FL**);
- Bearing (or shear key) deformation is triggered by seismic loading (i.e. hazard event **EQ**) and may be modified by the state of the pier foundations (i.e. component event **Pf**12);
- Piers foundations (i.e. component event **Pf**) are altered by scour due to fluvial flood (i.e. hazard event **FL**);
- The seismic response of shear keys in the transversal direction is also influenced by the damage to shear keys by deck tranversal discplacement (i.e. component event **De**1) due to fluvial flood (i.e. hazard event **FL**).

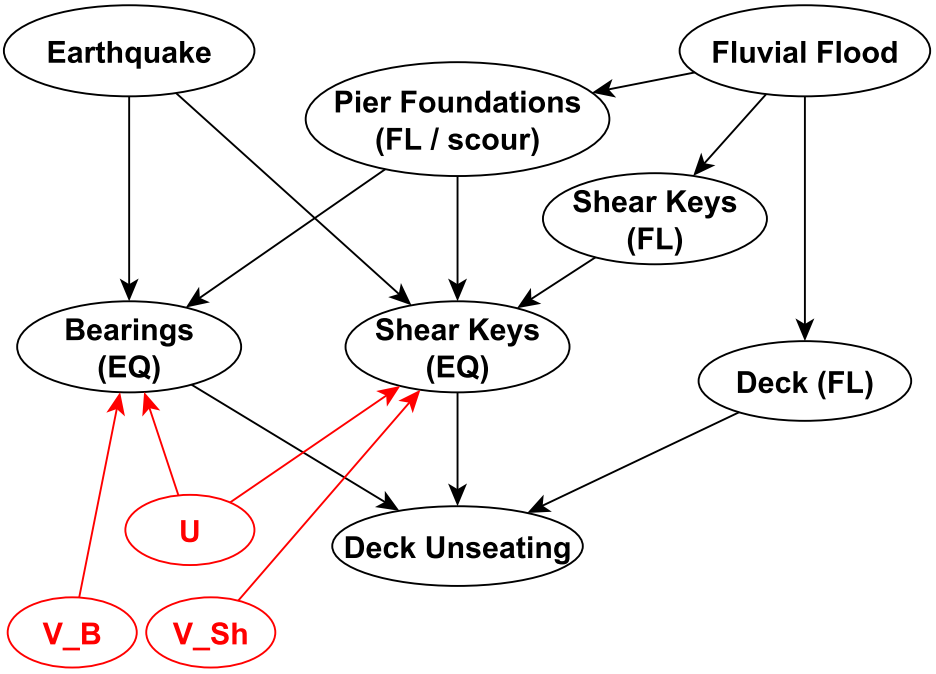

FIGURE 5.9: Simplified Bayesian Network summarizing the chain of events potentially leading to deck unseating.

For comparison purposes, a simplified event tree with deck unseating as a potential outcome is also proposed in Figure 5.10. Such a graphical representation may be useful to understand the chain of events that may lead to deck unseating, however it suffers from many shortcomings when compared to the BN formulation:

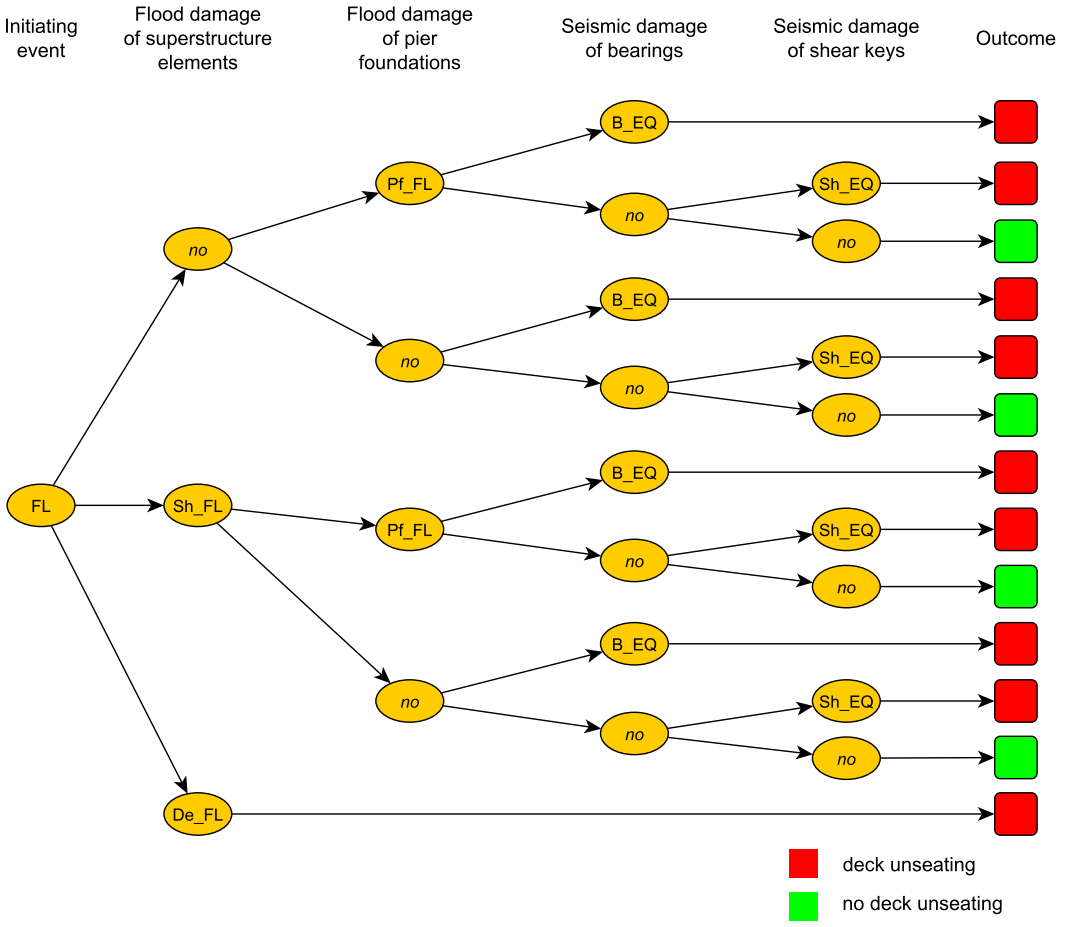

FIGURE 5.10: Simplified event tree summarizing the chain of events potentially leading to deck unseating.

- The fact that the damage events must be represented in a sequential manner in the event tree may compel the modeller to adopt arbitrary choices that have no bearing on reality. For instance, in the case of seismic loading, the damage to bearings is considered before the damage to shear keys, while the opposite configuration could have been chosen as well. Therefore there is a risk that such an event tree might be misinterpreted as a temporal sequence of events.

- The logical relations between damage events is not as obvious as in the case of the BN formulation, where the presence of an edge necessarily implies an dependence between two nodes. In the event tree, it becomes unclear whether the occurrence of a given event will have an influence on the probability of occurrence of a subsequent event. For instance, it has been demonstrated that the damage of pier foundations due to scour will alter the seismic behaviour of other components, however both options (i.e. scour effect or not) are represented the same way in the event tree.

The probabilities of seismic damage to bearings should then be explicitely be written on the event tree, in order to show that they are not the same depending on the scour damage. Conversely, shear keys damaged by flood should have no effect on the seismic behaviour of longitudinal bearings, therefore the same probabilities have to be repeated for some branches of the event tree.

- The correlation structure between the damage event (especially for the seismic loading) is not explicit in the event tree, even though it is implied by the event probabilities (i.e. the joint probability of no damage to bearings and damage to shear keys, $P\left(\overline{B_{EQ}}, SH_{EQ}\right) = P\left(\overline{B_{EQ}}\right) \cdot P\left(SH_{EQ}|\overline{B_{EQ}}\right)$, can be found from the event tree). However, as seen in Figure 5.5, the BN may be built so that it computes the joint occurrence of all four failure modes, while such a feature would only be accessible through an overcomplicated event tree that would lead to cumbersome computations.

For each selected combination of values [PGA ; Q], the BN algorithm performs an inference in order to estimate the probability of occurrence of each of the failure modes. As a result, it is possible to express a system fragility function with respect to both seismic and flood intensity measures (see Figure 5.11). The output of the BN inference can be represented as fragility surfaces that express the failure probabilities with respect to two statistically independent intensity measures. If either an FL event or an EQ (triggering a GF) event has to be considered separately, the corresponding probabilities of functional damage can be evaluated just by reading the function values along the corresponding horizontal axis.

It can be seen that the effect of fluvial flood is mainly significant for heavier damage states, such as full collapse (i.e. F4). This observation is in line with the fact that pier foundation scour or shear key removal have the greatest influence on the seismic response of bridge components for damage state D2. The [PGA ; Q] space where deck unseating (i.e. F3) is the most likely to occur corresponds to very specific values of the intensity measures: this is another interesting feature of the proposed BN approach, since it enables to capture low probability failure modes that may only occur under narrow ranges of combination of uncorrelated hazard events' intensities. Although the joint probability is low, the range of intensity of both hazards is relatively modest and hence their probability of occurrence commensurable to the life span of the structure and

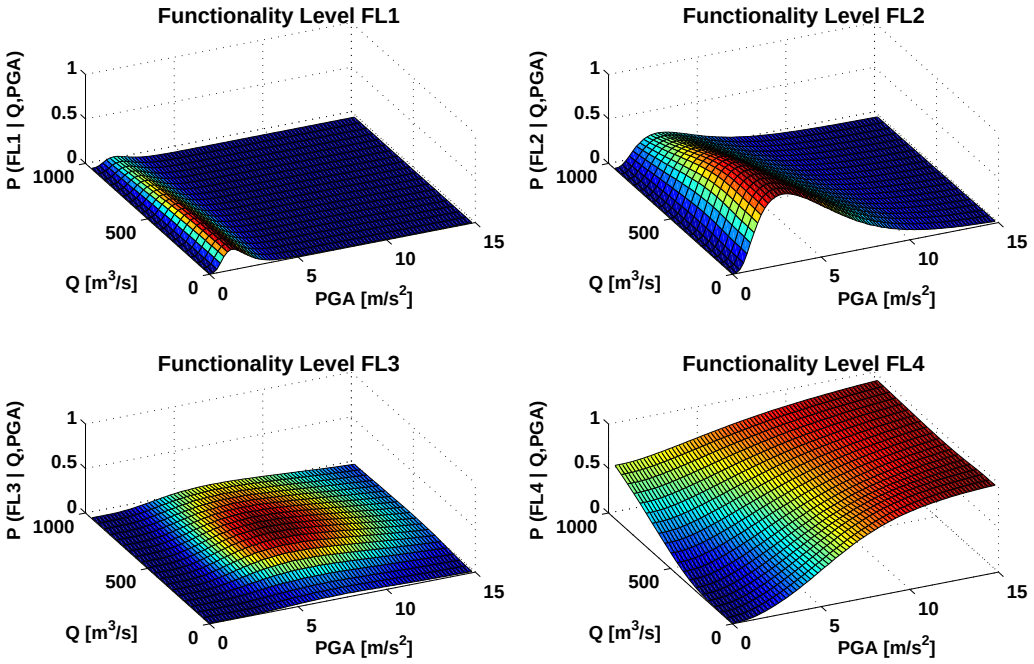

FIGURE 5.11: Multi-hazard fragility functions for the four functionality levels, expressed as a function of Q (flow discharge) and PGA (peak ground acceleration).

comparable in intensity to their reference design value: hence the functionality losses can be severe as they are unexpected. Such a result is very useful when low-probability high-consequence events need to be identified, since it highlights the potential occurrence of uncommon failure modes due to joint or cascading events, which may not have been foreseen during the design of the bridge.

The proposed BN-based approach has proven its ability to isolate system failure modes that are defined by specific damage events at the component level. The choice to convert the four failure modes into four functionality levels (see Figure 5.7), which constitute MECE events, has led to fragility functions that are directly applicable to multi-risk analyses, since the functionality levels may be directly sampled from the four fragility surfaces in Figure 5.11. Finally, these fragility functions may be referred to as hazard-harmonized or even hazard-independent, since they are based on a unique functionality scale, whatever the hazard type considered. Morevoer, the same fragility model may be used for any hazard type, thus greatly simplifying multi-risk assessment procedures.

5.6 Application: Functionality-driven Fragility Functions for Seismic Risk

This section presents a more quantitative application of the proposed BN approach, i.e. the component loss models from Section 3.4 are directly fed into the Bayesian analysis with the objective of deriving probabilistic functionality curves for the bridge system. This concept is demonstrated through the same bridge model that has been presented in Section 5.5, except that initial intact conditions are assumed (i.e. seismic fragility assessment only): as seen in Chapter 3, loss models are the most constrained for earthquake-related damages, while the effects of other hazards on functionality loss would require more investigations before being used in quantitative models.

5.6.1 Proposed BN Formulation

As discussed before, the proposed BN is based on the basic layouts presented in Figures 5.3 and 5.4. The main difference lies in the addition of a layer of functionality nodes that convert the physical damages into functionality metrics (see Figure 5.12). Out of the various metrics that have been considered, only two are selected here for more clarity, i.e. (i) the repair duration and (ii) and the functional loss expressed either in speed reduction or in lane closure. These two metrics are essential for the evaluation of restoration scenarios or the application of traffic models to the road network.

For each loss metric, the component-level events are assembled into a system event $\mathbf{S}_1$ or $\mathbf{S}_2$ through intermediate nodes $\mathbf{I}_i$ that form a chain structure. Both loss metrics at the system level are finally converging towards a final node **SYS**, which is mainly used to compute the joint probability of occurrence of various repair durations and levels of functional loss.

Finally, the components are considered to be able to take multiple damage states or functionality states: the number of potential damage states corresponds to the ones defined in Table 3.8, while a discretisation of the continuous loss variables is performed (e.g. repair duration is divided into 10 time invervals). In the chain structure, the rule for the aggregation of multi-state components is based on the assumption that the maximum of the loss induced by each component is kept at each step. Other assumptions

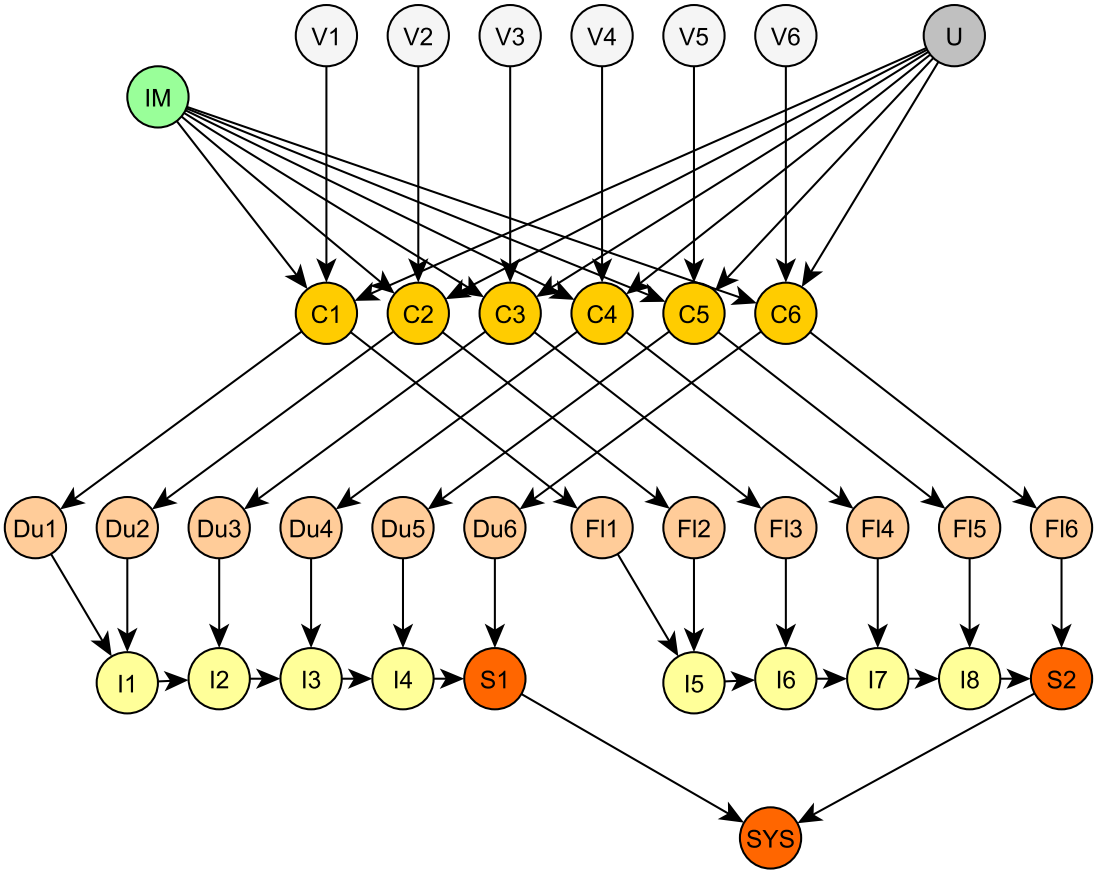

FIGURE 5.12: BN formulation for the quantification of functional consequences, for a bridge system with six structural components. $\mathbf{Du}_i$ nodes represent repair duration and $\mathbf{Fl}_i$ the functional loss induced by each component.

could be made, such as performing the sum of each component-induced loss instead of taking the maximum. However, the maximum value makes more sense when dealing with functional losses: the component event that is the most penalising for the system performance takes precedence. In the case of repair duration, it might be argued that intervention times are more likely to be aggregated: however, it is very likely that repair operations are performed at the same time for all structural components, thus resulting in a repair duration that is not necessarily much higher than the one required for the worst hit component.

5.6.2 Component Fragility Curves

In order to associate the component damage states with the component loss models, the same component failure modes as the ones detailed in Table 3.8 must be selected. In

the present example, the type of components present in the bridge system (e.g. piers, abutments, elastomeric bearings and shear keys) leads to the selection of failure modes #1, 4, 5, 6 and 13. The shear failure of piers is not included, since a preliminary analysis has shown that the piers in this example are only damaged through flexural behaviour.

A series of pushover analyses is then performed on the structural model of each component type (while adopting the same kinematic conditions as if the components were connected to the bridge system), in order to identify the specific limit states that should correspond to the qualitative descriptions of the failure modes (see Table 5.6):

- *Piers*: the four limit states are determined by using the Bayesian updated limit scale proposed by Nielson [2005], which is based on ratios of the yield curvature.
- *Abutments*: the successive knees of the stiffness model are taken as limit states for both active and passive behaviours, as they correspond roughly to the description of the damage states. Along the transversal loading direction (Y), only piles are solicited and no passive behaviour is taken into account.
- *Shear keys*: the first damage state, corresponding to gap closure, is identified by the deformation level that starts to activate the actual RC key. Since a pure shear failure model is used in the example, second and third damage states occur for the same deformation level, i.e. when the RC key fails. Finally, the last damage state is described by deck unseating, which corresponds to a deformation that exceeds the dimensions of the elastomeric pad in the Y direction.
- *Bearings*: the first damage state (i.e. noticeable deformation) is reached when the bearing is deformed up to the acceptable limit (i.e. steel dowel reached). The second damage state actually corresponds to the same limit state in the present case, since it corresponds to possible dowel fracture (i.e. the dowel's resistance is beginning to get solicited). The third damage state corresponds to definite dowel fracture, which can be easily spotted in the pushover curve. Finally, the last damage state is described by deck unseating, which corresponds to a deformation that exceeds the dimensions of the elastomeric pad in the X direction.

The component fragility curves are then derived by following the same procedure detailed in Subsection 4.3 and they are detailed in Figure 5.13.

TABLE 5.6: Proposed limit states for the selected component failure modes along both loading directions. Damage 'severity' refers to the conventional damage states that are used at the level of the bridge system (see Table 3.8).

				Damage 'Severity'			
ID	Component	Failure mode	EDP	DS1	DS2	DS3	DS4
1	Pier	Bending	Section curvature	0.005	0.008	0.014	0.020 (X)
				0.015	0.024	0.041	0.061 (Y)
4	Abutment	Piles	Deformation in	7.6	25.4	200.0	– (X)
			tension [mm]	7.6	25.4	200.0	– (Y)
5	Abutment	Backfill	Deformation in	19.2	25.4	–	192.0 (X)
			compression [mm]	–	–	–	– (Y)
6	Shear key	-	Deformation [mm]	–	–	–	– (X)
				25.0	25.5	25.5	406.0 (Y)
13	Fixed	-	Deformation [mm]	10.5	10.5	12.5	152.0 (X)
	bearing			–	–	–	– (Y)
	Expansion	-	Deformation [mm]	10.5	25.0	34.5	152.0 (X)
	bearing			–	–	–	– (Y)

The component fragility curves provide a first indication on which components are the most vulnerable and, therefore, the most likely to contribute to the functional losses. For instance, the component failure modes that are the most likely to occur at lower intensity levels are the minor cracking of abutment piles (i.e. active behaviour) and the deformation of bearings at the end spans. On the other hand, piers and bearings at the middle span appear to be less vulnerable in this specific bridge configuration.

5.6.3 Loss Models

The results of the expert-based survey of functional consequences (see Section 3.4) are used to build a loss model for each component failure mode. The intervals of loss values proposed by the different groups of experts may be reconciled by building a probabilistic functionality model for each type of loss metric: an empirical cumulative distribution function is then assembled for each component damage state, as shown in Figure 5.14, using equal weights ('pooling' step in Cooke's method). Unlike what has been carried out in Section 3.4 for global states with the same damage 'severity', Figure 5.14 details loss models at the component level. Therefore the resulting models are much coarser than the ones from Section 3.4, since the expert-based data points are decomposed into specific component failure modes (i.e. less data to use in the pooling step).

For heavier damage states the lane closure metric takes precedence, while the speed reduction metric may only be used when there is no lane closure (i.e. lighter damage states). The functionality loss models are very coarse and it can be seen that most

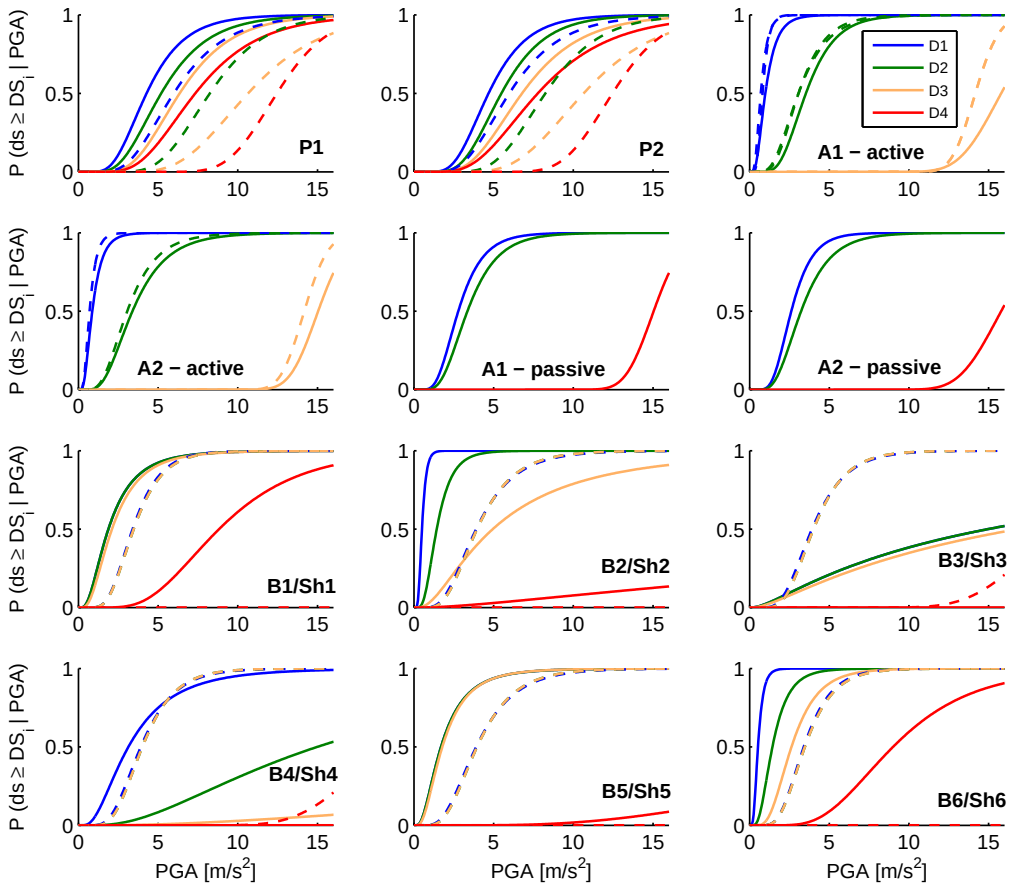

FIGURE 5.13: Component fragility curves for the bridge components in the X (solid lines) and Y (dashed lines) loading directions.

of them are only steps functions, since intervals of values have not been proposed by all experts. Therefore, pending a refinement of the functionality loss models, these values should only be considered for illustrative purposes, i.e. the demonstration of the proposed method.

5.6.4 Derivation of Probabilistic Functionality Curves

Once the component fragility curves are derived and the Dunnett-Sobel variables are identified, the BN can be assembled according to the formulation presented in Figure 5.12. For the considered bridge example, 22 components are considered (i.e. 12 components in X-direction, 10 in Y-direction), resulting in a global BN containing 133 nodes and 196 edges. All Bayesian nodes **IM**, **U**, $\mathbf{V_i}$ and $\mathbf{C_i}$ have exactly the same

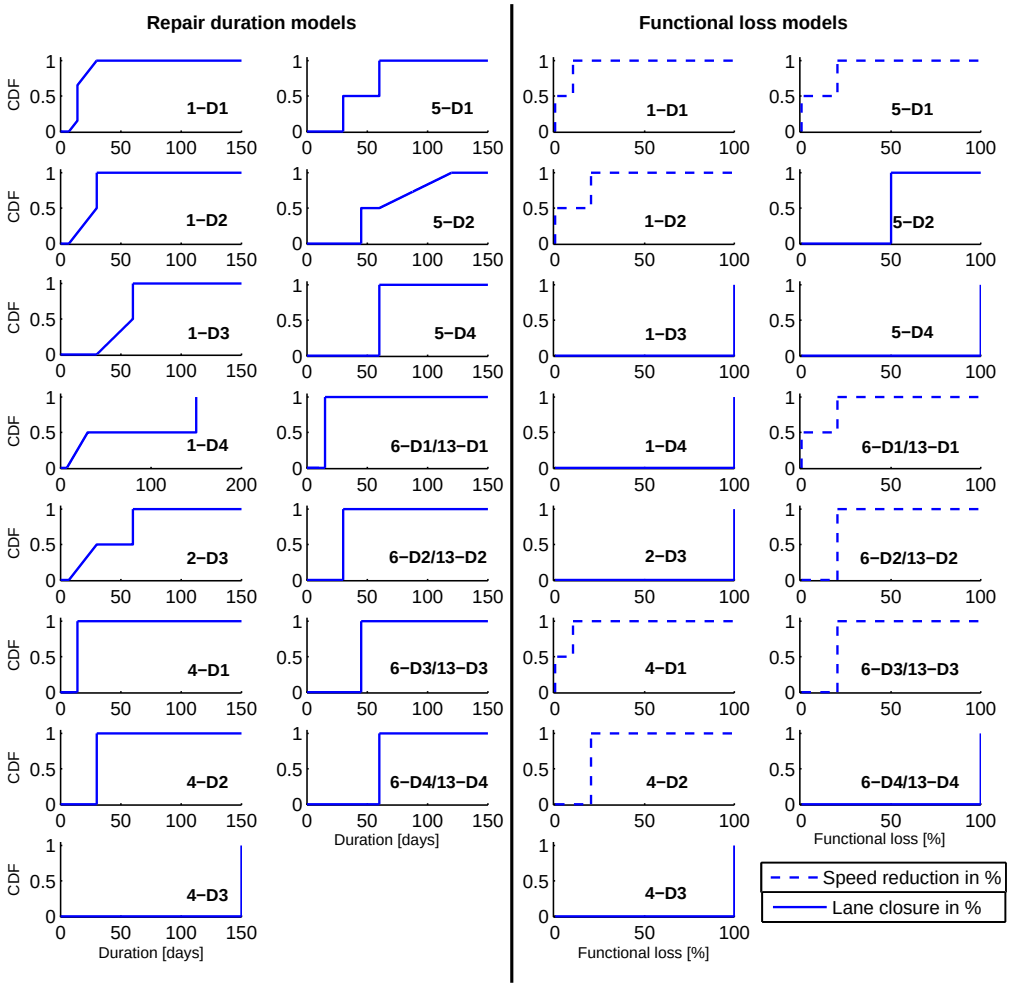

FIGURE 5.14: Expert-based repair duration (left) and functional loss (right) models for each component failure and damage state identified in Table 5.6.

structure and CPTs as the ones described in the BN for multi-hazard fragility assessement (see Appendix F). Intermediate and output nodes $\mathbf{I_i}$, $\mathbf{S_i}$ and $\mathbf{S}$ have CPTs that are constructed as Boolean tables, in order to assemble the component-level losses up to the level of the bridge system. Finally, nodes $\mathbf{Du_i}$ and $\mathbf{Fl_i}$ are characterized thanks to the loss models detailed in Figure 5.14: discrete levels of functional consequences are selected (e.g. ten states for repair duration, as shown in Figure 5.15), so that the probabilities of sampling the various states can be used to build the CPTs of these nodes.

During the initialisation of the junction tree, the largest generated clique potential is comprised of 10 450 000 elements, which still leads to reasonable computation times (i.e. one inference operation is performed in around 2.6 *s* on an Intel(R) Core(TM) i7 processor with 16 GB RAM). Therefore the Bayesian analysis may directly quantify

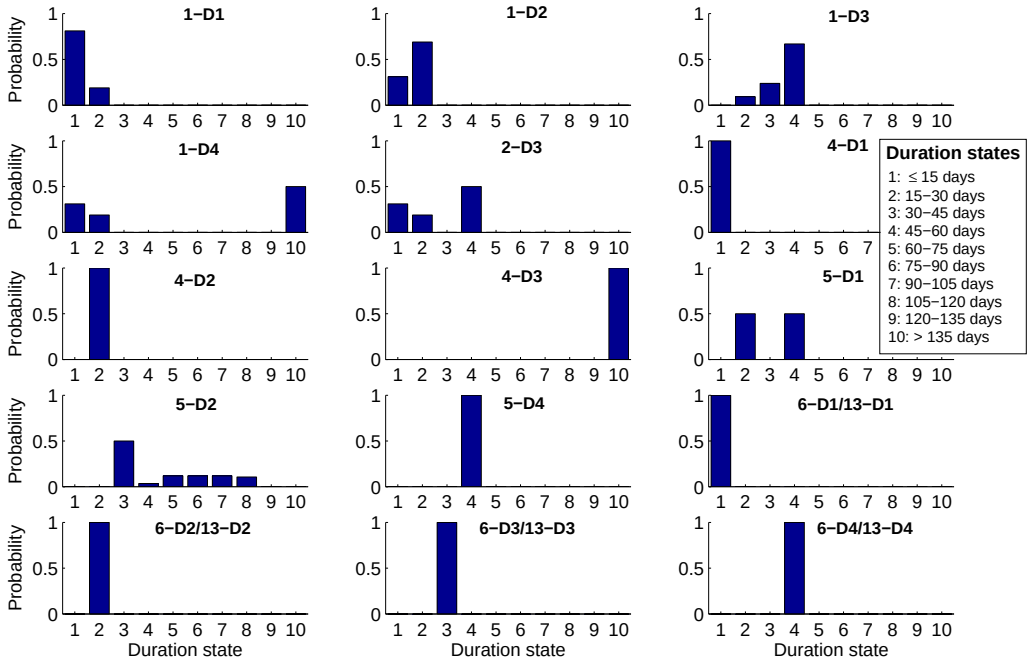

FIGURE 5.15: Probabilities of sampling discrete repair duration intervals, given the occurrence of the component failure modes.

the probability of exceeding these functionality loss levels given the seismic intensity, as shown in Figure 5.16.

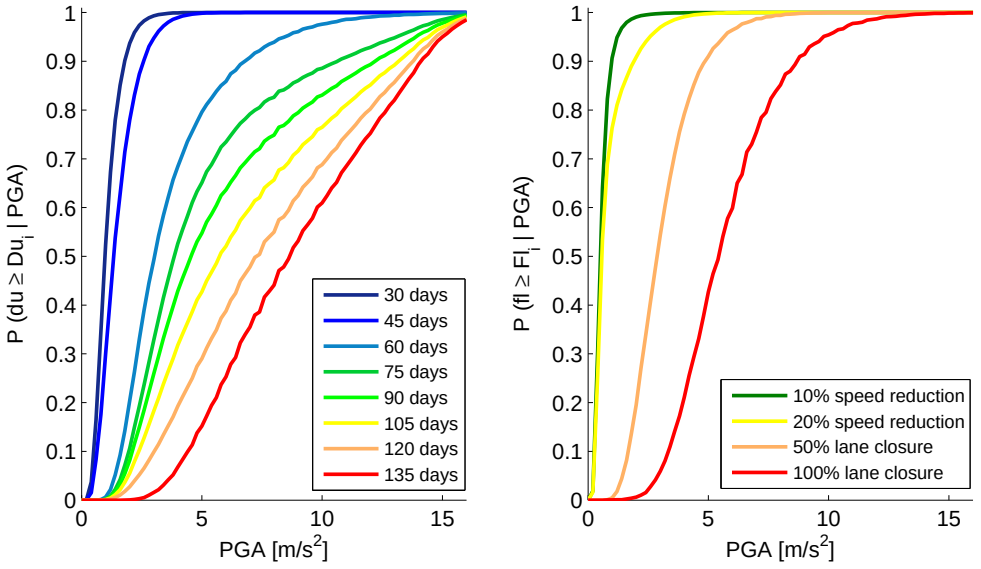

FIGURE 5.16: Probabilistic functionality curves for repair duration (left) and functional loss (right).

As expected, these probabilistic functionality curves reveal that the losses increase with

the seismic intensities. Minor losses (e.g. short repair times or slight traffic disruption) appear to be induced by really low intensity levels, which is mostly due to the abutment piles reaching damage very quickly. It should also be noted that the composition of various fragility curves does not necessarily lead to cumulative lognormal distributions: this observation prevents the use of simple statistical parameters to represent these curves, which have then to be expressed as tabulated values. In the case of repair duration curves, the shape of the longer duration curves (i.e. 120 and 135 days) tends towards a uniform cumulative distribution, as opposed to a lognormal distribution: this particular feature might be explained by the type of component failure modes that generate such levels of downtime duration, and by their specific fragility parameters (i.e. especially if the mean parameters cover a wide range of values).

Finally, the curves in Figure 5.16 provide the marginal distributions for each loss metric taken separately, while the application of restoration strategies for a road network would require the joint knowledge of both the functional state and repair time of the elements at risk. The BN has been formulated in such a way that the repair duration node (i.e. node $\mathbf{S}1$ in Figure 5.12) and the functional loss node (i.e. node $\mathbf{S}_2$) belong to the same clique during the generation of the junction tree. Therefore it becomes possible to quantify the joint probability of occurrence of the two loss metrics, as shown in Figure 5.17. This result is fundamental for the evaluation of the performance of the global road network, since such a representation enables the sampling of various consistent functionality loss scenarios (e.g. for PGA $= 3$ m/s^2, probability of 0.346 of experiencing 20% speed reduction for 45 days, probability of 0.075 of experiencing 50% lane closure for 120 days, etc.). It should be borne in mind that there is some degree of correlation between the two loss metrics (i.e. the more severe the loss, the longer the repair time), even though some component failure modes may lead to complete closure while requiring reasonable restoration times (see Figure 5.14): therefore this aspect can be correctly captured by the representation of the joint distribution of both metrics, which is easily accessed through Bayesian analysis. It should be noted that the proposed BN-based approach is flexible enough to add the functionality layer to the physical damage and to compute the joint probabilities of various metrics; while such an analysis would not be achievable through more conventional methods such as matrix-based system reliability, which is not primarily designed to treat such problems with multiple output variables.

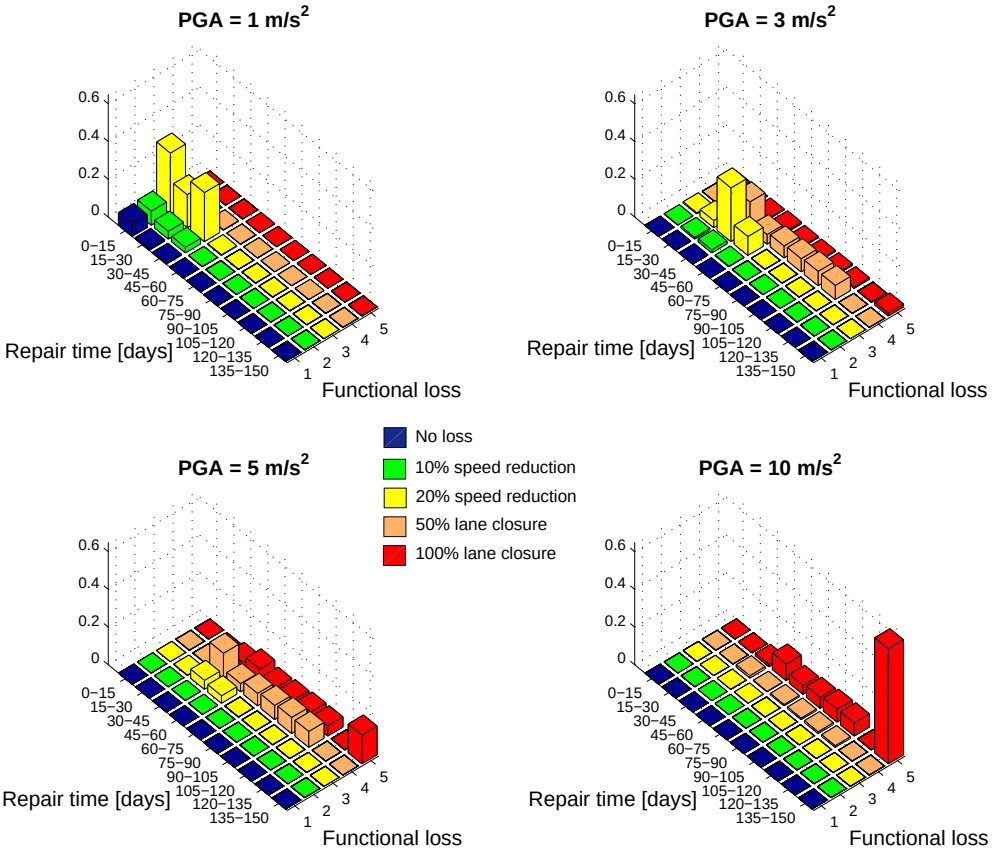

FIGURE 5.17: Joint distribution of the repair time and functional loss for different seismic intensity levels.

5.6.5 Bayesian Inference

Aside from deriving probabilistic functionality curves, the proposed BN formulation can also be used to quantify the respective role of each component in the functional state of the bridge system. Bayesian inference offers indeed endless possibilities in terms of assuming evidence at given nodes and observing the updated probabilities at other locations of the BN.

For instance, one can assume a given hazard distribution at the location of the bridge (i.e. annual probability of occurrence), so that the Bayesian analysis can provide the expected distribution of component damage states (see scenario A in Figure 5.18). On the other hand, Bayesian inference may also be used to identify which components contribute the most to the long-term bridge closure. To this end, two additional configurations are considered:

- Scenario B: bridge closure for the maximum duration is entered as evidence and the updated distributions of component damage states and seismic intensity are observed.

- Scenario C: the updated seismic intensity from scenario B is entered as evidence and the updated distribution of component damage states is observed.

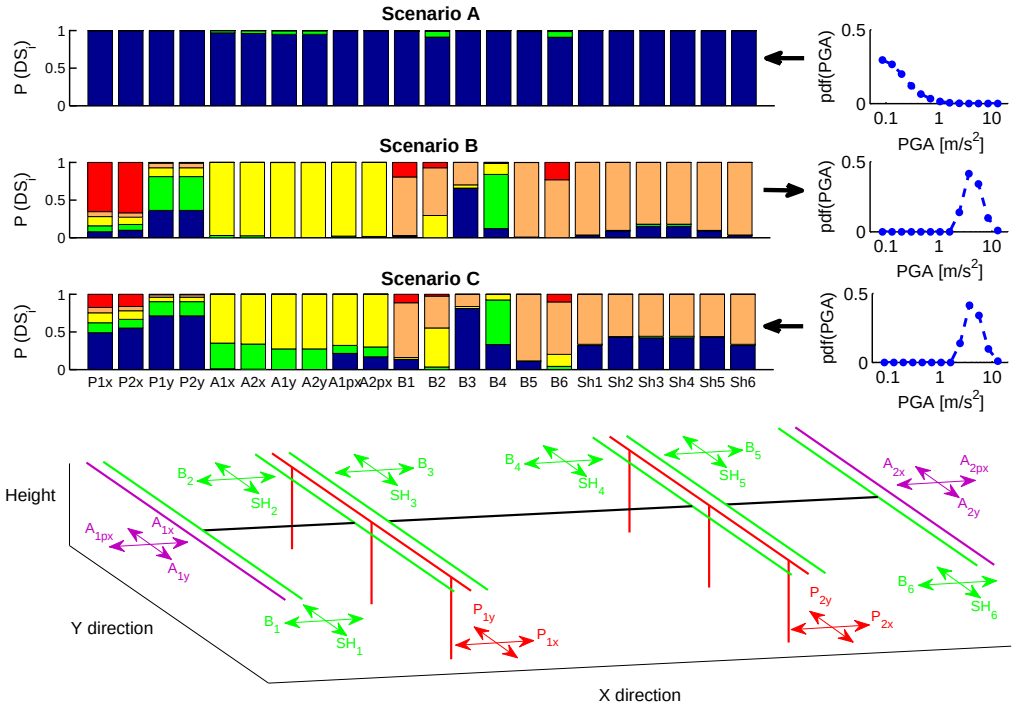

FIGURE 5.18: Distribution of component damage states and hazard levels for different evidence scenarios. Intact state is represented in blue, D1 in green, D2 in yellow, D3 in orange and D4 in red. The damage states are defined in Table 5.6.

As expected, there is barely any damage in scenario A, which corresponds to the annual damage that is expected yearly, for the assumed seismicity level. However there is a difference between the next two scenarios B and C, even though they are based on the same hazard distribution: in scenario B the fixed evidence on the functional state of the bridge directly influences the damage distribution of components (i.e. especially components that are likely to generate full closure), while scenario C only provide a damage distribution with no constraints on the functional consequences. Therefore comparison between scenarios B and C brings valuable insight on the influence of each component on bridge closure. For instance, piers in the X-direction appear to be the most influencing components since their damage distributions change dramatically between scenarios B

and C. This observation is in line with the significant role of substructure components in the bridge's total collapse. The limited influence of piers in the Y-direction also reveals the coupling with the actual physical vulnerability of components (i.e. these components have higher fragility means for heavier damage states). Finally, the changes in the damage distribution of other components is mostly due to the statistical dependence between component events (i.e. correlation structure).

5.6.6 Comparison with Global Loss Models

The component-based functionality curves that are presented in Figure 5.16 may be compared to the more conventional approach that directly convolves the bridge's global damage states with tabulated loss curves, such as the HAZUS model [FEMA, 2003]. To this end, the same component fragility curves that have been derived in Subsection 5.6.2 are used to assemble system fragility curves, which follow the global damage scale with consistent damage 'severity' indices (see Table 5.6). These damage states are then associated with the repair duration and functional loss curves that have been defined in Chapter 3 (Figures 3.14 to 3.15): these global loss models are based on the same expert survey, except that the loss values have been aggregated in order to integrate the potential contributions from all component damage states. Following this approach, the global functionality curves are assembled through a simple convolution and they are presented in Figure 5.19.

Several observations can be made from the analysis of Figure 5.19:

- In the case of repair duration, some curves do not present a monotonic increase (e.g. duration $\geq$ 105 days), which shows that the losses are not necessarily more severe for heavier damage states. This is due to the poorly constrained global loss models that are created when considering global damage states only: an overlap between the DS3 and DS4 repair duration curves is therefore observed (see Figure 3.14).
- Longer repair durations never reach a probability of occurrence of 1 for large seismic intensities. This shows again that the global loss models contain large uncertainties, thus leading to a poor prediction of expected losses and an underestimation of the indirect consequences.

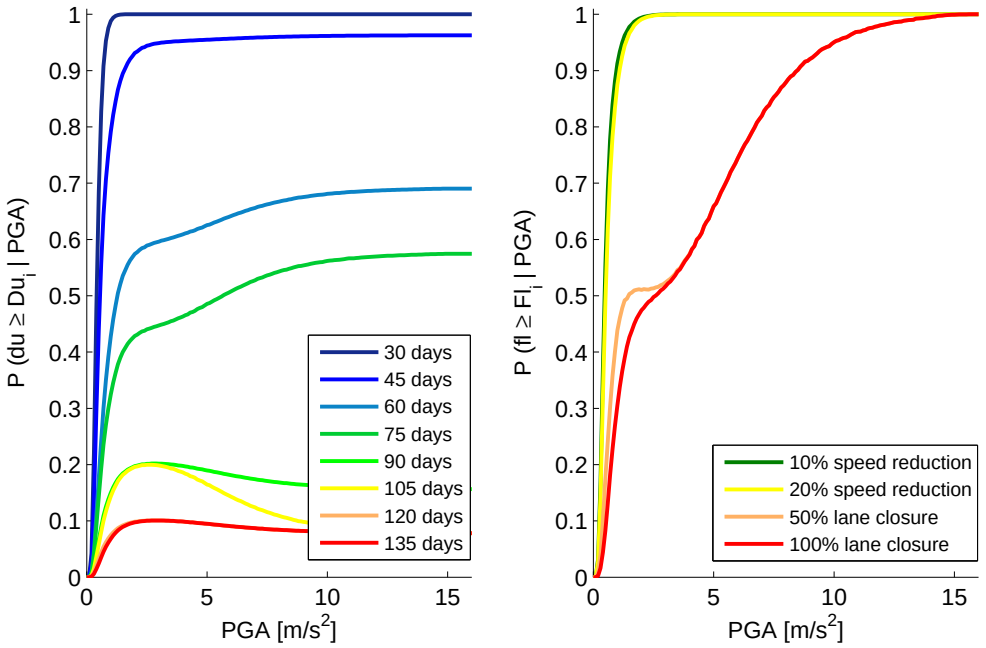

FIGURE 5.19: Probabilistic functionality curves for repair duration (left) and functional loss (right), based on the loss models computed from the global damage states.

- For low seismic intensities, there are non-negligible probabilities of exceeding long repair durations or full lane closure. The definition of global damage states merges the contributions from various component types. Therefore a component that has a high impact on the bridge functionality will contribute to the losses that are aggregated with the global damage states, even though its component damage state might only be reached for higher seismic intensities.

Therefore this comparison demonstrates the benefits of using the component-based functionality curves that have been derived here, instead of considering aggregated loss models based on global damage states. Keeping track of specific failure modes through BN analysis is necessary in order to refine the functionality analysis.

5.7 Conclusion

This Chapter has presented a BN framework for the construction of system fragility curves based on specific component damage states. Once the efficiency and accuracy of this BN approach has been demonstrated with respect to conventional system reliability methods, the proposed framework has been successfully used to predict the probability

of occurrence of four failures modes for a bridge system with multi-state components and multiple hazard loadings. The application of this approach presents several benefits:

- Provided that the appropriate modelling strategies are used, the BN method is efficient and robust enough to solve large and complex structural systems, whatever the number of failure modes or damage states.
- Component fragility curves derived for different hazard loadings and different failure mechanisms, with different methods (e.g. analytical or empirical), may still be assembled in order to build up a harmonized system fragility function.
- In a multi-hazard context, possible interactions between loading events can be taken into account by developing damage-dependent fragility curves at the component level and then by propagating the beneficial or detrimental effects up to the system level.

Therefore the BN framework represents a significant step towards the integration of multiple risks at the vulnerability level, following the recent developments regarding interactions between hazard events (i.e. triggered or combined hazard events versus independent ones within a given time window [Selva, 2013]).

A second application has used the quantification of functionality losses at the component level in order to derive probability functionality curves for a bridge system subjected to seismic hazard. The necessary change of scale between component and system levels proves to be instrumental in the refinement of the loss models, which can then be used to feed subsequent network analysis models. Moreover the integration of component damage events and resulting functional losses in the same BN enables various inference operations to be performed, such as the identification of the most critical components with respect to the functional loss of the bridge, for mitigation or retrofitting purposes.

The BN application to the bridge case study has raised some issues relative to the treatment of uncertainties for the various component fragility curves, which have been derived using a wide range of methods and modelling assumptions, as discussed in Chapter 4. Both aleatory and epistemic uncertainties may be accounted for in some fragility curves, while others only include the variability of some modelling parameters and make use of deterministic quantities to evaluate the thresholds for the damage

states. Ultimately, this aspect will require further enquiry in order to fully harmonize the multi-hazard fragility model, both in terms of functionality losses and associated uncertainties. Although this issue is out of the scope of the present work, Chapter 6 dwells on the quantification and propagation of uncertainties that may influence the assessment of low-probability high-consequence events.

Chapter 6

Uncertainty Treatment

6.1 Introduction

Risk analyses are of probabilistic nature by definition, therefore uncertainty needs to be integrated into all the steps of the risk assessment process, namely the modelling of the hazard event(s), the characterisation of the exposure and the response of the vulnerable exposed infrastructure [Douglas, 2007, Thywissen, 2006]. To this end, the robustness of various probabilistic models that are proposed or developed in this thesis requires a clear identification of the various sources of uncertainty in the single risk analyses. Aleatory uncertainties are related to the inherent variability of a system, which cannot be sufficiently modelled; while epistemic uncertainties are related to the variability that could be reduced in theory, but is difficult to fully characterise in practice due to a lack of knowledge. Following the common classification between aleatory and epistemic uncertainties [Wen et al., 2003], it is then possible to find out which uncertainty source contributes the most to the overall variability of the loss distribution at the level of the infrastructure system. Such studies have been recently carried out in order to compare uncertainties between single risk analyses from different hazard types, as shown by Rohmer [2013].

While aleatory uncertainties are commonly viewed as contributing to the true randomness of the studied physical phenomenon, they are mostly considered as irreducible. Conversely, the characterisation and quantification of epistemic uncertainties will provide indications on which steps of the risk assessment process to focus modelling efforts,

in order to obtain the greatest improvement in accuracy for the risk curve. For instance, statistical tools such as variance-based sensitivity analysis have been used by Rohmer et al. [2014] or Gehl et al. [2013b] to quantify the effects of epistemic uncertainties on the seismic risk assessment of buildings. In terms of uncertainty representation, Paté-Cornell [2002] and Tyagunov et al. [2014] have proposed to represent aleatory uncertainties through the shape of the risk curve (i.e. annual probability of exceedance of a given loss level), while epistemic uncertainties may be represented by confidence intervals around the median curve (see example in Figure 6.1).

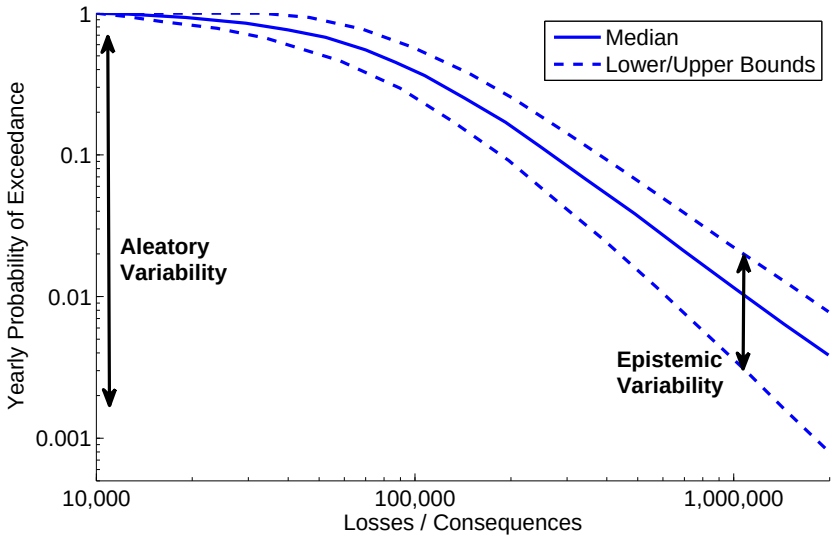

FIGURE 6.1: Representation of aleatory and epistemic uncertainties on a risk curve.

A similar distinction has been introduced by Abrahamson and Bommer [2005] in the case of seismic hazard assessment; the authors claim that the inherent variability considered directly in the hazard computation (i.e. aleatory variability) determines the shape of the hazard curve, while the epistemic uncertainty leads to alternative hazard curves. However, a caveat should be added to this distinction, since the strict Bayesians argue that all uncertainty is epistemic, in the sense that what appears as a physical property of randomness can always be viewed as an uncertain state of knowledge [Der Kiureghian and Ditlevsen, 2007].

Rather than detailing the issues of general statistical treatment, this Chapter intends to present uncertainty sources and statistical tools that are very specific to the problem at hand, namely the quantification of losses to infrastructure in a multi-risk context.

It presents first a review of the various uncertainty sources along the risk quantification process (Section 6.2), for all hazard types considered (i.e. earthquakes, ground failures and floods). Then, Section 6.3 addresses the issue of uncertainty propagation, which can be performed through simulation-based methods or reliability approaches (e.g. event trees, Bayesian Network, etc.). Finally, Section 6.4 explores the quantification of uncertainty sources through two examples, namely the uncertainty due to the choice of GMPEs in the seismic hazard assessment and the uncertainty due to the selection of literature-based fragility curves.

6.2 Sources of Uncertainty in Risk Analyses

In the frame of the MATRIX project, an extensive study of uncertainties by Rohmer [2013] led to a taxonomy of uncertainty sources, as summarized in Table 6.1. It consists in a more generic review than the very detailed work performed by Wen et al. [2003] on uncertainty sources in earthquake engineering. The uncertainty sources follow the common aleatory/epistemic classification, while further distinctions are made depending on the reason for the lack of knowledge (i.e. data-, parameter-, model- or science-related).

TABLE 6.1: Taxonomy of uncertainty sources, according to Rohmer [2013].

Uncertainty type	Description
Aleatory	Inherent variability (temporal and/or spatial)
Epistemic (data-related)	Measurement errors, representativeness of the samples, bias in the measurement process
Epistemic (parameter-related)	Incompleteness and imprecision of observations, experts' judgments (vagueness, conflicting views)
Epistemic (model-related)	Structure, several choices of 'good' models
Epistemic (science-related)	Ignorance, indeterminacy, immeasurability, conflicting views

This classification is adopted in the present work in order to enumerate the most common uncertainty sources that should be taken into account in risk analyses. It should be noted that the aleatory / epistemic classification is somewhat artificial, in the sense that it is highly dependent on the type of model that is used. If a model is developed which includes a large number of parameters to describe a given phenomenon, the associated aleatory uncertainty may be reduced and translated into epistemic uncertainties. An example is the use of multivariate fragility functions with respect to seismic hazard. While a mono-variate fragility curve (e.g. use of a scalar intensity measure – IM – such as peak ground acceleration – PGA – to represent the ground motion) may be associated

with a large aleatory uncertainty (i.e. high standard-deviation β), the use of a fragility function with a vector IM (e.g. spectral acceleration – Sa – at different periods) is likely to reduce the aleatory uncertainty (i.e. the ground motion is better described), even though the characterisation of the input IMs may be the source of additional epistemic uncertainties. Therefore a single-IM fragility curve may be view as a model with a high aleatory uncertainty, while a vector-IM fragility curve would reduce the part of aleatory uncertainty. However, using the latter model without the knowledge of the second IM would lead to larger epistemic uncertainties.

6.2.1 Uncertainties Related to Hazard Assessment

Different uncertainty sources may be identified based on the type of hazard considered, even though a similar structure can be observed (e.g. uncertainties due to the definition of the source event, model or parameter uncertainties in the estimation of the hazard intensities, etc.). Using mostly the inventory proposed by Rohmer [2013], common uncertainty sources for the hazard assessment are the following:

- **Flood hazard assessment:**
  - **Estimation of design rainfall event** *[epistemic/data-parameter]*: Design rainfall events are usually estimated through historical rainfall records, which may be subject to measurement errors or incomplete time series.
  - **Occurrence of rainfall event** *[aleatory]*: Dependence on aleatory meteorological patterns.
  - **Variation of river geometry over time/space** *[aleatory]*: Aleatory distribution of riverbed parameters, which may evolve with time.
  - **Selection of models to estimate flood propagation** *[epistemic/model]*: Flow discharge may be estimated through a wide range of methods and prediction models.
  - **Estimation of model parameters** *[epistemic/parameter]*: Physical parameters feeding the models (e.g. riverbed gradient, surface roughness, catchment area...) are usually incompletely characterized.
  - **Correlation of main channels and tributary flows** *[aleatory]*: The flow discharge at a given point may depend on the flow upstream, and on different

(and usually correlated) rainfall events that may affect different tributary streams and different catchment areas.

- **Seismic hazard assessment:**
  - **Estimation of design earthquake event (e.g. parameters of Gutenberg-Richter law)** *[epistemic/data-parameter]*: Design earthquake events are usually estimated through historical seismicity, which may be subject to measurement errors or incomplete time series.
  - **Occurrence of earthquake event** *[aleatory]*: Dependence on aleatory fault rupture mechanisms.
  - **Choice of GMPEs** *[epistemic/model]*: Seismic intensity may be predicted through a wide range of valid ground-motion prediction equations.
  - **Dispersion of GMPE (intra- and inter- event variability)** *[aleatory]*: The GMPE provides a distribution of the expected seismic intensity, which standard deviation is a combination of intra- and inter-event variability (site-to-site and earthquake-to-earthquake variability, respectively).
  - **Choice of truncation level for GMPE dispersion** *[epistemic/model]*: An unbounded aleatory uncertainty model for the GMPE may result in unrealistic values when low-probability high-consequence events are investigated. A truncated aleatory distribution is therefore a more common approach.
  - **Spatial correlation between hazard intensities** *[aleatory]*: The spatial correlation of the ground motion field generated by GMPEs is built by using a correlation distance and the intra-event variability. It is an essential component of the seismic risk analysis for infrastructure.
  - **Estimation of the site amplification factor for a specific site** *[epistemic/data-parameter-model]*: Amplified seismic intensities due to site effects are estimated through the study of the site of interest (e.g. soil class, measure of shear wave velocity...).
- **Landslide hazard assessment:**
  - **Digital Elevation Model** *[epistemic/data-parameter]*: The quality of the DEM depends on the level of resolution and the way data has been acquired.

- **Failure surface depth** *[epistemic/model-parameter]*: The depth of the failure surface is an input parameter for the hazard assessment. The way this parameter is defined and used depends also on the type of model used.
- **Soil parameters** *[aleatory ; epistemic/parameter]*: Parameters such as soil unit weight, soil cohesion or angle of friction may be incompletely characterized.
- **Slope stability model** *[epistemic/model]*: The type of landslide model considered will have a great influence on the expected displacements (e.g. infinite slope mode vs circular slope failure).
- **Soil saturation ratio** *[aleatory ; epistemic/data-parameter-model]*: The estimation of the soil saturation ratio is usually a complex process which is dependent on many factors (e.g. climate, water table location, rainfall pattern, etc.).

6.2.2 Uncertainties Related to Damage Assessment

Uncertainty sources that are involved in the estimation of physical damage may be considered as common to all hazard types, thanks to the harmonization tasks described in Chapters 3 and 4 (i.e. derivation of component fragility functions for each failure mode). They are summarized as follows:

- **Characterization of the elements at risk (geometry, structural properties, etc.)** *[epistemic/data-parameter]*: Parameters relative to the physical assets cannot always be accurately characterized, either due to imprecise measurements or lack of census data.
- **Choice of fragility curves** *[epistemic/model]*: A wide range of fragility curves may be applied to a given element, depending on the derivation method, the modelling assumptions, etc.
- **Dispersion of fragility curve** *[aleatory]*: The standard deviation that is inherent to a fragility curve represents the aleatory uncertainty that may be due to the hazard representation or the physical process leading to the failure of the element.

- **Choice of intensity measure** *[epistemic/model]*: Different intensity measures may be chosen as hazard descriptors, leading to the choice of different fragility curves or hazard prediction models. Some damage mechanisms may be more sensitive to different parameters representing the hazard intensity (e.g. drift- or acceleration-sensitive components in the case of seismic loading).

- **Definition of damage states** *[aleatory ; epistemic/model]*: Physical damage states are usually defined with a qualitative damage scale, while quantitative physical measures may be used to actually determine whether the element has reached the damage state or not. Threshold's choices are both of epistemic and aleatory nature.

6.2.3 Uncertainties Related to Loss Assessment

Uncertainty sources that are involved in the estimation of functional losses may be considered as common to all hazard types, thanks to the harmonization tasks described in Chapters 5 (i.e. derivation of system fragility functions expressing functional losses). They are summarized as follows:

- **Transformation of damage states into functional losses / direct repair costs / repair duration** *[epistemic/model-parameter]*: How the physical damage states can be translated in terms of functional consequences depends on the type of model used and on some input parameters (e.g. size/design of infrastructure/element).

- **Choice of system performance indicator** *[epistemic/model]*: The type of performance indicator has a significant influence on the way the system's failure or survival is perceived (e.g. connectivity-based vs capacity-based performance indicators).

6.3 Propagation of Uncertainties: Review of Available Methods

Once the various sources of uncertainty have been identified, they need to be associated with a set of probabilistic distributions. The variability of the uncertain sources can be expressed through many forms, such as analytical probabilistic density functions (e.g. shape of fragility curves or sigma values characterising GMPEs), empirical distributions (e.g. activity parameters of a given seismogenic area) or expert-based weighting coefficients (e.g. weighting of various GMPEs, as proposed by Delavaud et al. [2012]).

The final uncertainty, which represents the dispersion of the chosen loss metric at the end of the risk analysis, can be quantified by estimating how the input uncertainties propagate up to the final analysis step. Therefore the goal is to generate a probabilistic distribution of the final loss metric, based on the initial assumptions on the distribution of the input variables (i.e. choice of models and parameters) and the associated aleatory uncertainties (see Figure 6.2). In parallel, a sensitivity analysis may also be carried out in order to rank the respective influence of all uncertainty sources, so that the least significant ones can be neglected.

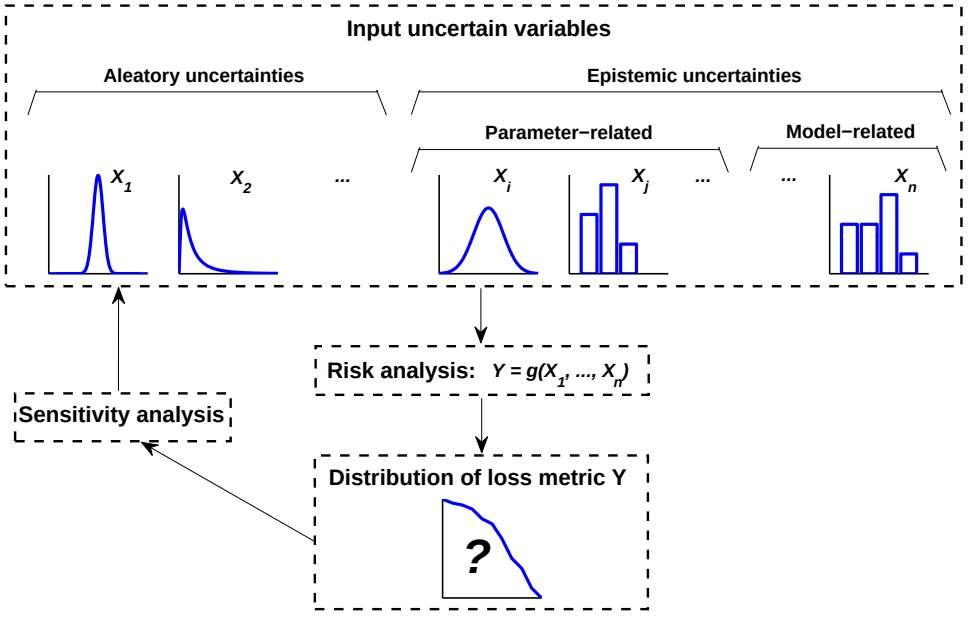

FIGURE 6.2: General principle of uncertainty propagation.

In theory, uncertainty propagation could be performed through an exact analysis, as mentioned by Wen et al. [2003], by integrating the joint probability density function of

all uncertain variables over the whole space of solution. However, such an approach is not feasible in practice, except for linear cases with independent variables. The possibility of using Second Moment or First-Order Second Moment analyses is also detailed by Wen et al. [2003], but the use of these methods also requires a linearization of the various models, which may not be possible in the complex context of risk analyses. Finally, Monte Carlo simulation techniques are also proposed as a viable alternative to generate numerous random samples of risk outcomes.

Similarly, the review of single-risk uncertainties within the FP7 MATRIX project [Rohmer, 2013] details three possible approaches for uncertainty propagation, namely Monte Carlo simulation techniques, logic trees and Bayesian event trees. Their description will be the object of the sub-sections below.

6.3.1 Monte-Carlo Simulations

A Monte-Carlo simulation consists in the sampling of random realizations of the various input variables and the estimation of the final risk metric for each run. After a larger number of runs, a stable estimation of the probabilistic distribution of the outcome can be constructed. Even though it is very straightforward in principle, the Monte-Carlo approach may require an almost intractable number of runs to achieve convergence, especially when extreme risk values (i.e. low probability outcomes) have to be sampled. However, being robust to the number of input variables (i.e. high-dimensionality) is one of the main merits of Monte-Carlo methods.

Such issues have been thoroughly investigated and referenced, and variance reduction techniques have been proposed in order to reduce the number of required runs. Some of the most common techniques are the following:

- *Latin Hypercube sampling (LHS)*: this sampling technique is used to optimize the sampling of variables from multi-dimensional distributions (i.e. simultaneous sampling of n various input variables). Each input variable has its value range divided into m equally probable intervals, and an optimization technique is used in order to ensure that the m Monte-Carlo samples efficiently cover the n-dimension space of variables. If $n = 2$, the variable space becomes a square of m rows and m columns and the LHS algorithm (Latin Square in two dimensions) selects samples

so that each row and each column is occupied by one and only one sample (see Figure 6.3).

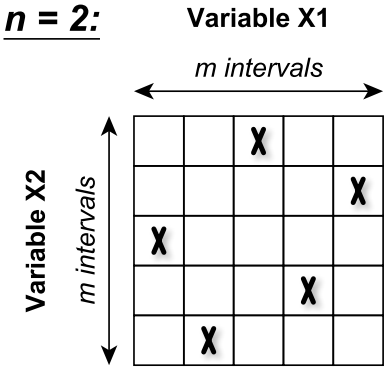

FIGURE 6.3: Example of Latin Hypercube sampling in a two-dimension case.

- *Importance sampling (IS)*: this sampling approach alters the original distribution of the input variable, in order to preferably sample values of interest that would have a very low probability of being sampled otherwise. For instance, if an input variable is associated with a normal probability distribution and if the upper tail of the distribution is of specific interest for the outcome, importance sampling can be used to ensure that the input variable is preferably sampled from the distribution tails, for instance, thus artificially raising the proportions of extreme value samples in the Monte-Carlo runs. As a result, the outcome from each run will also have to be weighted when estimating the final statistics, based on the ratio between the original density probability and the one that has been used in the IS. While this approach is very useful to efficiently explore low probability combinations, it requires an a priori knowledge of what are the probable values of the input variables when failure occurs, in order to construct an efficient importance sampling distribution.

- *Adaptive sampling (AS)*: this sampling method consists in the updating of the sampling scheme based on the results of the previous runs. For instance, specific ranges of input variables could be further investigated, if the previous Monte-Carlo runs have demonstrated a high dependency of the outcomes on a given range of sampled variables.

Finally, it should be noted that Monte-Carlo simulation techniques are especially suitable for complex systems with non-linear behaviour, while being able to treat all types of uncertainties (i.e. both aleatory and epistemic). The studied system may indeed be seen as a black box, into which various sampled inputs are fed, and the distribution of the system's output (e.g. loss indicators in the case of a risk analysis) is generated from the Monte Carlo simulations. Therefore there is no need to analytically characterise the system through closed-from solutions, even though an enhanced knowledge of the studied system would be preferable in order to select the sources of uncertainty that are the most influent (see Subsection 6.3.5).

6.3.2 Logic Trees with Monte-Carlo Simulations

Logic trees are an efficient way to represent and model epistemic uncertainties. More specifically, model-related epistemic uncertainties are very commonly represented with logic trees, since the associated variables have a discrete or categorical distribution. A logic tree starts from a source point and branches out into various options (i.e. different models) over several level depths, from a generic problem definition down to very specific details (see Figure 6.4).

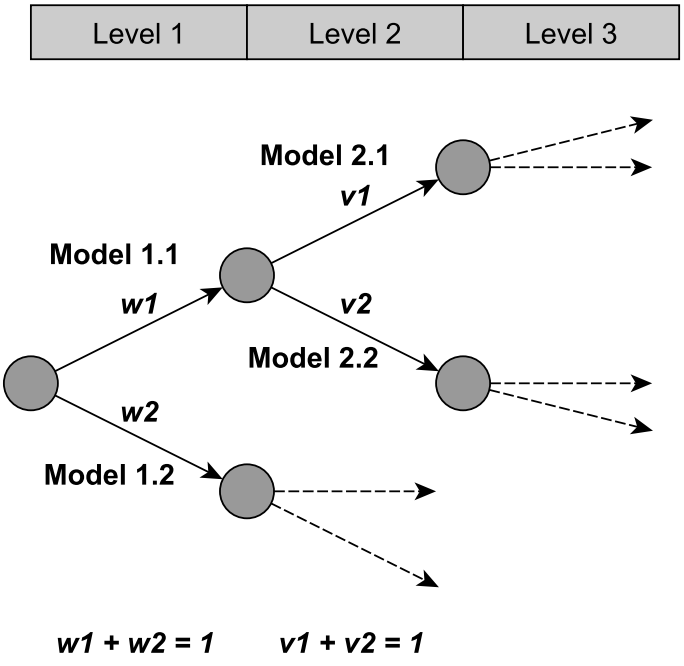

FIGURE 6.4: Example of a logic tree structure.

For instance, logic trees have been used to propagate model uncertainties in probabilistic seismic hazard assessment, through the selection of different ground motion prediction equations – GMPEs [Delavaud et al., 2012]. In a logic tree, each branch is associated with a weight, which is usually estimated through an expert-elicitation process. The same type of logic tree could also be used for fragility assessment, where different fragility models could be weighted for a given typology. These weights reflect the analyst's view on the plausibility of models, so that they can be seen as prior probabilities. Once model uncertainties are represented on the logic tree branches with their respective weights, the remaining epistemic uncertainties (i.e. parameter-related) as well as the aleatory uncertainties can be propagated by running MC simulations for each branch of the logic tree. The final probabilistic distribution of the outcome metric is then obtained via a weighted sum of the results over all the branches (i.e. the branch weights are used as a probability). For this reason, one important constraint is that logic tree branches must be mutually exclusive and collectively exhaustive (MECE), as stated by Bommer and Scherbaum [2008].

6.3.3 Bayesian Event Trees

Bayesian event trees (BET) have been introduced by Marzocchi et al. [2004, 2010] for probabilistic volcanic hazard assessment and eruption forecasting. They are similar to logic trees in structure (i.e. graphical representation of a tree structure with branches, see Figure 6.5), however they do not serve the same purpose and they contain fundamental differences with respect to logic trees:

- BETs focus on events (and not just model choices, like in logic trees): each branch represents a logical step that ensure the transition from an anterior event to a subsequent event, so that the entire risk analysis can be represented by a chain of intermediate events and outcomes up to the final outcome.
- BETs are based on conditional probabilities and Bayesian theory, in the sense that the probability of event n occurring is expressed as the probability of event k given event $k-1$ has occurred, and so forth.

- Each branch of the BET is associated with a conditional probability, and not just a weighting coefficient like in logic trees. Therefore the MECE assumption is not a prerequisite for BETs.

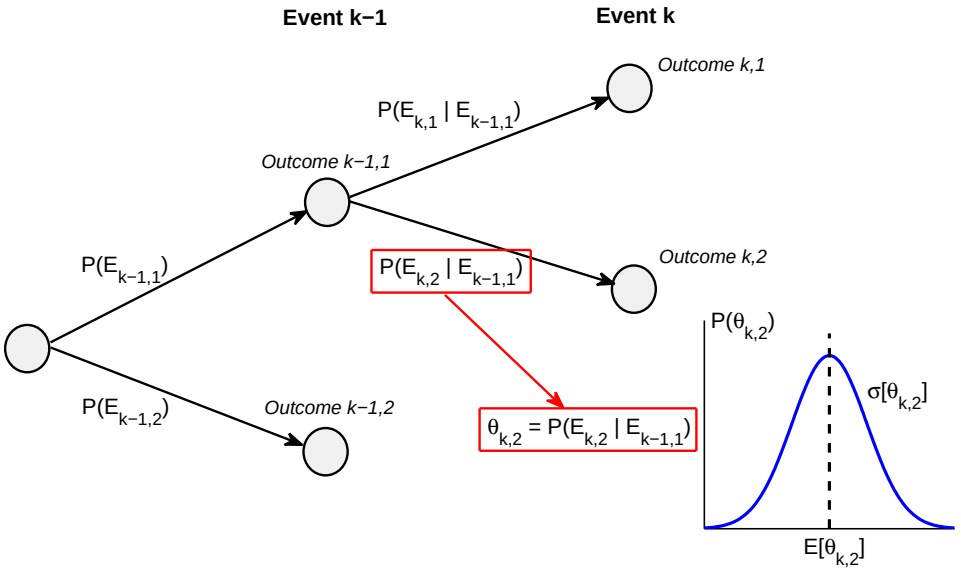

FIGURE 6.5: Example of a Bayesian event tree structure with uncertain event probabilities.

One of the most notable BET functionalities featured in Marzocchi et al. [2004] is the way the conditional probability is defined for a given event k. This event probability $\mathrm{P}\left(\mathrm{Event}_k|\mathrm{Event}_{k-1}\right) = \theta_k$ is not necessarily a single scalar value, as it can also be associated with uncertainties that represent the difficulty to accurately quantify each event probability, due to lack of knowledge or field evidence. Therefore each event probability θ_k can be associated with a probabilistic distribution (i.e. also referred to as a 'probability of probability', see Woo [1999]):

- The average $\mathrm{E}\left[\theta_k\right]$ can be seen as the probability due to aleatory uncertainties (i.e. the pure randomness of the process predicting the event k).
- The standard deviation $\sigma\left[\theta_k\right]$ of the distribution of θ_k represents the level of uncertainty that is associated with the estimation of event probability θ_k: it can be considered as the epistemic uncertainty, i.e. the variability due the lack of knowledge on the models and parameters to be used.

Marzocchi et al. [2004] proposed a Bayesian updating process, based on empirical or historical data, in order to refine the prior distribution of θ_k: the addition of actual

observations enables one to obtain a posterior distribution of θ_k with a greatly reduced standard deviation $\sigma[\theta_k]$. Therefore BETs could be used to represent both aleatory and epistemic uncertainties. The distribution of θ_k is obtained by sampling the various model- and parameter-related uncertainties, while aleatory uncertainties are represented by the expected value of θ_k. Finally, with the probabilistic distribution of θ_k defined for each branch of the BET, the conditional probabilities can be sequentially computed in order to estimate the distribution of the final loss metric, which will contain both aleatory and epistemic uncertainties.

6.3.4 Bayesian Networks

One of the main issues in the probabilistic estimation of infrastructure losses lies in the high dimensionality of the problem (i.e. each individual element within the system plays a specific role with respect to the global performance), which usually leads to an intractable number of potential outcomes. This effect is even more magnified when epistemic uncertainties are included, since each realisation of a potential input variable leads to another multiplication of the space of solutions. While Monte Carlo simulations have been shown to yield rather stable risk estimates after a reasonable number of samples [Cavalieri et al., 2012], these methods may prove to be insufficient when very low-probability and high-consequence events are investigated: in this context, it is very likely that the Monte Carlo methods will overlook such events, thus resulting in an underestimation of the risk.

For all the reasons detailed above, Bayesian Networks emerge as the most appropriate tool for infrastructure risk assessment and decision support [Bensi et al., 2013, 2011]. Their main advantage resides in the inference process, which enables to update probabilities of any nodes in the BN after specifying the value or state of a given node (i.e. evidence): Bayesian inference can work either way, i.e. generating a forward or a backward analysis depending on whether the evidence is entered at the start or the end of the BN, respectively. Moreover, exact inference algorithms such as junction trees generate the exact probability distributions for any nodes, while such quantities are usually only approximated when performing Monte Carlo simulations. This feature is an essential requirement when extreme events are considered.

6.3.5 Sensitivity Analysis

When a large number of input variables are associated with various uncertainties, the amount of mathematical constructions and computations that are needed to propagate all uncertainties can soon become intractable. To this end, sensitivity analyses usually constitute an efficient way to identify the role of the different uncertainty sources. According to Rohmer [2013], sensitivity analyses can be used to:

- identify which input factors contribute most to the output uncertainty;
- identify which input factors are insignificant and can then be eliminated to reduce the dimensions of the problem;
- determine which input factors interact with each other.

The simplest way to assess the influence of the various uncertainty sources consists in changing one input variable at a time (i.e. 'one-factor-at-a-time' analysis). However this approach does not lead to the identification of the interactions between factors and it is only valid in the case of a linear problem.

Another way to perform a sensitivity analysis is the First-Order Reliability Method (FORM), since the sensitivity factors of each input variable are a by-product of the reliability analysis. However FORM analyses can be applied as long as there is a single dominant failure mode, or otherwise all failure modes need to be found to avoid gross underestimation of failure probability. Whilst numerous computation strategies have been developed in order to bypass these limitations, their application to complex non-linear problems remains cumbersome.

As an alternative, variance decomposition (i.e. computation of Sobol' indices) provides the most informative sensitivity analysis, while being applicable to any kind of problem. The variance-based global sensitivity analysis (GSA) detailed by Saltelli et al. [2008] enables to provide the main and total effects associated to each source of uncertainty. The main effects (i.e. first-order contributions of each parameter, without accounting for interaction terms) can be used to individually rank the various sources of uncertainties, while total effects (i.e. second-order indices including contributions from interaction terms) should be used to identify negligible parameters (i.e. input factors with a low

main effect and low interactions with other terms) and to measure the level of complexity of the studied problem (i.e. high differences between total and main effects imply a high degree of interaction between the uncertainty sources).

An interesting feature of the variance-based global sensitivity analysis is its ability to combine various types of input factors (i.e. uncertain variables with either continuous or discrete distributions). The estimation of the Sobol' indices (i.e. total and main effects) may be carried out through various algorithms, such as the Monte-Carlo-based Sobol' algorithm [Saltelli, 2002]: even though this approach is the most complete and the most versatile form of sensitivity analysis, the associated Monte-Carlo simulations require a large number of model evaluations. Gehl et al. [2013b] applied variance-based global sensitivity analysis to the case of uncertainty ranking for seismic risk scenarios. The large number of intensive model computations led to the development of surrogate meta-models in order to reduce the computational load. A similar approach has also been used by Rohmer et al. [2014] for the comparison of the influence of model-related uncertainties against parameter-related uncertainties in earthquake loss assessment procedures.

6.4 Specification of Quantitative Uncertainty Models

The quantification of some of the aforementioned uncertainty sources is presented through two examples, which aim at demonstrating how to specify the variability of important parameters before computing the distribution of losses. The two applications focus on the epistemic uncertainties due to the choice between different models, which is a common issue when performing a risk analysis. First, the variability induced by the availability of multiple GMPEs in the seismic hazard assessment is investigated. Then, the uncertainty due to the selection of literature-based seismic fragility curves for bridges is quantified, in the case that no specific fragility model has been developed. These two examples have been chosen since the study by Rohmer et al. [2014] has shown that the choice of GMPEs and vulnerability models are among the most influent sources of uncertainties when performing a seismic risk analysis. A similar work might be carried out for variables related to flood risk, however the focus is put here on seismic risk, due to the availability of well established methods and data sets.

6.4.1 Epistemic Uncertainties due to the Choice of GMPEs

When performing a seismic risk analysis, the assessment of the seismic intensities at the vulnerable sites constitutes an essential step. The compilation of existing GMPEs by Douglas [2014] reveals a wide range of potential ground-motion prediction models that may be applied to a given area. It is interesting to note that the multiplicity of these GMPEs does not necessarily lead to a more accurate prediction of the seismic intensities, since the epistemic uncertainties due to the choice among various ground-motion prediction models are not reduced.

To this end, logic trees have become a popular tool to account for the possible selection of multiple GMPEs. For instance, in the framework of the FP7 SHARE project [Giardini and the SHARE Consortium, 2009–2012], logic trees have been designed for the selection of GMPEs for the definition of the pan-European probabilistic seismic hazard assessment [Delavaud et al., 2012], through the use of expert judgements and data-driven rankings. Other GMPE selection exercises have been carried out recently for the Global Earthquake Model hazards maps [Stewart et al., 2015] or the update of the U.S. national seismic hazard maps [Petersen et al., 2014]. The merits and issues of this multi-GMPE approach and alternative methods are discussed in Atkinson et al. [2014].

6.4.1.1 Method Proposed by Atkinson and Adams [2013]

Recently, Atkinson and Adams [2013] have proposed an alternative method that consists in the definition of three representative GMPEs – lower, central and upper – in order to express the epistemic uncertainty due to the choice of GMPEs. The three representative GMPEs are derived from existing median models, such as the ones contained in the GMPE compendium [Douglas, 2014]. It is shown by Atkinson and Adams [2013] that the three-equation model is equivalent to the use of multiple GMPEs, provided that the same range of epistemic uncertainty is sampled. This model still requires a careful selection of existing GMPEs, in order to ensure that the epistemic uncertainties that are represented by the three-branch GMPE still capture the variability than can be found between available GMPEs. The proposed approach presents several benefits:

- The selection of existing GMPEs to build the representative model can be done without applying weighting coefficients, which eliminates the subjective expert-based judgement that is usually associated with the logic tree approach.
- Values are computed for discrete combinations of magnitudes and distances, thus allowing for a flexible expression of the median and the epistemic uncertainties, without requiring a given functional form.
- The three-equation representative model can be readily used as an input to the risk analysis, since the central equation and the upper/lower bounds can be sampled with appropriate weights (i.e. the relative weights are defined by the Gaussian probability density function). Since only three possible inputs are sampled, the associated computational effort is reduced when compared to a logic tree with more choices of GMPEs.

The successive steps in the construction of the representative GMPEs are summarised as follows:

1. Selection of a set of n GMPEs that are potential candidates as ground motion models for the area of interest.
2. For each combination of magnitude and distance, computation of the corresponding ground-motion parameters $y_1 \dots y_n$ from the selected GMPEs.
3. Computation of the central representative value $\bar{y}$ by processing the geometric mean: $\bar{y} = (y_1 \cdot \dots \cdot y_n)^{1/n}$.
4. Expression of the epistemic uncertainty with the standard deviation of the logarithms of the ground-motion parameters: $\sigma_{\log y} = \text{stdev}\,(\log_{10} y_1, \dots, \log_{10} y_n)$.
5. Smoothing of the standard deviations between the discrete distances. For example, the smoothed standard deviation at distance k is computed as follows: $\sigma^s_{\log y,k} = 0.25 \cdot \sigma_{\log y,k-1} + 0.5 \cdot \sigma_{\log y,k} + 0.25 \cdot \sigma_{\log y,k+1}$. This step enables to reduce the pinching effect of the confidence intervals if the various $y_1 \dots y_n$ values are close to each other for some combinations of magnitude and distance.
6. Computation of the upper/lower epistemic bounds: $y_{-/+} = 10\hat{}\left(\log_{10} \bar{y} \pm \sigma^s_{\log y}\right)$.

7. Representation of the three-branch GMPE in a tabulated format for various combinations of magnitude and distance, without any fitting to a functional form.

6.4.1.2 Application to the European context

While Atkinson and Adams [2013] have developed the approach described in the previous section to the generation of probabilistic seismic hazard maps for Canada, a similar representative GMPE approach is applied here to the European context. To this end, a selection is made from recent GMPEs that are presented in the Bulletin of Earthquake Engineering Special Issue on the new generation of ground-motion models for Europe and the Middle East: four GMPEs are chosen as the basis for the derivation of the representative GMPE model (see Appendix G), namely GMPEs from Akkar et al. [2014a] (AB14), Bindi et al. [2014] (BI14), Bora et al. [2014] (BO14) and Derras et al. [2014] (DE14). These GMPEs are all based on the RESORCE database of ground motion records [Akkar et al., 2014b] and they share a common validity domain (i.e. M_w between 4.0 and 7.6, distance between 1 and 200 km). These GMPEs represent the most up-to-date models and they are based on a recent database of records, which covers all Europe and Middle East areas. The main difference between the GMPEs lies in the computational methods that have been used to derive them (e.g. from conventional regression techniques to data-driven approaches based on neural networks): therefore it is expected that the resulting representative GMPE will cover the uncertainties due to the various modelling assumptions used in the underlying GMPEs. The following assumptions are used to generate a representative GMPE model for EC8 soil class B:

- Normal faulting style with 10 km focal depth is assumed by default.
- Since the selected models directly use shear wave velocity as a proxy to soil amplification, $V_{s,30}$ = 580 m/s is assumed for soil class B. Since the objective is to assess the uncertainty due to the choice between various GMPEs, a deterministic $V_{s,30}$ value has be chosen: further computations could be carried out in order to quantify the uncertainties due to the description of the soil class (i.e. sampling of $V_{s,30}$ in order to cover all possible values within the range of soil class B).

- PGA is chosen as the output ground motion parameter in the present case, even though the derived representative GMPE is able to also predict PGV and SA at various periods (i.e. $T = 0.05$ s, 0.1 s, 0.2 s, 0.3 s, 0.5 s, 1.0 s and 2.0 s).
- The common distance metric is the epicentral distance. For models that use the Joyner-Boore distance, the conversion is ensured by the equations from Atkinson and Adams [2013], which are based on the Wells and Coppersmith [1994] fault model.

These four GMPEs are plotted in Figure 6.6, for three selected magnitudes. They are compared to actual ground-motion records that are extracted from the RESORCE database with the following criteria: normal faulting style, focal depth between 0 and 20 km, $V_{s,30}$ between 360 and 800 m/s, and $M_w \pm 0.25$ magnitude bins.

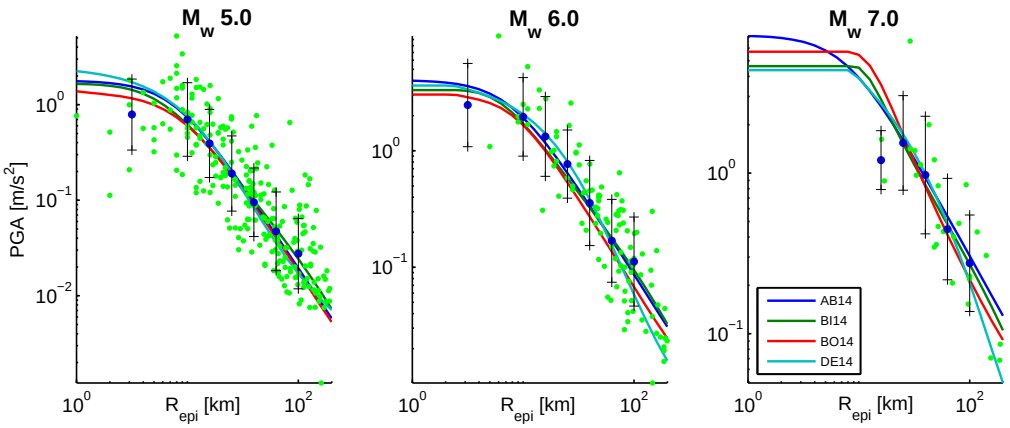

FIGURE 6.6: Selected GMPEs with $V_{s,30} = 580$ m/s, normal faulting and 10 km focal depth. The green points represent records from the RESORCE database.

The aforementioned method is then applied and the resulting three-equation representative GMPE are plotted for a few magnitudes in Figure 6.7: the lower and upper bounds representing the epistemic uncertainties are estimated for the 16^{th} and 84^{th} percentiles (i.e. one time the standard deviation). Therefore the proposed model enables a complex problem to be represented by a minimum number of branches for single-site hazard analysis and mapping: respective weights for the median, upper and lower bounds could for instance be $[0.4518; 0.2741; 0.2741]$, according to the probability density function of the normal distribution.

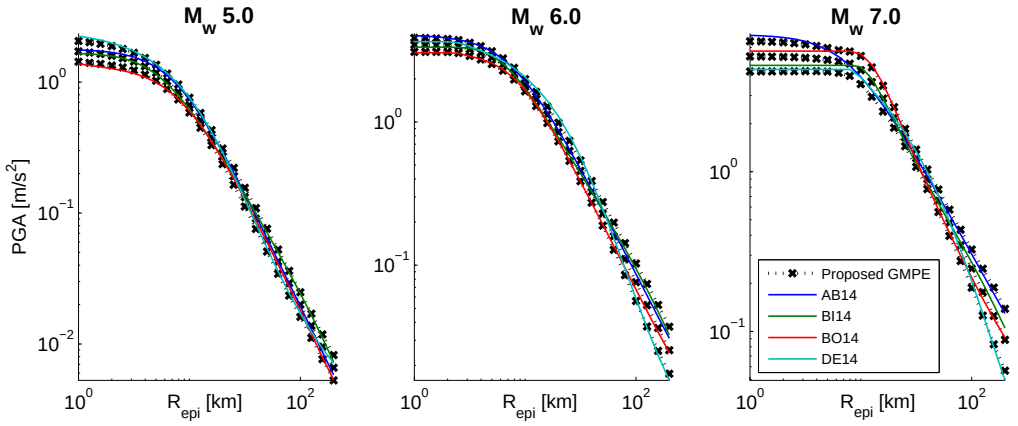

FIGURE 6.7: Three-branch representative GMPE for soil class B and its underlying models.

6.4.1.3 Aleatory uncertainties

Once the epistemic uncertainties have been quantified for the proposed representative GMPE, aleatory uncertainties – which are represented by the intra-event and inter-event variability – need to be assessed as well, in order to ensure that the model is fully characterized and usable in the context of a seismic risk analysis.

The aleatory uncertainty can be decomposed into intra-event and inter-event variabilities, which are represented by the standard deviations σ_{intra} and σ_{inter}. A quadratic combination is then a common and valid approximation to express the total standard deviation that corresponds to aleatory uncertainty [Kennedy et al., 1980]:

$$\sigma_{alea} = \sqrt{\sigma_{intra}^2 + \sigma_{inter}^2} \tag{6.1}$$

Similarly, the total uncertainty that intervenes in the prediction of the ground motion parameters is expressed as follows:

$$\sigma_{tot} = \sqrt{\sigma_{epis}^2 + \sigma_{alea}^2} = \sqrt{\sigma_{epis}^2 + \sigma_{intra}^2 + \sigma_{inter}^2} \tag{6.2}$$

where σ_{epis} is the standard deviation representing the epistemic uncertainty that results from the choice between different GMPEs: this quantity is directly obtained by following the procedure described in the previous sub-section. Therefore, in order to extract the terms composing the aleatory uncertainty, the following procedure is proposed:

1. For each combination of magnitude and distance, ground-motion parameters are computed from the selected GMPEs by randomly sampling the intra-event variability, for a high number of artificially generated outcomes (e.g. 10 000 values) (i.e. Monte Carlo process).

2. All the sampled outcomes enable to compute an approximation of the total standard deviation $\sigma_{tot,intra}$, which is then used to extract the intra-event variability: $\sigma^2_{intra} = \sigma^2_{tot,intra} - \sigma^2_{epis}$.

3. The same process is applied for the inter-event variability, which is expressed as: $\sigma^2_{inter} = \sigma^2_{tot,inter} - \sigma^2_{epis}$.

4. The aleatory standard deviations are smoothed in the same way as the epistemic standard deviations, as detailed in the previous sub-section.

As a result, the complete three-branch representative GMPE with its aleatory confidence bounds is represented in Figure 6.8 for a few magnitude values. It can be noted that the aleatory part is dominating in the overall variability, especially for higher magnitude ranges: this observation should moderate the importance of the epistemic uncertainties due to the choice of GMPEs. This may be especially true in the present situation, where the four original GMPEs that have been selected are from the same era and are based on the same ground-motion dataset (i.e. RESORCE database).

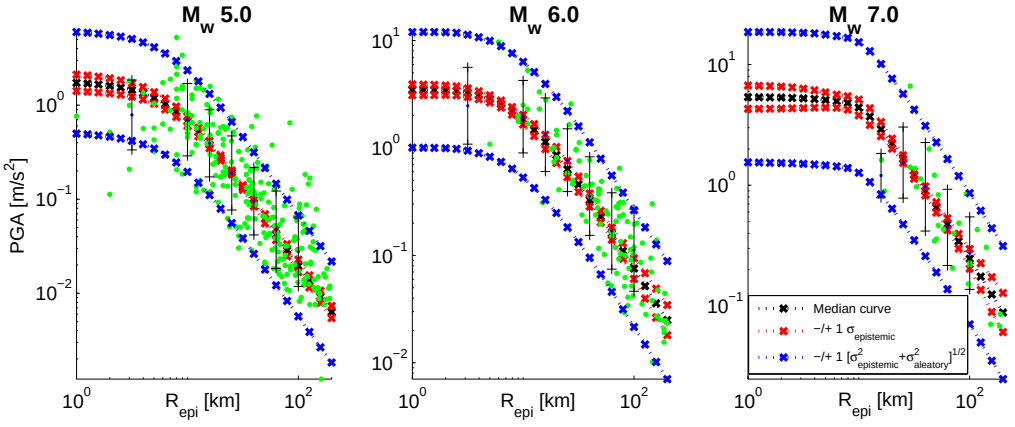

FIGURE 6.8: Three-branch representative GMPE (black and red dotted lines) with aleatory uncertainties (blue dotted lines). The green points represent records from the RESORCE database, while the associated standard deviations over distance bins is represented by vertical black lines.

6.4.1.4 Validation

The potential bias of the proposed GMPE is checked by comparing the PGA predictions to the ground-motion records that have been extracted from the RESORCE database (see Figure 6.8). Eight discrete magnitude values are used in the representative GMPE, therefore the database records are selected within $M_w \pm 0.25$ magnitude bins, as shown in Table 6.2. The geometric mean of the two horizontal components of each record is computed as the reference PGA.

TABLE 6.2: Number of available records for each magnitude range.

M_w	4.0	4.5	5.0	5.5	6.0	6.5	7.0	7.5
Records	207	265	257	174	109	56	26	12

As a result, Figure 6.9 shows the proportion of RESORCE ground motions records that are found to be above or below the GMPE predictions, for each magnitude bin:

- Green bars represent the records that are below the median GMPE (light green for records between the median curve and the aleatory bound, dark green for records below the aleatory bound). These correspond to an overestimation of the PGA by the GMPEs.
- Red bars represent the records that are above the median GMPE (light red for records between the median curve and the aleatory bound, dark red for records above the aleatory bound). These correspond to an underestimation of the PGA by the GMPEs.

It appears that the three-branch representative GMPE tends to be more balanced than the individual GMPE models, since it combines the specific underestimations or overestimations of its underlying models. Some GMPEs (i.e. AB14 and BO14) present large aleatory uncertainties, as opposed to the narrower intervals that are found for the BI14 and DE14 models: again, the use of the representative GMPE enables the generation of averaged uncertainty bounds. The clearest trend can be observed for M_w 5.0 to 6.0 events: these magnitude bins correspond to the highest numbers of records, thus ensuring a good statistical distribution of the samples. Conversely, the results become more difficult to interpret for M_w 7.5, due to the scarcity of available records. The slightly higher proportion of IMs that are underestimated might be due to the choice of the $V_{s,30}$

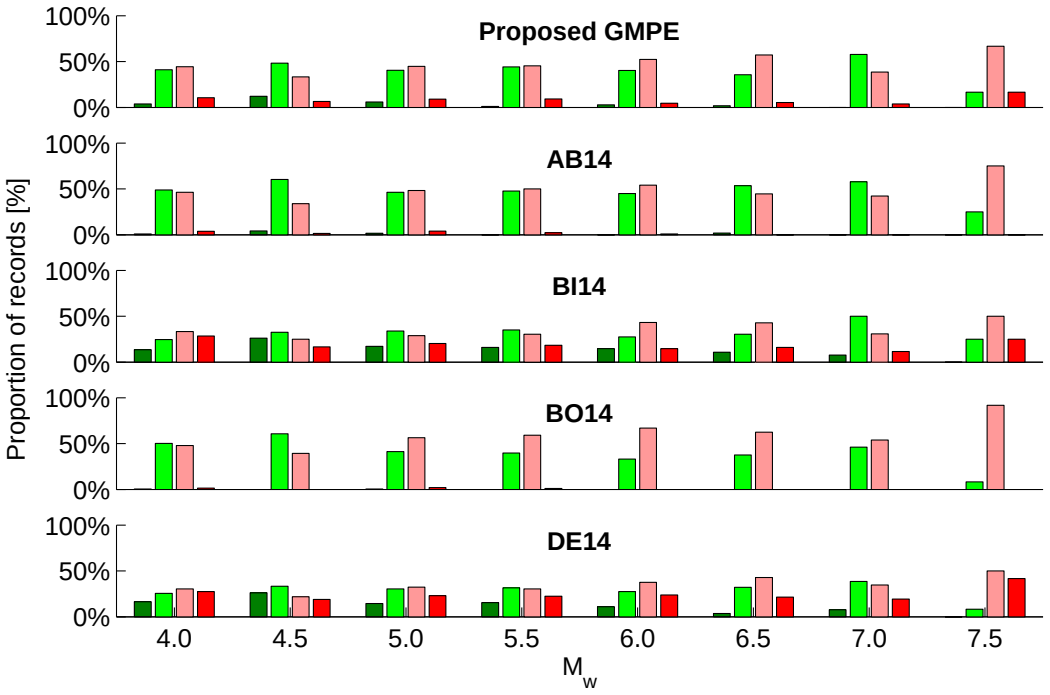

FIGURE 6.9: Proportions of RESORCE ground motions accurately predicted by the different GMPEs.

value to represent the soil class (i.e. 580 m/s corresponds to the middle of the velocity range), while the lower bound of class B might lead to less conservative results.

In conclusion, this three-branch representative GMPE may be considered as a generic model that accounts for epistemic uncertainties due to the choice between the most recent GMPEs for Europe. Since no functional form is proposed, the values for some combinations of magnitude and distance are detailed in Appendix H.

6.4.2 Epistemic Uncertainties due to the Choice of Fragility Curves

In the case that the collected structural data is insufficient or if a large number of bridges are considered in a given study, the derivation of specific bridge fragility curves might prove difficult or even irrelevant. An alternative consists in using fragility curves that have been previously derived for some bridge typologies: such an approach presents the merit of only requiring very limited data (e.g. visual inspection or photographs). However it may result in very large uncertainties, which are quantified in the following subsections.

6.4.2.1 Available Data

The SYNER-G database of bridge fragility curves [Silva et al., 2014, Tsionis and Fardis, 2014], which has already been presented in Subsection 2.1.1.2, is designed as a catalogue from which suitable fragility models can be selected for a given application. However, before the directly application of the database, it is proposed to perform a preliminary selection in order to choose only suitable fragility curves:

- The selected fragility curves must be analytically derived, since it appears that most empirical studies are based on a single event, i.e. either 1994 Northridge or 1995 Kobe earthquakes (typology of bridges in these two events differs from European ones).
- The selected fragility curves must be based on a generic bridge model (i.e. representative of a given type), preferably with several samples of mechanical or geometrical variables.
- The selected fragility curves must contain enough information on key structural parameters, in order to avoid poorly constrained models. Following the SYNER-G taxonomy, the characteristics **MM1** (main material), **LS** (level of seismic design), **DSS** (deck structural system) and **TC1** (type of pier) have been used as descriptors of the bridge types: these characteristics have been identified as having the most influence on the fragility parameters, after a quick sensitivity analysis. They are also the ones that are easily identifiable with a visual inspection of the bridge, as opposed to characteristics related to the structural features of the bridge (e.g. type of bearing, pier detailing, etc.). If too many characteristics are considered for the specification of bridge types, then there is a risk of finding too few valid candidates.
- The selected fragility curves must use PGA as IM, for obvious harmonisation reasons.

As a result, the original database of 30 references is reduced to 9 references that describe 6 bridge types (i.e. combinations of the four aforementioned bridge characteristics) for a total of 39 data points, as shown in Table 6.3. The number of points represents the number of fragility curves that correspond to the selected characteristics: some

references propose multiple fragility curves for the same bridge type because these are further classified with other characteristics that are not considered here.

TABLE 6.3: Summary of the selected fragility curves for each bridge type.

Bridge typology ID	MM1	LS	DSS	TC1	# of points	# of references
1	C	NSD	SSu	McP	8	6
2	C	NSD	SSu	ScP	7	1
3	C	SD	Co	McP	3	3
4	C	SD	Co	ScP	8	2
5	C	SD	SSu	McP	4	3
6	C	SD	SSu	ScP	9	3

As expected, there are important disparities across the different bridge types, both in terms of available fragility curves and in terms of associated references. For each fragility curve, the mean α and the standard deviation β are selected for the global damage states DS1 (yield) and DS4 (collapse): the four usual damage states are not considered by all selected fragility curves, therefore only the ones for which all models are available are kept.

6.4.2.2 Statistical Model

The objective is to propose fragility parameters, along with their confidence bounds, for each of the six bridge types. To this end, it is proposed to build a statistical model that uses the fragility parameters from the literature as 'observations' in order to reduce the variability for each bridge type. The problem at hand fits well with the derivation of a random effects model, since the fragility parameters from the literature represent hierarchical data: a single hierarchical level (i.e. one-way model) can be drawn from different populaions of fragility parameters that correspond to different bridge typologies. As opposed to fixed effects, random effects allow for individual effects (i.e. random variability within a population belonging to the same group), which should be the case in the present application. As a result, the following one-way random effects model is proposed:

$$\begin{cases} \log \alpha_{i,j} = \mu_0^{(1)} + \delta_{\text{ID}}^{(1)}(\text{ID}_i) + \epsilon_{i,j}^{(1)} \\ \log \beta_{i,j} = \mu_0^{(2)} + \delta_{\text{ID}}^{(2)}(\text{ID}_i) + \epsilon_{i,j}^{(2)} \end{cases} \quad \text{for } i = 1 \dots N_{br} \text{ , for } j = 1 \dots n_i \tag{6.3}$$

where N_{br} is the number of bridge types (i.e. $N_{br} = 6$ here), n_i is the number of fragility curves corresponding to bridge type i (see Table 6.3) and $\epsilon_{i,j}$ is the individual error term, which is assumed to follow a normal distribution:

$$\epsilon \sim \mathcal{N}\left(0, \sigma^2\right) \tag{6.4}$$

The factor δ_{ID} is specific to each bridge type and is assumed to follow a normal distribution:

$$\delta_{\text{ID}}(i) \sim \mathcal{N}\left(\mu_i, \sigma^2_{\text{ID}}\right) \qquad \text{for } i = 1 \dots N_{br} \tag{6.5}$$

Finally, the fragility parameters $\log \alpha$ and $\log \beta$ are assumed to be correlated through the following covariance matrix:

$$\mathbf{M} = \begin{pmatrix} \sigma^2_{(1)} & \sigma_{(1)} \cdot \sigma_{(2)} \cdot \rho \\ \sigma_{(1)} \cdot \sigma_{(2)} \cdot \rho & \sigma^2_{(2)} \end{pmatrix} \tag{6.6}$$

Therefore the correlation factor ρ, the standard deviations σ and σ_{ID} and the means μ_0 and μ_i are the variables that need to be determined in order to obtain a fully defined statistical model. It is then proposed to use a Markov Chain Monte Carlo (MCMC) Bayesian analysis to update the posterior distribution of these variables given the observations of the fragility parameters (i.e. data points from the literature).

The problem at hand can be represented as a graphical structure (see Figure 6.10), where the one-way random effect introduced by the bridge type term δ_{ID} is explicated.

6.4.2.3 Results

The proposed statistical model is implemented in the OpenBUGS software [Lunn et al., 2009], where three MCMC chains of 10 000 samples are simulated in order to check convergence: each MCMC chain starts with different starting points, so that the stability of the statistical model can be checked by comparing the outcomes from several MCMC chains. The prior distributions of the different variables are assumed to be rather uninformative (e.g. normal distribution with zero mean and standard deviation

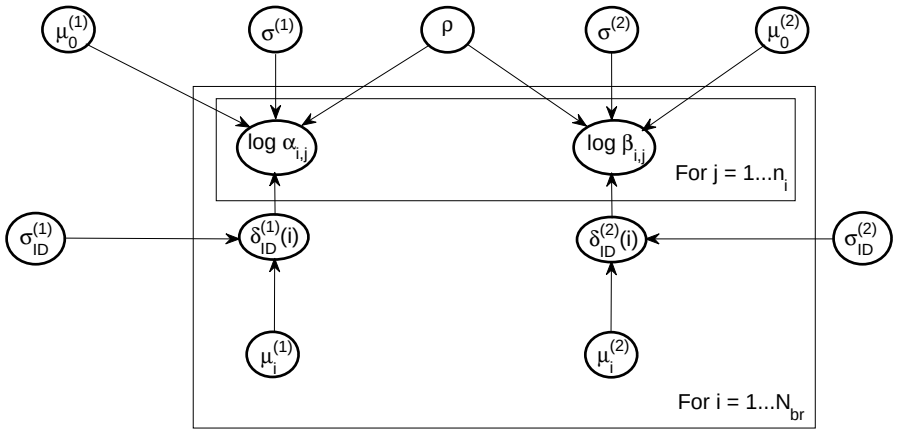

FIGURE 6.10: Proposed random effects model for the prediction of fragility parameters.

10, or uniform distribution between -1 and 1) in order to limit their influence on the posterior estimation. Some statistics of the updated distributions of the target variables are detailed in Table 6.4, as a direct outcome of the OpenBUGS runs.

TABLE 6.4: Outcomes of the MCMC Bayesian analysis for the fragility parameters of damage state DS1.

Variable	Mean	Standard deviation	Variable	Mean	Standard deviation
$\mu_0^{(1)}$	-1.68	0.26	$\mu_0^{(2)}$	-1.15	0.26
$\sigma^{(1)}$	0.47	0.06	$\sigma^{(2)}$	0.49	0.06
$\sigma_{ID}^{(1)}$	0.57	0.24	$\sigma_{ID}^{(2)}$	0.56	0.24
$\mu_1^{(1)}$	-0.45	0.29	$\mu_1^{(2)}$	-0.39	0.29
$\mu_2^{(1)}$	0.41	0.30	$\mu_2^{(2)}$	0.13	0.30
$\mu_3^{(1)}$	-0.20	0.33	$\mu_3^{(2)}$	-0.13	0.32
$\mu_4^{(1)}$	-0.56	0.29	$\mu_4^{(2)}$	-0.63	0.30
$\mu_5^{(1)}$	0.13	0.32	$\mu_5^{(2)}$	0.50	0.33
$\mu_6^{(1)}$	0.65	0.29	$\mu_6^{(2)}$	0.52	0.29
ρ	0.36	0.15			

The updated distributions of these variables can then be used to specify the statistical model in Figure 6.10. A simple sampling of the different variables may be performed in order to extract possible realisations of the fragility parameters α and β for damage states DS1 and DS4. The generated samples can finally be used to compute the 16% and 84% confidence bounds of the fragility parameters, which correspond roughly to a ± 1 standard deviation interval (see Figure 6.11).

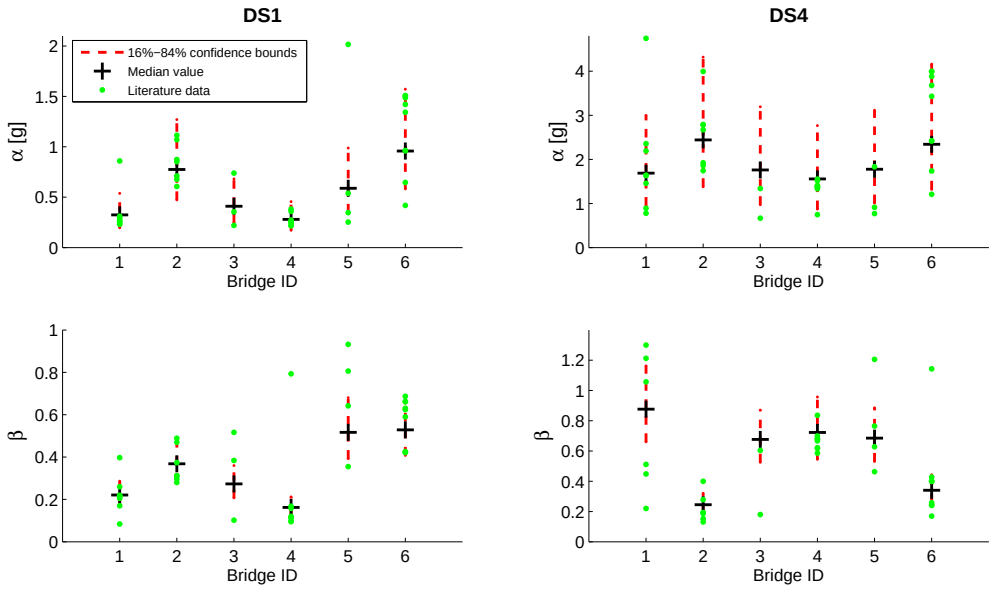

FIGURE 6.11: Median values (black crosses) and 16%-84% confidence bounds (red dashed lines) of the fragility parameters for the six bridge types. The green dots represent the actual values that are been selected from the literature.

Regarding the prediction of parameter α, the results show that the variability within each bridge type is rather large, while there is no significant gap between the different bridge types (e.g. especially for DS4). Moreover, the taxonomy parameters that have been used for the selection of fragility curves and for the description of bridge types (see Table 6.4) do not seem to have a consistent contribution to the predictions. For instance, bridge #1 (non-seismically designed) appears to be the most vulnerable, however this is not the case for the other non-seismically-designed bridge #2. It seems that single-column piers may lead to a more favourable configuration than multi-column piers, except in the case of continuous decks with monolithic connections (i.e. bridges #3 and #4). In order to investigate this aspect, a mixed effects model has been designed, where the four structural parameters have been added as fixed effects to the existing one-way random effects model. However, the difficulties to make this new model converge and the evidence of a large auto-correlation in the sampling of the fixed effects do not enable a reliable exploration of these new results.

The simple one-way random effects model that is considered here is the most robust estimation of confidence bounds that is currently feasible, while more elaborate models cannot be supported by the limited amount of data that has been selected. Moreover, there is a large variability between the fragility curves given by the references for the

same bridge type, which is due to the wide range of analytical approaches and modelling assumptions that can be adopted by different groups of authors. Therefore it may be concluded that the catalogue of bridge fragility curves cannot yield reliable fragility estimates in its current state. It needs to be augmented with additional entries that are generated by consistent derivation methods, in order to limit the variability between the references. If such a catalogue must still be used due to insufficient knowledge on the considered bridges, it is necessary to consider the confidence bounds estimated here in order to account for the large uncertainties that are generated by this simplified approach (e.g. coefficients of variation between 45% and 55% for the estimation of fragility mean α).

6.5 Conclusion

This Chapter has reviewed the various sources of uncertainty that may be found in the risk assessment of infrastructure systems exposed to earthquakes, ground failures and floods. A conventional distinction between aleatory and epistemic uncertainties is adopted, while it appears that a further classification among epistemic uncertainties can be made, such as the identification of model-based or parameter-based uncertainty sources.

Various statistical tools have also been detailed for the management of uncertainties, which may be comprised of various tasks, such as uncertainty quantification, uncertainty propagation and sensitivity analysis. Regarding the quantification of uncertainties, two examples have been proposed, with the objective of specifying the possible sampling range of these variables:

- model-based uncertainty due to the choice of a seismic fragility curve for bridges;
- model-based uncertainty due to the choice of a GMPE for seismic hazard assessment.

Both applications have led to the definition of confidence bounds that cover $\pm$ one standard deviation of the identified uncertainties. Such a formulation constitutes a convenient way to propagate the uncertainties, since upper or lower confidence bounds

may be sampled in order to generate results with low or high hypotheses. Therefore the propagation and the influence of these uncertainties will be investigated through a small example in Chapter 7.

Chapter 7

Bayesian Networks for the Multi-Risk Analysis of Infrastructure Systems

7.1 Introduction

The risk analysis of a Critical Infrastructure (CI) system that is subjected to multiple hazards requires the specification of all the variables that are involved in the various modelling steps. Based on the harmonisation work performed in the previous Chapters, for a given hazard type the chain of analysis can be decomposed into the following events:

- *Source event*: an initiating event that may induce a given hazard level. This event can usually be associated with a return period.
- *Hazard event*: this event represents the distributed loadings that may be applied to the CI system, depending on the magnitude of the source event. It represents the specific distributed demand on the system.
- *Infrastructure (or Element) event*: the physical state of all the infrastructure objects composing the CI system, based on the applied hazard event. Each one of them have a propobability of being in a given state as determined by component-specific fragility curves and performance indicators.

- *Network event*: the state of the CI objects in terms of network functionality (e.g. functionality loss, required restoration time, etc.), based on the physical infrastructure events, depending on the correlations of failures among components.
- *Societal event*: the direct and indirect consequences of the previous events, in terms of global network performance indicators.

As shown in Chapter 6, uncertainty sources are present within all the aforementioned steps. Therefore a full probabilistic framework is required to propagate uncertainties and to derive the global risk curve (i.e. yearly probability of exceedance of a given system performance indicator). Simulation-based methods such as the OOFIMS tool [Franchin and Cavalieri, 2013] have proven to be robust and able to account for many uncertainty sources. In parallel, BNs promise to deliver exact probabilities as opposed to sampling methods, which is a valuable feature when the objective is the quantification of extreme events. However, BNs suffer from computational limitations when processing large and complex systems. Moreover, current BN formulations are mostly based on connectivity analyses and they fail to predict capacity and serviceability losses, which are seen as the more relevant performance indicators in most systems [Modaressi et al., 2014].

Therefore Section 7.2 investigates the efficiency and computational bottlenecks of current BN formulations for the exact inference of systems. A hybrid approach, based on the construction of a simplified BN from simulation results, is then presented as an alternative to overcome the computational burden and as a decision support system for real-life infrastructure.

These theoretical developments are then applied in Section 7.3 to a hypothetical road network that is exposed to multiple hazards (i.e. earthquakes, floods and ground failures): this case study is used to demonstrate the applicability of the various findings of this thesis, such as the multi-hazard fragility models, the functionality curves, the quantification of epistemic uncertainties and the multi-risk framework. The reduced size and complexity of the studied network will allow for an exact BN formulation to be applied, thus proving the feasibility of the developed concepts.

Finally, Section 7.4 demonstrates the applicability of the multi-risk framework to a large scale real-world road network (i.e. road network beetwen Bologna and Florence). Due to the size of such a network (i.e. almost 300 vulnerable elements), a Monte Carlo

simulation only is adopted here, since the objective in this section will be to demonstrate the applicability of the multi-risk framework to realistic systems.

7.2 BN Formulation for Infrastructure Systems

The BN structure for the description of an infrastructure system globally follows the same principles as the BNs for the reliability assessment of bridge systems (see Section 5.4), with a different spatial scale. However two main differences can be noted:

- BNs for an infrastructure system require the inclusion of a spatially distributed hazard layer, while a unique IM node is enough to represent the hazard for a single bridge system.
- While the identification of system failure modes for a given bridge usually leads to the construction of series subsystems of a reduced number of structural components (e.g. failure of at least one pier within the bridge), the system performance indicator of a given road network is based on more complex assemblies of damage events which do not strictly correspond to series or parallel subsystems. Moreover, a road network at the urban or regional level is usually composed of hundreds of vulnerable elements, thus generating a much larger problem than for a bridge system.

For the reasons above, additional modelling strategies have to be designed in order to build BNs that are able to deal with real-life network systems. The following subsections review the performance of some of the BN formulations that have been adopted in the literature, while a simulation-based hybrid formulation is also introduced.

7.2.1 Modelling of Spatially Distributed Hazard Intensities

In the case of seismic hazard, different types of BN modelling strategies have been proposed: Bensi et al. [2011] have introduced multiple models (e.g. point-source, finite-rupture, directivity effects, etc.), all of them accounting for the spatial correlation of the ground-motion field. Franchin and Laura [2014] have also introduced a BN formulation where the seismic hazard is first evaluated over a grid, before being interpolated at the

vulnerable sites, while accounting for the soil amplification effects. The point-source BN model from Bensi et al. [2011] has been adopted in the present study for simplification purposes: it has the merit of generating less BN nodes, which leaves more latitude to the study of the BN part that deals with the prediction of the system performance given the states of the components.

The different models and results are demonstrated on the simple example network that is presented in Figure 7.1. It has been originally introduced by Kang and Lee [2015] as a water pipe network, with two reservoirs (i.e. sources) and one outflow location (i.e. sink). This layout has been selected in order to represent a hypothetical road network with two origin points and one destination, while the edges represent vulnerable road segments or bridges. A seismic source area is assumed to be located around the North-West of the network, from which epicentre locations can be sampled. The magnitude range is assumed to be bounded between 4.5 and 6.5, while the distribution follows a Gutenberg-Richter law. Other hazards such as ground failure or flood have not been considered here in order to concentrate on the complexity of the BN in terms of components-system interactions.

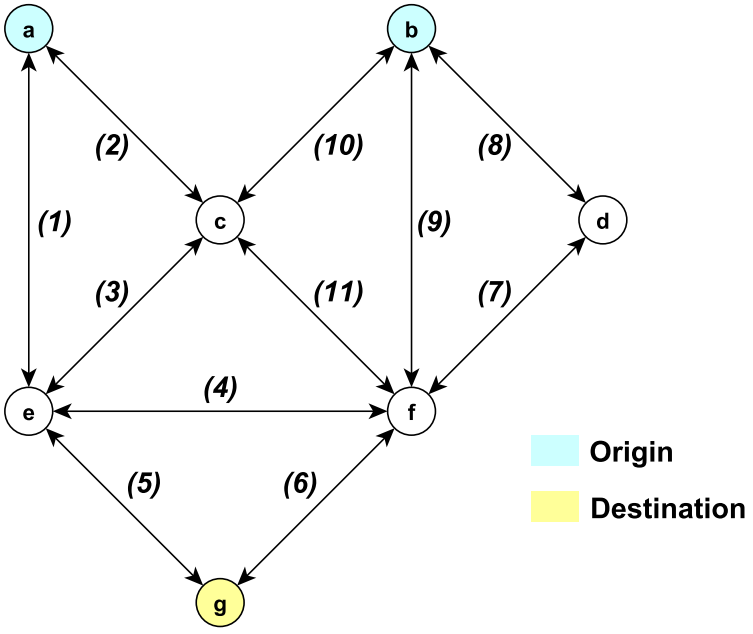

FIGURE 7.1: Layout of the example network, adapted from Kang and Lee [2015].

The distributed seismic hazard part of the BN for the 11 vulnerable components is represented in Figure 7.2. The different BN nodes have the following meaning:

- **M**: magnitude range of the possible earthquake events;
- **Epi**: discretized locations of the epicentre of the earthquake events;
- $\mathbf{R_i}$: epicentral distance from the infrastructure elements;
- $\mathbf{Q_i}$: median PGA values at the sites of interest, without any uncertainty terms;
- **U** and $\mathbf{V_i}$: nodes containing the standard normal distribution in order to represent the spatial correlation of the seismic hazard at the 11 vulnerable sites;
- $\mathbf{e_i}$: intra-event uncertainty term, specific to each element, due to the spatial correlation assumption;
- **n**: inter-event uncertainty term, common to all elements;
- $\mathbf{S_i}$: final PGA values at the sites of interest, including intra- and inter-event uncertainties;
- $\mathbf{C_i}$: damage states of the infrastructure elements.

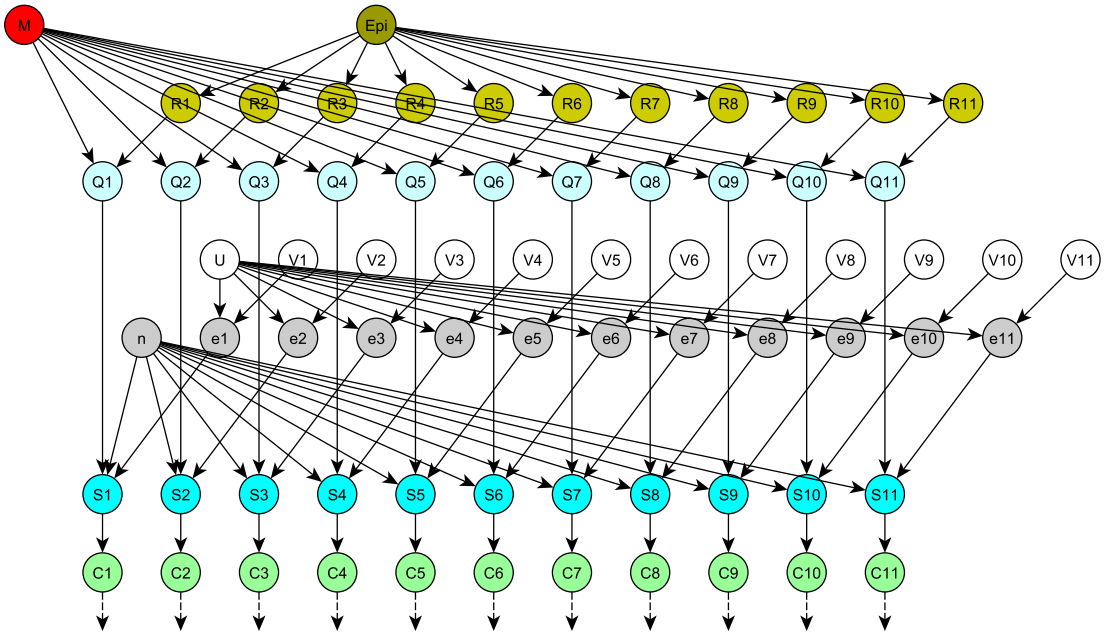

FIGURE 7.2: Seismic hazard layer of the BN for the example network.

The spatial correlation of the ground-motion field is ensured by the inclusion of the intra-event variability terms $\mathbf{e_i}$, which are modelled from a spatially correlated random field. As stated by Bensi et al. [2011], the generation of a Gaussian random field would

require a densely connected BN in order to show the dependency of all sites with each other. Therefore a Dunnett-Sobel class of random variables [Dunnett and Sobel, 1955] has been adopted as an approximation, so that the correlation structure between the intra-event terms at the vulnerable sites is emulated by the **U** and $\mathbf{V}_i$ nodes.

7.2.2 BN Formulations for Exact Inference

Exact inference algorithms such as junction tree or variable elimination should be the first choice when solving a BN because they directly allow the quantification of exact probabilities for tail events (e.g. high-consequence low-probability), as opposed to sampling algorithms that yield approximate solutions. However, as detailed in Subsection 5.3.2, the junction tree algorithm is based on the assembly of matrices of potentials for the different cliques of nodes, which may lead to memory problems for large BNs. Therefore various BN formulations may be introduced and reviewed, with the objective of enabling the efficient inference of large and complex systems.

7.2.2.1 Naive formulation

The most intuitive formulation is the construction of a converging structure (i.e. also referred to as naive formulation), where all the vulnerable elements are converging towards the single system node that represents the performance measure of the infrastructure. While straightforward to assemble and understand, this formulation is mainly hindered by the size of the system CPT, which grows exponentially with the number of components. For instance, if elements with binary states are considered, n elements in the network will result in a system CPT size of 2^{n+1} lines. Using the example network that has been introduced in the previous subsection, the corresponding naive formulation is represented in Figure 7.3.

7.2.2.2 MLS formulation

If the selected performance indicator is solely based on the connectivity of the network, then it is possible to decompose the system into subsystems of strictly parallel or series elements, thus reducing the system to a more straightforward problem. For instance,

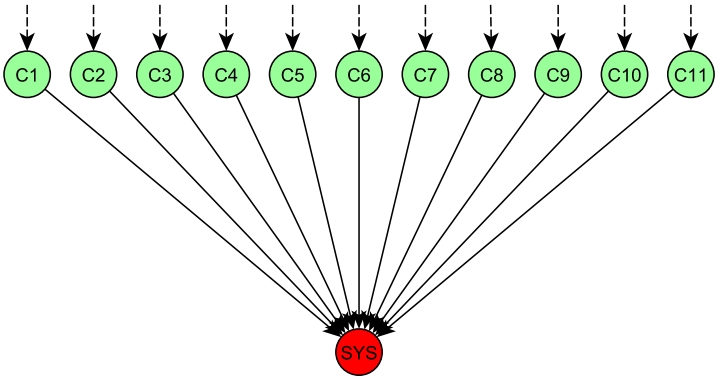

FIGURE 7.3: Naive formulation for the system performance assessment of the example network. The hazard layer has been left out for more clarity.

Bensi et al. [2013] have introduced the concept of Mininum Link Sets (MLSs) and Minimum Cut Sets (MCSs). In a given system, an MLS (respectively an MCS) represents the smallest set of components where the joint survival (respectively the failure) of the components induces the survival (respectively the failure) of the system. Therefore the identification of all MLSs (respectively MCSs) results in the decomposition of the given system into parallel (respectively in-series) sub-systems of in-series (respectively parallel) components.

A preliminary step of this MLS formulation consists in the identification of all MLSs within a system, since failure to provide an exhaustive inventory of the MLSs will result in an underestimation of the performance of the system (i.e. overestimation of the system's losses). Therefore, in the present work, a recursive algorithm has been developed and implemented in order to find all the MLSs that ensure the connection between a source and a sink in a given system. In the scope of this study, network edges (e.g. road segments, bridges, etc.) are considered as the vulnerable components, even though the MLS-finding algorithm can be easily extended to vulnerable nodes as well. The algorithm has been designed in a way that both cases of directed and undirected edges can be treated, thus generalizing its application to several types of network systems (e.g. road network, water supply system, electric power network, etc.). The main stages of the MLS-finding algorithm are summarized in Figure 7.4: its structure is based on the fact that identifying the shortest path between two vertices is a straightforward operation, which is applied to updated versions of the network when the different edges composing the shortest path are successively removed.

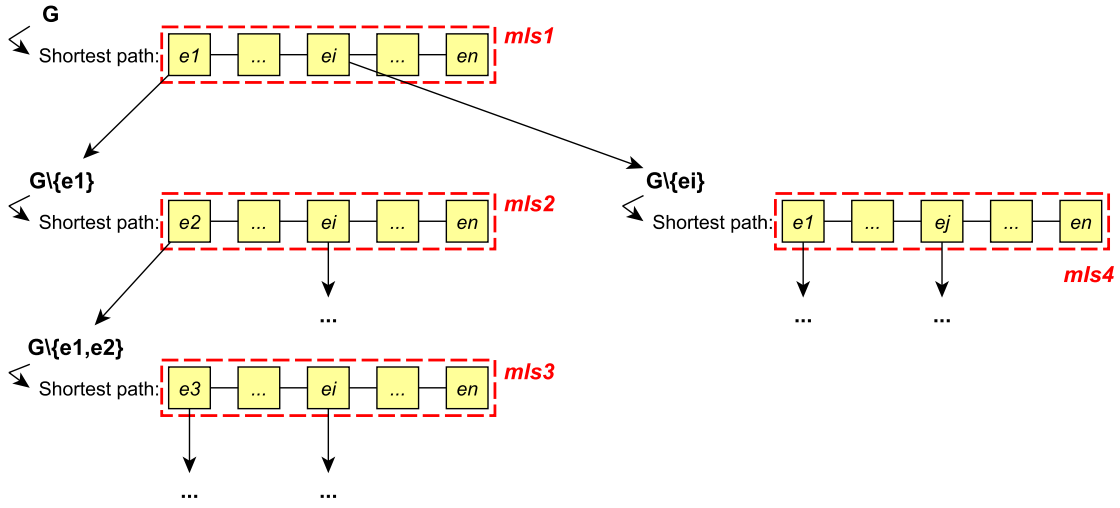

FIGURE 7.4: Summary of the recursive MLS-finding algorithm for a graph **G** composed of a series of edges e_i, leading to the successive identification of MLS chains.

The recursive nature of the algorithm implies that the computational load increases exponentially with the size and complexity of the network. For instance, if the initial shortest path contains a long chain of components, the number of edge removal combinations to be explored may become intractable. This limitation may be overcome by the preliminary identification of critical disjoint link sets or cut sets, as proposed by Lim and Song [2012]. When applied to the example network in Figure 7.1, the algorithm has identified 13 MLSs for the a-g connectivity and 14 MLSs for the b-g connectivity. The MLSs for the first origin-destination couple (a-g) are detailed in Table 7.1.

TABLE 7.1: MLSs identified for the a-g connectivity in the example network.

MLS	Edge numbers	MLS	Edge numbers
mls_1	$[1, 5]$	mls_8	$[2, 10, 7, 8, 6]$
mls_2	$[1, 4, 6]$	mls_9	$[2, 10, 9, 4, 5]$
mls_3	$[2, 3, 5]$	mls_{10}	$[2, 10, 7, 8, 4, 5]$
mls_4	$[2, 3, 4, 6]$	mls_{11}	$[1, 3, 10, 9, 6]$
mls_5	$[2, 11, 6]$	mls_{12}	$[1, 3, 10, 7, 8, 6]$
mls_6	$[1, 3, 11, 6]$	mls_{13}	$[2, 11, 4, 5]$
mls_7	$[2, 10, 9, 6]$		

The MLS formulation can then be applied to the BN, as shown in Figure 7.5. For simplification purposes, only the MLSs that represent the a-g connectivity are represented, while the BN structure should be completed by the MLS formulation corresponding to the second origin-destination couple (b-g).

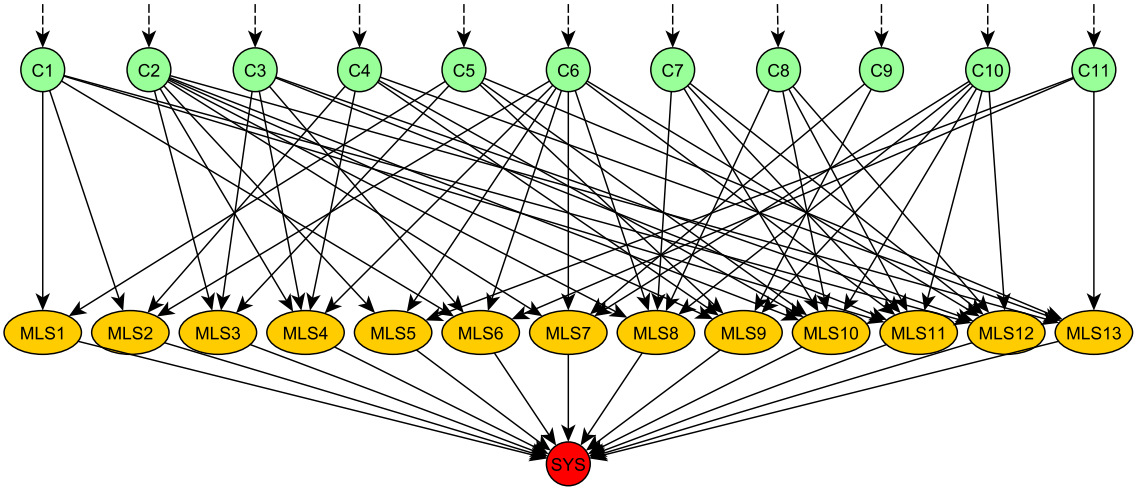

FIGURE 7.5: MLS formulation for the system performance assessment of the example network (connectivity between nodes a and g).

The MLS formulation allows the number of parent nodes to be reduced, since the studied system may be decomposed into smaller sub-systems. However, additional nodes $\mathbf{MLS_i}$ need to be added in order to represent the survival or failure of all MLSs. This formulation has the merit of generating smaller CPTs, even though it requires additional steps to identify the MLSs and build the corresponding BN structure.

7.2.2.3 Efficient MLS formulation

The MLS formulation detailed above has resulted in smaller CPTs for the MLS nodes, instead of using a single CPT for the whole system. However, in the case that some MLSs contain many components, the same issue may arise, since a naive formulation is still used to represent the relation between the components and MLS nodes. Therefore advantage can be taken from the fact that each MLS is a series sub-system of components, which can be represented as a chain structure instead of a naive formulation. As suggested by Bensi et al. [2013], this efficient MLS formulation considers that each MLS constitute a survival path sequence (SPS) where all components are represented by survival path events (SPEs). $\mathbf{Es_i}$ nodes are then introduced in order to represent SPEs within each MLS: the logic behind this formulation is that successive checks are performed along the SPS in order to ensure that a given SPE $\mathbf{Es_i}$ is still in survival state, based on the state of the previous SPEs and the state of the new component that is added to the chain.

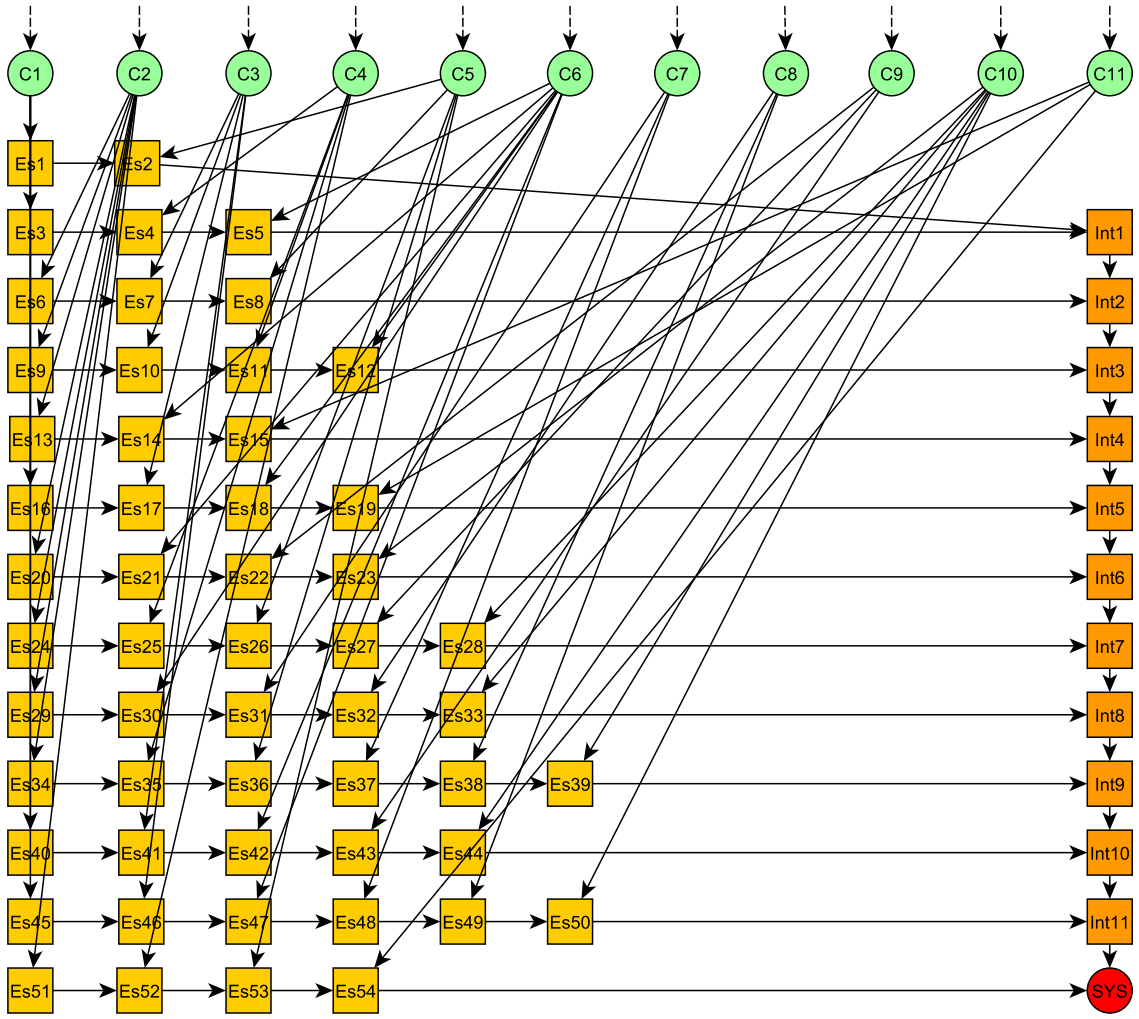

FIGURE 7.6: Efficient MLS formulation for the system performance assessment of the example network (connection between nodes a and g).

On the other hand, a similar chain structure may be assembled to represent the transition from the SPE nodes to the global system node. This structure becomes necessary when the given system has to be decomposed into many MLSs. To this end, intermediate nodes $\mathbf{Int_i}$ are introduced: they follow the same principles as the $\mathbf{Es_i}$ nodes, except that they represent a parallel assembly of the MLSs. Finally, this efficient MLS formulation is represented in Figure 7.6, when applied to the previous example network.

It can be seen that the efficient MLS formulation strictly limits the number of parent nodes to 2, which generates very small CPTs (i.e. 8 elements in the case of binary states). However, this formulation comes at the cost of the number of nodes that have to be modelled: 54 SPE nodes are required, even though only 11 components are considered.

This is due to the fact that most components contribute to several MLSs at the same time, thus leading to multiple instances of SPE nodes.

7.2.2.4 Efficient MLS formulation with coalesced SPSs

In order to reduce the number of instances of SPE nodes, Bensi et al. [2013] have introduced an optimization process that aims to coalesce the different SPSs so that a minimum of SPE instances are required. In the present work, this optimization step has been implemented as an algorithm, whose main steps are summarized in Figure 7.7.

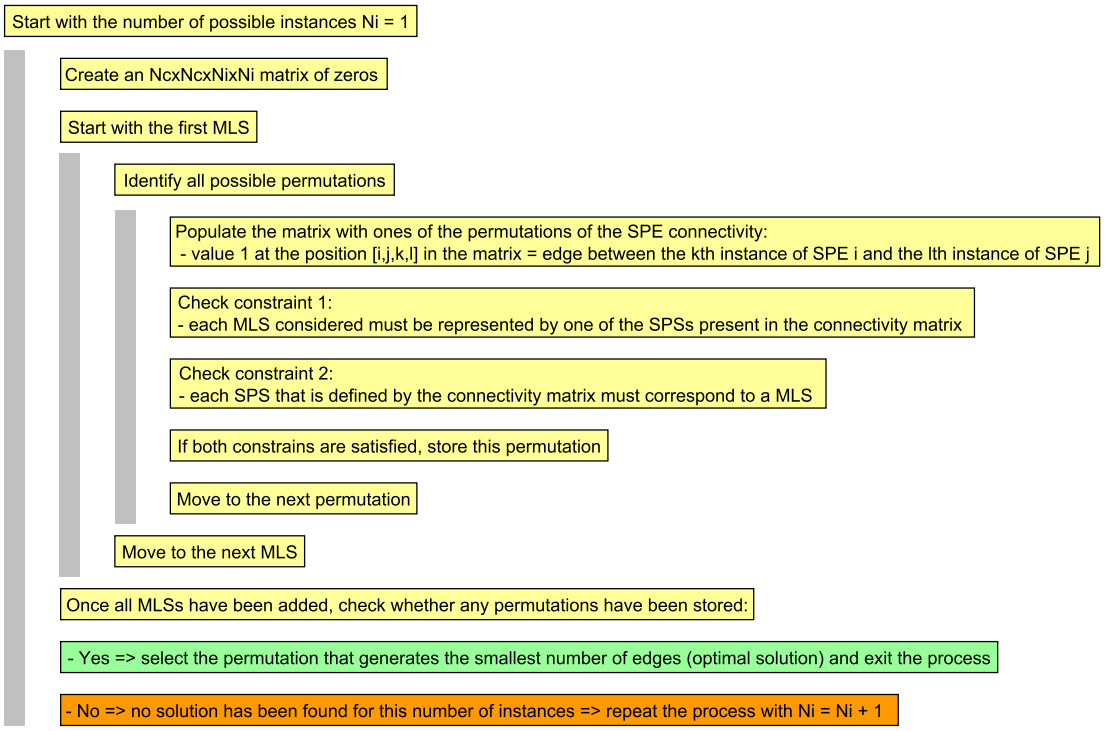

FIGURE 7.7: Main steps of the optimization algorithm of the SPE permutations. Nc represents the number of components that are involved in the MLSs.

The main issue of the optimization algorithm is that the number of possible permutations increases exponentially with the number of instances and the number of components within the MLSs, potentially leading to high computation times before the actual start of the Bayesian inference process. Therefore Bensi et al. [2013] propose the use of two heuristics that aims at reducing the size of the problem space:

- Heuristic 1 consists in the identification and creation of super-components based on the composition of the MLSs. Two types of super-components may be generated:

class A super-components (in series) identify groups of components that always appear together in the MLSs, and class B super-components (in parallel) identify components that appear in different MLSs while sharing these MLSs with the same set of other components.

- Heuristic 2 blocks the permutation order of some components within the MLSs, based on their occurrence frequency in the MLSs. This heuristic allows the number of possible permutations to be reduced, even though it may prevent the identification of the most optimal permutation solution.

This efficient MLS formulation with coalesced SPSs is also built in the case of the example network. First, heuristic 1 is applied to the MLSs in Table 7.1, in order to reduce the number of elements to be permuted. As a result, the simplified set of MLSs is detailed in Table 7.2: only 10 MLSs remain out of the original 13, since the class B super-component $\mathrm{SC2} = \{9, \mathrm{SC1}\}$ has been generated, where SC1 is a class A super-component containing the components $\{7, 8\}$.

TABLE 7.2: MLSs of the example network (a-g connectivity) after the application of heuristic 1.

MLS	Edge numbers	MLS	Edge numbers
mls_1	$[1, 5]$	mls_6	$[2, 4, 5, 11]$
mls_2	$[2, 3, 5]$	mls_7	$[2, 3, 4, 6]$
mls_3	$[2, 6, 11]$	mls_8	$[1, 4, 6]$
mls_4	$[2, 6, 10, \mathrm{SC2}]$	mls_9	$[1, 3, 6, 11]$
mls_5	$[2, 4, 5, 10, \mathrm{SC2}]$	mls_{10}	$[1, 3, 6, 10, \mathrm{SC2}]$

The optimization algorithm can then be applied and the optimal permutation of SPEs is shown in Figure 7.8. A maximum number of $N_i = 3$ instances has been required, for a total of 16 SPEs nodes: it can be easily checked that all the chains of SPE nodes correspond to the MLSs in Table 7.2.

While this formulation leads to a drastic reduction of the number of SPE nodes, it can be argued that the computational load is transferred to the execution of the optimization algorithm, where the size of the permutation space has an exponential increase rate. For instance, in the example network considered, the optimization of the SPE permutations for the a and g connectivity has required several hours of computation. Bensi et al. [2013] state that the implementation of the optimization process into the Tomlab toolbox [Holmström, 2008] dramatically reduces the computation times, even though the

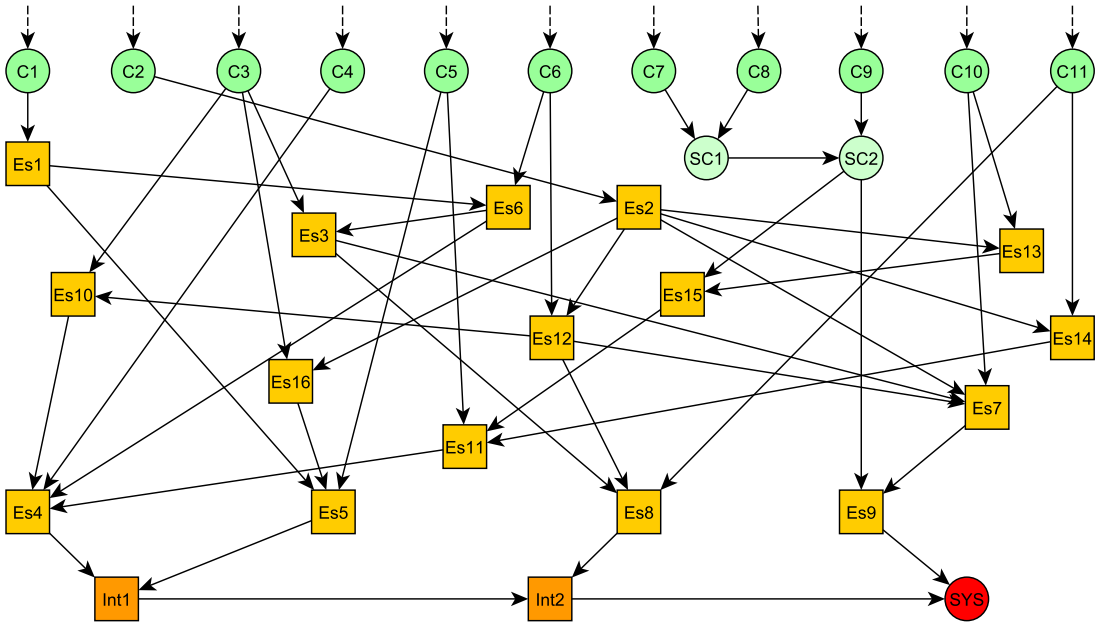

FIGURE 7.8: Efficient MLS formulation with coalesced SPSs for the system performance assessment of the example network (connectivity between nodes a and g).

execution of the optimization algorithm does not seem feasible for large and complex systems (e.g. MLSs containing hundreds of elements).

7.2.2.5 Naive formulation with compression algorithm

As an alternative to the MLS-based formulations, Tien and Der Kiureghian [2015] have introduced a compression algorithm that is applied to the system CPT when the naive formulation is used. The authors take advantage of the repeating structure of the CPT to jointly apply two compression methods (see Figure 7.9):

- Algorithm 1: representation of the data by consecutive bits of the same value (i.e. runs).
- Algorithm 2: for mixed values that cannot be efficiently compressed for algorithm 1, a Lempel-Ziv algorithm [Ziv and Lempel, 1977] based on the encoding of recurring phrases is applied.

In the example provided by Tien and Der Kiureghian [2015], only system and component nodes are considered, without the hazard assessment part. Consequently, these variables

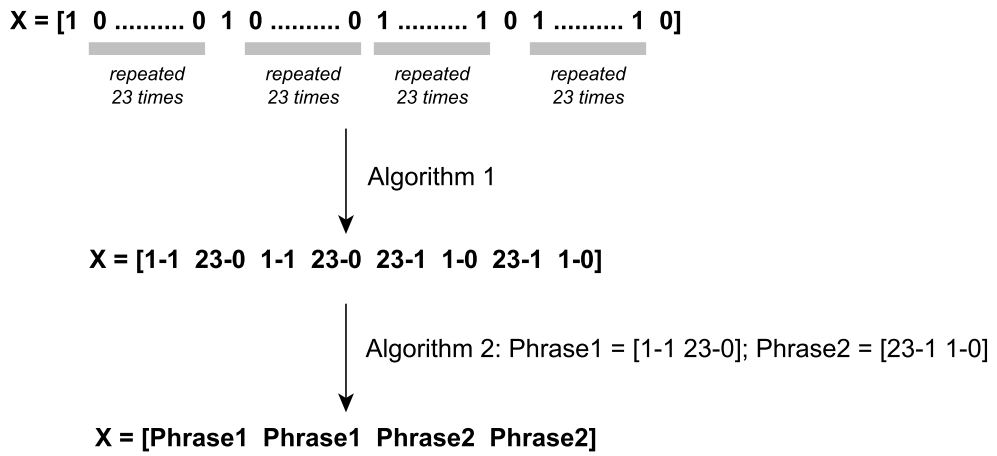

FIGURE 7.9: Compression of a vector with the two algorithms proposed by Tien and Der Kiureghian [2015].

belong to a single clique and the variable elimination algorithm (i.e. bucket elimination) is used to perform the inference. This enables to sequentially update the compressed CPT when a variable is eliminated. The authors have shown that the memory storage space only increases linearly with the compression algorithm, whereas the computation time due the compression operations has an exponential rate with respect to the number of components. Tien and Der Kiureghian [2015] have partially solved the computational time issue through a careful ordering of the component variables within the system CPT and by taking advantage of single-component MLSs (i.e. single components whose failure leads to the system failure).

However, the compression algorithm has only been demonstrated for a trivial BN structure where the hazard assessment has been left out: in the case of more generic systems, such as the ones presented in this study, the variable elimination algorithm may not be used any more and the ordering of the variables becomes less transparent. Moreover, seismic intensity nodes have to be added to the clique containing the system nodes, which may complicate the structure of the table of potentials and dramatically reduce the efficiency of the compression algorithm. It is also unclear how sum and product operations can be performed on the compressed matrices without requiring preliminary decompression/recompression operations. Therefore the compression algorithm approach has not been considered in the following benchmark, pending further investigation of the aforementioned issues.

7.2.2.6 Summary and performance of the various formulations

The various BN formulations detailed above are benchmarked with the problem presented in Figure 7.1. The global system performance is assumed to be represented by the single connectivity loss (SCL) [Poljansek et al., 2012], which represents the ratio of the remaining number of connected sources after the event over the initial number of connected sources, averaged over the sinks. In our example, the two sources a and b are supposed to be connected to a single sink g, which leads to the following expression of SCL:

$$\text{SCL} = 1 - \frac{\delta_a + \delta_b}{2} \tag{7.1}$$

where the δ symbol takes the value 1 if the source is still connected, and 0 if not. Therefore it can be seen that, in this simple example, SCL can only take three values, namely 0, 0.5 and 1.

It is proposed to test the different BN formulations with two types of inference problems:

- Forward analysis: updating of the distribution of SCL given the observation of the highest magnitude earthquake events;
- Backward analysis: updating of the distribution of magnitude given the total disconnection of network (i.e. SCL = 1).

The results of the Bayesian updating are presented in Figure 7.10. It has been checked that the results are identical for all BN formulations, which confirms the validity of these constructions and the ability of the exact inference algorithm (i.e. junction tree) to yield accurate probability distributions. The prior distribution represents the distribution of a variable when no evidence has been entered into the BN (e.g. magnitude distribution that is assumed for the area), while the posterior distribution represents the updated distribution once one or more evidences are propagated in the BN.

However, the performance of these formulations in terms of complexity and computation time is not equal, as shown in Table 7.3. The results are quite counter-intuitive, since the inference performance seems to degrade as more elaborate BN formulations are applied.

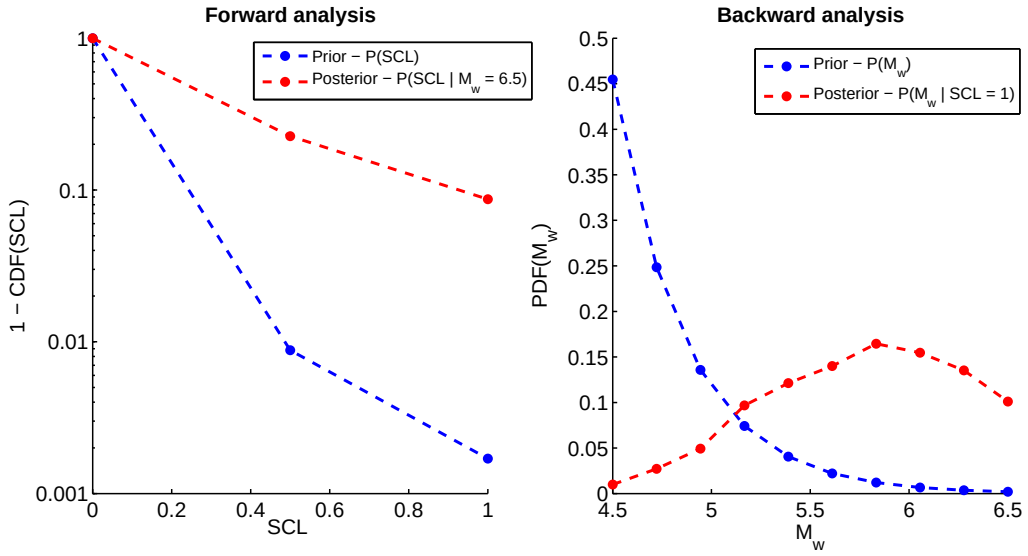

FIGURE 7.10: Prior and posterior distributions for the forward (left) and backward (right) analyses.

This observation can actually be explained by the fact that the inference time is closely related to the size of the cliques, while the number of nodes or the size of the CPTs does not seem to play a significant role, as shown in the table.

TABLE 7.3: Comparison of the performance of the different BN formulations.

Formulation	♯ of SPE and intermediate nodes	Maximum clique size	Inference time Forward	Backward
Naive	–	24 576 000	0.4 s	3.5 s
MLS	27	24 576 000	0.6 s	3.6 s
Efficient MLS	132	24 576 000	0.6 s	3.6 s
Efficient MLS (coalesced)	34	196 608 000	2.1 s	17.5 s

As a result, the MLS-based formulations, which aim mainly at reducing the size of CPTs, have no impact on the inference time. It appears that the triangulation of the BN within the junction tree algorithm invariably leads to the same size of cliques, thus showing that some parts of the BN constitute a computational bottleneck that cannot be reduced, irrespective of the formulation that is adopted. A notable and disappointing exception is the efficient MLS formulation with coalesced SPSs, where the inference time appears to be much longer. A possible reason for this is the greater connectivity level between the different SPE nodes, which tends to create a more complex structure that induces larger cliques during the triangulation. The issue of the partial optimization of the elimination order (i.e. see Subsection 5.3.2) may also be highlighted by this observation, since applications to other network systems with different SPSs chains have shown that this formulation performs better than the simpler ones in some cases. Therefore it may be

concluded that MLS-based formulations do not necessarily provide better performances in terms of inference. At best, they guarantee the treatment of slightly larger networks than the naive formulation, which is quickly limited by the CPT size.

The review of the various BN formulations has highlighted the difficulty to find a modelling strategy that enables the effortless and straightforward assessment of real-life systems. Different types of computational bottlenecks can be found in each of the BN formulations, as summarized in Table 7.4:

- The size of CPTs is the most obvious issue, since these objects are directly manipulated when using the Bayes Net toolbox. This issue is the main motivation for the development of the MLS-based formulations.
- However, MLS-based formulations require the preliminary identification of MLSs, which can be a non-trivial and time consuming task for larger systems (i.e. recursive algorithm).
- The aggregation of SPE chains requires an initial optimization step to build up the coalesced SPSs that can lead to significant computation times, especially if numerous SPE instances are required.
- More than the size of CPTs, it appears that the main issue resides in the size of the cliques that are assembled. The clique size depends on the CPT size of the nodes (i.e. number of parents and discrete states) and on the elimination order, which is much more difficult to predict and quantify, since it is linked to the more global connectivity of the 'vicinity' of the nodes.
- Finally, the compression algorithm proposed by Tien and Der Kiureghian [2015] is also based on the identification of MLSs in order to sequentially construct the system CPT, while the compression operations end up converting memory storage space into high computation time.

The summary in Table 7.4 reveals that there is no straightforward BN formulation that is able to tackle large and complex systems. Each modelling strategy is hindered by one or more computational bottlenecks: the reduction of the size of CPTs or cliques invariably requires time-consuming preliminary steps such as the identification of MLSs or the optimization of SPSs. Moreover, it should be noted that the example network

TABLE 7.4: Qualitative description of the main criticalities that are involved in the various BN formulations.

Formulation	CPT size	MLS identification	SPE optimization	Compression	Inference (clique size)
Naive	X				X
Naive with compression		X		X	
MLS	X	X			X
Efficient MLS		X			X
Efficient MLS (coalesced)		X	X		X

presented here is based on components with only binary states and that the selected performance indicator is solely based on the system connectivity. Therefore, the objective of assessing more complex systems with realistic performance indicators based on serviceability cannot be reached by the single use of the BN formulations detailed above.

7.2.3 BN Formulations based on Physical Simulations

The work presented in this sub-section is the outcome of a collaboration with University of Roma La Sapienza [Cavalieri et al., 2017], which has been conducted in order to improve the applicability of BNs to real-life systems.

7.2.3.1 Outline of the Proposed Method

Since the aforementioned BN formulations for exact inference are bound to present some computational bottlenecks and are limited to the prediction of connectivity metrics, it is proposed to take advantage of the versatility of simulation-based methods by developing a hybrid procedure. It is based on the following steps (see Figure 7.11):

1. Monte-Carlo simulation of n runs of damage scenarios on the considered infrastructure system: for instance, the OOFIMS tool may be used to compute the system performance of a given network, starting from the probability of occurrence of hazard source events.

2. Computation of either connectivity- or capacity-based system performance indicators for the n runs.

3. Computation of the correlation coefficients ρ_i between the component damage events and the system performance indicator, for $i = 1 \cdots k$ components.

4. Selection of a correlation threshold ρ_{th} below which the components are considered to be insufficiently correlated with the system's response.

5. Construction of a BN structure with a naive formulation, where only the components that are well correlated (i.e. $\rho_i \geq \rho_{th}$) contribute to the system node.

6. Construction of the system CPT by counting the simulation results (i.e. proportion of system failures for each damage configuration of the selected components).

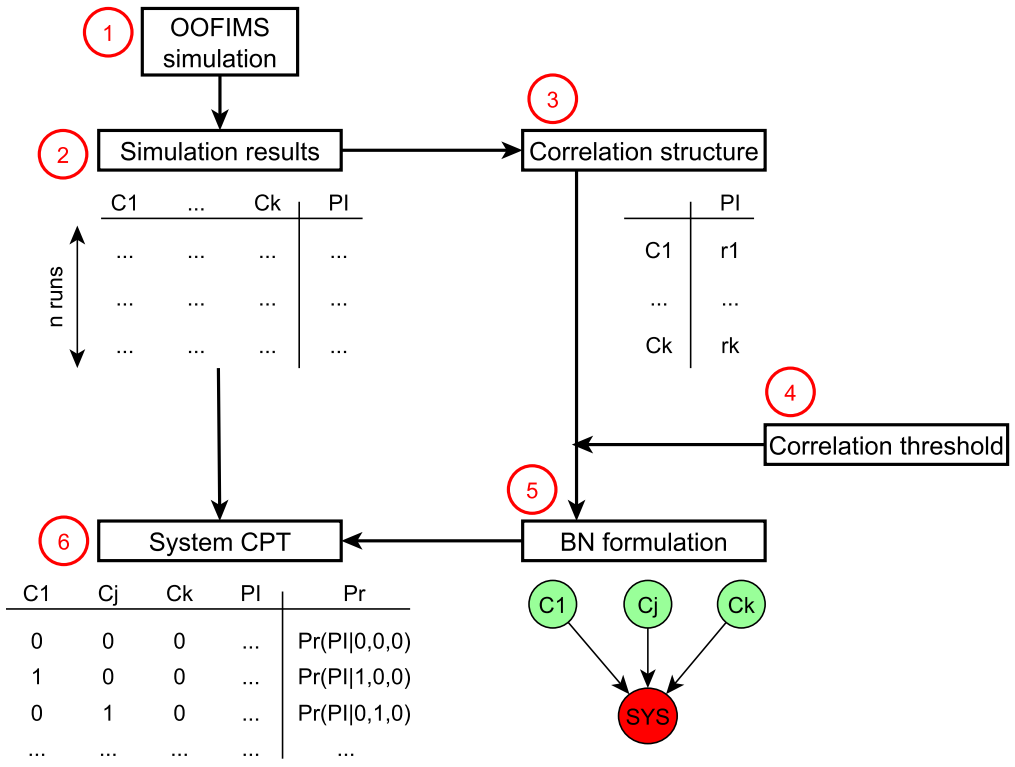

FIGURE 7.11: Outline of the t-Naive formulation.

This approach, later referred to as a thrifty-naive (t-Naive) formulation, enables the development of a BN that only retains the most influential components, thus reducing the computation load. The ρ_{th} threshold is used to adjust the number of components that are considered in the analysis, which results from a trade-off between the computational load and the accuracy of the predictions. Further investigations on the adequate values of ρ_{th} for different types of systems and performance indicators are still needed.

A variant of the t-Naive formulation may also be considered in order to refine the results. It is based on the observation that most system performance indicators are aggregated from local performance indicators, such as the number of sources connected to a given

sink, the head ratio of a given water tank, or the travel time between an origin and a destination. Therefore a similar approach may be adopted, by evaluating the specific correlations of the components with respect to these local indicators. An exact BN formulation can then be designed in order to quantify the global indicators from the knowledge of the local measures. It is likely that most components have a direct impact on a few local performance measures, while having less influence on the rest of the system. Therefore this variant, referred to as second-order t-Naive formulation, may be able to offer a better resolution of the loss distribution, while maintaining computational loads to an acceptable level.

7.2.3.2 Comparison with Exact Formulations

The t-Naive formulation is applied to the network layout that has been presented in Figure 7.1. Additional sinks and sources are now considered in order to add complexity to the system: nodes g and f are sinks, while nodes a, b and d are sources (see Figure 7.12). The layout is here assumed to represent a water-supply system, so that flow-based analyses are possible.

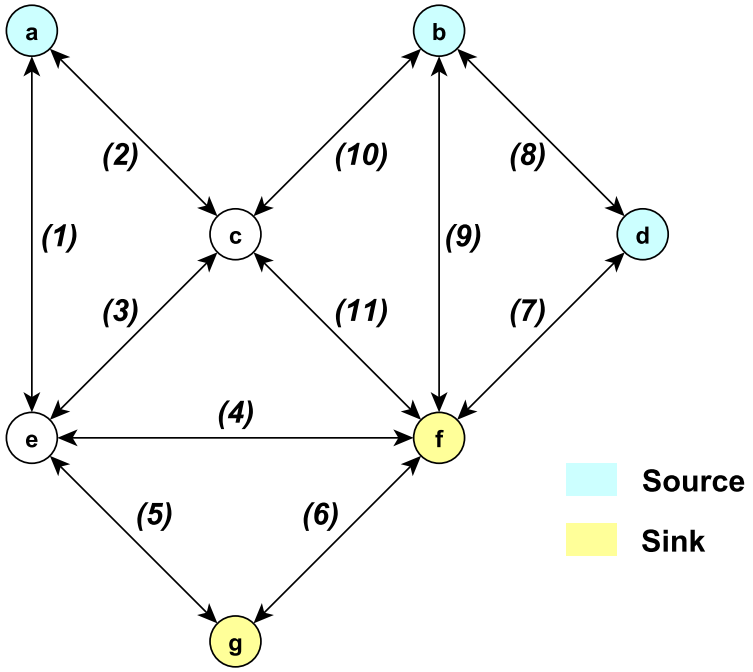

FIGURE 7.12: Layout of the example network with additional source and sink nodes, adapted from Kang and Lee [2015].

An OOFIMS simulation is then conducted with 10 000 runs, and two system performance indicators are computed:

- the Single Connectivity Loss (SCL);
- the System Serviceability Index (SSI), which is a flow-based metric [Vanzi, 2004] representing the averaged ratios of water heads at the sinks, after and before the hazard event.

For each of the two performance indicators, the correlation coefficients with the component damage events is then estimated and a cut-off threshold is chosen in order to significantly reduce the number of components: a threshold $\rho_{th} = 0.6$ is arbitrarily chosen, and any component C_i that is correlated to the performance indicator with a correlation coefficient $\rho_i \geq \rho_{th}$ is kept for the Bayesian analysis. As a result, components #1, 2, 7 and 9 are selected for the prediction of SCL, while components #4, 7, 9 and 11 are the most influential for the determination of SSI. The lists of components are not exactly the same for both performance indicators, thus reflecting the differences of accuracy between connectivity- and capacity-based loss measures. The corresponding BN can then be constructed for the two performance indicators, as shown in Figure 7.13.

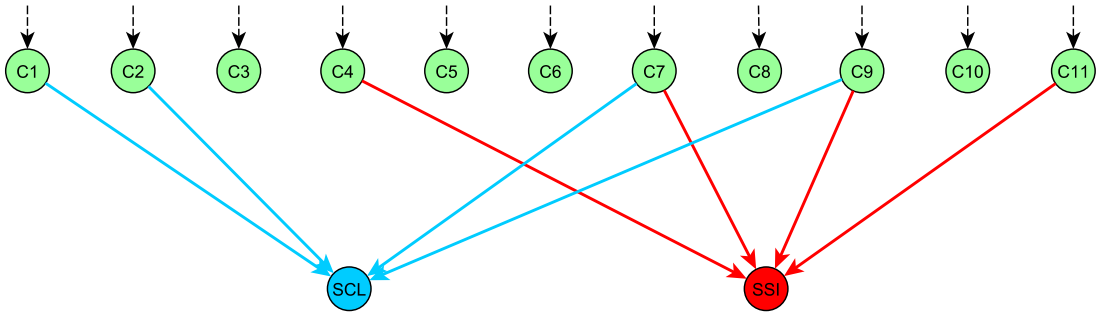

FIGURE 7.13: T-Naive formulation for the two performance indicators of the example network.

The second-order t-Naive formulation may also be designed by considering the correlations of the components with the local performance measure of each sink (i.e. water head ratio or number of connected sources). Therefore intermediate nodes **I** and **J** are introduced in order to represent the local measures (at sinks g and f) that are needed for the computation of SCL and SSI, respectively. The new BN formulation in Figure 7.14

shows that this refinement in scale enables new components to be taken into account, while the size of the system CPTs remains reasonable.

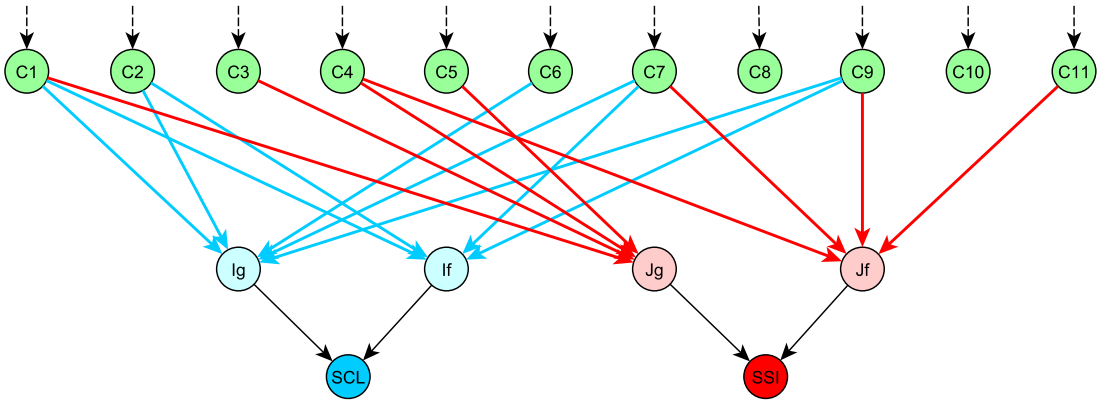

FIGURE 7.14: Second-order t-Naive formulation for the two performance indicators of the example network.

The efficiency and accuracy of this hybrid approach is then tested by running two inference cases on the example network:

- Bayesian updating of the magnitude distribution and of the IM distribution at component C7, given full connectivity loss (i.e. SCL = 1);
- Bayesian updating of the magnitude distribution and of the IM distribution at component C7, given severe serviceability loss (i.e. SSI < 20%).

Different BN formulations are benchmarked, such as the exact inference with the efficient MLS formulation, the hybrid method with all components (i.e. $\rho_{th} = 0$, referred to as naive formulation from now on), and the t-Naive formulations (first- and second-order).

The posterior distributions represented in Figure 7.15 demonstrate the ability of the t-Naive formulations to emulate the results of the exact inference, at least partially. Applying a cut-off threshold to reduce the number of components does not seem to have a significant impact on the accuracy, however it appears that the second-order t-Naive formulation is able to follow more closely the full naive formulation. The results highlight once again the need to consider flow- or capacity-based performance indicators: a serviceability index below 20% require lower levels of magnitude or PGA than when SCL is used as the loss metric.

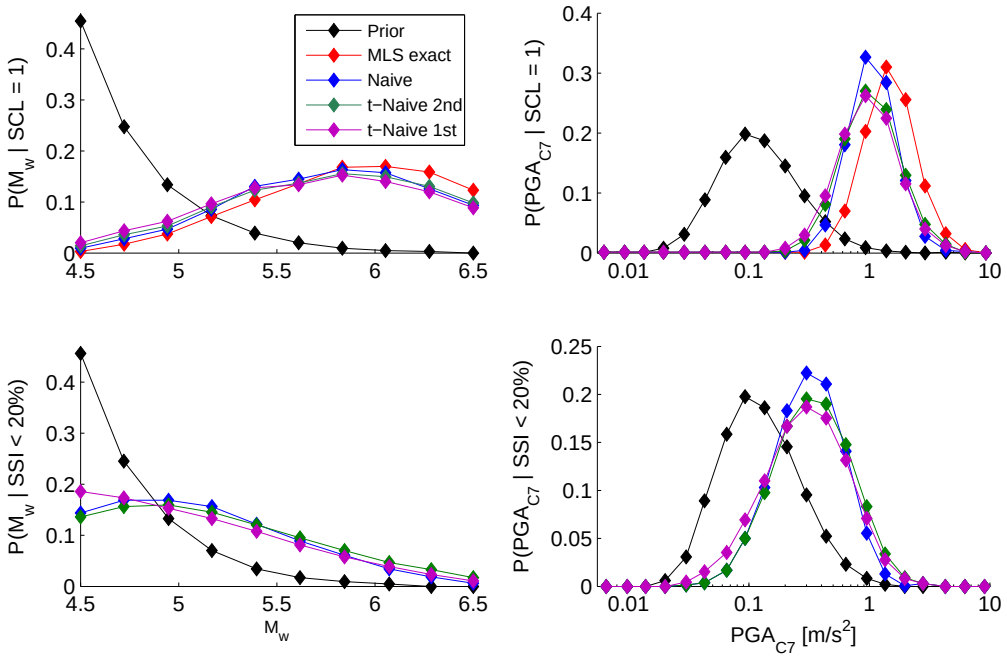

FIGURE 7.15: Posterior distribution of the selected variables, based on the different BN formulations.

TABLE 7.5: Computation time (in seconds) of the different BN formulations.

Evidence	SCL = 1		SSI < 20%	
Formulation	M_w	PGA_{C7}	M_w	PGA_{C7}
Efficient MLS (coalesced)	9.0	9.1	–	–
Naive	26.9	25.9	26.0	26.7
t-Naive 1st	3.3	3.2	3.3	3.2
t-Naive 2nd	2.9	2.9	2.9	2.9

The computation time taken by the different inference operations is detailed in Table 7.5. The t-Naive formulations represent a substantial gain in terms of computational loads in all cases. The duration of the OOFIMS simulations should still be taken into account, however it may be argued that the simulations are only run once in order to generate the BN structure. The preliminary analyses of this hybrid approach are encouraging, even though more in-depth investigations should be conducted on the role of the correlation threshold or on the way the OOFIMS simulations may influence the accuracy of the results.

7.3 Application: Multi-Risk Assessment of a Simplifed Road Network

The theoretical concepts described in the previous section are applied to a virtual proof-of-concept example, in order to demonstrate the various steps involved and to estimate which uncertainty sources are the most influential.

7.3.1 Characterization of the virtual proof-of-concept example

The virtual proof-of-concept example is presented in terms of asset types, network topology and potential hazards.

7.3.1.1 General presentation

A hypothetical application is proposed in order to demonstrate the applicability of BN modelling in the context of multi-risk analyses and uncertainty modelling. Due to the difficulty to obtain reliable data on infrastructure elements and to find a well characterized area exposed to multiple hazards, it has been decided to assume a virtual case-study in order to have total control of the variables of interest. Since the aim of this exercise is limited to the feasibility study of the BN methods that have been detailed in the sections above, this assumption is acknowledged as long as the results are not considered as the outcome of an actual risk analysis.

The application site is arbitrarily located somewhere around Northern Central Italy. A virtual road network is imagined, with the following components (see Figure 7.16):

- Plain road segments, connecting B1 to B3, B2 to B3, B2 to C2 and B3 to C1;
- A road on an embankment, connecting B1 to B2 and B1 to C3;
- A road along a slope, on the B2-B3 segment;
- Three bridges (B1, B2, B3): they are assumed to be identical structures, with a span length of 48.8 m (see bridge model in Section 4.2) over two river streams (in blue in Figure 7.16). The arrows show the direction of flow of the rivers

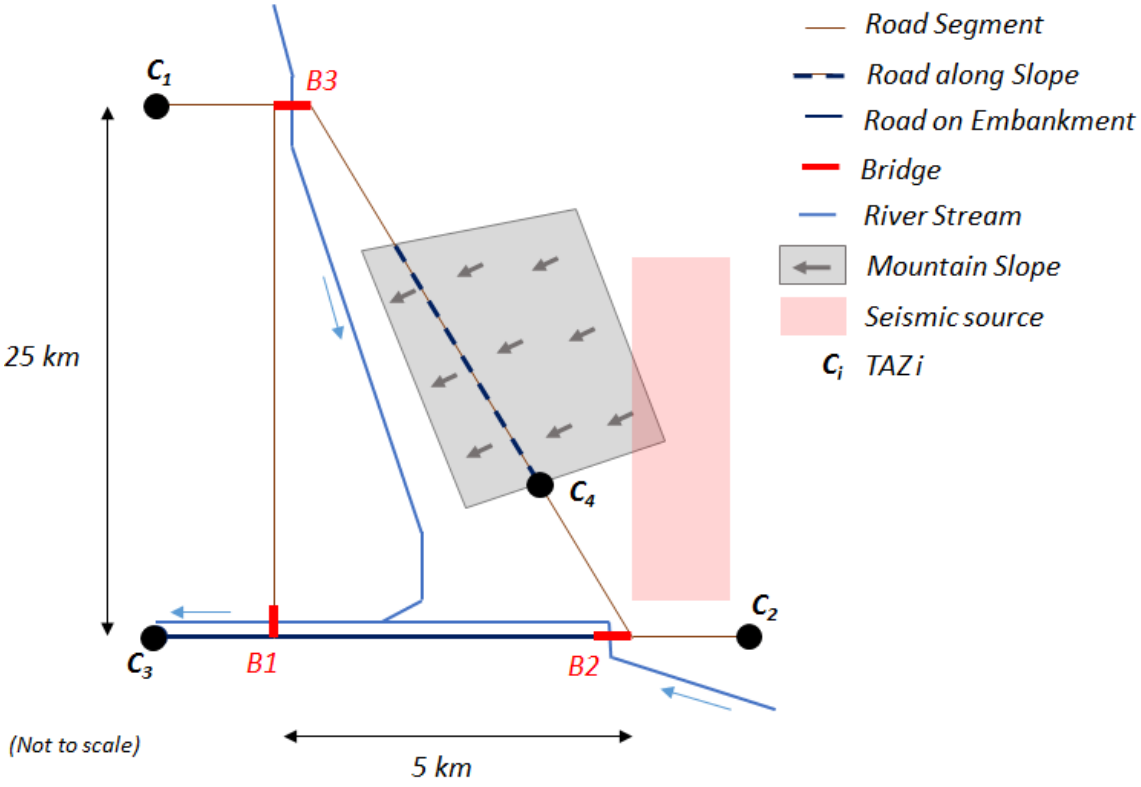

FIGURE 7.16: Layout of the proposed virtual application, with its different components.

with a larger flow discharge under bridge B1. More detail about this is given in Subsection 7.3.2.1.

- Four points of interest (C1, C2, C3, C4): they can be considered as hospitals, cities or exits/entrances to the network, also referred to as Traffic Analysis Zones (TAZs).

7.3.1.2 Network Topology

The topology of this simplified road network may be schematized as represented in Figure 7.17.

The graph and the attributes of its nodes and edges can also be represented in tabular form (see Tables 7.6 and 7.7). An undirected graph is assumed for this road network, meaning that each edge can be travelled in both directions.

Only the edges are considered as vulnerable in the proposed example, since the nodes may be seen as virtual objects representing the TAZs (i.e. traffic analysis zones) of the network or the extremities of edges (i.e. intersections). Therefore the MLSs between

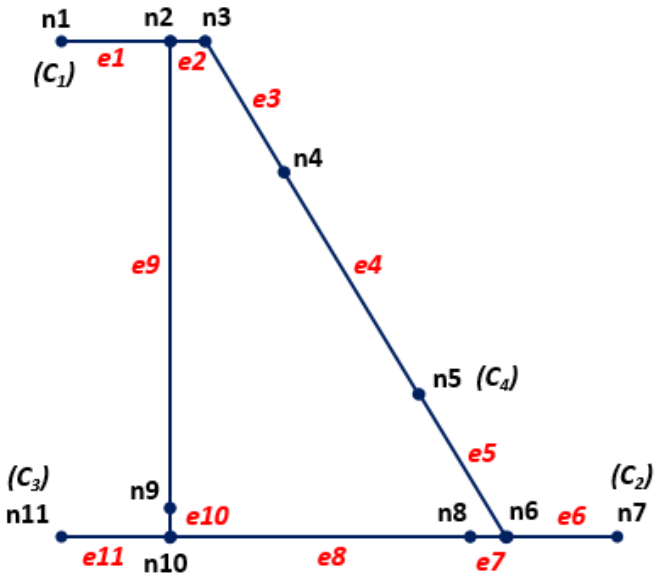

FIGURE 7.17: Topology of the proposed network. Edge numbers are represented in red, and nodes numbers in black.

TABLE 7.6: Location and description of the nodes composing the graph.

Node number	Longitude	Latitude	Description
1	11.1794	44.2753	TAZ 1
2	11.2000	44.2753	Intersection
3	11.2006	44.2753	Intersection
4	11.2156	44.2212	Intersection
5	11.2472	44.1073	TAZ 4
6	11.2631	44.0500	Intersection
7	11.3411	44.0500	TAZ 2
8	11.2625	44.0500	Intersection
9	11.2000	44.0506	Intersection
10	11.2000	44.0500	Intersection
11	11.1836	44.0446	TAZ 3

each couple of TAZs are represented by enumerating the list of travelled edges only (see Table 7.8). In the present example, it is assumed that TAZs #3 and #4 are sources (i.e. origins), while TAZs #1 and #2 are potential sinks (i.e. destinations). This enables the representation of the corresponding origin-destination matrix, along with the MLSs that are associated with each travel, as shown in Table 7.8.

7.3.1.3 Hazard Types and Potential Damage Modes

The following hazard events are considered in the application:

- Earthquakes: the three bridges are assumed to be susceptible to seismic loading.

TABLE 7.7: Connectivity and description of the edges composing the graph.

Edge number	Start node	End node	Description
1	1	2	Road segment
2	2	3	Bridge B3
3	3	4	Road segment
4	4	5	Road along slope
5	5	6	Road segment
6	6	7	Road segment
7	6	8	Bridge B2
8	8	10	Road on embankment
9	2	9	Road segment
10	9	10	Bridge B1
11	10	11	Road on embankment

TABLE 7.8: Edge numbers composing the different MLSs for all inter-TAZ travels.

Origin / Destination	TAZ #1	TAZ #2
TAZ #3	$[11, 10, 9, 1]$	$[11, 8, 7, 6]$
	$[11, 8, 7, 5, 4, 3, 2, 1]$	$[11, 10, 9, 2, 3, 4, 5, 6]$
TAZ #4	$[4, 3, 2, 1]$	$[5, 6]$
	$[5, 7, 8, 10, 9, 1]$	$[4, 3, 2, 9, 10, 8, 7, 6]$

- Landslides: they are expected to happen mainly on the mountain slope, due to the occurrence of earthquakes (ground shaking) or heavy rainfall (soil saturation). Ground failure (lateral spreading) could also happen at the level of the embankment road.
- Fluvial floods due to the presence of the river streams.
- Scour at bridges due to the fluvial floods.

7.3.2 Modelling Assumptions

Although the proposed approach is applied to a virtual example, the underlying models and input data are selected so that they are realistic and consistent with the type of hazards and infrastructure elements that may be found in Northern Central Italy.

7.3.2.1 Hazard Models

Hazard data and models are selected for the infrastructure area, using mainly the methods and results from D'Ayala et al. [2014b] developed within the framework of the INFRARISK project and described in detail in the following subsections.

a. Earthquakes

A single seismic source area is assumed, from which epicentre locations are randomly sampled: a rectangular shape is assumed, for which the geographical coordinates are detailed in Table 7.9.

TABLE 7.9: Coordinates of the assumed seismic source area.

Area corner	Longitude	Latitude
North-West	11.2700	44.1500
South-East	11.3100	44.0700

The distribution of the magnitude events is assumed to follow the truncated Gutenberg-Richter law, for which the activity parameters are selected from the SHARE source model [Woessner et al., 2015]. The seismic activity parameters are detailed in Table 7.10.

TABLE 7.10: Assumed seismic activity parameters for the source area.

Parameter		Value
Lower magnitude	M_{low}	4.0
Upper magnitude	M_{up}	7.5
Mean annual rate	λ_0	0.01
b-value	β	1.95

Finally, the distributed hazard intensities are computed thanks to the median of the three-branch GMPE that has been derived in Section 6.4.1, based on four original European GMPEs. The soil class of all vulnerable sites is assumed to correspond to the EC8 soil class B, except for ther embankment which is assumed to be soil class D and the road segments on soil class C (see Subsection 7.3.2.2).

b. Floods

The rational method is used for the estimation of flow discharge at the various bridge locations, as detailed in INFRARISK deliverable D3.1 [D'Ayala et al., 2014b]. The flow discharge Q is expressed as follows:

$$Q = \frac{C \cdot I \cdot A}{3.6} \cdot K_u \tag{7.2}$$

where C is the run-off coefficient of the drainage area, I is the maximum rainfall intensity during concentration time T_c, A is the catchment area and K_u is the uniformity coefficient [Ferrer, 1993, Temez, 1991].

The concentration time T_c may be obtained as a function of the length of the waterway between the bridge location and the catchment area, as well as the gradient of the main watercourse. The run-off coefficient is estimated through the following equation:

$$C = \frac{\left(\frac{P_d}{P_0} - 1\right) \cdot \left(\frac{P_d}{P_0} + 23\right)}{\left(\frac{P_d}{P_0} + 11\right)^2} \tag{7.3}$$

where P_d is the design daily rainfall and P_0 is the run-off threshold, which mainly depends on the type of terrain.

Finally, the maximum rainfall intensity is obtained as a function of I_d, the design hourly intensity for an event of a given return period:

$$I = I_d \cdot \left(\frac{I_1}{I_d}\right)^{\frac{28^{0.1} - T_c^{0.1}}{28^{0.1} - 1}} \tag{7.4}$$

The ratio I_1/I_d represents the ratio of the maximum hourly intensity over the daily-averaged intensity for the given case-study area. This value is usually tabulated in guidelines or standards. I_d may be directly estimated from the daily rainfall P_d (i.e. $I_d = (P_d/24) \cdot R$, where R is a reduction factor). The design daily rainfall P_d is usually obtained through the analysis of rain records of weather stations over the area of interest. Sufficient time series then allow different return periods to be associated with given levels of daily rainfall.

In the present example, two catchment areas are assumed, i.e. one feeding the river branch under bridge B2 and the other linked to the river stream under bridge B3. Based on the examples and assumptions used in D'Ayala et al. [2014b], three return periods are proposed, as shown in Table 7.11.

TABLE 7.11: Rainfall events for each return period and each catchment area.

	Daily rainfall	
Return period	Catchment area 1 (B2)	Catchment area 2 (B3)
50 years	154 mm	235 mm
100 years	174 mm	289 mm
500 years	226 mm	362 mm

These design rainfall events are then used to estimate the maximum flow discharge that is expected under bridges B2 and B3 (see Table 7.12), again using some of the parameters that have been assumed in INFRARISK deliverable D3.1 [D'Ayala et al., 2014b].

TABLE 7.12: Assumed parameters for rainfall events and resulting flow discharge from the rational method, for different return periods and bridge locations.

	T [y]	A [km^2]	P_d [mm]	T_C [h]	P_0 [mm]	I_1/I_d	I_d [mm/h]	C	K_u	Q [m^3/s]
B2	50	11.96	154	1.04	40	9	6.1	0.33	1.07	63.22
	100	11.96	174	1.04	40	9	6.9	0.37	1.07	80.34
	500	11.96	226	1.04	40	9	8.9	0.47	1.07	129.86
B3	50	44.46	235	2.13	40	9	9.3	0.48	1.07	339.39
	100	44.46	289	2.13	40	9	11.4	0.55	1.07	481.02
	500	44.46	362	2.13	40	9	14.3	0.62	1.07	686.44

It should be noted that the bridge B1 is located at the confluence of the two river streams that cross bridge B2 and B3. For simplification purposes, it is then assumed that the maximum flow discharge at B1 is the sum of the flow discharges under B2 plus B3 for the various return periods. This simplistic model may still be reasonably accurate, if it can be assumed that the rainfall events over the two catchment areas are strongly correlated due to their geographical proximity (i.e. joint occurrence of maximum daily rainfall).

c. Landslides

As detailed in INFRARISK deliverable D3.1 [D'Ayala et al., 2014b], an infinite slope model for superficial landslides is adopted for road segments that run along slopes. In the case of earthquake-triggered landslides, the yield acceleration k_y can be expressed as follows [Saygili, 2008, Saygili and Rathje, 2009]:

$$k_y = \frac{(FS - 1) \cdot g}{\tan \phi' + \frac{1}{\tan \alpha}} \tag{7.5}$$

where FS represents the factor of safety, ϕ' is the internal friction angle and α is the slope angle. The factor of safety under static conditions is estimated as follows:

$$FS = \frac{c'}{\gamma \cdot t \cdot \sin \alpha} + \frac{\tan \phi'}{\tan \alpha} - \frac{\gamma_w \cdot m \cdot \tan \phi'}{\tan \alpha} \tag{7.6}$$

where c' is the effective cohesion of the soil, γ is the soil unit weight, γ_w is the water unit weight and m is the saturation ratio. The soil parameters are summarised in Table 7.13 due to lack of knowledge on the shear strength of the soil, a cohesion of 0 kPa and a friction angle of 40° are assumed, as suggested by CDMG [1998]. Regarding the thickness of the moving layer, Jibson et al. [2000] have stated that a typical value for superficial landslides on natural slopes is several feet, i.e. 8 ft translating to 2.43 m.

TABLE 7.13: Soil parameters assumed for the landslide hazard analysis.

Paramer	Value
Effective cohesion (c')	0 kPa
Internal friction angle (ϕ')	40°
Soil unit weight γ	19 kN/m^3
Failure surface thickness (t)	2.43 m

The major difficulty lies in the estimation of the saturation ratio m, which potentially depends on many factors [Saygili, 2008] including: depth of the groundwater table, precipitation pattern, soil transmissivity, slope geometry, etc. It is usually estimated through detailed hydrology models or expert judgement. In the present exercise, due to the lack of relevant data, an arbitrary probability distribution of the saturation ratio as a function of the type of rainfall event is proposed (see Table 7.14), in order to demonstrate the impact of rainfall on the landslide hazard and to account for the uncertainties surrounding the estimation of this parameter.

TABLE 7.14: Proposed distribution of the soil saturation ratio according to the type of rainfall event.

Rainfall	Saturation ratio [m]			
event	0.20	0.50	0.75	1.00
None	80%	20%	–	–
50 y	15%	70%	15%	–
100 y	–	15%	70%	15%
500 y	–	–	20%	80%

Therefore the proposed model allows the prediction of the occurrence of earthquake-triggered superficial landslides, by comparing the PGA value at the site with the yield acceleration k_y of the slope. Since the yield acceleration is a function of the saturation ratio, which depends on the amount of rainfall, this landslide hazard model is dependent on both the earthquake and rainfall events.

7.3.2.2 Fragility Models

Fragility models are selected for the various infrastructure elements at risk, using mainly the results from the previous chapters for bridges, or literature surveys for other road elements [D'Ayala et al., 2015].

a. Bridges

All bridges are assumed to be identical multi-span simply-supported concrete girder bridges, as described in Nielson [2005]. These bridges have been the object of a specific fragility assessment for cumulated hazards (see Section 5.5). In the present context, since the measure of interest is the potential disconnection of the TAZs from the network, the failure modes that are bound to lead to the closure of the bridge are considered, namely deck unseating (failure mode 3) and collapse of substructure components (failure mode 4). The corresponding fragility model is displayed in Figure 7.18 (aggregation of failure modes 3 and 4).

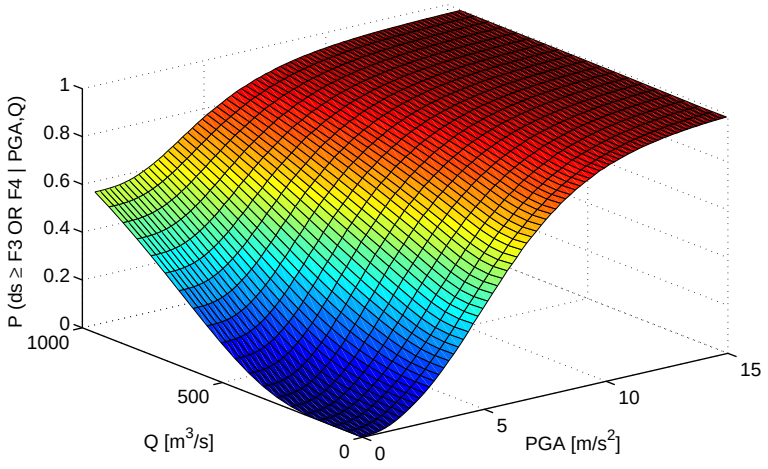

FIGURE 7.18: Fragility model for the closure of bridges B1 and B3, as a function of flow discharge Q and peak ground acceleration PGA.

This fragility surface is able to predict the bridge failure probability due to earthquake or flood alone, as well as the interaction between flood and earthquake cumulated damages, in the case where an earthquake occurs during the period when a bridge has been damaged by a flood (i.e. submersion and scour effects). Damage due to earthquake-induced ground failure is also accounted for.

b. Embankments

Fragility curves for embankments exposed to earthquake-induced ground failure are selected from the study by Argyroudis and Kaynia [2015]. An EC8 soil type D and an embankment height of 6 m are assumed. As a result, the fragility parameters for the extensive/complete damage to these types of embankments are: $\alpha = 4.807$ m/s^2 and $\beta = 0.800$.

c. Road segments

Fragility curves for plain road segments exposed to earthquake-induced ground failure are also selected from Argyroudis and Kaynia [2015]. Even though this study is focused on the fragility of embankments and cuts, it could be assumed that the road segments of the present case-study are built on a layer of compacted soil, which may correspond to a shallow embankment with stiffer soil (i.e. $h = 2$ m and EC8 soil type C). As a result, the fragility parameters for the extensive/complete damage to these types of road segments are: $\alpha = 15.402$ m/s^2 and $\beta = 1.000$.

d. Roads along a slope

Fragility curves for roads running along a slope and exposed to landslides have been developed in D'Ayala et al. [2015]. They are characterized by the yield acceleration of the slope, as shown in Table 7.15. The extent of the damage is given by the amount of displacement that is induced, which is usually obtained through empirical equations such as the one by Bray and Travasarou [2007]. Therefore the road fragiltiy curves are directly linked to the yield acceleration k_y, which determines whether displacement is initiatied on the slope or not.

TABLE 7.15: Fragility curves for extensive damage to urban roads along a slope, as a function of k_y [D'Ayala et al., 2015].

k_y [g]	α [m/s^2]	β
0.05	4.517	0.406
0.10	7.226	0.382
0.20	13.318	0.349
0.30	18.418	0.328

The proposed fragility curves can be considered as a multi-hazard fragility model, since they are expressed as a function of PGA for different values of k_y, which is linked to flood events through the soil saturation ratio m.

7.3.3 Corresponding Bayesian Network

Based on the previously discussed assumptions, a BN can be built in order to perform the multi-risk analysis of the road network (see Figure 7.19): all the successive steps of the risk analysis are present, i.e. the definition of the source events, the hazard events, the physical damage events and the functional consequences at the system level.

The BN nodes that are involved in the prediction of the distributed seismic hazard intensities have already been defined in Subsection 7.2.1. The other nodes involved in this BN are the following:

- **FL**: range of rainfall events for the three return periods, being directly linked to the flow discharge value at each bridge location.
- **ky**: possible values of yield acceleration based on the extent of rainfall event.
- **SCi**: super-components, i.e. groups of elements that are found to be in series within the MLSs.
- **Esi**: survival events for the elements within the same MLS.
- **Nsi**: number of sources still connected to sink i.
- **SCL**: single connectivity loss.

On Figure 7.19, the red nodes represent the input to the Bayesian Network in terms of potential source events (i.e. earthquakes and rainfall). The blue nodes represent the computation of the distributed hazard values, based on the geographical coordinates of the system (brown nodes). The green nodes represent the damages to infrastructure elements, while the yellow nodes represent the computation of the disconnected TAZs and the SCL based on the failures of elements. Finally, the grey nodes represent aleatory uncertainty sources (i.e. intra- and inter-event variability of the ground motion levels).

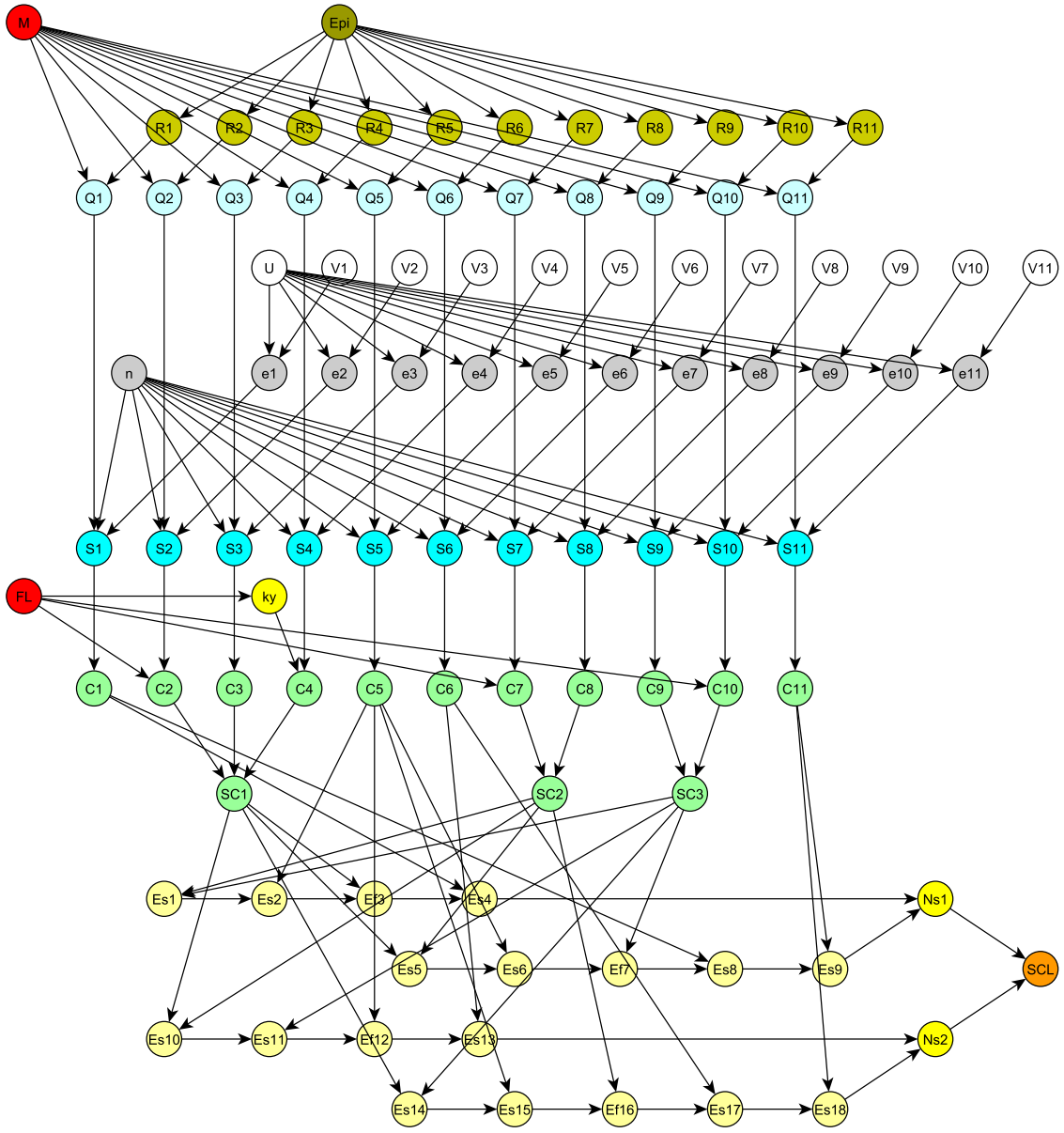

FIGURE 7.19: Bayesian Network for the multi-risk analysis of the infrastructure system.

The efficient MLS formulation has been adopted to represent the system performance, however the limited size of the MLSs does not require the application of the optimisation algorithm to coalesce the SPE chains. Still, three class A super-components (in series) have been created, since they enable a straightforward reduction of the number of SPE nodes. The details of the equations and contents of the CPTs of the various BN nodes are presented in Appendix I.

7.3.4 Multi-Risk Analysis

Currently, there are limited examples in the literature of multi-risk analyses that account for all possible interactions, from the source events to the loss estimations. Selva [2013] relies on a formal statistical model to include multi-risk interactions at hazard, vulnerability and exposure levels. This approach is applied to two hypothetical cases, i.e. (i) seismic risk and volcanic ash deposits and (ii) tsunami risk induced by damaging earthquakes. Mignan et al. [2014] have simulated time series that may include any number of source events or triggered events, depending on their rate of occurrence. These time-dependent scenarios are randomly generated through a sequential Monte Carlo method that is able to treat either independent coinciding events or triggered/cascading events. This approach is applied to a virtual city that is potentially exposed to a wide range of hazard types (i.e. the 'MATRIX Virtual City' concept). The results are presented under the form of a risk matrix (i.e. loss vs frequency) and the risk migration between different interaction assumptions can be observed.

Since the BN approach proposed in the present study may not be easily applicable to a time-dependent framework with sequential events, it is first checked whether the BN can comply with the multi-risk probabilistic model that has been introduced by Selva [2013]. He introduces the concept of a persistence time window ΔT_p, which is crucial to properly model the effect of a second hazard event while the effects of the first event in terms of vulnerability and exposure are still present. Considering two potential events E1 and E2, the probability of E1 occurring while the effects of E2 are still present is given by the following expression [Selva, 2013]:

$$H^{(E1,E2)}\left(x_j\right) = H^{(E1|E2)}\left(x_j; \Delta T_p\right) \cdot P\left(E2; \Delta T\right) \tag{7.7}$$

where $H^{(.)}\left(x_j\right)$ represents the probability of having a given hazard event with the value $x \geq x_j$, and ΔT is the global exposure time over which the risk is estimated. In the context of the present case-study example, E2 represents the rainfall event, E1 the earthquake event and the exposure time is set as $\Delta T = 1$ year; this corresponds to the objective of quantifying the yearly losses for the road infrastructure. Finally, it is assumed that the persistence time window ΔT_p could be around 1 month (i.e. accounting

for the time needed by the flood to recede and the duration of the subsequent repair operations).

Regarding the risk factor $R_c\,(\geq l)$, which gives the probability of exceeding losses l over time period ΔT, Selva [2013] defines the following expression for the risk due to E1 with possible interactions with E2:

$$R_c^{(E1)}\,(\geq l) = R_c^{(E1,E2)}\,(\geq l) + R_c^{\left(E1,\bar{E}2\right)}\,(\geq l) \tag{7.8}$$

where the total risk is decompose into two disjoints configuration (i.e. with or without the contribution of the second event E2). The first term on the right side is referred to as the co-active risk factor: it represents the part of the risk that is only generated by the joint occurrence of E1 and E2 in the same time window ΔT_p. The second term is the isolated risk factor, which can be seen as the part of risk that remains when E1 is not interacting with E2. It can be further decomposed into two distinct parts:

$$R_c^{\left(E1,\bar{E}2\right)}\,(\geq l) = R_c^{(E1,s)}\,(\geq l) - R_c^{(E1,v)}\,(\geq l) \tag{7.9}$$

The first term is referred to as the single risk factor for E1, since it represents the risk due to E1 over the whole ΔT period, without considering the effects of E2. The second term is referred to as the virtual risk factor, since it represents the risk due to both E1 and E2 over ΔT, except that the fragility and exposure models are not updated due to the potential impacts of E2.

This framework is then applied to the BN approach proposed here. The modularity of the BN and its ability to handle different types of evidence (i.e. assumptions or observations) permits the generation of risk curves for the different assumptions above:

- Earthquake risk only (single risk): the **FL** node (flood intensity) is evidenced with $P\,(FL = 0) = 1$, while the probability of occurrence of the **M** node is set for $\Delta T = 1$ year.
- Flood risk only (single risk): the **M** node (magnitude range) is evidenced with $P\,(M = 0) = 1$, while the probability of occurrence of the **FL** node is set for $\Delta T = 1$ year.

- Interacting earthquake and flood risks (co-active risk): the full distributions of **FL** and **M** nodes are sampled. The probability of occurrence of **FL** is set for $\Delta T = 1$ year, while $\Delta T_p = 1$ month is used for **M**.
- Interacting earthquake and flood risks without updating fragility model (virtual risk): it is obtained by summing the flood single risk (with $\Delta T = 1$ year) and the earthquake single risk (with $\Delta T_p = 1$ month).
- Earthquake risk outside the time window of flood risk (isolated risk): it is obtained by subtracting the virtual risk from the sum of the flood and earthquake single risks (both with $\Delta T = 1$ year).
- Global risk from both earthquake and rainfall events over a year (multi-risk): it is obtained by summing the isolated risk factor and the co-active risk factor.

The BN can then be solved for these different scenarios, and the resulting risk curves (i.e. yearly probability of exceedance for the different SCL values) are presented in Figure 7.20 and Table 7.16.

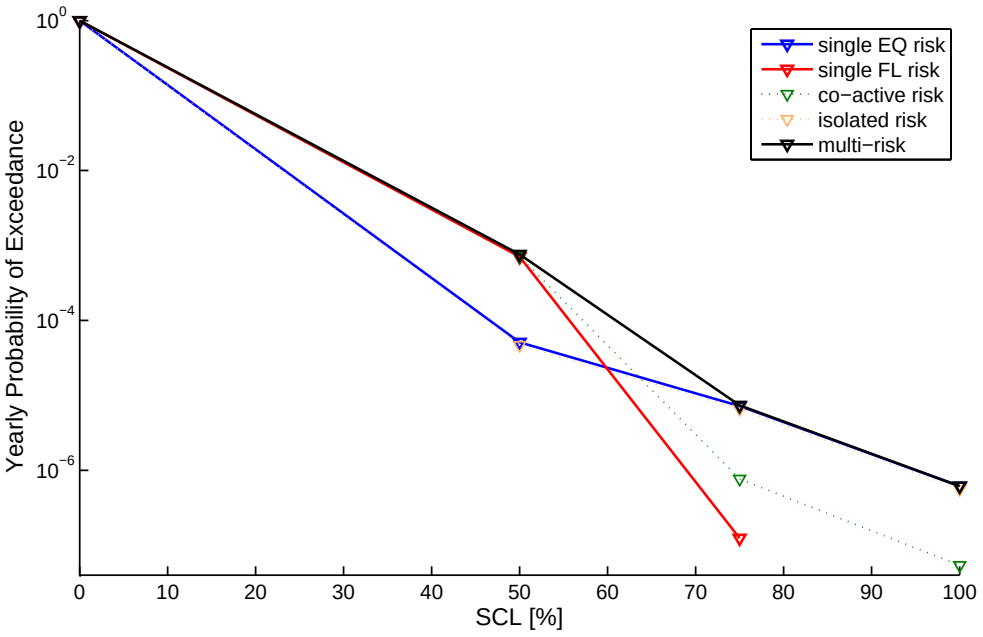

FIGURE 7.20: Risk curves for the SCL index, using the different risk factors.

Selva [2013] has also introduced δR, a single risk bias measure which estimates the bias in the risk measure when only single risk analyses are performed, without accounting for the interaction effects:

TABLE 7.16: Yearly probability of exceeding the given SCL value with the different risk factors considered.

SCL	Risk factor					
	Single EQ	Single FL	Co-active	Virtual	Isolated	Multi
50%	5.0967E-05	7.0933E-04	7.1378E-04	7.1360E-04	4.6701E-05	7.6049E-04
75%	7.1977E-06	1.2414E-07	7.6648E-07	7.2671E-07	6.5951E-06	7.3616E-06
100%	6.1278E-07	–	5.4186E-08	5.1300E-08	5.6148E-07	6.1566E-07

$$\delta R = R_c^{(E1,E2)} - R_c^{(E1,v)} \tag{7.10}$$

It consists in the difference between the virtual risk factor and the co-active risk factor. Selva [2013] also proposes to normalise this bias measure by the single risk factor. However, in the present case-study, both hazard events have damaging potential and E2 (i.e. rainfall event) is not limited to the role of an aggravating risk factor. Therefore it is proposed here to normalize by the sum of both single risk factors:

$$\delta R_{\%} = \frac{R_c^{(E1,E2)} - R_c^{(E1,v)}}{R_c^{(E1)} + R_c^{(E2)}} \tag{7.11}$$

The multi-risk bias values for the present example are detailed in Table 7.17. The effect of multi-risk interaction looks rather light, i.e. the bias measure is not exceeding 1% with $\Delta T_p = 1$ month, however it is interesting to observe that the bias follows the same trend as the risk migration estimated by Mignan et al. [2014]: when considering multi-risk interactions, extreme consequence events tend to have a large rate of occurrence (i.e. SCL = 75% and SCL = 100% in the present case), which seems to have partly migrated from the rate of occurrence of less severe events (e.g. SCL = 50%). The risk bias measure is also presented for different values of the persistence time window ΔT_p, thus showing the significant influence of the temporal aspect on multi-risk analyses.

TABLE 7.17: Relative risk bias measure using SCL as the system's loss measure.

SCL	$\delta R_{\%}$ with $\Delta T_p = 1$ week	$\delta R_{\%}$ with $\Delta T_p = 1$ month	$\delta R_{\%}$ with $\Delta T_p = 3$ months
50%	0.004%	0.027%	0.058%
75%	0.127%	0.574%	1.648%
100%	0.109%	0.495%	1.412%

7.3.5 Sensitivity from Uncertainty Sources

This section details the effects of some of the uncertainty sources that have been identified. Such a task can be efficiently conducted by taking advantage of the BN approach, which enables the value of some nodes to be forced (i.e. evidence input) and the distribution of the outputs through an exact inference to be observed.

7.3.5.1 Summary of Uncertainty Sources

The models and assumptions used in the present examples include the following sources of uncertainty, based on the general uncertainty framework described in Section 6.2:

- **Aleatory uncertainties:**
  - Inter-event variability of the GMPE model: it is represented by the normally distributed term η that is associated with each GMPE.
  - Intra-event variability of the GMPE model: it is specific to each site i and is represented by the normally distributed term ϵ_i. A spatial correlation structure is adopted between the vulnerable sites to generate the terms ϵ_i, based on a correlation distance.
  - Dispersion inherent to the fragility models: it corresponds the standard-deviation of the fragility functions. It does necessarily include aleatory uncertainties, since it is usually a combination of record-to-record variability, modelling assumptions and definition of the damage state.
- **Epistemic uncertainties:**
  - Choice of a GMPE: the 3-branch representative GMPE that has been discussed in Section 6.4.1 is used here in order to represent the epistemic uncertainties due to model choice.
  - Choice of a fragility curve: if only global features are identified (e.g. deck type, spans, pier type, etc.), a hybrid fragility model is derived from existing references, along with confidence bounds (see Section 6.4.2).
  - Dispersion inherent to the functionality models: for bridges, a probabilistic functionality loss model may be adopted given the physical damage states,

since closure of the bridge may not be accurately predicted due to the lack of knowledge (i.e. interpretation of the damage states considered).

- Estimation of the yield acceleration k_y: the evolution of the soil saturation ratio, which is used in the computation of the yield acceleration, along with the rainfall pattern, is completely assumed due the absence of any predictive model and relevant expertise on this aspect.
- Interactions between the different risks: the interaction between the flood and the seismic hazard is represented by the development of a multi-risk fragility model for bridges. This model is based on the assumption that a given bridge might still be damaged after a flood event, thus increasing its vulnerability from a subsequent earthquake: therefore a time frame is needed in order to account for this risk interaction (i.e. duration during which the bridge might remain unrepaired).

7.3.5.2 Aleatory Uncertainties

The aforementioned computations have been conducted by bounding the aleatory uncertainties of the GMPE to the $\pm$ 1 $\sigma_{a,tot}$ interval, where $\sigma_{a,tot}$ is the standard deviation that results from the composition of intra- and inter-event variability (which are inherent to the GMPE model):

$$\sigma_{a,tot} = \sqrt{\sigma_{intra}^2 + \sigma_{inter}^2} \tag{7.12}$$

The effect of the range of the possible uncertainty values is illustrated in Figure 7.21. As expected, the inclusion of aleatory uncertainties in the hazard prediction models results in a significant increase of the expected losses. It is interesting to note that the loss probabilities tend to converge and even slightly decrease for $\pm$ 3 $\sigma_{a,tot}$. For such a level of variability, very high and unrealistic hazard intensity values are sampled, which may lead to a saturation of the fragility functions (i.e. failure probabilities equal to 1), while in the meantime, very low hazard intensities are also sampled, thus resulting in no failure at all. Truncating the ground motion variability at $\pm$ 1 $\sigma_{a,tot}$ appears to constitute a sound assumption in the present case: the highest generated values with this sigma level

are of the order of 20-25 m/s, while the use of $\pm$ 2 $\sigma_{a,tot}$ or above would lead to intensity values that are not physically realistic.

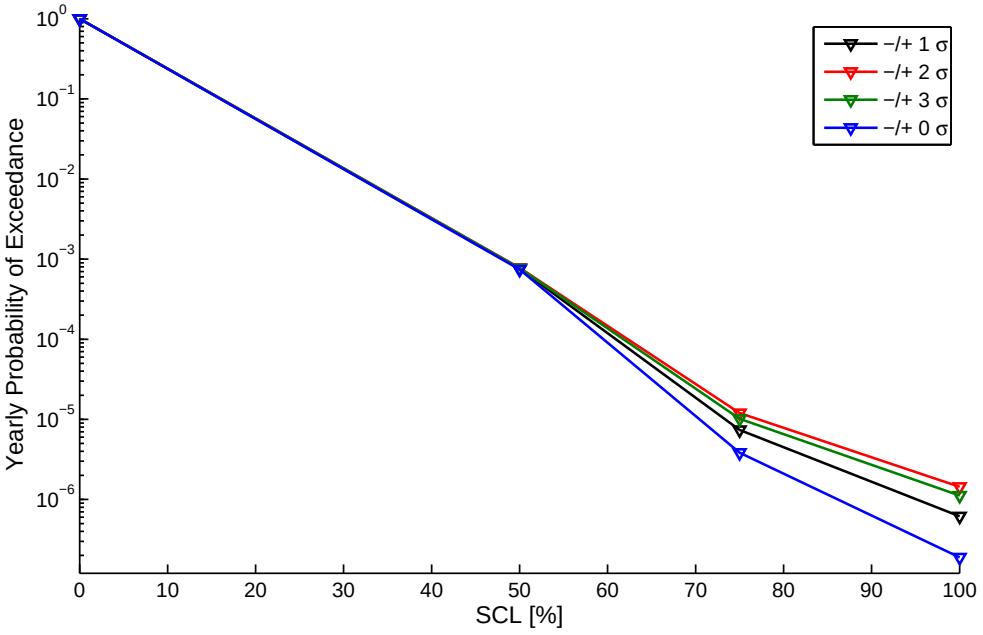

FIGURE 7.21: Risk curves for the SCL index, with different assumptions on the aleatory uncertainties associated with the GMPE model.

Another variable that is related to the GMPE aleatory uncertainties is the correlation distance of the ground motion field, which is used to express the spatial correlation of the intra-event error term. In the present study, a correlation distance of 13.5 km for PGA has been assumed, based on the recommendations of Akkar and Bommer [2010]. The effect of other assumptions (i.e. no spatial correlation or infinite correlation distance) on the global loss of the infrastructure system is represented in Figure 7.22. It can be observed that the removal of the spatial correlation factor will lead to an underestimation of the risk. This phenomenon may be explained by the definition of the system performance indicator that has been selected. The single connectivity loss SCL counts the number of sources that are still connected to a given sink, while the topology of the present virtual network generates multiple MLSs between each couple of source and sink. Therefore the studied example may be assimilated to a 'parallel' system, where multiple paths need to be disrupted for a source to be disconnected and the SCL value to change. Finally, the present problem with a correlation distance of 13.5 km may be adequately bounded by the two extreme assumptions, i.e. no correlation (lower bound) and full correlation (upper bound).

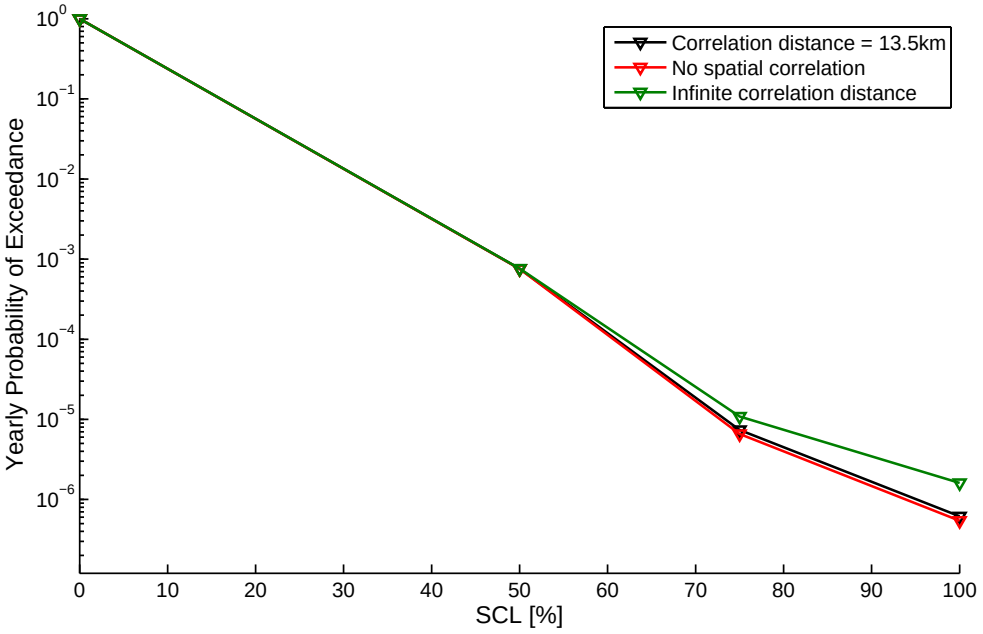

FIGURE 7.22: Risk curves for the SCL index, with different assumptions on the spatial correlation distance.

7.3.5.3 Epistemic Uncertainties

Regarding epistemic uncertainties, the variability that is linked to the choice of ground motion model (i.e. **GMPE** node), to the estimation of the slope yield acceleration (i.e. **ky** node) and the persistence time window is investigated by successively entering different input variables into the BN. The assumptions for each uncertainty sources are summarised in Table 7.18.

TABLE 7.18: Assumptions used for the epistemic uncertainty sources.

Uncertainty source	Median value	Lower bound	Upper bound
GMPE	Median GMPE curve	Lower GMPE curve	Upper GMPE curve
ky	Median k_y values from Table 7.14	Lower k_y values from Table 7.14	Upper k_y values from Table 7.14
ΔT_p	1 month	1 week	3 months

The effect of these epistemic uncertainty sources is represented in Figure 7.23. The largest change is observed when epistemic uncertainties on the ground motion model are considered, however it is much smaller than the discrepancies generated by the aleatory uncertainties (see Figure 7.21). On the other hand, epistemic uncertainties associated with the **ky** node have a very limited impact on the final losses: this may be due mostly to the fact that they are only feeding into a small portion of the infrastructure

system (i.e. road segment along slope). Finally, the temporal effect, i.e. the change in the value of the persistence time window, is not visible at this level, even though it has been shown that it has a major impact on the risk bias measure (see Table 7.17). Presently, the only interactions at the fragility level that have been taken into account are the detrimental effect of floods on the seismic fragility of the three bridges. Therefore more multi-risk models for more infrastructure component types and more failure modes should be developed in order to better account for these interaction effects.

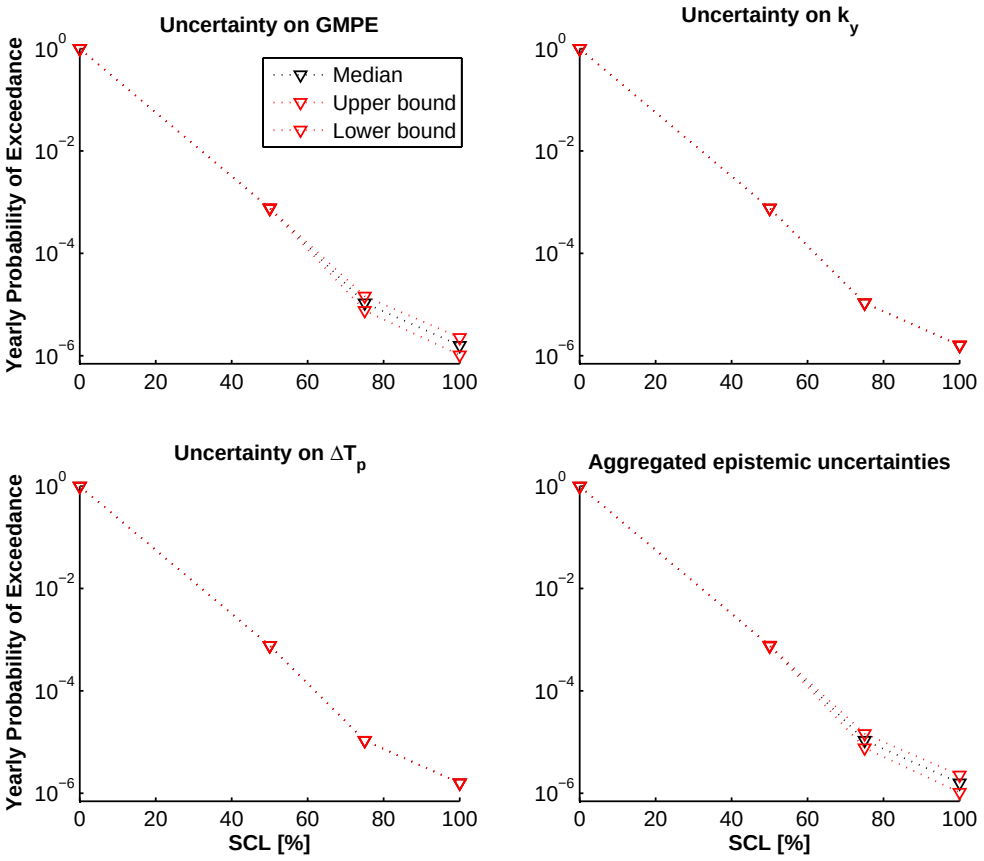

FIGURE 7.23: Effect of some sources of epistemic uncertainties on the risk curve.

The aggregated effects of all epistemic uncertainties are summarised in Figure 7.23, where the upper and lower bounds are defined by computing the 16^{th}-84^{th} percentiles of the various realisations of the different variables considered in Table 7.18. The epistemic uncertainties are mostly concentrated at the higher loss levels, where a factor of 2 is observed between the probabilities of the upper and lower bounds at SCL = 100% (i.e. 1.04E-06 vs 2.27E-06). However, the present results should come with a significant

caveat, since only seismic risk assessment has been the object of uncertainty quantification. The development of a proper assessment method for the flood hazard along with the corresponding uncertainties should be carried out in order to accurately quantify the uncertainty sources that are brought by the different hazard types.

7.3.5.4 Investigation of Fragility Models

In the previous sub-section, the multi-risk analysis have been conducted with the assumption that functionality loss of the bridges is directly obtained from the specific multi-hazard fragility function. However, different levels of complexity and accuracy may also be tested through the following fragility models:

- Model 1: it is assumed that no specific knowledge on the bridges is available, therefore the literature-based fragility curves that have been proposed in Section 6.4.2 are used, along with their 16%-84% confidence bounds. In the present example, the attributes of the bridges are 'C-SSu-NSD-McP' (i.e. concrete, simply-supported, non-seismically designed, multi-column piers), which correspond to bridge ID #1. Only the curve corresponding to global damage state DS4 is considered, while assuming bridge closure when DS4 is reached.
- Model 2: probabilistic functionality curves are used instead of fragility functions. Therefore the curve from Figure 5.16 corresponding to 100% lane closure is used here, in order to directly predict bridge closure.
- Model 3: probabilistic functionality curves are also used, but functionality losses are based on the aggregation of global damage states (i.e. the 100% lane closure curve from Figure 5.19).

The effect of fluvial flood has also to be integrated to these models, which consider only seismic hazard. A simple way is to directly use the fragility curve for deck unseating due to hydraulic forces, which will lead to the closure of the bridge by definition. The seismic damage states and the flood-induced damage states can then be merged into a functionality node, which assesses the closure or not of the bridge, as shown in Figure 7.24. Such a formulation has the merit of integrating the potential bridge closure

due to floods. However, scour fragility curves are not included, since cumulated damages cannot be modelled by the use of separate fragility functions for seismic and flood hazards.

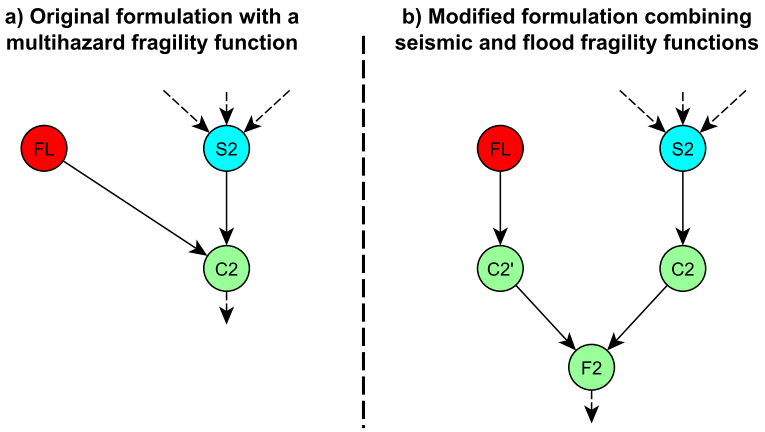

FIGURE 7.24: BN formulations for multi-hazard (left) and single hazard (right) fragility functions, for component #2 exposed to both seismic and flood hazards.

The multi-risk analysis is then performed with this modified BN formulation, for the different fragility models, as shown in Figure 7.25.

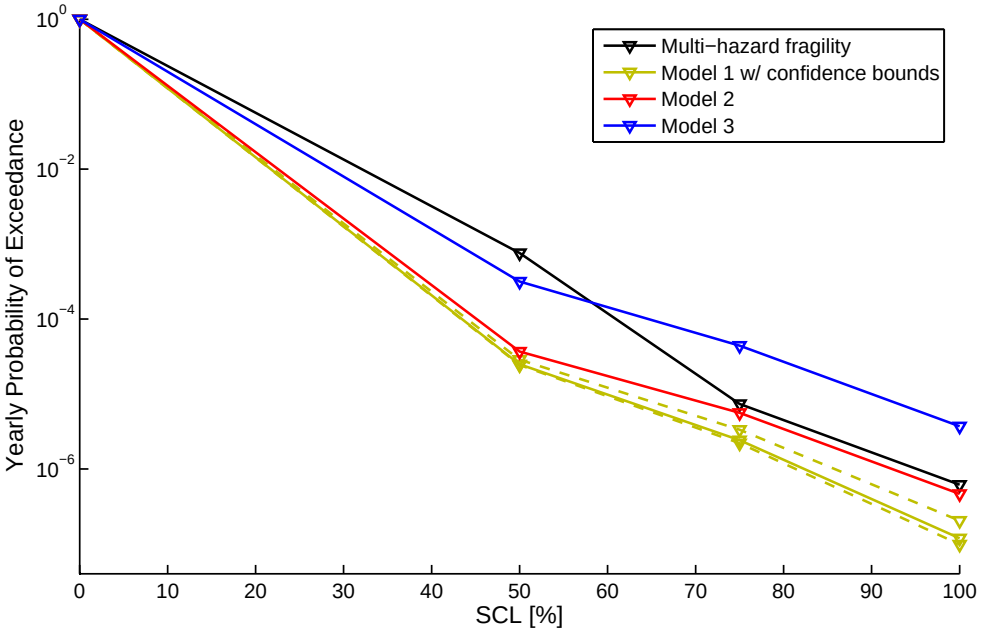

FIGURE 7.25: Multi-risk analyses using different fragility models.

The different loss curves using the single hazard fragility models present the same shape, which widely diverges from the multi-hazard model. It appears that the effects of scour

and cumulated damages (i.e. scour-earthquake interactions) lead to substantial additional losses, especially for SCL = 50%, which cannot be taken into account by the single hazard models. The fit improves for heavier losses (e.g. SCL = 100%), which is due to the integration of the flood-induced fragility curve (i.e. Figure 7.24). Although the adopted limit states are not exactly the same, there is a good agreement between Model 2 and the multi-hazard model. However, Model 3, which is based on global damage states, does not present a good fit, thus demonstrating the necessity to refine functionality models. Finally, as expected, Model 1 performs rather poorly, since a significant underestimation of losses is observed. It appears also that choosing between these different fragility models leads to a significant scatter in the loss curves, which may be compared to the relatively narrow confidence bounds that are found with the other epistemic uncertainties (i.e. Figure 7.23). Therefore this observation demonstrates the necessity to derive refined fragility functions that integrate functionality looses and multi-hazard interactions.

7.4 Application: Multi-Risk Assessment of a Real-World Road Network

The above detailed models and developments are also applied to a road network system that is representative of a real-world infrastructure, in order to check their ability to be implemented on wider scales.

7.4.1 Characterization of the case-study

The road network around Bologna, Italy, has been chosen as a realistic case-study, as detailed in the sub-sections below.

7.4.1.1 General Presentation

The area surrounding Bologna in Italy constitutes one of the case-studies selected in the FP7 INFRARISK project, due to the variety of hazard types that are present (e.g. seismic faults, riverine floods on the Arno and its tributaries, landslides in the Tuscan-Emilian Apennines, etc.). Furthermore, the highway connecting the cities of Bologna

and Florence represents a critical part of the traffic between the North and the South of Italy (see Figure 7.26). Therefore this case-study area has been chosen here in order to demonstrate the capabilities of the proposed approach.

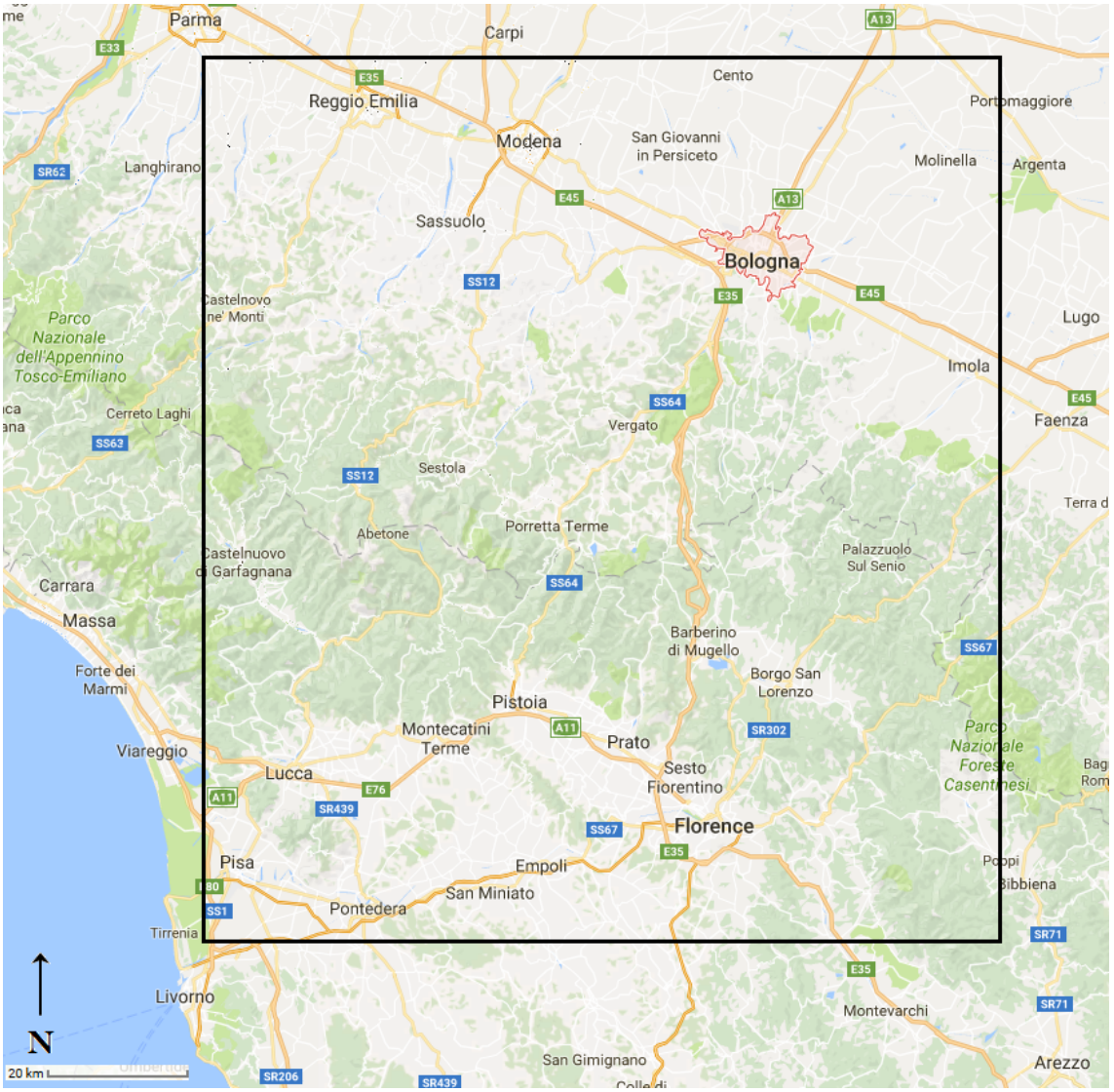

FIGURE 7.26: Location of the case-study area with the black frame showing the spatial extent of the network considered.

7.4.1.2 Network Topology

The road network layout has been vectorised, and, after a quick treatment in a Geographical Information System, the simplified topology of the network may be extracted as shown in Figure 7.27.

The topological representation of the network does not account for the shape of the road segments between two nodes: however, the proper length of each edge is extracted

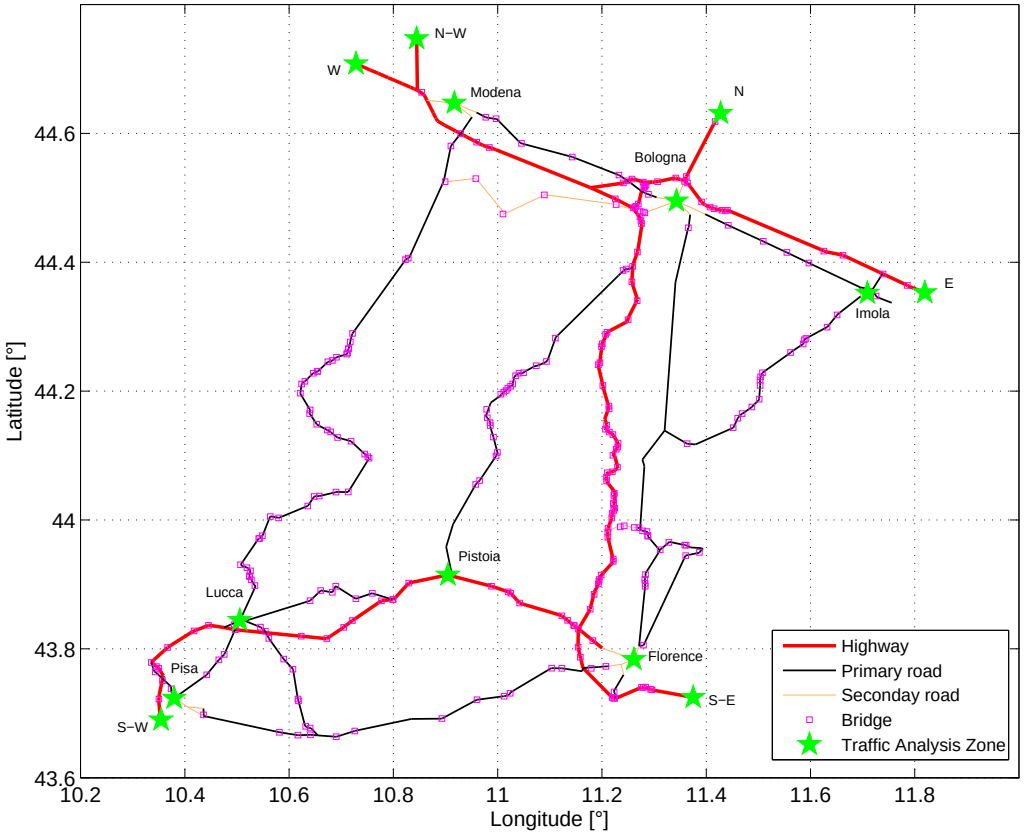

FIGURE 7.27: Road network considered in the case-study area.

from the Geographical Information System and is stored as an attribute of the edge. Morevover, three different road types are identified, to which free-flow travel speeds may be assigned, i.e. highways (110 km/h), primary roads (70 km/h) and secondary roads (50 km/h). This treatment enables an efficient computation of the road network, while providing realistic estimates of the travel times. In total, the model of the studied network is comprised of 647 edges and 625 nodes: 13 of these nodes are selected as TAZs, out of which 7 are cities (i.e. Bologna, Florence, Modena, Lucca, Pisa, Pistoia and Imola) and 6 are external nodes representing exits and entrances to the network (i.e. South-West, West, North-West, North, East and South-East directions). Finally, 280 bridges are identified along the road network: therefore the edges to which they belong are considered as vulnerable elements and they will govern the performance of the system in the subsequent risk analysis.

7.4.2 Modelling Assumptions

The hazard and fragility models used in the analysis are detailed in the following subsections: several assumptions are proposed, since the objective is less to deliver a thorough risk assessment of the area than to demonstrate the applicability of the proposed approach to real-world systems.

7.4.2.1 Hazard models

Seismic hazard events are based on the results of the FP7 SHARE project, which proposes a harmonized probabilistic seimisc hazard map for Europe. The seismic source areas identified in SHARE are used here in order to sample seismic events based on the activity parameters of the sources. Seven source areas are selected around the studied road network, as shown in Figure 7.28, while the corresponding Gutenberg-Richter parameters are described in Table 7.19.

TABLE 7.19: Activity parameters of the selected seismic source areas, taken from Woessner et al. [2013]. λ_0 represents the yearly occurrence of events of magnitude greater than 0, while β stands for the b-value parameter in the Gutenberg-Richter relationship.

Area ID	λ_0 ($M_w \geq 0$)	β	Maximum M_w
ITAS293	3.70	1.0	7.3
ITAS292	3.95	1.0	7.3
ITAS297	3.80	1.0	7.3
ITAS295	3.90	1.0	7.3
ITAS299	3.60	1.0	7.3
ITAS305	3.80	1.0	6.6

While the previous virtual example was based on a single seismic source, the presence of multiple seismic sources in this case-study requires to first sample which seismic source will generate the potential earthquake event, as described by Cavalieri et al. [2012]. Let us assume n seismic sources with yearly occurrence rates $\lambda_{0,i}$. Then the yearly occurrence rate of a given loss metric y may be expressed as follows:

$$\lambda_Y(y) = \sum_i^n \lambda_{0,i} \cdot \mathrm{G}_{Y|i}(y|i) = \lambda_{0,tot} \sum_i^n p_i \cdot \mathrm{G}_{Y|i}(y|i) = \lambda_{0,tot} \cdot \mathrm{G}_Y(y) \tag{7.13}$$

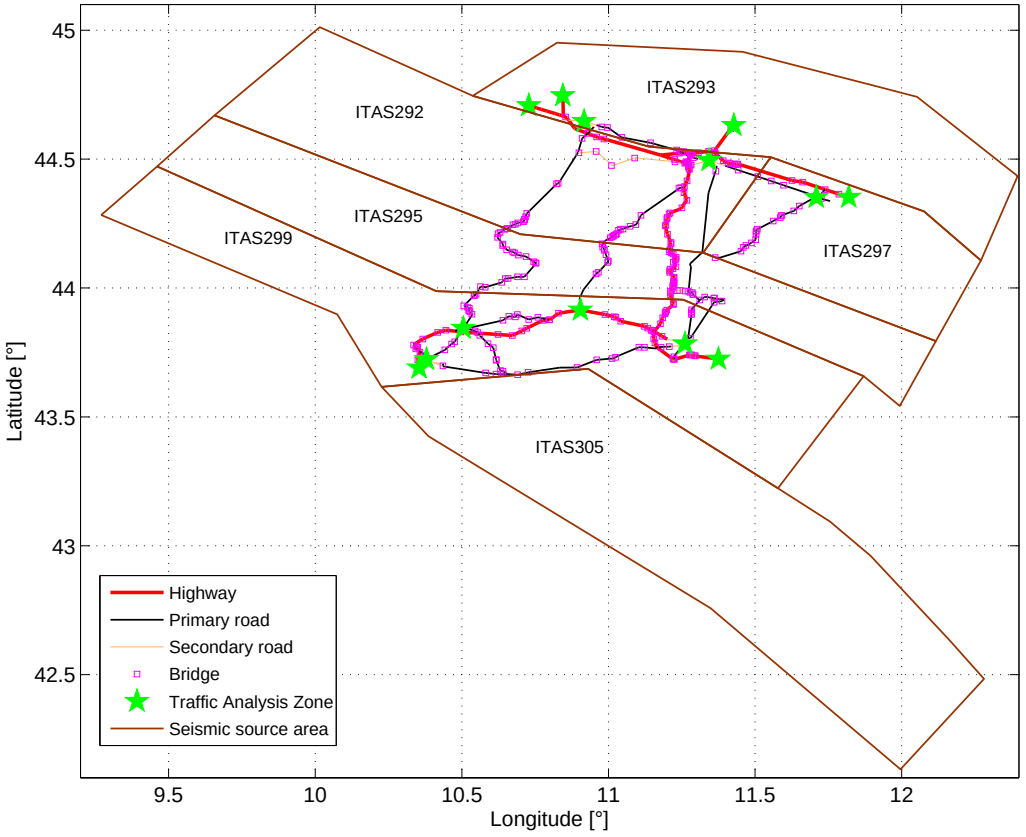

FIGURE 7.28: Selected seismic source areas around the road network, from Woessner et al. [2013].

where p_i represents the probability of sampling source i (i.e. relative weight of each source) and $G_{Y|i}(y|i)$ represents the probability of exceeding annual losses y due to source i.

Therefore, the global yearly occurrence rate of an earthquake event $\lambda_{0,tot}$ is aggregated from the activity rate of all seismic areas, while the p_i terms represent the relative weight of each source in the sampling. Once an earthquake event is sampled, the estimation of the ground motion field at the vulnerable sites (i.e. location of bridges) is performed with the three-branch representative GMPE that has been presented in Chapter 6, while accounting for the spatial correlation of the intra-event residuals.

In the case of flood hazard events, existing models and data for the studied area are much scarcer. The main waterways crossing the road networks are identified, which results in 163 bridges over water streams (see Figure 7.29), meaning that such elements are potentially exposed to both earthquake and flood events.

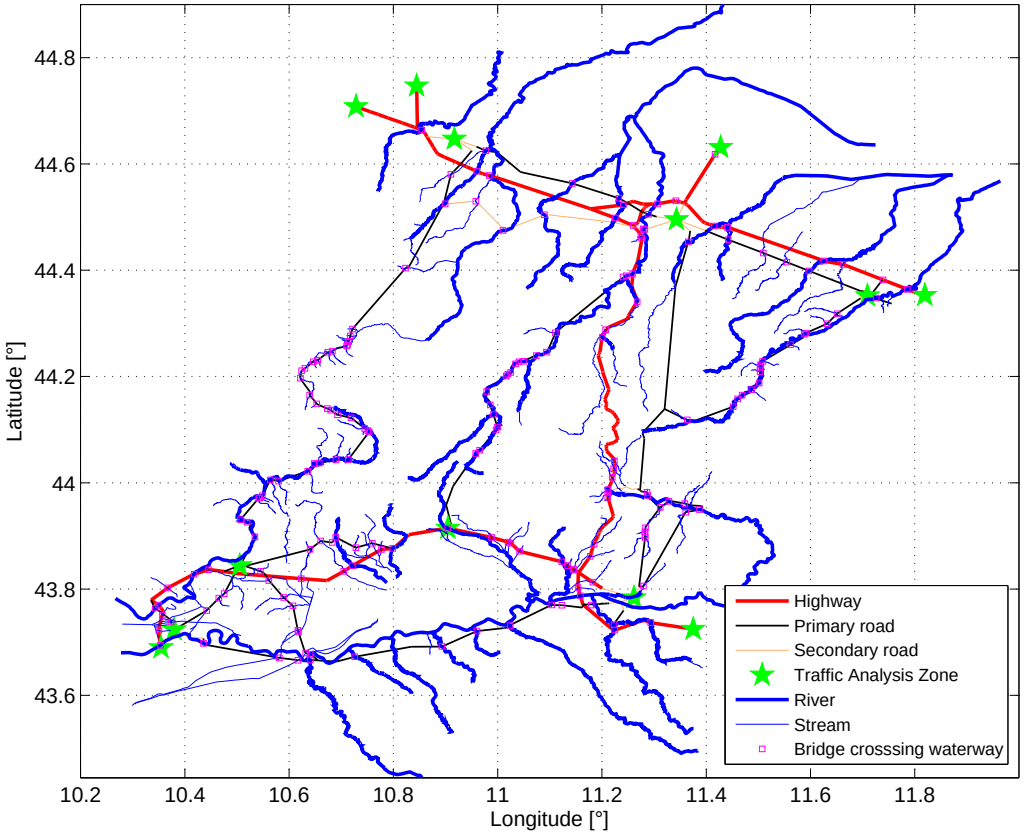

FIGURE 7.29: Main waterways crossing the road network.

The study by Caporali et al. [2005] on the historical flood events of the Arno river provides valuable information on the intensity and frequency of recorded events in the Tuscany area. The 1966 flood of the Arno river, with maximum flow discharges of 2 290 m^3/s at the river mouth and 3 540 m^3/s upstream from Florence, is considered as an exceptional event (i.e. 8 events of this type have been identified since the XII^{th} century). On the other hand, events such as the 1992 flood, with around 2 000 m^3/s flow discharge recorded upstream from Florence, are considered as large events. Based on these events, three levels of flood intensity with distinct return periods are assumed for the studied area, as detailed in Table 7.20. The maximum flow discharge values are the ones assumed at the mouth of the Arno, while the values at other locations are deduced by considering the relative size of the rivers and the contributions from their tributaries. For simplification purposes, it is assumed that a flood event correponds to a global elevation of the flow discharge across the whole studied area (i.e. assumption

that the catchment areas of the different rivers are not too far away and are thus subjected to similar rainfall events). As previously stated, the flood hazard assessment step contains many shortcomings and assumptions, since this specific task is out of the scope of the thesis, which concentrates on how multiple hazard events may influence multi-risk analyses.

TABLE 7.20: Assumed parameters for the flood hazard events.

Flood event	Peak flow $[m^3/s]$	Return period
Medium	300	$\sim$ 25 years
Large	1 200	$\sim$ 50 years
Exceptional	2 300	$\sim$ 100 years

7.4.2.2 Fragility Models

A short investigation of the bridges present in the case-study area has led to the identification of the most common types, which consist mostly of multi-span simply-supported concrete bridges. For the sake of the demonstration, four specific bridges are selected and modelled (see Table 7.21), in order to test the ability of the multi-hazard fragility model presented in Chapter 5 to cover various bridge configurations.

TABLE 7.21: Assumed bridge types for the case-study area.

Bridge type	Length [m]	# of spans	Columns per pier	Seismic design
1	198	5	4	Yes
2	84	3	4	Yes
3	68	2	3	No
4	20	1	–	No

These four bridges are arbitraly assigned to the various locations of the road network, based on the following considerations:

- Bridge type 1 corresponds to long-span viaducts, which may be used on highways crossing moutainous areas (e.g. highway segment between Bologna and Florence) or main waterways (e.g. highway crossing the Arno river).
- Bridge type 2 corresponds to bridges on primary roads or highways in flat areas. They are assumed to be mostly found in the Emilia-Romagna region.
- Bridge type 3 is the same as type 2, except that the bridges are not seismically designed. Therefore they are assumed to be located in the southern part of the case-study (Tuscany region), where the seismic zonation is less compelling.

- Bridge type 4 corresponds to small single-span bridges that may be found on secondary roads in mountainous areas, for the crossing of small water streams.

An accurate survey of all 280 bridges selected in the case-study area would require a tremendous effort, which would not efficiently serve the purpose of the study. Therefore only four bridge types are assumed in order to emulate the performance of a somewhat realistic road network. This choice represents a strong limitation of the study, however the main purpose is to identify potential multi-risk interactions, which are not strongly dependent on the accuracy of the exposure catalogue.

In total, 86 bridge types 1, 24 bridge types 2, 54 bridge types 3 and 116 bridge types 4 are assigned as vulnerable elements. The procedure detailed in Chapter 5 is applied in order to derive multi-hazard fragility functions that may be used independently from the hazard loading (i.e. earthquake only, flood only, or joint flood and earthquake effects). The resulting fragility models are displayed in Appendix J, for the four system failure modes that have been defined in Table 5.5. Therefore the functionality metrics that are derived from the system failure modes may be directly used in the subsequent network analysis.

7.4.3 Multi-Risk Analysis

In the case of this complex real-world road network, two system performance indicators are considered:

- A purely connectivity-based indicator, SCL (see Equation 7.1), which measures the amount of inter-TAZ connections that are lost;
- Another connectivity-based indicator, R_{TT}, which accounts for the extra travel time between each TAZ (i.e. the loss of some edges may not induce the disconnection between two points, however it may lengthen the path between them). The R_{TT} metric is estimated through the following steps:
  - For n TAZs, $n(n-1)/2$ inter-TAZ travel times are evaluated under normal conditions, assuming two-way roads everywhere and considering free-flow speed on the various road segments.

- For each couple of TAZs, the path TT_i leading to the shortest travel time is computed with the weighted adjacency matrix.
- The ratio of extra travel time TT_i / $TT_{i,0}$ is computed for each travel i, where $TT_{i,0}$ is the travel time in normal conditions.
- The global performance indicator R_{TT} corresponds then to the average of all travel ratios across all inter-TAZ travels.

The R_{TT} metric may not be considered as a capacity-based indicator since it assumes a free-flow traffic speed, without accounting for demand on the road network and potential evolution before and after the event. However, this performance indicator is expected to provide a more refined picture of the network's functionality than the SCL indicator, especially in the case of a densely connected network with numerous alternate routes.

The multi-risk framework presented in Section 7.4.3 is then applied, thus requiring successive simulations of single earthquake events, single flood events and potential joint events. A plain Monte Carlo approach with 100 000 samples is adopted in the present case, due to the large number of vulnerable elements and the need to compute travel times for the R_{TT} indicator (i.e. such a metric is hardly computable using Bayesian Networks alone). As a result, the yearly probability of exceedance of the two performance indicators is presented is Figures 7.30 and 7.31, assuming a persistence time window $\Delta T_p = 1$ month.

The probabilistic loss curves that have been derived clearly show the profile of the single earthquake and flood risks in the studied area: flood events mostly occur for shorter return periods, thus disrupting the road network on a moderate scale, while earthquake events tend to induce widespread losses for long return periods. The multi-risk losses result from the aggregation of both single risks, as well as the potential cumulated damages when hazard events have a joint occurrence. The risk bias measure, which has been introduced in Equation 7.11, highlights the effect of cumulated damages on the aggregated losses. It may be seen as the difference between an analysis that accounts for multi-risk interactions and an analysis that simply sums the contributions of the single risk. For shorter return period, the bias measure is found to be in the order of magnitude of 1%, however it increases dramatically for extreme events (i.e. up to 10-20%): this observation is in agreement with the hypothesis that catastrophic infrastructure failures

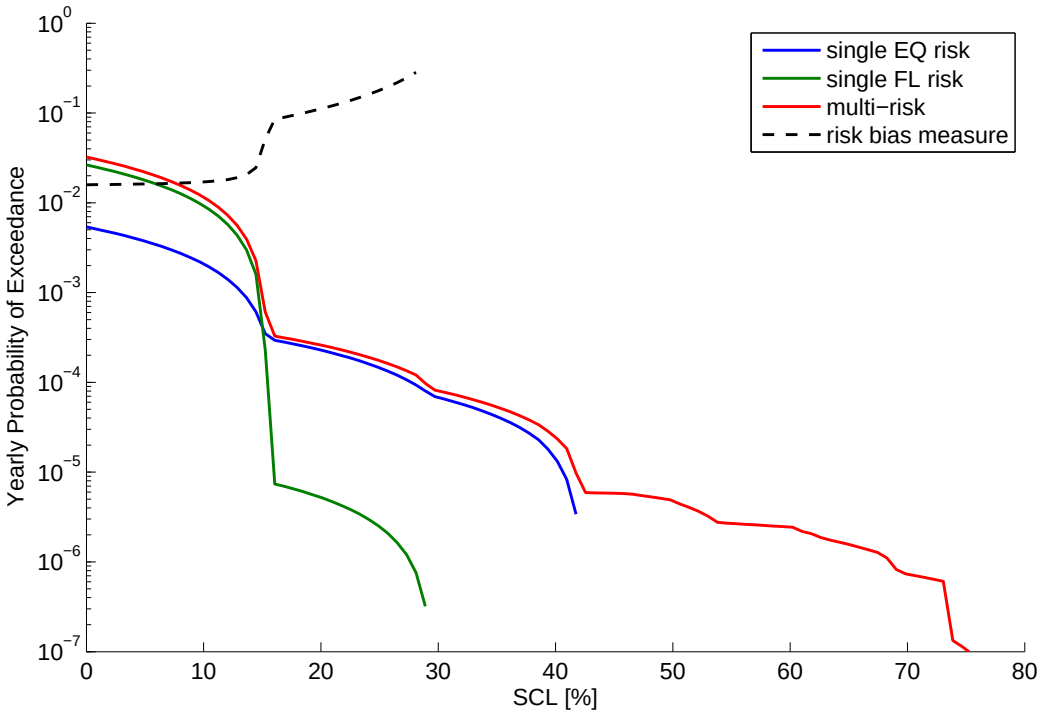

FIGURE 7.30: Yearly probability of exceedance of SCL.

usually result from unforeseen cascading events, such as interacting hazard loadings that are not taken into account in design guidelines.

Finally, it is worth noting that the R_{TT} indicator is able to better capture the response of the network for low-consequence events: for instance, the SCL curve shows a system degradation starting with $3 \cdot 10^{-2}$ yearly probability, while the use of the R_{TT} demonstrates that travel times may already be altered with a $8 \cdot 10^{-2}$ yearly probability. Measuring the losses with the R_{TT} indicator also reveals a clear threshold effect in the system (i.e. starting from $R_{TT} = 2.34$ at a $1.9 \cdot 10^{-2}$ probability), which may be used to identify potential mitigation measures in order to get a more evenly distributed degradation rate. Lastly, the risk bias measure appears to be higher when considering the SCL measure: road disconnections are only based on functionality levels FL3 and FL4, which show a strong interacting effect between earthquake and flood loadings (see Appendix J). On the other hand, the R_{TT} indicator is also influenced by functionality levels FL2, which is less dependent on the flood intensity.

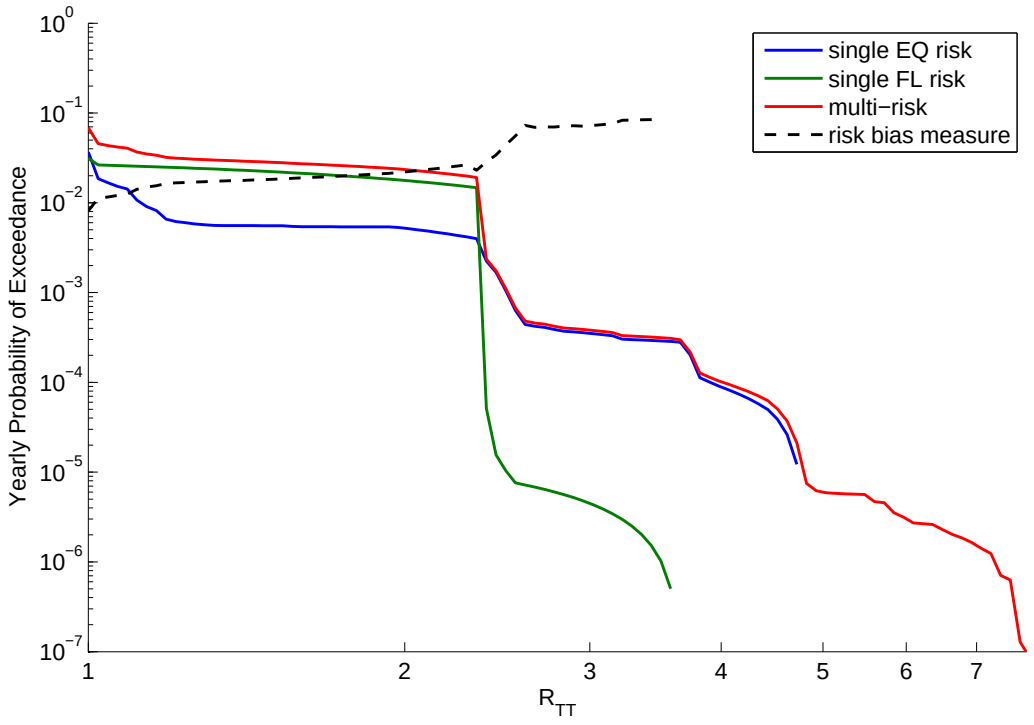

FIGURE 7.31: Yearly probability of exceedance of R_{TT}.

7.5 Conclusion

This Chapter has investigated the application of BNs to the risk assessment of infrastructure systems. To this end, exact BN formulations based on the identification of link sets have been benchmarked. It appears that these formulations do not fully avoid the current computational issues, since they mostly tend to displace the bottlenecks to other locations of the treatment chain. An alternative, using a simplified BN that is generated by simulation results, is therefore introduced, with the objective of treating complex and real-life systems and computing capacity- or serviceability-based performance indicators.

Then, the adoption of a BN model on a virtual, yet realistic, proof-of-concept example has led to a twofold result:

- The use of an exact inference algorithm provides access to an exact loss distribution, even in the case of extreme events, as opposed to Monte Carlo simulation schemes. Thanks to this feature, the effect of various sources of uncertainties can be quantified, by adding an evidence on the Bayesian nodes of interest and observing the updated loss distributions.

- The Bayesian Network presented here has been used to study multi-risk interactions at both hazard and fragility levels, thanks to the risk decomposition proposed by Selva [2013]. By changing the evidences in the BN (e.g. absence or not of the flood or earthquake events, change of the occurrence rate of the earthquake events, etc.), the different risk factors such as single risk, co-active risk, virtual risk and isolated risk, can be easily quantified by using the Bayesian inference.

The study of the effect of the different uncertainty sources has revealed that aleatory uncertainties due to the evaluation of the seismic hazard play an important part in the global risk assessment. Especially, the spatial correlation of the intra-event variability is an essential component of the analysis when considering a distributed system of interdependent components. It has been shown that the global risk may be underestimated when omitting this spatial dependency. Regarding epistemic uncertainties, their combined effect has also been found to be significant, especially for low-probability high-consequence events, even though additional uncertainty sources should be accounted for when performing a proper flood hazard assessment. The comparison between various models of fragility functions has also demonstrated that the proposed multi-hazard fragility functions accounting for functionality losses are key elements for an accurate estimation of losses in a multi-risk context.

The use of the persistence time window ΔT_p is critical in order to account for the risk interaction between floods and earthquakes. These two hazard events are independent; however it is possible to account for their joint occurrence within a given time frame that would see flood-damaged components being exposed to potential earthquakes. This time window has a huge effect on the risk bias measure, which identifies the discrepancies between a multi-risk analysis with interactions and superimposed single risk analyses. A bias in the order of 0.5%-1% has been estimated in the case of a simplified hypothetical network, which may seem quite modest, especially when comparing with all the other uncertainty sources involved. However, it should be noted that only four components in the considered infrastructure system account for flood-earthquake interactions (i.e. the three bridges and the road segment exposed to slope failure). On the other hand, the Bologna case-study, which contains many bridges exposed to multiple hazard, has provided a risk bias measure in the order of 1% for shorter return periods, while the bias tends to increase up to 10-20% in the case of extreme events. The complexity and the

size of the real-world case-study has prevented the use of an exact BN formulation (i.e. use of Monte Carlo simulations only), however further efforts should be devoted to the design of a couple BN – Monte Carlo approach, which would give access to elaborate performance indicators within a decision support system.

Chapter 8

Conclusions and Impact

8.1 Summary and Conclusions

The seismic risk assessment of road infrastructure systems has been the subject of several studies in the years 2000s, the most notable examples being the SYNER-G project in Europe [Pitilakis and the SYNER-G Consortium, 2009–2013] or the REDARS methodology in the United States [Werner et al., 2000]. The main steps of such a risk analysis may be summarised as follows:

- Seismic hazard assessment of the exposed area, usually through the generation of spatially correlated ground motion fields;
- Fragility analysis of the exposed physical elements, such as bridges;
- Performance assessment at the system level, such as the estimation of disconnected locations or the quantification of additional travel times.

At the element level, most existing fragility functions for bridges use a global damage scale, which renders the interpretation of physical damage in terms of functionality loss impractical and somewhat inaccurate. Moreover, in a multi-risk context, fragility functions for other hazard types, such as floods or ground failures, much scarcer. Finally, the use of different types of fragility models raises the issue of the harmonization between different damage scales and intensity measures.

Therefore a procedure has been proposed here for the derivation of hazard-harmonized fragility functions, which present the twofold merit of (i) directly providing the damage consequences in terms of functionality, through the definition of consistent system damage states, and (ii) using a single functional form that accommodates different types of intensity measures (i.e. different types of hazard loadings) and potentially accounts for cumulated damages. To this end, the proposed framework is based on the following steps:

1. Identification of the main failure modes that are susceptible to affect the various bridge components (e.g. piers, foundations, deck, etc.), in the case of earthquake, flood and ground failure hazards.

2. For each component failure mode, derivation of component fragility curves following state-of-the-art methods.

3. For each component failure mode, quantification of induced losses in terms of repair durations, functional losses (i.e. speed reduction and lane closure) and relative repair costs, through an expert-based survey sent to infrastructure managers.

4. Definition of functionality-consistent damage scales at the level of the bridge system, so that functional consequences can directly be deduced from the fragility functions, whatever the hazard type that triggered them.

5. Derivation of system fragility functions based on the component fragility curves, using BNs in order to account for correlation between component damages and joint failure events.

The use of BNs has proven to be very efficient and accurate for this task, with respect to more conventional system reliability methods. The modularity of this approach offers many choices to the modeller, such as computing the joint probability occurrence of damage events, or performing a Bayesian inference (i.e. backward analysis) in order to disaggregate the different source events that lead to a given event.

As a result, this procedure has been applied to a generic bridge model, for which a multi-hazard fragility surface has been derived: one intensity measure represents the loading due to ground shaking and earthquake-induced ground failure, while the other represents the effect of flood-induced scour and hydraulic lateral forces on the deck.

This fragility surface can then quantify the probability of occurrence of different system failure modes that are directly correlated to specific functional consequences. It is also valid for various combinations of hazard events (i.e. single events or combined events where an earthquake follows a flood), since it accounts for cumulated damages due to previous damage events.

In the case of single seismic risk assessment, the BN structure is slightly modified in order to develop probabilistic functionality curves for the same bridge model. The functionality loss models that have been obtained through the expert-based survey are used to create a new layer of nodes in the BN, which enables the probability of different levels of functionality loss to be estimated given various levels of seismic input.

On the other hand, at the road network level, the use of BNs has also been investigated following the previous developments by Bensi et al. [2011]. A benchmark of various BN formulations for exact inference has shown that this approach is not yet ready to tackle large and complex systems, let alone systems that require elaborate performance indicators based on flow capacity or serviceability. The computational bottlenecks that have been identified might be avoided by adopting a hybrid formulation that makes use of Monte-Carlo simulations. These simulation results are used to select only the most critical elements (i.e. bridges that are have the most impact on the network's performance) and to build CPTs by counting the occurrences of the different damage events. The resulting simplified BN is liberated from most computational issues and it seems to be able to satisfyingly emulate the probability updating that is obtained from exact inference. However, the results are limited by the sampling techniques used during the simulations, which may overlook extreme events. Therefore such an approach might not be the most suitable for the specific objectives of the present study, even though it may prove useful as a decision support system: the inference capabilities of the BN are helpful to infrastructure managers in an operational context, as opposed to pure Monte Carlo simulations.

Finally, a simple small-scale road network has been designed in order to demonstrate the ability of an exact BN formulation to perform a multi-risk analysis, with earthquake and flood hazards represented as independent events. Meanwhile, a Monte Carlo simulation approach has been adopted to perform the multi-risk assessment of a complex real-world road network. The multi-risk framework by Selva [2013], originally developed

for single independent assets, has been successfully applied to a spatially distributed system of interdependent elements. As expected, the persistence time window is an essential parameter for the treatment of multi-risk interactions. Different assumptions for the bridge fragility models have also been compared, from the most conventional to the most elaborate. The results validate the proposed framework for the derivation of hazard-harmonized fragility functions, which possess the double ability to account for cumulated damages from different hazard events and to directly express the consequences in terms of functionality.

8.2 Impact

A robust and original methodological framework has been developed for the multi-risk assessment of infrastructure systems, with an emphasis on the derivation of functionality-based multi-hazard fragility functions. While the present work has focused on road networks and bridges potentially exposed to earthquakes, floods and ground failures, the developed procedure is generic enough to be applied to a wide range of physical infrastructure systems or critical facilities (e.g. hospitals, emergency services, etc.), for any type of natural or man-made hazards.

The preliminary steps of the fragility analysis of bridges have led to the compilation of a table of potential failure modes, which may be used as a state-of-the-art reference for the construction of bridge damage scales. Similarly, different methods for the derivation of fragility curves have been investigated and demonstrated, thus revealing a need for further efforts in terms of quantifying vulnerability to floods or ground failures.

The quantification of functional consequences for each component failure mode has been made possible through a straightforward expert-based survey. Though incomplete and over-simplistic, such a task has led to the construction of a damage-loss correspondence matrix for bridge components. This original result constitutes a significant step towards the development of more robust functionality models, which have been shown to be essential tools within infrastructure risk analyses.

The main lesson that may be taken from the BN analysis of the example road network (see Chapter 7) is the key role played by multi-risk interactions. While network elements, such as bridges, or network systems are designed to withstand specific levels of single

hazard events (e.g. through seismic design or additional redundancies in the system), these measures might prove insufficient in the case of joint or cascading hazard events. In the case of a spatially distributed system, multi-risk effects are especially enhanced: hazard events occurring at the same location on the same element might increase its chance of failure, while hazards events occurring at different locations of the system might also induce the loss of the whole system, due to the interdependency between network elements.

Therefore the aforementioned results and the proposed method are expected to be of particular interest to infrastructure managers or catastrophe modellers. The application of this method to a given infrastructure will highlight its weakness with respect to multi-risk interactions, while yielding more accurate results thanks to the use of functionality-based fragility functions.

8.3 Recommendations for Future Work

While the present work has been mainly devoted to methodological developments, applications to real case-studies have been hindered by the lack of available data for the specification of an existing road network. Close interactions with infrastructure managers are necessary at this stage, due to the huge amount of data this is required by such analyses. However, the applications to the generic examples that have been presented in this study have still revealed the following gaps:

- The loss models based on the expert-based damage-functionality matrix are currently very coarse. They should be significantly improved by conducting a more robust and larger-scale elicitation process, which would involve a wider range of experts and infrastructure managers.
- For some component failure modes, especially for flood-related damages, there are barely any existing fragility functions or derivation methods. Moreover, seismic fragility curves appear to be the most advanced in terms of robustness and uncertainty treatment, with respect to other hazard types. Therefore significant efforts should be devoted to either the analytical derivation of flood fragility curves (e.g. treatment of fluid-structure interactions) or the collation of empirical data from past disasters.

- Similarly, in terms of hazard assessment, methods for the generation of seismic ground motion fields are rather mature and are able to account for various uncertainty sources, as well as spatial correlations. This is not the case of flood hazard assessment, where a more systematic approach should be adopted for the multi-risk analysis. Presently, the rational method that has been considered here appears to be too simplistic, while the uncertainties on its parameters should be properly quantified.

A more general issue lies in the applicability of BNs to any type of systems. It has been shown that the BN formulation for the derivation of system fragility functions at the bridge level is very robust and is able to deal with a large number of bridge components. On the other hand, the investigated BN formulations for infrastructure systems appear to be much more limited: such a difference is due to the complex structure of networks (i.e. presence of many link sets or cut sets) and to the additional hazard nodes that are needed for the generation of spatially distributed intensity measures. In other words, spatial variability - and more specifically spatial correlation - is one of the reasons the resulting BNs are very complex when assessing a spatially distributed infrastructure system (i.e. it requires the creation of many nodes in the BN in order to reproduce this correlation). The other computational bottleneck is due to the computation of the system performance based on the components' damage states, especially when a system does not mainly contain in-series or in-parallel components. As a result, the combination of these two effects has the potential of generating huge cliques of strongly interconnected nodes, so that their computation through an exact inference algorithm is often unfeasible.

Therefore the development of a BN procedure that would be able to avoid these computational issues remains the main challenge. The t-Naive BN formulation that has been described here might be a viable alternative, even though more extensive tests and validations are required.

Finally, the application of the proposed framework to other types of physical systems looks very promising, since it would lead to a fully harmonized 'system of systems', which would account for both multi-risk interactions and system interdependencies.

Appendix A

Glossary of Graph Theory Terms

This glossary defines the most common terms that are used throughout the thesis to describe graphs and Bayesian Networks. Most definitions have been taken from Wikipedia and Gross and Yellen [2004].

+ **acyclic**: A graph is acyclic if it has no cycles.

+ **adjacency matrix**: The adjacency matrix of a graph is a matrix whose rows and columns are both indexed by vertices of the graph, with a one in the cell for row i and column j when vertices i and j are adjacent, and a zero otherwise.

+ **adjacent**: The relation between two vertices that are both endpoints of the same edge.

+ **arc**: An edge of a directed graph, also sometimes called an arrow.

+ **child**: In a rooted tree, a child of a vertex v is a neighbor of v along an outgoing edge, one that is directed away from the root.

+ **clique**: A clique is a maximal complete subgraph, i.e. one that is not part of any larger complete subgraph.

+ **complete**: A complete graph is one in which every two vertices are adjacent: all edges that could exist are present.

+ **connected**: A connected graph is one in which each pair of vertices forms the endpoints of a path.

+ **DAG**: Abbreviation for directed acyclic graph, a directed graph without any directed cycles.

+ **directed**: A directed graph is one in which the edges have a distinguished direction, from one vertex to another.

+ **edge**: An edge is (together with vertices) one of the two basic units out of which graphs are constructed. Each edge has two vertices to which it is attached, called its endpoints. Edges may be directed or undirected.

+ **graph**: A system of vertices connected in pairs by edges. A graph G is often represented as $G(V, E)$, where V is the set of vertices and E the set of edges.

+ **incidence matrix**: The incidence matrix of a graph is a matrix whose rows are indexed by vertices of the graph, and whose columns are indexed by edges, with a one in the cell for row i and column j when vertex i and edge j are incident, and a zero otherwise.

+ **MCS**: Abbreviation for miminum cut-set, i.e. the smallest path whose disconnection ensures the disconnection between two given vertices.

+ **MLS**: Abbreviation for miminum link-set, i.e. the smallest path whose connection ensures the connection between two given vertices.

+ **neighbour**: A vertex that is adjacent to a given vertex.

+ **network**: A graph in which attributes (e.g. names) are associated with the nodes and/or edges.

+ **node**: A synonym for vertex.

+ **path**: A path is usually a sequence of vertices and edges, with both endpoints of an edge appearing adjacent to it in the sequence.

+ **root**: A designated vertex in a graph, particularly in directed graphs.

+ **sink**: A sink, in a directed graph, is a vertex with no outgoing edges.

+ **source**: A source, in a directed graph, is a vertex with no incoming edges.

+ **subgraph**: A subgraph of a graph G is another graph formed from a subset of the vertices and edges of G.

+ **undirected**: An undirected graph is a graph in which the two endpoints of each edge are not distinguished from each other.

+ **vertex**: A vertex (plural vertices) is (together with edges) one of the two basic units out of which graphs are constructed.

Appendix B

Regression using Generalized Linear Models

The Generalized Linear Model (GLM) is considered as a generalisation of the conventional linear regression and it is usually applied to cases where the errors of a set of response variables may not be expressed as a normal distribution. A GLM is defined by three components, namely:

- a probability distribution, which belongs to the family of exponential distributions;
- a linear predictor η, which is expressed as a linear combination of variables x_i through coefficients θ_i;
- a link function g, which defines the relation with the probability of having the response y given the x_i, i.e.: $\mathrm{P}\left(y|x_i\right) = g^{-1}\left(\eta\right)$

In the case where a GLM is used for the derivation of fragility curves, the response variable y corresponds to the discrete damage indicator, which is defined as follows:

$$\begin{cases} y_k = 1 & \text{if damage is reached} \\ y_k = 0 & \text{if not} \end{cases} \quad \text{for each simulation outcome k} \tag{B.1}$$

This sampling of binary success/failure occurrences corresponds to the Bernouilli or binomial distributions, therefore the following link functions are popular choices:

$$g(\mu) = \begin{cases} \Phi^{-1}(\mu) & \text{probit} \\ \log\left(\frac{\mu}{1-\mu}\right) & \text{logit} \\ \log\left[\log(1-\mu)\right] & \text{complementatry loglog} \end{cases} \tag{B.2}$$

The use of the probit as a link function constitutes an interesting way to express the fragility curvs as a lognormal distribution, so that the outcome of the regression may be compared to most available fragility curves, which are usually represented under the lognormal form. For illustration purposes, consider the outcome of n simulations, where the binary damage states y_k, for $k = 1 \ldots n$, are recorded. If a single-parameter fragility curve is derived (i.e. probability of damage expressed as a function of intensity measure im), the linear prediction may be expressed as follows:

$$\eta = \theta_0 + \theta_1 \cdot \log im \tag{B.3}$$

where θ_0 and θ_1 are the GLM regression coefficients, which may be quantified through various optimization algorithms, such as maximum likelihood methods.

The probability of reaching or exceeding the damage state (i.e. $y = 1$) given im can then be written as:

$$\mathrm{P}(ds \geq DS|im) = g^{-1}(\eta) \tag{B.4}$$

If the probit function is used, the damage probability becomes:

$$\mathrm{P}(ds \geq DS|im) = \Phi(\theta_0 + \theta_1 \cdot \log im) \tag{B.5}$$

As written in Chapter 2, the following functional form is usually proposed for a fragility curve under the lognormal assumption (see Equation 2.1):

$$\mathrm{P}(\mathrm{DS} \geq ds|im) = \phi\left(\frac{\log im - \log \alpha}{\beta}\right) \tag{B.6}$$

where α and β represent the mean and the standard deviation of the fragility curves, respectively.

Therefore, these fragility parameters may be obtained from the GLM regression parameters through a simple identification between Equations B.5 and B.6:

$$\begin{cases} \alpha = \exp\left(-\frac{\theta_0}{\theta_1}\right) \\ \beta = \frac{1}{\theta_1} \end{cases} \tag{B.7}$$

Appendix C

Survey Form of Functionality Losses

This Appendix presents an excerpt of the form that has been sent to various experts for the survey of functionality losses for bridges, as described in Chapter 3.

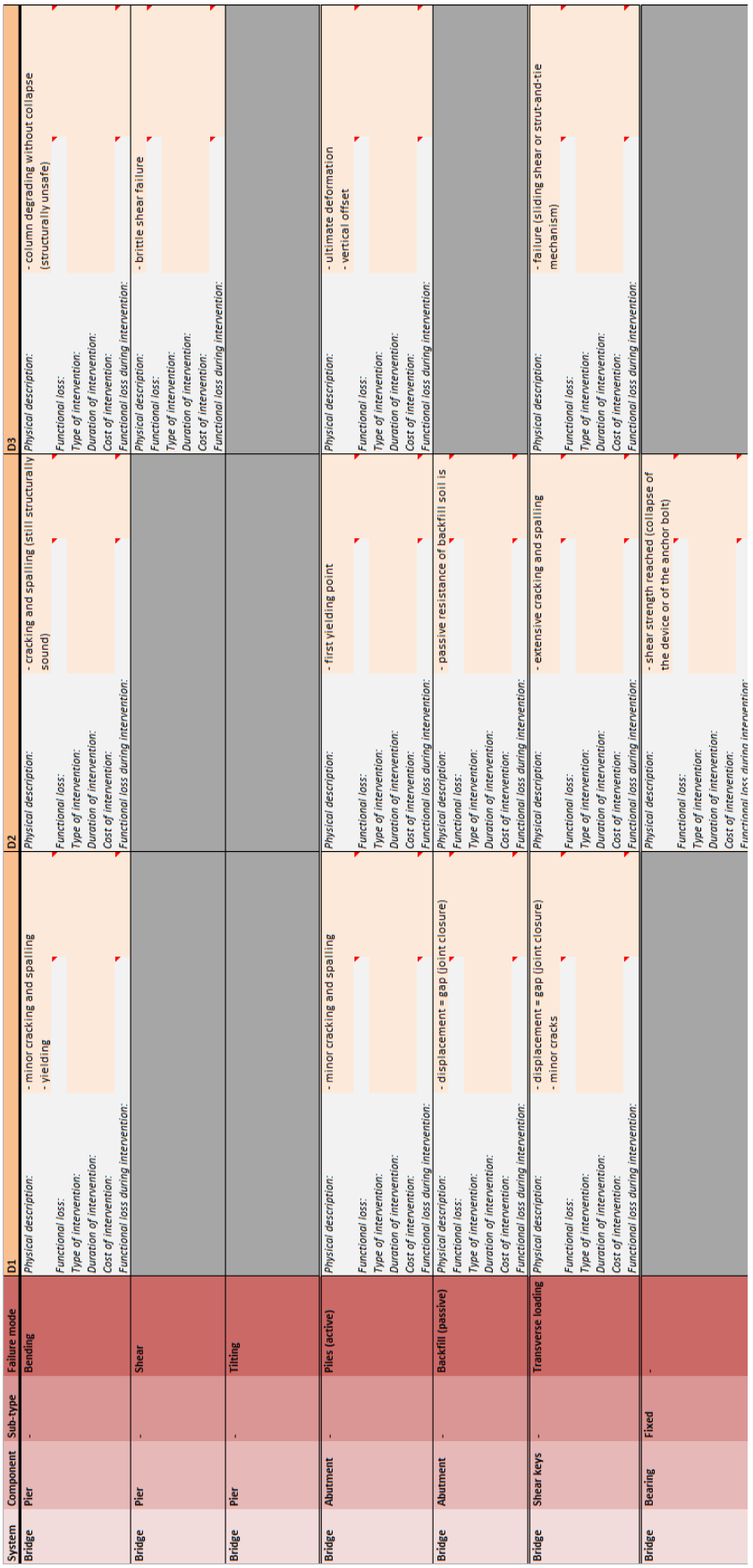

System	Component	Sub-type	Failure mode	D1		D2		D3	
Bridge	Pier	-	Bending	*Physical description:* *Functional loss:* *Type of intervention:* *Duration of intervention:* *Cost of intervention:* *Functional loss during intervention:*	- minor cracking and spalling - yielding	*Physical description:* *Functional loss:* *Type of intervention:* *Duration of intervention:* *Cost of intervention:* *Functional loss during intervention:*	- cracking and spalling (still structurally sound)	*Physical description:* *Functional loss:* *Type of intervention:* *Duration of intervention:* *Cost of intervention:* *Functional loss during intervention:*	- column degrading without collapse (structurally unsafe)
Bridge	Pier	-	Shear					*Physical description:* *Functional loss:* *Type of intervention:* *Duration of intervention:* *Cost of intervention:* *Functional loss during intervention:*	- brittle shear failure
Bridge	Pier	-	Tilting						
Bridge	Abutment	-	Piles (active)	*Physical description:* *Functional loss:* *Type of intervention:* *Duration of intervention:* *Cost of intervention:* *Functional loss during intervention:*	- minor cracking and spalling	*Physical description:* *Functional loss:* *Type of intervention:* *Duration of intervention:* *Cost of intervention:* *Functional loss during intervention:*	- first yielding point	*Physical description:* *Functional loss:* *Type of intervention:* *Duration of intervention:* *Cost of intervention:* *Functional loss during intervention:*	- ultimate deformation - vertical offset
Bridge	Abutment	-	Backfill (passive)	*Physical description:* *Functional loss:* *Type of intervention:* *Duration of intervention:* *Cost of intervention:* *Functional loss during intervention:*	- displacement = gap (joint closure)	*Physical description:* *Functional loss:* *Type of intervention:* *Duration of intervention:* *Cost of intervention:* *Functional loss during intervention:*	- passive resistance of backfill soil is		
Bridge	Shear keys	-	Transverse loading	*Physical description:* *Functional loss:* *Type of intervention:* *Duration of intervention:* *Cost of intervention:* *Functional loss during intervention:*	- displacement = gap (joint closure) - minor cracks	*Physical description:* *Functional loss:* *Type of intervention:* *Duration of intervention:* *Cost of intervention:* *Functional loss during intervention:*	- extensive cracking and spalling	*Physical description:* *Functional loss:* *Type of intervention:* *Duration of intervention:* *Cost of intervention:* *Functional loss during intervention:*	- failure (sliding shear or strut-and-tie mechanism)
Bridge	Bearing	Fixed	-			*Physical description:* *Functional loss:* *Type of intervention:* *Duration of intervention:* *Cost of intervention:* *Functional loss during intervention:*	- shear strength reached (collapse of the device or of the anchor bolt)		

FIGURE C.1: Excerpt of the bridge functionality survey form.

Appendix D

Expert-based Functionality Losses

This appendix details the results of the expert-based survey: as stated before, the following numerical values should be considered for illustrative purposes only, due to the scarcity of collected data.

TABLE D.1: Duration of repair operations (lower and upper bounds in days) for each of the component failure modes identified. Multiple lines for a given damage states indicate multiple propositions from the different groups of experts.

ID	Du-	Du+	ID	Du-	Du+	ID	Du-	Du+
1-D1	7	30	7-D2	15	15	13-D3	45	45
	14	14	7-D4	30	30	13-D4	60	60
1-D2	7	30	8-D1	15	15	14-D1	7	7
	30	30	8-D2	30	30	14-D4	30	30
1-D3	30	60	8-D4	30	30	15-D1	30	90
	60	60	9-D1	30	30		60	60
1-D4	7	30		15	15	16-D1	15	15
	150	150	9-D4	45	45		1	1
2-D3	7	30	10-D1	30	30		60	60
	60	60		15	15	17-D1	7	60
3-D4	30	60	10-D2	15	15		30	30
	75	75	10-D3	30	30	18-D1	7	60
4-D1	14	14	10-D4	60	60		30	30
4-D2	30	30	11-D1	30	30	19-D1	7	60
4-D3	150	150		15	15		30	30
5-D1	60	60	11-D2	30	30	20-D1	7	60
	30	30	11-D3	60	60		30	30
5-D2	60	120	12-D1	30	30	21-D1	120	120
	45	45		15	15		60	60
5-D4	60	60	12-D2	15	15	22-D1	7	7
6-D1	60	120	12-D3	30	30		15	15
	30	30	12-D4	60	60	23-D1	7	7
6-D2	60	60	13-D1	15	15		30	30
6-D3	90	90	13-D2	30	30			

TABLE D.2: Reduction of functionality in % (lower and upper bounds, either for proportion of closed lanes, speed reduction or vertical load capacity reduction) for each of the component failure modes identified. Multiple lines for a given damage states indicate multiple propositions from the different groups of experts. The 'emerg' index means that the infrastructure element is open for emergency vehicles only.

ID	Metric	FL-	FL+	ID	Metric	FL-	FL+
1-D1	speed	0%	0%	10-D2	speed	20%	20%
	speed	10%	10%	10-D3	speed	20%	20%
1-D2	speed	0%	0%	10-D4	speed	25%	25%
	speed	20%	20%	11-D1	speed	20%	20%
1-D3	load	40%	40%	11-D2	speed	20%	20%
	load	100%	100%	11-D3	speed	25%	25%
1-D4	closed	100%	100%	12-D1	speed	20%	20%
	load	100%	100%	12-D2	speed	20%	20%
2-D3	load	40%	40%	12-D3	speed	20%	20%
	load	100%	100%	12-D4	speed	25%	25%
3-D4	closed	100%	100%	13-D1	speed	20%	20%
	load	100%	100%	13-D2	speed	20%	20%
4-D1	speed	0%	0%	13-D3	speed	20%	20%
	speed	10%	10%	13-D4	speed	25%	25%
4-D2	speed	20%	20%	14-D1	speed	–	–
4-D3	closed	100%	100%	14-D4	closed	100%	100%
5-D1	speed	0%	0%	15-D1	closed	0%	100%
	speed	20%	20%		closed	100%	100%
5-D2	speed	20%	20%	16-D1	speed	25%	25%
	closed	50%	50%		emerg	–	–
5-D4	closed	100%	100%	17-D1	load	20%	20%
6-D1	speed	0%	0%		load	0%	100%
	speed	20%	20%	18-D1	closed	50%	50%
6-D2	load	25%	25%		load	0%	100%
6-D3	load	40%	40%	19-D1	load	20%	20%
7-D2	speed	25%	25%		load	0%	100%
7-D4	speed	25%	25%	20-D1	closed	50%	50%
8-D1	closed	0%	0%		load	0%	100%
8-D2	closed	50%	50%	21-D1	load	25%	25%
8-D4	speed	25%	25%		closed	100%	100%
9-D1	speed	20%	20%	22-D1	speed	0%	0%
9-D4	speed	25%	25%	23-D1	speed	0%	0%
10-D1	speed	20%	20%		speed	20%	20%

TABLE D.3: Reduction of functionality during repair operations in % (lower and upper bounds, either for proportion of closed lanes, speed reduction or vertical load capacity reduction) for each of the component failure modes identified. Multiple lines for a given damage states indicate multiple propositions from the different groups of experts. The 'emerg' index means that the infrastructure element is open for emergency vehicles only.

ID	Metric	FLI-	FLI+	ID	Metric	FLI-	FLI+
1-D1	speed	0%	0%	10-D3	closed	50%	50%
	speed	10%	10%	10-D4	closed	75%	75%
1-D2	speed	0%	0%	11-D1	speed	50%	50%
	speed	20%	20%		closed	50%	50%
1-D3	load	100%	100%	11-D2	closed	50%	50%
	load	40%	40%	11-D3	closed	75%	75%
1-D4	closed	100%	100%	12-D1	speed	50%	50%
	load	100%	100%		closed	50%	50%
2-D3	closed	100%	100%	12-D2	closed	50%	50%
	load	40%	40%	12-D3	closed	50%	50%
3-D4	closed	50%	50%	12-D4	closed	75%	75%
	closed	100%	100%	13-D1	closed	50%	50%
4-D1	speed	0%	0%	13-D2	closed	50%	50%
	speed	10%	10%	13-D3	closed	50%	50%
4-D2	speed	20%	20%	13-D4	closed	75%	75%
4-D3	closed	100%	100%	14-D1	closed	−%	−%
5-D1	closed	25%	25%	14-D4	closed	100%	100%
	closed	50%	50%	15-D1	closed	100%	100%
5-D2	closed	50%	50%		closed	25%	25%
	closed	50%	50%		emerg	−%	−%
5-D4	closed	100%	100%	16-D1	emerg	−%	−%
6-D1	closed	0%	0%		closed	50%	50%
	closed	50%	50%	17-D1	closed	0%	100%
6-D2	closed	50%	50%		load	20%	20%
6-D3	closed	50%	50%	18-D1	closed	0%	100%
7-D2	closed	50%	50%		closed	50%	50%
7-D4	closed	75%	75%	19-D1	closed	0%	100%
8-D1	closed	0%	0%		load	20%	20%
8-D2	closed	50%	50%	20-D1	closed	0%	100%
8-D4	closed	75%	75%		closed	50%	50%
9-D1	speed	50%	50%	21-D1	closed	100%	100%
	closed	50%	50%		speed	50%	50%
9-D4	closed	75%	75%	22-D1	speed	50%	50%
10-D1	speed	50%	50%		speed	20%	20%
	closed	50%	50%	23-D1	speed	0%	0%
10-D2	closed	50%	50%		speed	20%	20%

Appendix E

Component-Level Fragility Parameters

This appendix summarizes the fragility parameters that have been derived for the main bridge system described in Chapters 4 and 5.

TABLE E.1: Component-level fragility parameters for the three hazard types and for all affected bridge components. For EQ events and EQ-induced GF events, the IM of choice is PGA (peak ground acceleration) in m/s^2, while the flow discharge Q in m^3/s is used to represent FL events. In the y direction, since the bridge system has a symmetric behaviour, only the components representing the first half of the bridge are displayed.

	D1		D2			D1		D2	
Comp.	α	β	α	β	Comp.	α	β	α	β
FL									
De	3789.9	0.500	4433.1	0.436	Pf	285.77	0.574	847.62	0.530
EQx - scour D0									
P1	4.295	0.420	8.214	0.427	P2	4.514	0.0.415	8.531	0.430
A1	2.500	0.446	-	-	A2	2.569	0.391	-	-
B1	1.994	0.647	10.299	0.465	B2	4.083	0.746	Inf	1
B3	12.795	1.105	Inf	1	B4	Inf	1	Inf	1
B5	1.776	0.688	Inf	1	B6	2.660	0.471	10.752	0.419
EQx - scour D1									
P1	5.279	0.471	9.878	0.445	P2	5.336	0.479	10.001	0.438
A1	2.527	0.456	-	-	A2	2.517	0.426	-	-
B1	1.933	0.615	9.409	0.461	B2	3.628	0.737	Inf	1
B3	14.164	1.020	Inf	1	B4	Inf	1	Inf	1
B5	1.634	0.677	Inf	1	B6	2.639	0.504	9.982	0.416
EQx - scour D2									
P1	17.245	0.539	17.837	0.558	P2	17.245	0.539	17.837	0.558
A1	2.498	0.475	-	-	A2	2.498	0.475	-	-
B1	2.042	0.660	6.917	0.564	B2	2.892	0.618	17.997	1.021
B3	Inf	1	Inf	1	B4	Inf	1	Inf	1
B5	1.400	0.702	Inf	1	B6	2.597	0.519	6.468	0.543
EQy - scour D0 - fluvial flood D0									
P1	9.124	0.331	18.841	0.330	A1	2.422	0.482	-	-
Sh1	3.287	0.436	14.558	0.091	Sh2	3.767	0.450	Inf	1
Sh3	4.219	0.428	13.938	0.187					
EQy - scour D1 - fluvial flood D0									
P1	14.458	0.319	18.591	0.267	A1	2.389	0.488	-	-
Sh1	2.561	0.521	13.559	0.301	Sh2	3.036	0.445	18.919	0.286
Sh3	10.260	0.740	15.375	0.193					
EQy - scour D2 - fluvial flood D0									
P1	14.896	0.251	14.896	0.251	A1	2.385	0.495	-	-
Sh1	2.180	0.525	11.475	0.415	Sh2	2.663	0.437	14.446	0.183
Sh3	14.199	0.101	Inf	1					
EQy - scour D0 - fluvial flood D1									
P1	9.605	0.338	16.180	0.170	A1	2.317	0.459	-	-
Sh1	-	-	12.663	0.151	Sh2	-	-	12.998	0.149
Sh3	-	-	12.958	0.196					
EQy - scour D1 - fluvial flood D1									
P1	13.655	0.320	16.062	0.225	A1	2.334	0.464	-	-
Sh1	-	-	10.875	0.548	Sh2	-	-	14.764	0.128
Sh3	-	-	15.739	0.335					
EQy - scour D2 - fluvial flood D1									
P1	14.189	0.260	14.189	0.260	A1	2.362	0.483	-	-
Sh1	-	-	7.940	0.561	Sh2	-	-	Inf	1
Sh3	-	-	Inf	1					
GF									
Em1	1.962	0.700	4.120	0.700	Em2	1.962	0.700	4.120	0.700
Af1	12.617	1.032	-	-	Af2	12.617	1.032	-	-

Appendix F

Structure of the Bayesian Network for System Fragility Assessment

The formulation of a Bayesian Network for the reliability assessment of a bridge system (see Section 5.4) is detailed here, through the example of a system with six components (see Figure F.1).

F.1 Construction of the CPTs

Each Bayesian node in Figure F.1 is characterized by discrete states, in order to facilitate an exact inference of the probabilities (i.e. junction-tree algorithm). Therefore the CPT of each node, which provides the probability of occurrence of each state given the states of the parent nodes, must be specified when constructing the BN.

F.1.1 CPT for Node IM

This root node is defined with a unique, which represents the IM value (e.g. PGA) that is applied to the structural system. This parameter will be changed for each step when deriving the fragility function over a given IM range. Therefore the correponding CPT is reduced to its simplest expression, as shown in Table F.1.

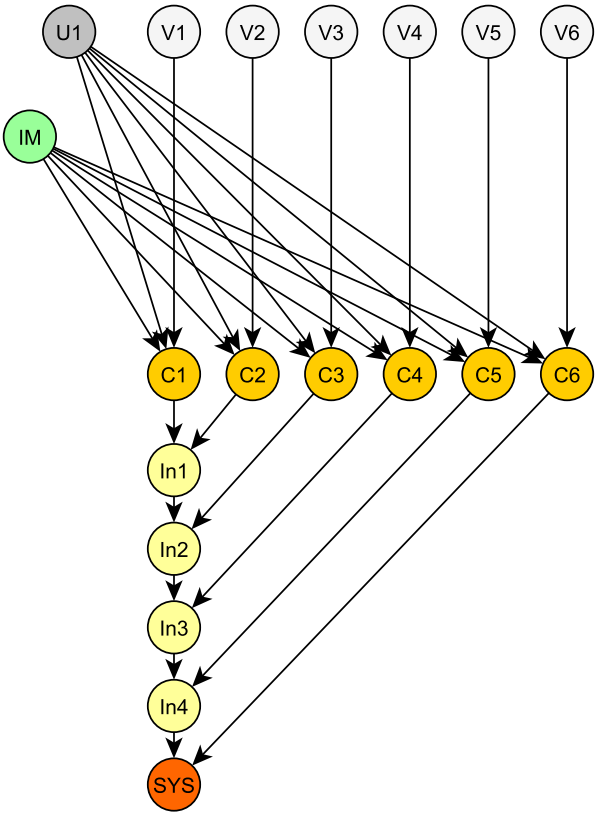

FIGURE F.1: Layout of the proposed BN for the reliability assessment of a 6-component system, with one CSRV U_1.

TABLE F.1: CPT for node **IM**.

IM state	CPT
im_{val}	1

F.1.2 CPT for Nodes U1 and V1...V6

All of these root nodes represent variables with a standard normal distribution. They are discretized into 19 discrete states, as shown in Table F.2.

F.1.3 CPT for Nodes C1...C6

Each component node $\mathbf{C_i}$ has three parents, namely **IM**, $\mathbf{U_1}$ and $\mathbf{V_i}$. If it is assumed that the component has binary states (i.e. 0 for *survival* and 1 for *failure*), then the CPT contains 722 elements (i.e. $1x19x19x2$), as shown in Table F.3.

The probability $p_{j,k}$ is equal to 1 if the following condition is verified, and 0 otherwise:

TABLE F.2: CPT for nodes **U** and **V**.

U/V state	CPT
−1.6449	0.0184
−1.2816	0.0312
−1.0364	0.0415
−0.8416	0.0498
−0.6745	0.0566
−0.5244	0.0619
−0.3853	0.0659
−0.2533	0.0688
−0.1257	0.0704
0	0.0710
0.1257	0.0704
0.2533	0.0688
0.3853	0.0659
0.5244	0.0619
0.6745	0.0566
0.8416	0.0498
1.0364	0.0415
1.2816	0.0312
1.6449	0.0184

TABLE F.3: CPT for nodes **C**. These lines are repeated for each value of j and k (number of discrete states in $\mathbf{U_1}$ and $\mathbf{V_i}$).

IM state	U_1 state	V_i state	C_i state	CPT
...	...	...	...	...
im_{val}	$u_{val,j}$	$v_{val,k}$	0	$1 - p_{j,k}$
...	...	...	...	...
im_{val}	$u_{val,j}$	$v_{val,k}$	1	$p_{j,k}$
...	...	...	...	...

$$\sqrt{1 - r_i^2} \cdot v_{val,k}^2 + r_i \cdot u_{val,j} \geq -\frac{\log im_{val} - \log \alpha_i}{\beta_i} \tag{F.1}$$

where α_i and β_i are the fragility parameters of component i (mean and standard deviation, respectively), and r_i is the correlation coefficient estimated from the Dunnet-Sobel approximation (see Chapter 5 for more details).

F.1.4 CPT for Nodes In1...In6 and SYS

The intermediate nodes $\mathbf{In_1}$ and the system node **SYS** have a similar structure. They are based on an in-series assembly of the components and they check whether the system is still in *survival* state (i.e. state 0) everytime a new component is added to the chain. Such a CPT contains 8 elements (i.e. $2x2x2$), as shown in Table F.4.

TABLE F.4: CPT for nodes **Int** and **SYS**.

Int_{i-1} state	C_i state	Int_i state	CPT
0	0	0	1
1	0	0	0
0	1	0	0
1	1	0	0
0	0	1	0
1	0	1	1
0	1	1	1
1	1	1	1

F.2 Application of the Junction-Tree Inference Algorithm

This section details the main steps of the junction-tree algorithm, applied to the example in Figure F.1.

F.2.1 Estimation of the Elimination Order

As stated in Section 5.4, finding the optimal elimination order (i.e. smallest clique sizes) constitutes an NP-hard problem, which cannot be solved on a large scale by automated procedures. Therefore most software such as the Bayes Net toolbox adopt a sequential algorithm, which finds the node that generates the fewest fill-in edges when eliminated, one node at a time: as a result, the solution may not represent the optimal elimination order that would be obtained when considering the BN globally.

The first step consists in the moralization of the BN graph (i.e. parent nodes are linked by undirected edges), as shown in Figure F.2.

The algorithm finds the node which elimination generates the fewest extra edges to add to the moralized graph (i.e. when a node is eliminated, all neighbours must be connected again with each other with undirected edges). In the case that some nodes would lead to the same number of fill-in edges (i.e. ties), the second criteria is the small clique size that is generated (i.e. size of the neighbour nodes that are assembled as a clique). The step-by-step elimination algorithm for the studied example is detailed in Table F.5.

F.2.2 Construction of the Junction Tree

The elimination order that has been detailed above is then used to identify the cliques of nodes that are created: when a given node is eliminated, it is assembled into a clique

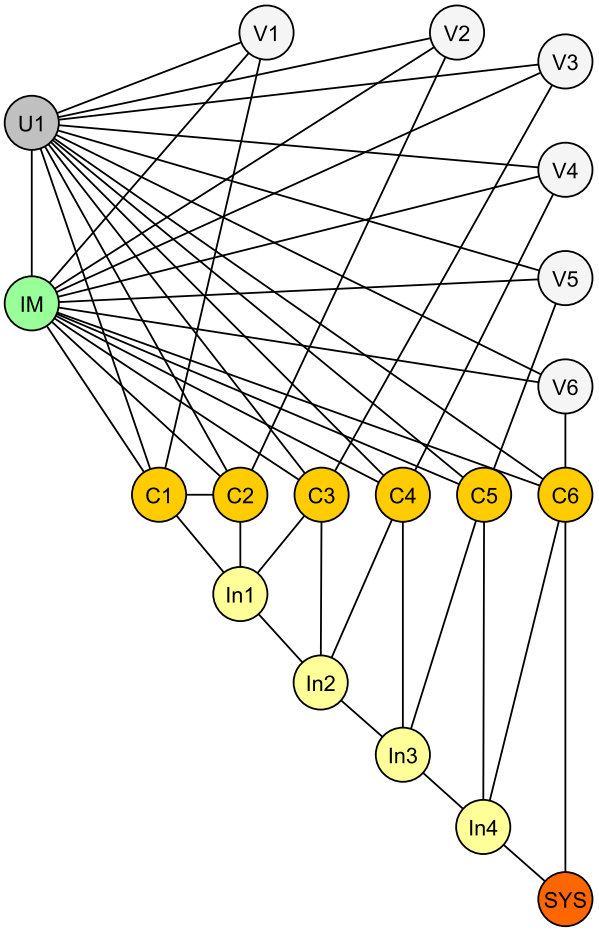

FIGURE F.2: Layout of the moralized BN.

along with its neighbours (i.e. all nodes that are connected to the eliminated node through an edge). When a node elimination leads to a clique that is a sub-part of a previously assemble clique, it is not added to thej unction tree. Following these rules, the elimination order from Table F.5 leads to the construction of the junction-tree in Figure F.3.

With the selected elimination order, 12 cliques are created and are connected through separator variables (i.e. the nodes that are common to both cliques). The potential of each clique must then be computed and stored into multi-dimensional matrices: a potential refers to all possible joint probabilities that may be found within a clique (i.e. the combinations of all node states). The objective of an optimal elimination order is to limit the size of the potentials to be computed: in the present example, this operation amounts to 4 964 joint probabilities (i.e. the sum of the element sizes over the 12 cliques). One of the main advantages of the junction-tree algorithm is that, once the junction tree

TABLE F.5: Step-by-step elimination algorithm, where the best canditate nodes for the first and second criteria are detailed.

Step	Fewest fill-in edges *(number)*	Smallest clique *(size)*	Eliminated node
1	V_1...V_6, SYS (*0*)	SYS (*8*)	SYS
2	V_1...V_6 (*0*)	V_1...V_6 (*722*)	V_1
3	V_2...V_6 (*0*)	V_2...V_6 (*722*)	V_2
4	V_3...V_6 (*0*)	V_3...V_6 (*722*)	V_3
5	V_4...V_6 (*0*)	V_4...V_6 (*722*)	V_4
6	V_5, V_6 (*0*)	V_5, V_6 (*722*)	V_5
7	V_6 (*0*)	–	V_6
8	C_1, C_2, C_6, In_4 (*2*)	In_4 (*16*)	In_4
9	C_1, C_2, C_6 (*2*)	C_1, C_2, C_6 (*152*)	C_1
10	C_2, C_6 (*2*)	C_2 (*76*)	C_2
11	C_6, In_1 (*2*)	C_6, In_1 (*152*)	C_6
12	C_5, In_1 (*2*)	C_5 (*76*)	C_5
13	In_1, In_3 (*2*)	In_1, In_3 (*152*)	In_1
14	C_3, In_3 (*2*)	C_3 (*76*)	C_3
15	IM, U_1, In_2, In_3 (*2*)	IM, U_1, In_2, In_3 (*152*)	IM
16	U_1 (*0*)	–	U_1
17	C_4, In_2, In_3 (*0*)	C_4, In_2, In_3 (*8*)	C_4
18	In_2, In_3 (*0*)	In_2, In_3 (*4*)	In_2
19	In_3 (*0*)	–	In_3

is built, it can be used to perform inference on any node without the need to redo this step.

F.2.3 Bayesian Inference

Bayesian inference is carried out by selecting one or more nodes as evidence nodes (i.e. a state of the node is preset) and by propagating this evidence through the junction tree. The updated probabilities of the states of any nodes can then be observed.

In the present example, **IM** is considered as the evidence node: however, since this node has been defined with only one state, the distribution of the evidence has no consequence on the structure of the clique potentials. In the case where a multi-state node is considered as an evidence, the dimensions of the potentials that contain this node are reduced in order to consider only the state of the node that is entered as evidence. The junction tree is then used to propagate the evidence up to the output node (here, **SYS**).

The updated probabilities at the output node are collected by marginilazing the potential of a clique that contains the given node. For better computational performances, the clique with the smallest size that contains the output node is chosen. In the present

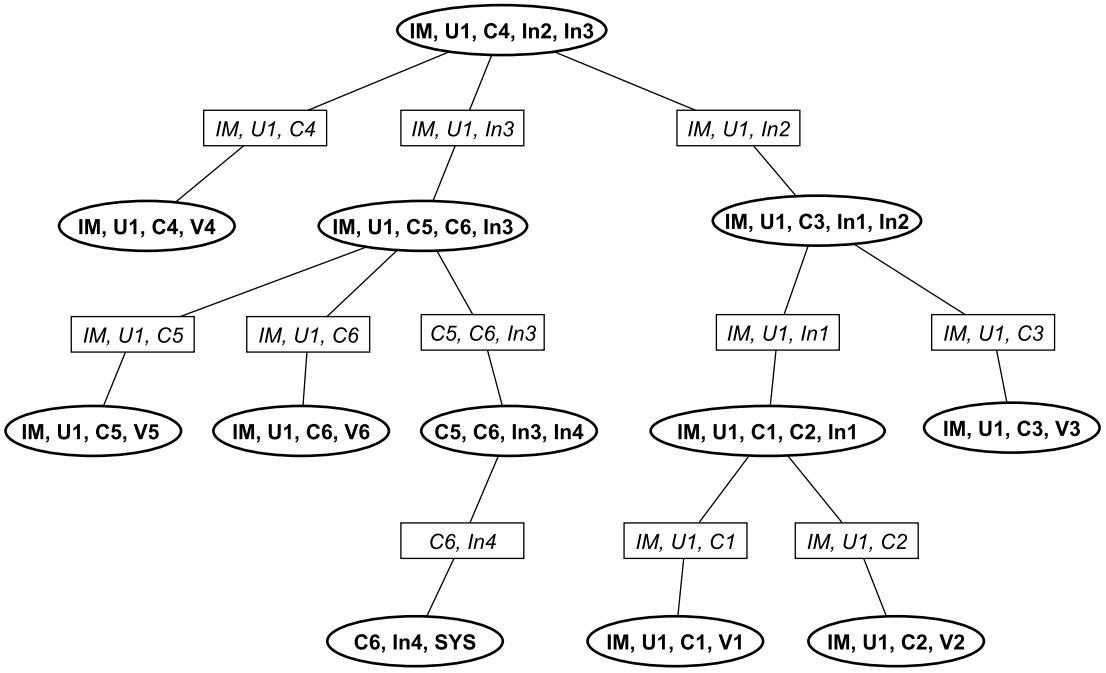

FIGURE F.3: Junction-tree of the BN, containing the cliques (bolded spherical shapes) and the separators (rectangles).

TABLE F.6: Marginalization of the potential of clique 1, with respect to node **SYS**.

Joint probabilities				
	$\mathbf{C_6} = 0$		$\mathbf{C_6} = 1$	
	$\mathbf{In_4} = 0$	$\mathbf{In_4} = 1$	$\mathbf{In_4} = 0$	$\mathbf{In_4} = 1$
$\mathbf{SYS} = 0$	$P\left(\overline{sys}, \overline{c_6}, \overline{in_4}\right)$	$P\left(\overline{sys}, \overline{c_6}, in_4\right)$	$P\left(\overline{sys}, c_6, \overline{in_4}\right)$	$P\left(\overline{sys}, c_6, in_4\right)$
$\mathbf{SYS} = 1$	$P\left(sys, \overline{c_6}, \overline{in_4}\right)$	$P\left(sys, \overline{c_6}, in_4\right)$	$P\left(sys, c_6, \overline{in_4}\right)$	$P\left(sys, c_6, in_4\right)$
Marginal probabilities				
$\mathbf{SYS} = 0$	$P\left(\overline{sys}\right) = P\left(\overline{sys}, \overline{c_6}, \overline{in_4}\right) + P\left(\overline{sys}, \overline{c_6}, in_4\right) + P\left(\overline{sys}, c_6, \overline{in_4}\right) + P\left(\overline{sys}, c_6, in_4\right)$			
$\mathbf{SYS} = 1$	$P\left(sys\right) = P\left(sys, \overline{c_6}, \overline{in_4}\right) + P\left(sys, \overline{c_6}, in_4\right) + P\left(sys, c_6, \overline{in_4}\right) + P\left(sys, c_6, in_4\right)$			

example, the updated probabilities of **SYS** are extracted from clique number 1 (see Table F.6), by computing the marginal probabilities of the states of **SYS**.

Appendix G

GMPEs used for Uncertainty Quantification

This section describes the four GMPEs that have been selected in order to derive a three-branch representative GMPE, according to the method by Atkinson and Adams [2013].

G.1 GMPE by Akkar et al. [2014a]

The ground-motion parameter Y, expressed in g, is broken down into a reference term and a site-related term:

$$\log Y = \log Y_{REF} + \log S \tag{G.1}$$

where:

$$\log Y_{REF} = \begin{cases} a_1 + a_2\,(M - 6.75) + a_3\,(8.5 - M)^2 \\ + \left[a_4 + a_5\,(M - 6.75)\right] \log \sqrt{R^2 + a_6^2} + a_8 F_N + a_9 F_R & \text{if } M \leq 6.75 \\ \\ a_1 + a_7\,(M - 6.75) + a_3\,(8.5 - M)^2 \\ + \left[a_4 + a_5\,(M - 6.75)\right] \log \sqrt{R^2 + a_6^2} + a_8 F_N + a_9 F_R & \text{if } M > 6.75 \end{cases} \tag{G.2}$$

and:

$$\log S = \begin{cases} b_1 \log\left(V_{s,30}/V_{REF}\right) + b_2 \log\left[\frac{PGA_{REF} + c(V_{s,30}/V_{REF})^n}{(PGA_{REF}+c)(V_{s,30}/V_{REF})^n}\right] & \text{if } V_{s,30} \leq V_{REF} \\ b_1 \log\left[\frac{\min(V_{s,30};V_{CON})}{V_{REF}}\right] & \text{if } V_{s,30} > V_{REF} \end{cases} \tag{G.3}$$

The parameters of this GMPE are detailed in Table G.1, for $Y = PGA$ and $r = r_{epi}$. The F_i variables represent the fault mechanism, i.e. normal ($F_N = 1$ and $F_R = 0$), reverse ($F_N = 0$ and $F_R = 1$) or strike-slip ($F_N = F_R = 0$).

TABLE G.1: Parameters of the GMPE by Akkar et al. [2014a].

Parameter	Value	Parameter	Value
a_1	2.52977	b_1	−0.41997
a_2	0.0029	b_2	−0.28846
a_3	−0.05496	c	2.5
a_4	−1.31001	n	3.2
a_5	0.2529	V_{REF}	750 m/s
a_6	7.5	V_{CON}	1 000 m/s
a_7	−0.5096	σ_{intra}	0.6375
a_8	−0.1091	σ_{inter}	0.3581
a_9	0.0937		

G.2 GMPE by Bindi et al. [2014]

The ground-motion parameter Y, expressed in cm/s^2, is broken down into a distance term, a magnitude term, a site term and a style-of-faulting term:

$$\log_{10} Y = e_1 + F_D + F_M + F_S + F_{sof} \tag{G.4}$$

where:

$$F_D = [c_1 + c_2 (M - 5.5)] \log_{10} \sqrt{r^2 + h^2} - c_3 \left(\sqrt{r^2 + h^2} - 1 \right) \tag{G.5}$$

$$F_M = \begin{cases} b_1 (M - 6.75) + b_2 (8.5 - M)^2 & \text{if } M \leq 6.75 \\ b_3 (M - 6.75) & \text{if } M > 6.75 \end{cases} \tag{G.6}$$

$$F_S = \gamma \log_{10} (V_{s,30}/800) \tag{G.7}$$

$$F_{sof} = f_1 E_1 + f_2 E_2 + f_3 E_3 \tag{G.8}$$

The parameters of this GMPE are detailed in Table G.2, for $Y = PGA$ and $r = r_{jb}$. The E_i variables represent the fault mechanism, i.e. normal ($E_1 = 1$ and $E_2 = E_3 = 0$), reverse ($E_2 = 1$ and $E_1 = E_3 = 0$), strike-slip ($E_3 = 1$ and $E_1 = E_2 = 0$) or unspecified ($E_1 = E_2 = E_3 = 0$).

TABLE G.2: Parameters of the GMPE by Bindi et al. [2014].

Parameter	Value	Parameter	Value
e_1	3.32819	b_3	0
c_1	−1.2398	γ	−0.3019
c_2	0.21732	f_1	−0.03977
c_3	0.001186	f_2	0.077525
h	5.26486	f_3	−0.03776
b_1	−0.0855	σ_{intra}	0.282398
b_2	−0.09256	σ_{inter}	0.149977

G.3 GMPE by Bora et al. [2014]

This GMPE is based on the random vibration theory, which is used to predict the response spectral ordinates of a SDOF oscillator for an input ground motion of finite duration. Such a framework requires the estimation of the Fourier amplitude spectrum (FAS), Y_{FAS}, and of the ground motion duration, D_{gm}, as illustrated in Figure G.1.

The variables D_{gm} and Y_{FAS} are empirically estimated from earthquake records, under the following functional forms:

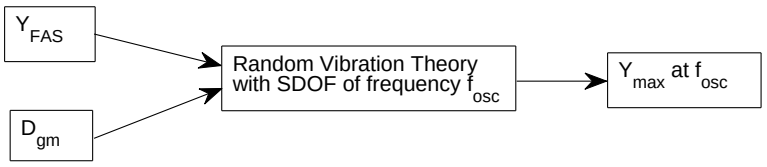

FIGURE G.1: Estimation of peak ground-motion parameter Y_{max} from Y_{FAS} and D_{gm} (adapted from Bora et al. [2014]).

$$\log D_{gm} = b_1 + b_2 M + (b_3 + b_4 M) \log \sqrt{r^2 + b_5^2} + b_6 \log V_{s,30} \tag{G.9}$$

$$\log Y_{FAS} = c_1 + c_2 M + c_3 M^2 + (c_4 + c_5 M) \log \sqrt{r^2 + c_6^2} - c_7 \sqrt{r^2 + c_6^2} + c_8 \log V_{s,30} \tag{G.10}$$

The parameters of these regression equations are detailed in Table G.3, for $Y = PGA$ and $r = r_{jb}$.

TABLE G.3: Parameters of the GMPE by Bora et al. [2014].

Parameter	Value	Parameter	Value
b_1	−2.4805	c_4	−4.4669
b_2	0.7907	c_5	0.3654
b_3	1.3711	c_6	8.9008
b_4	−0.1297	c_7	0
b_5	5.3554	c_8	0.6137
b_6	−0.3445	$\sigma_{D_{gm},intra}$	0.4809
c_1	−3.9567	$\sigma_{D_{gm},inter}$	0.3179
c_2	−0.7322	$\sigma_{Y_{FAS},intra}$	1.7329
c_3	0.0964	$\sigma_{Y_{FAS},inter}$	1.2349

G.4 GMPE by Derras et al. [2014]

The ground-motion parameter Y, expressed in m/s^2, takes the following form:

$$\log_{10} Y = \frac{1}{2} D_3 \left(T_{max} - T_{min}\right) + T_{min} \tag{G.11}$$

where:

$$D_3 = \mathbf{W_2} \cdot \tanh \mathbf{D_2} + b_2 + 1; \tag{G.12}$$

$$\mathbf{D_2} = \mathbf{W_1} \cdot \mathbf{D_1} + \mathbf{b_1}; \tag{G.13}$$

$$\mathbf{D_1} = 2\frac{\mathbf{P} - \mathbf{P_{min}}}{\mathbf{P_{max}} - \mathbf{P_{min}}} - 1; \tag{G.14}$$

The input parameters are specified in the vector P, which is bounded by vectors $\mathrm{P_{min}}$ and $\mathrm{P_{max}}$:

$$\mathbf{P} = \begin{pmatrix} \log_{10} r \\ M \\ \log_{10} V_{s,30} \\ h \\ F \end{pmatrix}; \quad \mathbf{P_{min}} = \begin{pmatrix} -1 \\ 3.6 \\ 1.964 \\ 0 \\ 1 \end{pmatrix}; \quad \mathbf{P_{max}} = \begin{pmatrix} 2.738 \\ 7.6 \\ 3.204 \\ 25 \\ 3 \end{pmatrix} \tag{G.15}$$

The weighting matrices are the following, for $Y = PGA$:

$$\mathbf{W_1} = \begin{pmatrix} 2.648 & -1.070 & 0.174 & 0.092 & -0.014 \\ -1.909 & -0.535 & -0.705 & 0.168 & -0.027 \\ 0.204 & 1.781 & -0.080 & 0.014 & 0.062 \\ -0.693 & 0.442 & 0.776 & -0.032 & -0.163 \\ 0.016 & 0.218 & -1.606 & -0.042 & 0.026 \end{pmatrix}; \quad \mathbf{W_2} = \begin{pmatrix} -0.541 \\ 0.254 \\ 0.11 \\ 0.076 \\ -0.02 \end{pmatrix}^t \tag{G.16}$$

The rest of the GMPE coefficients is presented below, for $Y = PGA$:

$$\mathbf{b_1} = \begin{pmatrix} -1.271 \\ 1.513 \\ 0.591 \\ -0.127 \\ -0.416 \end{pmatrix}; \quad b_2 = -0.143; \quad T_{min} = -2.979; \quad T_{max} = 0.981 \tag{G.17}$$

The derivation of this GMPE has led to the definition of intra-event and inter-event standard deviations, respectively $\sigma_{intra} = 0.267$ and $\sigma_{inter} = 0.155$.

Appendix H

Proposed Representative GMPE

This appendix details the values of the proposed three-branch GMPE, which cannot be represented under a functional form.

TABLE H.1: Predicted PGA [m/s^2] from the proposed three-branch representative GMPE (median branch).

	$\mathbf{M_w}$							
$\mathbf{R_{epi}}$ [km]	**4.0**	**4.5**	**5.0**	**5.5**	**6.0**	**6.5**	**7.0**	**7.5**
1.26	0.696	1.102	1.699	2.537	3.474	4.474	5.353	6.110
1.58	0.670	1.070	1.659	2.489	3.464	4.462	5.341	6.097
2.00	0.636	1.028	1.607	2.423	3.448	4.444	5.321	6.077
2.51	0.594	0.975	1.541	2.342	3.403	4.417	5.291	6.046
3.16	0.543	0.906	1.453	2.233	3.268	4.375	5.247	6.001
3.98	0.481	0.819	1.337	2.086	3.097	4.315	5.181	5.933
5.01	0.411	0.717	1.195	1.897	2.866	4.147	5.089	5.838
6.31	0.337	0.603	1.029	1.666	2.565	3.813	4.964	5.710
7.94	0.264	0.486	0.852	1.411	2.212	3.375	4.806	5.547
10.00	0.199	0.376	0.677	1.148	1.834	2.850	4.410	5.349
12.59	0.145	0.279	0.517	0.901	1.468	2.309	3.706	5.125
15.85	0.102	0.201	0.382	0.684	1.138	1.810	2.915	4.881
19.95	0.071	0.141	0.274	0.504	0.860	1.385	2.210	4.163
25.12	0.049	0.097	0.193	0.363	0.635	1.040	1.647	2.988
31.62	0.033	0.067	0.133	0.256	0.460	0.769	1.219	2.083
39.81	0.023	0.045	0.091	0.178	0.327	0.560	0.897	1.474
50.12	0.015	0.031	0.062	0.122	0.230	0.403	0.656	1.061
63.10	0.010	0.021	0.042	0.084	0.159	0.286	0.477	0.772
79.43	0.007	0.014	0.029	0.057	0.110	0.202	0.344	0.565
100.00	0.005	0.010	0.020	0.039	0.075	0.141	0.247	0.413
125.89	0.003	0.007	0.013	0.027	0.052	0.098	0.176	0.302
158.49	0.002	0.005	0.009	0.018	0.036	0.068	0.125	0.220
199.53	0.001	0.003	0.006	0.013	0.025	0.048	0.089	0.160

TABLE H.2: Predicted PGA [m/s^2] from the proposed three-branch representative GMPE (lower branch).

	$\mathbf{M_w}$							
$\mathbf{R_{epi}}$ [km]	**4.0**	**4.5**	**5.0**	**5.5**	**6.0**	**6.5**	**7.0**	**7.5**
1.26	0.470	0.840	1.393	2.194	3.098	3.790	4.298	4.776
1.58	0.467	0.829	1.367	2.154	3.103	3.801	4.306	4.779
2.00	0.460	0.812	1.335	2.098	3.110	3.817	4.317	4.781
2.51	0.448	0.788	1.292	2.033	3.090	3.843	4.335	4.784
3.16	0.426	0.749	1.232	1.949	2.981	3.880	4.359	4.784
3.98	0.392	0.694	1.147	1.831	2.841	3.921	4.388	4.776
5.01	0.343	0.620	1.035	1.672	2.649	3.847	4.410	4.745
6.31	0.283	0.529	0.900	1.470	2.380	3.580	4.383	4.663
7.94	0.220	0.431	0.751	1.238	2.038	3.200	4.231	4.493
10.00	0.163	0.335	0.601	0.998	1.657	2.716	3.793	4.21
12.59	0.116	0.249	0.465	0.775	1.290	2.172	3.158	3.825
15.85	0.081	0.179	0.349	0.586	0.976	1.654	2.546	3.408
19.95	0.057	0.125	0.256	0.434	0.725	1.226	2.007	2.820
25.12	0.040	0.086	0.183	0.318	0.533	0.899	1.532	2.134
31.62	0.028	0.059	0.126	0.229	0.391	0.658	1.132	1.646
39.81	0.020	0.040	0.084	0.162	0.284	0.481	0.823	1.275
50.12	0.014	0.028	0.055	0.110	0.203	0.350	0.595	0.966
63.10	0.009	0.019	0.037	0.073	0.140	0.249	0.426	0.708
79.43	0.006	0.013	0.025	0.048	0.093	0.171	0.299	0.504
100.00	0.003	0.009	0.017	0.032	0.061	0.113	0.204	0.353
125.89	0.002	0.005	0.012	0.021	0.040	0.074	0.136	0.244
158.49	0.001	0.003	0.008	0.015	0.026	0.048	0.089	0.166
199.53	0.001	0.002	0.005	0.010	0.018	0.033	0.061	0.116

TABLE H.3: Predicted PGA [m/s^2] from the proposed three-branch representative GMPE (upper branch).

	$\mathbf{M_w}$							
$\mathbf{R_{epi}}$ [km]	**4.0**	**4.5**	**5.0**	**5.5**	**6.0**	**6.5**	**7.0**	**7.5**
1.26	1.032	1.446	2.072	2.933	3.895	5.280	6.668	7.816
1.58	0.962	1.382	2.014	2.876	3.866	5.239	6.625	7.780
2.00	0.879	1.301	1.936	2.798	3.823	5.173	6.558	7.724
2.51	0.789	1.206	1.838	2.698	3.749	5.076	6.459	7.642
3.16	0.691	1.094	1.713	2.560	3.583	4.934	6.315	7.526
3.98	0.589	0.967	1.559	2.377	3.375	4.748	6.117	7.371
5.01	0.491	0.829	1.378	2.151	3.100	4.470	5.872	7.184
6.31	0.400	0.687	1.177	1.889	2.764	4.061	5.623	6.992
7.94	0.318	0.548	0.967	1.607	2.401	3.560	5.459	6.847
10.00	0.244	0.421	0.762	1.321	2.03	2.991	5.128	6.797
12.59	0.181	0.313	0.576	1.046	1.67	2.454	4.349	6.866
15.85	0.129	0.225	0.418	0.798	1.329	1.981	3.337	6.993
19.95	0.089	0.159	0.293	0.585	1.021	1.565	2.433	6.145
25.12	0.060	0.110	0.203	0.414	0.756	1.203	1.771	4.184
31.62	0.039	0.075	0.141	0.286	0.541	0.898	1.312	2.637
39.81	0.026	0.051	0.099	0.196	0.377	0.652	0.977	1.706
50.12	0.017	0.034	0.069	0.136	0.260	0.464	0.724	1.166
63.10	0.012	0.023	0.048	0.096	0.182	0.329	0.533	0.842
79.43	0.009	0.015	0.033	0.068	0.130	0.238	0.396	0.632
100.00	0.007	0.011	0.023	0.048	0.094	0.175	0.298	0.484
125.89	0.005	0.008	0.015	0.033	0.068	0.131	0.227	0.373
158.49	0.004	0.006	0.011	0.023	0.049	0.098	0.174	0.291
199.53	0.003	0.004	0.007	0.016	0.035	0.071	0.129	0.219

Appendix I

Underlying Equations in the Bayesian Network for Multi-Risk Assessment

This Appendix details the CPTs and equations that are defined for each node of the multi-risk Bayesian Network proposed in Chapter 7 (see Figure 7.19).

I.1 Earthquake Magnitude Node M

It is a root node of 11 states ($M_{low} \leq m_i \leq M_{up}$ for $i = 1 \dots 10$; $m_i = -\infty$ for i = 11), expressing the probability of occurrence of magnitude mi. For each magnitude value, the probability of occurrence is given by the Gutenberg-Richter distribution:

$$\begin{cases} P(m_i) = \gamma_0 \cdot \frac{\exp(-\beta \cdot m_i) - \exp(-\beta \cdot M_{up})}{\exp(-\beta \cdot M_{low}) - \exp(-\beta \cdot M_{up})} & \text{for } i = 1 \dots 10 \\ P(m_i) = 1 - \sum_{j=1}^{10} P(m_j) & \text{for } i = 11 \end{cases} \tag{I.1}$$

M_{low}, M_{up}, γ_0 and β are the lower and upper magnitude bounds, the mean annual rate of earthquake events and the b-value, respectively.

I.2 Epicentre Node Epi

It is a root node of 20 states, representing the earthquake generating area through a discretized grid of locations epi_i. The epicentre locations are assumed to be uniformly distributed:

$$P\left(epi_i\right) = 1/20 \quad \text{for } i = 1 \ldots 20 \tag{I.2}$$

I.3 Epicentre Distance Nodes R1...R11

It is a node of 20 states: the corresponding r_i values are linearly distributed between r_{min} and r_{max}, which are evaluated as the extreme distances of the problem (i.e. combination of closest/furthest epicentre location with the position of the infrastructure element considered). The probability of having epicentral distance r_i is conditional on the epicentre location epi_j:

$$\begin{cases} P\left(r_i|epi_j\right) = 1 & \text{if element-epicentre distance } \in [r_{i-}; r_{i+}] \\ P\left(r_i|epi_j\right) = 0 & \text{if element-epicentre distance } \notin [r_{i-}; r_{i+}] \end{cases} \quad \text{for } i = 1 \ldots 20 \tag{I.3}$$

I.4 Median Seismic Intensity Nodes Q1...Q11

This node of 20 states is conditional on the magnitude and the epicentral distance. The corresponding q_i values are logarithmically distributed between q_{min} and q_{max}, which are evaluated as the extreme intensity measures of the problem (i.e. ground motion resulting from the smallest/greatest epicentral distance with the smallest/greatest magnitude). For each combination of distance r_j and magnitude m_k, the median intensity q_{tmp} is deterministically computed and the CPT is built by checking whether the computed seismic intensity falls within the range of q_i:

$$\begin{cases} P\left(q_i|r_j, m_k\right) = 1 & \text{if } q_{tmp} = \mathrm{f}\left(r_j, m_k\right) \in [q_{i-}; q_{i+}] \\ P\left(q_i|r_j, m_k\right) = 0 & \text{if } q_{tmp} = \mathrm{f}\left(r_j, m_k\right) \notin [q_{i-}; q_{i+}] \end{cases} \quad \text{for } i = 1 \ldots 20 \tag{I.4}$$

I.5 Standard Normal Distribution Nodes U, V1...V11

It is a root node of 10 states that results from a discretization of the standard normal probability distribution function. The values u_i are linearly distributed between the 16% and 84% percentiles (i.e. corresponding to one level of σ) and the corresponding probabilities are expressed as follows (a normalization is performed so that the sum of probabilities is equal to 1):

$$P(u_i) = \frac{\phi(u_i)}{\sum_{j=1}^{10} \phi(u_j)} \quad \text{for } i = 1 \dots 10 \tag{I.5}$$

I.6 Intra-Event Variability Nodes e1...e11

This node of 10 states is conditional on two standard normal distribution nodes **U** (common to all components) and **V** (specific to each component). The corresponding e_i values are linearly distributed between e_{min} and e_{max}, which are evaluated as the extreme values of the combined standard normal variables multiplied by the intra-event variability ϵ. For each combination of standard normal variables u_j and v_k, the intra-event variability is deterministically computed as follows:

$$e_{tmp} = \sqrt{1 - t^2} \cdot v_k + t \cdot u_j \tag{I.6}$$

where t is an approximate correlation factor, which is based on the Dunnett-Sobel class [Dunnett and Sobel, 1955] and the correlation matrix between the infrastructure elements.

The elements of the correlation matrix are expressed as follows:

$$\rho_{l,m} = \exp\left(-\frac{3 \cdot d_{l,m}}{d_\rho}\right) \tag{I.7}$$

where d_ρ is the correlation distance of the seismic intensity (taken as 13.5 km here) and $d_{l,m}$ is the distance between infrastructure elements l and m.

Finally, the CPT is built by checking whether the computed intra-event variability falls within the range of e_i:

$$\begin{cases} P\left(e_i|u_j,v_k\right)=1 & \text{if } e_{tmp}=\mathrm{f}\left(u_j,v_k\right)\in[e_{i-};e_{i+}] \\ P\left(e_i|u_j,v_k\right)=0 & \text{if } e_{tmp}=\mathrm{f}\left(u_j,v_k\right)\notin[e_{i-};e_{i+}] \end{cases} \quad \text{for } i=1\ldots10 \tag{I.8}$$

I.7 Inter-Event Variability Node n

It is a root node of 10 states that results from a discretization of the standard normal probability distribution function. The values n_i are linearly distributed between the 16% and 84% percentiles (i.e. corresponding to one level of σ) and are multiplied by the inter-event variability η. The corresponding probabilities are expressed as follows (a normalization is performed so that the sum of probabilities is equal to 1):

$$P\left(n_i\right)=\frac{\phi\left(n_i\right)}{\sum_{j=1}^{10}\phi\left(n_j\right)} \quad \text{for } i=1\ldots10 \tag{I.9}$$

I.8 Distributed Seismic Intensity Nodes S1...S11

This node of 20 states is conditional on the intra- and inter-variabilities and on the median seismic intensity. The corresponding s_i values are logarithmically distributed between s_{min} and s_{max}, which are evaluated as the extreme intensity measures when uncertainties are added. For each combination of median intensity q_j, intra-event variability e_k and inter-event variability n_l, the distributed seismic intensity is deterministically computed as follows:

$$s_{tmp}=10\hat{}\left[\log_{10}q_j+e_k+n_l\right] \tag{I.10}$$

Finally, the CPT is built by checking whether the computed seismic intensity falls within the range of s_i:

$$\begin{cases} P\left(s_i|q_j,e_k,n_l\right)=1 & \text{if } s_{tmp}=\mathrm{f}\left(q_j,e_k,n_l\right)\in[s_{i-};s_{i+}] \\ P\left(s_i|q_j,e_k,n_l\right)=0 & \text{if } s_{tmp}=\mathrm{f}\left(q_j,e_k,n_l\right)\notin[s_{i-};s_{i+}] \end{cases} \quad \text{for } i=1\ldots20 \tag{I.11}$$

I.9 Flood Intensity Node FL

It is a root node of 4 states (fl_i values found in Table 7.12 for $i=1\ldots3$; $fl_i=0$ for $i=4$), expressing the probability of occurrence of flow discharge events. For each flood value, the probability of occurrence is given by the assumed return period T_i of the arbitrary events (i.e. 50, 100 and 500 years, respectively):

$$\begin{cases} P\left(fl_i\right)=\frac{1}{T_i} & \text{for } i=1\ldots3 \\ P\left(fl_i\right)=1-\sum_{j=1}^{3}P\left(fl_j\right) & \text{for } i=4 \end{cases} \tag{I.12}$$

I.10 Yield Acceleration Node ky

This node of 3 states is conditional on the rainfall event (**FL** node). An arbitrary distribution is assumed for demonstration purposes, due to the lack of knowledge and expertise to evaluate the soil saturation ratio based on the amount of rainfall. Therefore arbitrary values have been proposed in order to highlight the dependence between rainfall and landslide hazard and to demonstrate how account for hazard interactions. The corresponding CPT has already been presented in Table 7.14.

I.11 Component Nodes C1...C11

This node of 2 states is conditional on the distributed seismic intensity only, for most components. The probability of failure is directly provided by the fragility curve of the component, with fragility parameters α and β and normal cumulative distribution function ϕ:

$$\begin{cases} P\left(failure|s_j\right) = \phi\left(\frac{\log s_j - \log \alpha}{\beta}\right) \\ P\left(survival|s_j\right) = 1 - \phi\left(\frac{\log s_j - \log \alpha}{\beta}\right) \end{cases} \tag{I.13}$$

I.12 Super-Component Nodes SC1...SC3

Super-components are in-series assemblies of components. For instance, in the case of **SC1**, which is the super-component including **C2**, **C3** and **C4**, the CPT is formulated as follows:

$$\begin{cases} P\left(closed|\mathbf{C2}=0,\mathbf{C3}=0,\mathbf{C4}=0\right)=0 & P\left(open|\mathbf{C2}=0,\mathbf{C3}=0,\mathbf{C4}=0\right)=1 \\ P\left(closed|\mathbf{C2}=1,\mathbf{C3}=0,\mathbf{C4}=0\right)=1 & P\left(open|\mathbf{C2}=1,\mathbf{C3}=0,\mathbf{C4}=0\right)=0 \\ P\left(closed|\mathbf{C2}=0,\mathbf{C3}=1,\mathbf{C4}=0\right)=1 & P\left(open|\mathbf{C2}=0,\mathbf{C3}=1,\mathbf{C4}=0\right)=0 \\ P\left(closed|\mathbf{C2}=1,\mathbf{C3}=1,\mathbf{C4}=0\right)=1 & P\left(open|\mathbf{C2}=1,\mathbf{C3}=1,\mathbf{C4}=0\right)=0 \\ P\left(closed|\mathbf{C2}=0,\mathbf{C3}=0,\mathbf{C4}=1\right)=1 & P\left(open|\mathbf{C2}=0,\mathbf{C3}=0,\mathbf{C4}=1\right)=0 \\ P\left(closed|\mathbf{C2}=1,\mathbf{C3}=0,\mathbf{C4}=1\right)=1 & P\left(open|\mathbf{C2}=1,\mathbf{C3}=0,\mathbf{C4}=1\right)=0 \\ P\left(closed|\mathbf{C2}=0,\mathbf{C3}=1,\mathbf{C4}=1\right)=1 & P\left(open|\mathbf{C2}=0,\mathbf{C3}=1,\mathbf{C4}=1\right)=0 \\ P\left(closed|\mathbf{C2}=1,\mathbf{C3}=1,\mathbf{C4}=1\right)=1 & P\left(open|\mathbf{C2}=1,\mathbf{C3}=1,\mathbf{C4}=1\right)=0 \end{cases} \tag{I.14}$$

The convention used here is 0 for survival/open (i.e. damage state 0) and 1 for failure/-closed (i.e. damage state 1).

I.13 Survival Path Event Nodes Es1...Es18

The SPE nodes have two states (1 for failure / 0 for survival) and they have been introduced by Bensi et al. [2011]. Their CPTs are defined as follows:

$$\begin{cases} \begin{cases} P\left(E_{s,i}=0|E_{s,Pa(i)},C_i\right)=1 \\ P\left(E_{s,i}=1|E_{s,Pa(i)},C_i\right)=0 \end{cases} & \text{if } \left[\bigcup\left\{E_{s,Pa(i)}=0\right\}\right]\bigcap\{C_i=0\} \\ \begin{cases} P\left(E_{s,i}=0|E_{s,Pa(i)},C_i\right)=0 \\ P\left(E_{s,i}=1|E_{s,Pa(i)},C_i\right)=1 \end{cases} & \text{otherwise} \end{cases} \tag{I.15}$$

The convention used here is 0 for survival/open (i.e. damage state 0) and 1 for failure/-closed (i.e. damage state 1). The symbol $E_{s,Pa(i)}$ represents the SPE nodes that are parent nodes of the considered SPE node $E_{s,i}$.

I.14 Connected Sources Nodes Ns1 and Ns2

This node of 3 states is conditional on the SPE nodes that represent the MLSs involved in the considered Source-Sink (or Origin-Destination) couple. The 3 states represent the number of sources that are still connected to the sink, i.e. 0, 1 or 2 sources (in the present example, 2 sources are supposed to reach each of the 2 sinks). In the example of **Ns1**, the CPT is defined as follows:

$$\begin{cases} P\left(0|E_{s4}=0,E_{s9}=0\right)=0 & P\left(1|E_{s4}=0,E_{s9}=0\right)=0 & P\left(2|E_{s4}=0,E_{s9}=0\right)=1 \\ P\left(0|E_{s4}=1,E_{s9}=0\right)=0 & P\left(1|E_{s4}=1,E_{s9}=0\right)=1 & P\left(2|E_{s4}=1,E_{s9}=0\right)=0 \\ P\left(0|E_{s4}=0,E_{s9}=1\right)=0 & P\left(1|E_{s4}=0,E_{s9}=1\right)=1 & P\left(2|E_{s4}=0,E_{s9}=1\right)=0 \\ P\left(0|E_{s4}=1,E_{s9}=1\right)=1 & P\left(1|E_{s4}=1,E_{s9}=1\right)=0 & P\left(2|E_{s4}=1,E_{s9}=1\right)=0 \end{cases} \tag{I.16}$$

I.15 System Connectivity Loss Node SYS

This nodes of 10 states is conditional on the nodes of connected sources. The values sys_i are linearly distributed between 0 and 1, which are the extreme values of SCL. For each combination of the nodes **Ns1** and **Ns2** (values $ns_{1,j}$ and $ns_{2,k}$), the single connectivity loss is computed as follows:

$$scl_{tmp} = \frac{1}{2} \cdot \left(\frac{ns_{1,j}}{ns_{1,0}} + \frac{ns_{2,k}}{ns_{2,0}} \right) \tag{I.17}$$

where $ns_{1,0}$ and $ns_{2,0}$ are the number of sources initially connected to sinks 1 and 2. Finally, the CPT is built by checking whether the computed SCL falls within the range of sys_i:

$$\begin{cases} P\left(sys_i | ns_{1,j}, ns_{2,k}\right) = 1 & \text{if } scl_{tmp} = \mathrm{f}\left(ns_{1,j}, ns_{2,k}\right) \in [sys_{i-}; sys_{i+}] \\ P\left(sys_i | ns_{1,j}, ns_{2,k}\right) = 0 & \text{if } scl_{tmp} = \mathrm{f}\left(ns_{1,j}, ns_{2,k}\right) \notin [sys_{i-}; sys_{i+}] \end{cases} \quad \text{for } i = 1 \dots 10 \tag{I.18}$$

Appendix J

Multi-Hazard Fragility Functions for the Case-Study

This Appendix presents the multi-hazard fragility models that have been derived for the four bridge types proposed for the Bologna case-study, following the procedure detailed in Chapters 4 and 5.

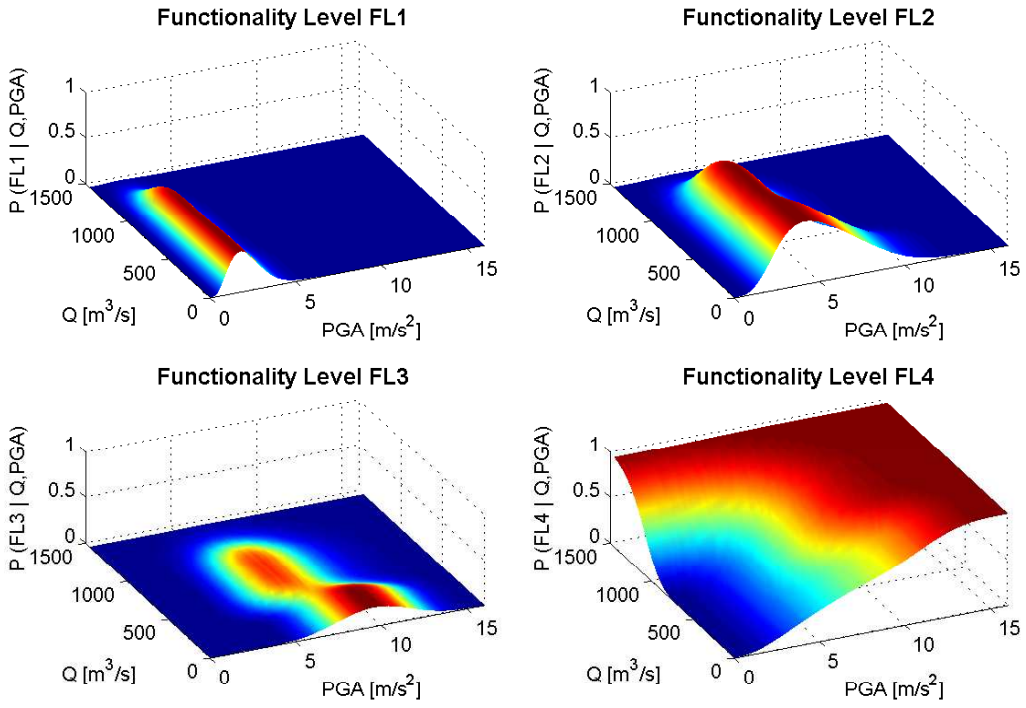

FIGURE J.1: Multi-hazard fragility model for bridge type 1, with respect to the four functionality levels described in Table 5.5.

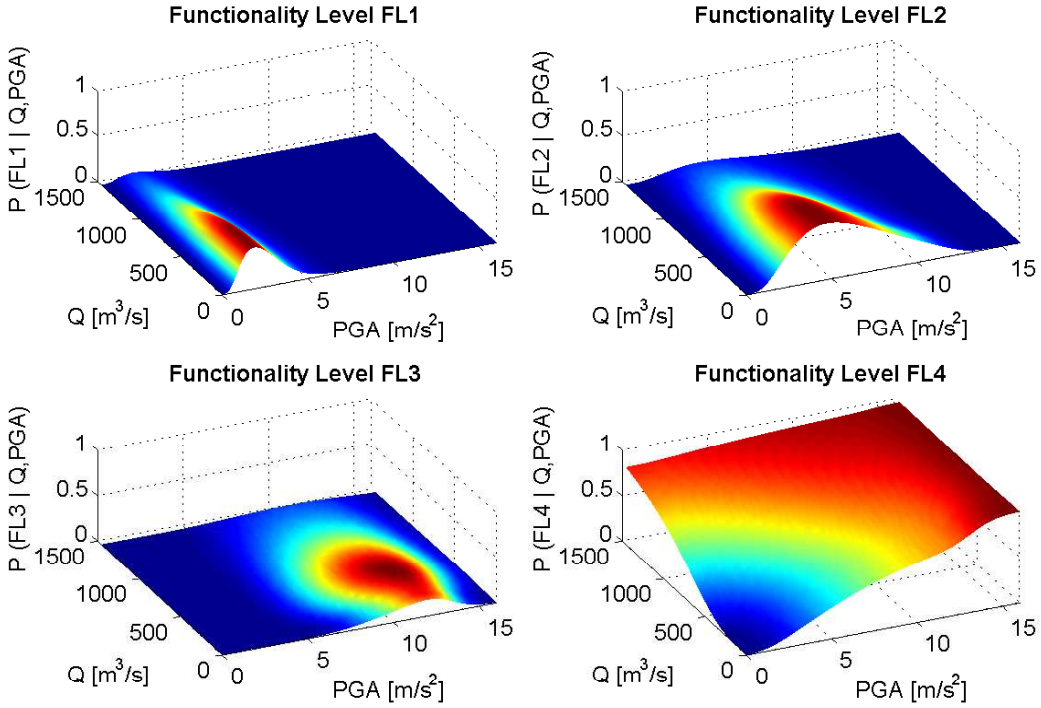

FIGURE J.2: Multi-hazard fragility model for bridge type 2, with respect to the four functionality levels described in Table 5.5.

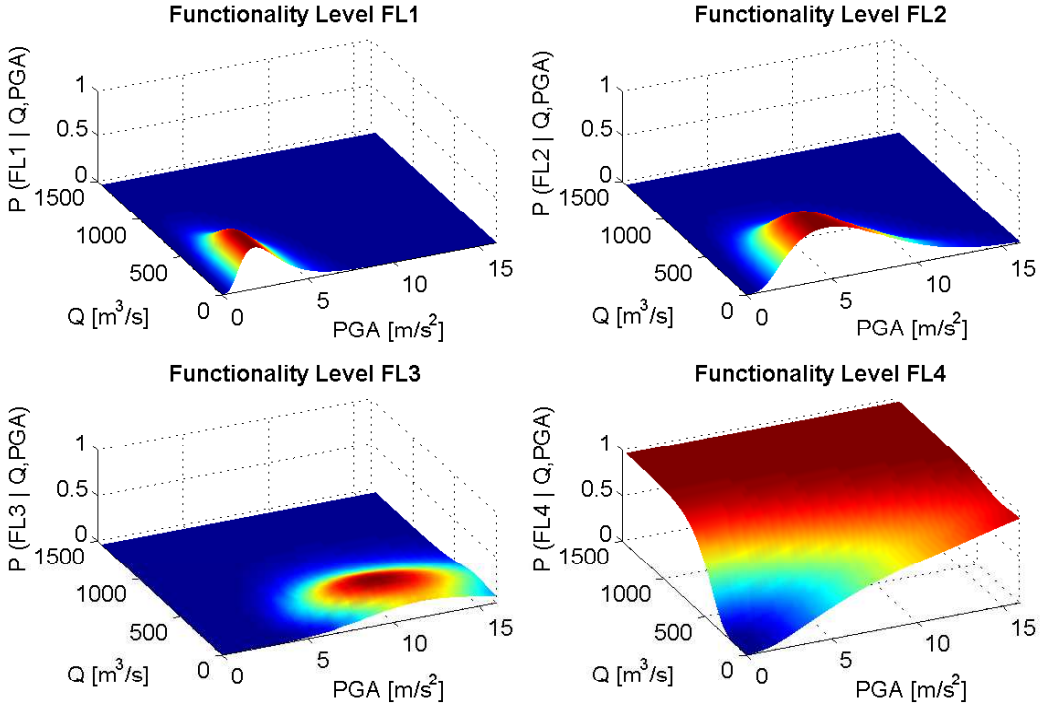

FIGURE J.3: Multi-hazard fragility model for bridge type 3, with respect to the four functionality levels described in Table 5.5.

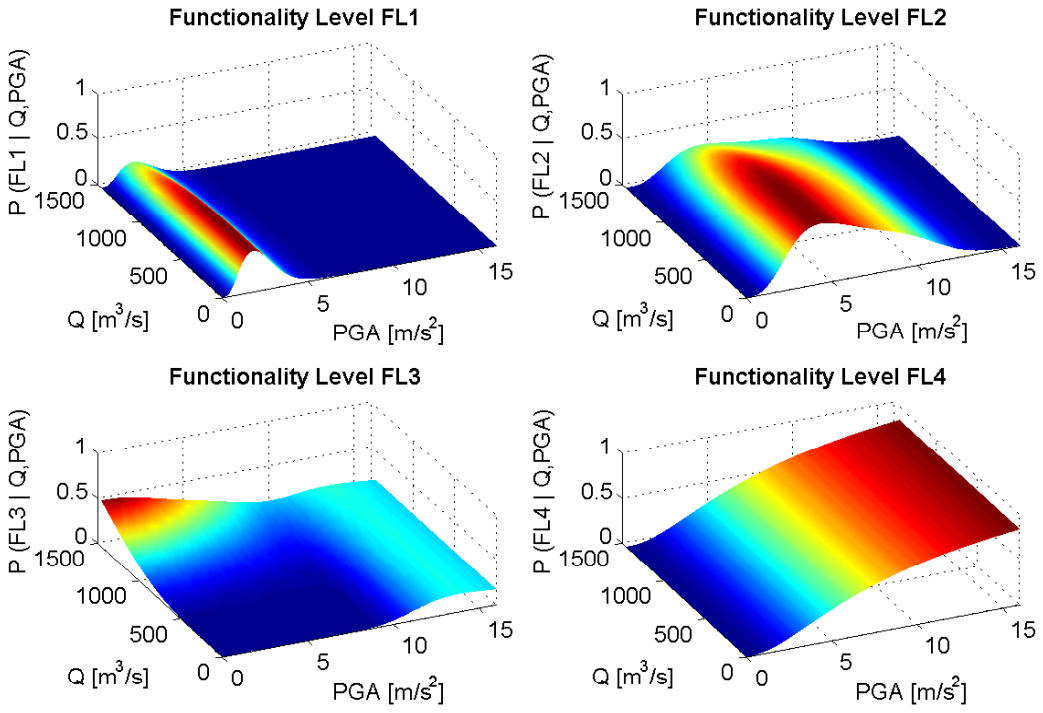

FIGURE J.4: Multi-hazard fragility model for bridge type 4, with respect to the four functionality levels described in Table 5.5.

Bibliography

Abrahamson, N. A. and Bommer, J. J. [2005]. Probability and uncertainty in seismic hazard analysis, *Earthquake Spectra* **21**(2): 603–607.

Adachi, T. and Ellingwood, B. R. [2008]. Serviceability of earthquake-damaged water systems: Effects of electrical power availability and power backup systems on system vulnerability, *Reliability Engineering and System Safety* **93**(1): 78–88.

Akkar, S. and Bommer, J. J. [2010]. Empirical equations for the prediction of PGA, PGV and spectral accelerations in Europe, the Mediterranean region and the Middle East, *Seismological Research Letters* **81**(2): 195–206.

Akkar, S., Sandikkaya, M. A. and Bommer, J. J. [2014]. Empirical ground-motion models for point- and extended-source crustal earthquake scenarios in Europe and the Middle East, *Bulletin of Earthquake Engineering* **12**(1): 359–387.

Akkar, S., Sandikkaya, M. A., Senyurt, M., Azari, S. A., Ay, B. O., Traversa, P., Douglas, J., Cotton, F., Luzi, L., Hernandez, B. and Godey, S. [2014]. Reference database for seismic ground-motion in Europe (RESORCE), *Bulletin of Earthquake Engineering* **12**(1): 311–339.

ALA [2005]. Flood-resistant local road systems: A report based on case studies, *Technical report*, American Lifeline Alliance.

Alipour, A. and Shafei, B. [2012]. Performance assessment of highway bridges under earthquake and scour effects, *Proceedings of the Fifteenth World Conference on Earthquake Engineering*, Lisbon, Portugal.

Alipour, A., Shafei, B. and Shinozuka, M. [2012]. Reliability-Based Calibration of Load and Resistance Factors for Design of RC Bridges under Multiple Extreme Events: Scour and Earthquake, *Journal of Bridge Engineering* **18**(5): 362–371.

Ambraseys, N., Smit, P., Douglas, J., Margaris, B., Sigbjornsson, R., Olafsson, S., Suhadolc, P. and Costa, G. [2004]. Internet site for European strong-motion data, *Bollettino di Geofisica Teorica ed Applicata* **45**(3): 113–129.

Antoniou, S. and Pinho, R. [2004]. Development and verification of a displacement-based adaptive pushover procedure, *Journal of Earthquake Engineering* **8**(5): 645–661.

API [2000]. Recommended practice for planning, designing and constructing fixed offshore platforms, *Technical Report 2A-WSD (RP 2A)*, American Petroleum Institute, Washington, D.C.

Argyroudis, S. and Kaynia, A. M. [2014]. Fragility functions of highway and railway infrastructure, *SYNER-G: Typology Definition and Fragility Functions for Physical Elements at Seismic Risk*, K. Pitilakis, H. Crowley, A.M. Kaynia (Eds), Springer, pp. 299–326.

Argyroudis, S. and Kaynia, A. M. [2015]. Analytical seismic fragility functions for highway and railway embankments and cuts, *Earthquake Engineering and Structural Dynamics* **44**(11): 1863–1879.

Argyroudis, S., Selva, J., Gehl, P. and Pitilakis, K. [2015]. Systemic seismic risk assessment of road networks considering interactions with the built environment, *Computer-Aided Civil and Infrastructure Engineering* **30**(7): 524–540.

Aspinall, W. P. [2006]. Structured elicitation of expert judgment for probabilistic hazard and risk assessment in volcanic eruptions, *Statistics in Volcanology* **1**: 15–30.

Aspinall, W. P. [2010]. A route to more tractable expert advice, *Nature* **463**(7279): 294–295.

Atkinson, G. M. and Adams, J. [2013]. Ground motion prediction equations for application to the 2015 Canadian national seismic hazard maps, *Canadian Journal of Civil Engineering* **40**(10): 988–998.

Atkinson, G. M., Bommer, J. J. and Abrahamson, N. A. [2014]. Alternative approaches to modeling epistemic uncertainty in ground motions in probabilistic seismic-hazard analysis, *Seismological Research Letters* **85**(6): 1–4.

Avsar, O., Yakut, A. and Caner, A. [2011]. Analytical fragility curves for ordinary highway bridges in Turkey, *Earthquake Spectra* **27**(4): 971–996.

Aygün, B., Dueñas Osorio, L., Padgett, J. E. and DesRoches, R. [2010]. Efficient longitudinal seismic fragility assessment of a multispan continuous steel bridge on liquefiable soils, *Journal of Bridge Engineering* **16**(1): 93–107.

Baker, J. W. [2007]. Probabilistic structural response assessment using vector-valued intensity measures, *Earthquake Engineering and Structural Dynamics* **36**(13): 1861–1883.

Baker, J. W. [2015]. Efficient analytical fragility function fitting using dynamic structural analysis, *Earthquake Spectra* **31**(1): 579–599.

Banazadeh, M. and Fereshtehnejad, S. E. [2011]. System reliability assessment of steel moment frames with different failure mechanisms using Bayesian Probability Network, *Proceedings of the Eighth International Conference on Structural Dynamics EURODYN*, Leuven, Belgium.

Banerjee, S. and Shinozuka, M. [2008]. Mechanistic quantification of RC bridge damage states under earthquake through fragility analysis, *Probabilistic Engineering Mechanics* **23**(1): 12–22.

Barbetta, S., Camici, S. and Moramarco, T. [2015]. Reappraisal of bridge piers scour vulnerability: a case study in the Upper Tiber River basin (central Italy), *Journal of Flood Risk Management* **In press**.

Bartlett, S. F. [2014]. Liquefaction-induced ground failures and bridge damage in Southern Alaska along the Alaskan railroad and highway during the 1964 Alaskan earthquake, *Proceedings of the Tenth National Conference on Earthquake Engineering*, Anchorage, Alaska.

Basoz, N. and Kiremidjian, A. S. [1996]. Risk assessment for highway transportation systems, *Technical Report NCEER-118*, John A. Blume Earthquake Engineering Center.

Basoz, N., Kiremidjian, A. S., King, S. A. and Law, K. H. [1999]. Statistical analysis of bridge damage data from 1994 Northridge, CA earthquake, *Earthquake Spectra* **15**(1): 25–54.

Benjamin, J. R. and Cornell, A. [1970]. *Probability, Statistics and Decision for Civil Engineers*, McGraw-Hill.

Benn, J. [2012]. Railway bridge failure during flood in the UK and Ireland : Learning from the past, *Technical report*, Institution of Civil Engineers.

Bensi, M., Der Kiureghian, A. and Straub, D. [2013]. Efficient Bayesian network modeling of systems, *Reliability Engineering and System Safety* **112**: 200–213.

Bensi, M. T., Der Kiureghian, A. and Straub, D. [2011]. A Bayesian Network methodology for infrastructure seismic risk assessment and decision support, *Technical Report 2011/02*, Pacific Earthquake Engineering Research Center, Berkeley, California.

Bindi, D., Massa, M., Luzi, L., Ameri, G., Pacor, F., Puglia, R. and Augliera, P. [2014]. Pan-European ground-motion prediction equations for the average horizontal component of PGA, PGV, and 5%-damped PSA at spectral periods up to 3.0s using the RESORCE dataset, *Bulletin of Earthquake Engineering* **12**(1): 391–430.

Bird, J. F. and Bommer, J. J. [2004]. Evaluating earthquake losses due to ground failure and identifying their relative contribution, *Proceedings of the Thirteenth World Conference on Earthquake Engineering*, Vancouver, Canada.

Blandon, C. A. and Priestley, M. J. N. [2010]. Equivalent viscous damping equations for direct displacement based design, *Journal of Earhquake Engineering* **9**(2): 257–278.

Bommer, J. J. and Scherbaum, F. [2008]. The use and misuse of logic trees in probabilistic seismic hazard analysis, *Earthquake Spectra* **24**(4): 997–1009.

Bora, S. S., Scherbaum, F., Kuehn, N. and Stafford, P. [2014]. Fourier spectral- and duration models for the generation of response spectra adjustable to different source-, propagation-, and site conditions, *Bulletin of Earthquake Engineering* **12**(1): 467–493.

Borzi, B., Ceresa, P., Franchin, P., Noto, F., Calvi, G. M. and Pinto, P. E. [2016]. Seismic vulnerability of the Italian roadway bridge stock, *Earthquake Spectra* **31**(4): 2137–2161.

Bousias, E., Palios, X., Fardis, M., Strepelias, I. and Alexakis, C. [1990]. Experimental and analytical investigation of seismic isolation with and without additional damping, *Technical Report Deliverable 4.2 (in Greek)*, ASProGe Project.

Bradley, B. A. [2010]. Epistemic uncertainties in component fragility functions, *Earthquake Spectra* **26**(1): 41–62.

Bray, J. D. and Travasarou, F. [2007]. Simplified procedure for estimating earthquake-induced deviatoric slope displacements, *Journal of Geotechnical and Geoenviromental Engineering* **133**(4): 381–392.

CALTRANS [2000]. Bridge design specifications, *Technical report*, California Department of Transportation, Sacramento, California.

Calvi, G. M., Pinho, R., Magenes, G., Bommer, J. J. and Crowley, H. [2006]. Development of seismic vulnerability assessment methodologies over the past 30 years, *Journal of Earthquake Technology* **43**(3): 75–104.

Caporali, E., Rinaldi, M. and Casagli, N. [2005]. The Arno river floods, *Giornale di Geologia Applicata* **1**: 117–192.

Cardone, D. [2014]. Displacement limits and performance displacement profiles in support of direct displacement-based seismic assessment of bridges, *Earthquake Engineering and Structural Dynamics* **43**(8): 1239–63.

Cardone, D., Perrone, G. and Sofia, S. [2011]. A performance-based adaptive methodology for the seismic evaluation of multi-span simply supported deck bridges, *Bulletin of Earthquake Engineering* **9**(5): 1463–1498.

Cavalieri, F., Franchin, P., Gehl, P. and D'Ayala, D. [2017]. Bayesian Networks and Infrastructure Systems: Computational and Methodological Challenges, *Risk and Reliability Analysis: Theory and Applications*, P. Gardoni (Ed.), Springer, pp. 385–415.

Cavalieri, F., Franchin, P., Gehl, P. and Khazai, B. [2012]. Quantitative assessment of social losses based on physical damage and interaction with infrastructural systems, *Earthquake Engineering and Structural Dynamics* **41**(11): 1569–1589.

CDMG [1998]. Seismic hazard zone report for the Mint Canyon 7.5-minute quadrangle, Los Angeles County, California, *Technical report*, California Division of Mines and Geology.

CEN [2004a]. Eurocode 2: Design of concrete structures – Part 1-1: General rules and rules for buildings, *Technical Report EN 1992-1-1*, European Committee for Standardization, Brussels, Belgium.

CEN [2004b]. Eurocode 8: Design of structures for earthquake resistance – Part 1: General rules, seismic actions and rules for buildings, *Technical Report EN 1998-1*, European Committee for Standardization, Brussels, Belgium.

Choi, E., DesRoches, R. and Nielson, B. [2004]. Seismic fragility of typical bridges in moderate seismic zones, *Engineering Structures* **26**(2): 187–199.

Cooke, R. M. [1991]. *Experts in uncertainty: Opinions and subjective probability in science*, Oxford University Press, New York.

Cornell, C. A., Jalayer, F., Hamburger, R. O. and Foutch, D. A. [2002]. Probabilistic basis for 2000 SAC Federal Emergency Management Agency steel moment frame guidelines, *Journal of Structural Engineering* **128**(4): 526–533.

Crowley, H., Colombi, M., Silva, V., Monteiro, R., Ozcebe, S., Fardis, M., Tsionis, G. and Askouni, P. [2011]. Fragility functions for roadway bridges, *Technical report*, SYNER-G Project Deliverable D3.6.

Davis-McDaniel, C. E. [2011]. *Fault-tree model for bridge collapse risk analysis*, Master's thesis, Clemson University, Clemson, South California.

D'Ayala, D. [2005]. Force and displacement based vulnerability assessment for traditional buildings, *Bulletin of Earthquake Engineering* **3**(3): 235–265.

D'Ayala, D., Gehl, P., Garcia Fernandez, M., Jimenez, M. J., Ni Choine, M., Tucker, M., Gavin, K., Martinovic, K., Avdeeva, Y. V., van Gelder, P., Salceda Page, M. T. and Segarra Martinez, M. J. [2014]. Hazard distribution matrix, *Technical report*, INFRARISK Project Deliverable D3.1.

D'Ayala, D., Gehl, P., Martinovic, K., Gavin, K., Clarke, J., Corbally, R., Tucker, M., Avdeeva, Y. V., van Gelder, P., Salceda Page, M. T. and Segarra Martinez, M. J. [2015]. Fragility functions matrix, *Technical report*, INFRARISK Project Deliverable D3.2.

D'Ayala, D., Meslem, A., Vamvatsikos, D., Porter, K., Rossetto, T., Crowley, H. and Silva, V. [2014]. Guidelines for analytical vulnerability assessment of low-mid-rise buildings – Methodology, *Technical report*, Vulnerability Global Component Project, Global Earthquake Model.

De Felice, G. and Giannini, R. [2010]. An efficient approach for seismic fraiglity assessment with application to old reinforced concrete bridges, *Journal of Earthquake Engineering* **14**(2): 231–251.

Delavaud, E., Cotton, F., Beauval, C., Akkar, S., Scherbaum, F. and Danciu, L. [2012]. Construction of a ground-motion logic tree for PSHA in Europe within the SHARE project, *Proceedings of the Fifteenth World Conference on Earthquake Engineering*, Lisbon, Portugal.

Deng, L., Wang, W. and Yu, Y. [2015]. State-of-the-art review on the causes and mechanisms of bridge collapse, *ASCE Journal of Performance of Constructed Facilities* **04015005**.

Der Kiureghian, A. and Ditlevsen, O. [2007]. Aleatory or epistemic? Does it matter?, *Proceedings of Special Workshop on Risk Acceptance and Risk Communication*, Stanford, CA.

Der Kiureghian, A., Haukaas, T., Hahnel, A., Franchin, P., Song, J., Pakzad, S. and Sudret, B. [1999]. FERUM, *Technical report*, University of California at Berkeley, Available at: www.ce.berkeley.edu/FERUM.

Der Kiureghian, A. and Song, J. [2008]. Multi-scale reliability analysis and updating of complex systems by use of linear programming, *Reliability Engineering & System Safety* **93**: 288–297.

Derras, B., Bard, P. Y. and Cotton, F. [2014]. Towards fully data driven ground-motion prediction models for Europe, *Bulletin of Earthquake Engineering* **12**(1): 495–516.

Dickenson, S. E., McCullough, N. J., Barkau, M. G. and Wavra, B. J. [2002]. Assessment and mitigation of liquefaction hazards to bridge approach embankments in Oregon, *Technical Report SPR 361*, Federal Highway Administration, Washington, D.C.

Diehl, T. H. [1997]. Potential drift accumulation at bridges, *Technical Report FHWA RD-97-28*, Turner-Fairbank Highway Research Center, Federal Highway Administration Research and Development, U.S. Department of Transportation, McLean, Virginia.

Doll, C. and Sieber, N. [2011]. Transport sector vulnerability: Vulnerability assessment for road transport, *Technical Report Deliverable 2*, WEATHER Project.

Douglas, J. [2007]. Physical vulnerability modelling in natural hazard risk assessment, *Natural Hazards and Earth System Sciences* **7**(2): 283–288.

Douglas, J. [2014]. Ground motion prediction equations 1964-2014, *Technical report*, Available at: www.gmpe.org.uk.

Dueñas Osorio, L., Craig, J. I. and Goodno, B. J. [2007]. Seismic response of critical interdependent networks, *Earthquake Engineering and Structural Dynamics* **36**(2): 285–306.

Dunnett, C. W. and Sobel, M. [1955]. Approximations to the probability integral and certain percentage points of a multivariate analogue of Student's t-distribution, *Biometrica* **42**(1-2): 258–260.

Elnashai, A. S., Borzi, B. and Vlachos, S. [2004]. Deformation-based vulnerability functions for RC bridges, *Structural Engineering* **17**(2): 215–244.

Elnashai, A. S., Gencturk, B., Kwon, O. S., Al-Qadi, I. L., Hashash, Y., Roesler, J. R., Kim, S. J., Jeong, S. H., Dukes, J. and Valdivia, A. [2010]. The Maule (Chile) earthquake of February 27, 2010: Consequence assessment and case studies, *Technical Report MAE/10-04*, Mid-America Earthquake Center.

Esposito, S., d'Onofrio, A., Santo, A., Cavalieri, F. and Franchin, P. [2015]. Simulation-based seismic risk assessment of gas distribution networks, *Computer-Aided Civil and Infrastructure Engineering* **30**(7): 508–523.

European Union [2013]. Regulation (EU) No 1316/2013 of the European Parliament and of the Council of 11 december 2013 establishing the Connecting Europe Facility, amending Regulation (EU) No 913/2010 and repealing Regulations (EC) No 680/2007 and (EC) No 67/2010 Text with EEA relevance, *Technical report*, European Union.

FEMA [2003]. HAZUS MR4 technical manual: Earthquake model, *Technical report*, Federal Emergency Management Agency, Washington D.C.

FEMA [2005]. HAZUS MR4 technical manual: Flood model, *Technical report*, Federal Emergency Management Agency, Washington D.C.

Ferrario, E. and Zio, E. [2014]. Goal tree success tree–dynamic master logic diagram and monte carlo simulation for the safety and resilience assessment of a multistate system of systems, *Engineering Structures* **59**: 411–433.

Ferrer, F. J. [1993]. Recomendaciones para el calculo hidrometeorológico de avenidas, *Technical Report 2A-WSD (RP 2A)*, Ministerio de Fomento, Madrid, Spain.

Foti, S. and Sabia, D. [2011]. Influence of foundation scour on the dynamic response of an existing bridge, *Journal of Bridge Engineering* **16**(2): 295–304.

Franchin, P. and Cavalieri, F. [2013]. *OOFIMS: Object-Oriented Framework for Infrastructure Modeling and Simulation*, Available at: sites.google.com/a/uniroma1.it/oofims.

Franchin, P. and Laura, L. [2014]. Probabilistic inference in the physical simulation of interdependent critical infrastructure systems, *Proceedings of the SAFECOMP 20014 Workshops, LNCS 8696*, pp. 328–338.

Franchin, P., Lupoi, A., Noto, F. and Tesfamarian, S. [2016]. Seismic fragility of reinforced concrete girder bridges using Bayesian belief network, *Earthquake Engineering and Structural Dynamics* **45**(1): 29–44.

Franchin, P., Lupoi, A. and Pinto, P. E. [2008]. On the role of road networks in reducing human losses after earthquakes, *Journal of Earthquake Engineering* **10**(2): 195–206.

Franchin, P. and Pinto, P. E. [2009]. Allowing traffic over mainshock-damaged bridges, *Journal of Earthquake Engineering* **13**(5): 598–599.

Gehl, P. and D'Ayala, D. [2015]. Integrated multi-hazard framework for the fragility analysis of roadway bridges, *Proceedings of the Twelfth International Conference on Applications of Statistics and Probability in Civil Engineering*, Vancouver, Canada.

Gehl, P. and D'Ayala, D. [2016]. Development of Bayesian Networks for the multi-hazard fragility assessment of bridge systems, *Structural Safety* **60**: 37–46.

Gehl, P., Douglas, J. and Seyedi, D. [2015]. Influence of the number of dynamic analyses on the accuracy of structural response estimates, *Earthquake Spectra* **31**(1): 97–113.

Gehl, P., Quinet, C., Le Cozannet, G., Kouokam, E. and Thierry, P. [2013]. Potential and limitations of risk scenario tools in volcanic areas through an example at Mount Cameroon, *Natural Hazards and Earth System Sciences* pp. 2409–2424.

Gehl, P., Seyedi, D. and Douglas, J. [2013]. Vector-valued fragility functions for seismic risk evaluation, *Bulletin of Earthquake Engineering* **11**(2): 365–384.

Gehl, P., Ulrich, T., Rohmer, J., Negulescu, C., Ducellier, A. and Douglas, J. [2013]. Ranking of epistemic uncertainties in scenario-based seismic risk evaluations, *Proceedings of the Eleventh International Conference on Structural Safety and Reliability*, New-York.

Ghosh, J. and Padgett, J. E. [2010]. Aging considerations in the development of time-dependent seismic fragility curves, *ASCE Journal of Structural Engineering* **136**(12): 1497–1511.

Giardini, D. and the SHARE Consortium [2009–2012]. *SHARE: Novel indicators for identifying critical infrastructure at risk from natural hazards*, Available at: www.share-eu.org.

Goretti, A. and Sarli, V. [2006]. Road network and damaged buildings in urban areas: short and long-term interaction, *Bulletin of Earthquake Engineering* **4**(2): 159–175.

Gross, J. L. and Yellen, J. [2004]. *Handbook of Graph Theory*, CRC Press.

Grünthal, G. [1998]. European Macroseismic Scale, *Technical report*, European Seismological Commission, Sub-commission on Engineering Seismology, Working Group on Macroseismic scales, Luxembourg.

Gulkan, P. and Sozen, M. A. [1974]. Inelastic responses of reinforced concrete structures to earthquake motions, *Proceedings of the ACI* **71**(12).

Guo, X., Wu, Y. and Guo, Y. [2015]. Earthquake damage potential and critical scour depth of bridges exposed to flood and seismic hazards under lateral seismic loads, *Earthquake Engineering and Engineering Vibration* **14**(4): 579–594.

Guo, X., Wu, Y. and Guo, Y. [2016]. Time-dependent seismic fragility analysis of bridge systems under scour hazard and earthquake loads, *Engineering Structures* **121**: 52–60.

Hassan, A. M. and Wolff, T. F. [1999]. Search algorithm for minimum reliability index of earth slopes, *Journal of Geotechnical and Geoenvironmental Engineering* **125**(4): 301–308.

Helwany, S., Koutnik, T. E. and Ghorbanpoor, A. [2007]. Evaluation of bridge approach settlement mitigation methods, *Technical report*, Wisconsin Highway Research Program, The University of Wisconsin-Milwaukee, Milwaukee, Wisconsin.

Holmström, K. [2008]. Tomlab optimization environment, *Technical report*, Available at: tomopt.com/tomlab.

Ioannou, I., Rossetto, T. and Grant, D. N. [2012]. Use of regression analysis for the construction of empirical fragility curves, *Proceedings of the Fifteenth World Conference on Earthquake Engineering*, Lisbon, Portugal.

Iwan, W. D. [1980]. Estimating inelastic response spectra from elastic spectra, *Earthquake Engineering and Structural Dynamics* **8**(4): 375–388.

Jacobsen, L. S. [1930]. Steady forced vibrations as influenced by damping, *Transactions ASME* **51**.

Jaiswal, K., Perkins, D., Aspinal, W. P. and Kiremidjian, A. S. [2013]. Estimating structural collapse fragility of generic building typologies using expert judgement, *Proceedings of the Eleventh International Conference on Structural Safety and Reliability*, New York.

Jaiswal, K., Wald, D. and D'Ayala, D. [2011]. Developing empirical collapse fragility functions for global building types, *Earthquake Spectra* **27**(3): 775–795.

Jayaler, F., Beck, J. L. and Zareian, F. [2012]. Analyzing the sufficiency of alternative scalar and vector intensity measures of ground shaking based on information theory, *Journal of Engineering Mechanics* **138**(3): 307–316.

Jeong, S. H. and Elnashai, A. S. [2007]. Probabilistic fragility analysis parameterized by fundamental response quantities, *Engineering Structures* **29**(6): 1238–1251.

Jibson, R. W., Harp, E. L. and Michael, J. A. [2000]. A method for producing digital probabilistic seismic landslide hazard maps, *Engineering Geology* **58**(3): 271–289.

Judi, H. J., Davidson, B. J. and Fenwick, R. C. [2000]. The direct displacement based design method: A damping perspective, *Proceedings of the Twelfth World Conference of Earthquake Engineering*, Auckland, New Zealand.

Kafali, C. [2008]. *System Performance under Multihazard Environment*, PhD thesis, Cornell University, Ithaca, NY.

Kameshwar, S. and Padgett, J. E. [2014]. Multi-hazard risk assessment of highway bridges subjected to earthquake and hurricane hazards, *Engineering Structures* **78**: 154–166.

Kang, W. H. and Lee, Y. J. [2015]. Efficient post-hazard probabilistic flow analysis of water pipe networks, *Proceedings of the Twelfth International Conference on Applications of Statistics and Probability in Civil Engineering*, Vancouver, Canada.

Kang, W. H., Lee, Y. J., Song, J. and Gencturk, B. [2012]. Further development of matrix-based system reliability method and applications to structural systems, *Structure and Infrastructure Engineering* **8**(5): 441–457.

Kang, W. H., Song, J. and Gardoni, P. [2008]. Matrix-based system reliability method and applications to bridge networks, *Reliability Engineering & System Safety* **93**: 1584–1593.

Kappos, A., Panagopoulos, G., Panagiotopoulos, C. and Penelis, G. [2006]. A hybrid method for the vulnerability assessment of RC and URM buildings, *Bulletin of Earthquake Engineering* **4**(4): 391–413.

Karim, K. R. and Yamazaki, F. [2001]. Effect of earthquake ground motions on fragility curves of highway bridge piers based on numerical simulation, *Earthquake Engineering and Structural Dynamics* **30**(12): 1839–1856.

Kennedy, R. P., Cornell, C. A., Campbell, R. D., Kaplan, S. and Perla, H. F. [1980]. Probabilistic seismic safety study of an existing nuclear power plant, *Nuclear Engineering and Design* **59**(2): 315–338.

Kibboua, A., Naili, M., Benouar, D. and Kehila, F. [2011]. Analytical fragility curves for typical Algerian reinforced concrete bridge piers, *Structural Engineering and Mechanics* **39**(3): 411–425.

Kim, S. H. and Feng, M. Q. [2003]. Fragility analysis of bridges under ground motion with spatial variation, *International Journal of Non-Linear Mechanics* **38**(5): 705–721.

Kim, S. H. and Shinozuka, M. [2004]. Development of fragility curves of bridges retrofitted by column jacketing, *Probabilistic Engineering Mechanics* **19**(1–2): 105–112.

Kjaerulff, U. [1990]. Triangulation of graphs - algorithms giving small total state space, *Technical report*, Institute for Electronic Systems, Aalborg, Denmark.

Klose, M. [2015]. *Landslide Databases as Tools for Integrated Assessment of Landslide Risk*, Springer Theses.

Kowalsky, M. J. [1994]. *Displacement-based design - a methodology for seismic design applied to reinforced concrete bridge columns*, Master's thesis, University of California, San Diego, California.

Krawinkler, H. [1999]. Challenges and progress in performance-based earthquake engineering, *International Seminar on Seismic Engineering for Tomorrow, In Honor of Professor Hiroshi Akiyama*, Tokyo, Japan.

Lagasse, P. F., Clopper, P. E., Zevenbergen, L. W., Spitz, W. J. and Girard, L. G. [2010]. Effects of debris on bridge pier scour, *Technical Report NCHRP-653*, Transportation Research Board of the National Academies, Washington, D.C.

Lebbe, M. F. K., Lokuge, W., Setunge, S. and Zhang, K. [2014]. Failure mechanisms of bridge infrastructure in an extreme flood event, *Proceedings of the First International Conference on Infrastructure Failures and Consequences*, Melbourne, Australia, pp. 124–132.

LeBeau, K. H. and Wadia-Fascetti, S. J. [2000]. A fault-tree model of bridge deterioration, *8th ASCE Specialty Conference on Probabilistic Mechanics and Structural Reliability*, Notre-Dame, Indiana.

Lee, G. C. and Sternberg, E. [2008]. A new system for preventing bridge collapses, *Issues in Science and Technology* **24**(3).

Lee, K. and Rosowsky, D. [2006]. Fragility analysis of woodframe buildings considering combined snow and earthquake loading, *Structural Safety* **28**(3): 289–303.

Lemaire, M., Chateauneuf, A. and Mitteau, J. C. [2005]. *Fiabilité des structures*, Hermes Science.

Li, J., Spencer, B. F. and Elnashai, A. S. [2012]. Bayesian updating of fragility functions using hybrid simulation, *ASCE Journal of Structural Engineering* **139**(7): 1160–1171.

Lim, H. W. and Song, J. [2012]. Efficient risk assessment of lifeline networks under spatially correlated ground motions using selective recursive decomposition algorithm, *Earthquake Engineeting and Structural Dynamics* **41**(13): 337–343.

Lin, C. [2012]. *Evaluation of lateral behavior of pile-supported bridges under scour conditions*, PhD thesis, University of Kansas, Lawrence, Kansas.

Lunn, D., Spiegelhalter, D., Thomas, A. and Best, N. [2009]. The BUGS project: Evolution, critique and future directions (with discussion), *Statistics in Medicine* **28**(25): 3049–3082.

Lupoi, A., Franchin, P., Pinto, P. E. and Monti, G. [2005]. Seismic design of bridges accounting for spatial variability of ground motion, *Earthquake Engineering and Structural Dynamics* **34**(4–5): 327–348.

Mackie, K. R. and Stojadinovic, B. [2006]. Post-earthquake functionality of highway overpass bridges, *Earthquake Engineering and Structural Dynamics* **35**(1): 77–93.

Mahadevan, S., Zhang, R. and Smith, N. [2001]. Bayesian networks for system reliability assessment, *Structural Safety* **23**(3): 231–251.

Mander, J. B. [1999]. Fragility curve development for assessing the seismic vulnerability of highway bridges, *Technical report*, MCEER Highway Project/FHWA, Buffalo, New-York.

Marzocchi, W., Garcia-Aristizabal, A., Gasparini, P., Mastellone, M. L. and Di Ruocco, A. [2012]. Basic principles of multi-risk assessment: a case study in Italy, *Natural Hazards* **62**(2): 551–573.

Marzocchi, W., Sandri, L., Gasparini, P., Newhall, C. and Boschi, E. [2004]. Quantifying probabilities of volcanic events: The example of volcanic hazard at Mount Vesuvius, *Journal of Geophysical Research* **109**(B11).

Marzocchi, W., Sandri, L. and Selva, J. [2010]. BET-VH: A probabilistic tool for long-term volcanic hazard assessment, *Bulletin of Volcanology* **72**(6): 705–716.

McKenna, F., Fenves, G. L. and Scott, M. H. [2000]. Open system for earthquake engineering simulation, *Technical report*, Pacific Earthquake Engineering Research Center, University of California, Berkeley, California.

Melville, B. W. and Dongol, D. M. [1992]. Bridge pier scour with debris accumulation, *Journal of Hydraulic Engineering* **118**(9): 1306–1310.

Michel, C., Gueguen, P., El Arem, S., Mazards, J. and Kotronis, P. [2010]. Full scale dynamic response of a RC building under weak seismic motions using earthquake loadings, ambient vibrations and modelling, *Earthquake Engineering and Structural Dynamics* **39**(4): 419–441.

Middleton, C. and Imhof, D. [2009]. Bridge collapse database, *Technical report*, Available at: www.bridgeforum.org/dir/collapse.

Mignan, A., Wiemer, S. and Giardini, D. [2014]. The quantification of low-probability–high-consequences events: Part I. A generic multi-risk approach, *Natural Hazards* .

Modaressi, H., Desramaut, N. and Gehl, P. [2014]. Specification of the vulnerability of physical systems, *SYNER-G: Systemic Seismic Vulnerability and Risk Assessment of Complex Urban, Utility, Lifeline Systems and Critical Facilities - Methodology and Applications*, K. Pitilakis, P. Franchin, B. Khazai, H. Wenzel (Eds), Springer, pp. 131–184.

Monti, G. and Nistico, N. [2002]. Simple probability-based assessment of bridges under scenario earthquakes, *Journal of Bridge Engineering* **7**(2): 104–114.

Moschonas, I. F., Kappos, A. J., Panetsos, P., Papadopoulos, V., Makarios, T. and Thanopoulos, P. [2009]. Seismic fragility curves for Greek bridges: methodology and case studies, *Bulletin of Earthquake Engineering* **7**(2): 439–468.

Mouroux, P., Bertrand, E., Bour, M., Le Brun, B., Depinois, S., Masure, P. and the RISK-UE team [2004]. The European Risk-UE project: an advanced approach to earthquake risk scenarios, *Thirteenth World Conference on Earthquake Engineering*, Vancouver, Canada.

Murphy, K. [2007]. Bayes Net Toolbox, *Technical report*, Available at: github.com/bayesnet/bnt.

Negulescu, C. and Gehl, P. [2013]. Mechanical methods: Fragility curves and pushover analysis, *Seismic Vulnerability of Structures (ISTE)*, P. Guéguen (Ed.), John Wiley & Sons, pp. 63–110.

Newmark, N. M. [1965]. Effects of earthquakes on dams and embankments, *Geotechnique* **15**(2): 139–160.

Nielson, B. G. [2005]. *Analytical Fragility Curves for Highway Bridges in Moderate Seismic Zones*, PhD thesis, Georgia Institute of Technology, Atlanta, Georgia.

Nielson, B. G. and DesRoches, R. [2004]. Improved methodology for generation of analytical fragility curves for highway bridges, *Proceedings of the Ninth ASCE Specialty*

Conference on Probabilistic Mechanics and Structural Reliability, Albuquerque, New Mexico.

Nielson, B. G. and DesRoches, R. [2007]. Seismic fragility methodology for highway bridges using a component level approach, *Earthquake Engineering and Structural Dynamics* **36**(6): 823–839.

Noda, S., Uwabe, T. and Chiba, T. [1975]. Relation between seismic coefficient and ground acceleration for gravity quay wall, *Report of the Port and Harbour Research Institute* **14**(4): 67–111.

NRC [1981]. Fault tree handbook, *Technical Report NUREG-0492*, System and Reliability Research, Office of Nuclear Regulatory Research, U.S. Nuclear Regulatory Commission, Washington, D.C.

O'Brien, E. and the INFRARISK Consortium [2013–2016]. *INFRARISK: Novel indicators for identifying critical infrastructure at risk from natural hazards*, Available at: www.infrarisk-fp7.eu.

Padgett, J. E. and DesRoches, R. [2007]. Sensitivity of seismic response and fragility to parameter uncertainty, *ASCE Journal of Structural Engineering* **133**(12): 1710–1718.

Padgett, J. E. and DesRoches, R. [2008]. Methodology for the development of analytical fragility curves for retrofitted bridges, *Earthquake Engineering and Structural Dynamics* **37**(8): 1157–1174.

Padgett, J. E. and DesRoches, R. [2009]. Retroffited bridge fragility analysis for typical classes of multispan bridges, *Earthquake Spectra* **25**(1): 117–141.

Padgett, J. E., DesRoches, R., Nielson, B. G., Yashinsky, M., Kwon, O. S., Burdette, N. and Tavera, E. [2008]. Bridge damage and repair costs from hurricane Katrina, *Journal of Bridge Engineering* **13**(1): 6–14.

Padgett, J. E., Nielson, B. G. and DesRoches, R. [2008]. Selection of optimal intensity measures in probabilistic seismic demand models of highway bridge portfolios, *Earthquake Engineering and Structural Dynamics* **37**(5): 711–725.

Park, J. and Towashiraporn, P. [2014]. Rapid seismic damage assessment of railway bridges using the response-surface statistical model, *Structural Safety* **47**: 1–12.

Paté-Cornell, E. [2002]. Risk and uncertainty analysis in government safety decisions, *Risk Analysis* **22**(3): 633–646.

Paté-Cornell, E. [2012]. On "Black Swans" and "Perfect Storms": Risk analysis and management when statistics are not enough, *Risk Analysis* **32**(11): 1823–33.

Paulotto, C., Ayala, A. G. and Taucer, F. [2007]. A procedure for the approximate calculation of the stiffness and energy dissipation characteristics of piers for the seismic DBD and performance evaluation of RC bridges, *XVI Congreso Nacional de Ingenieria Sismica*, Guerrero, Mexico.

Pearson, D., Stein, S. and Jones, J. S. [2002]. HYRISK methodology and user guide, *Technical Report FHWA-RD-02-XXX*, Federal Highway Administration, Virginia.

PEER [2010]. Technical report for the PEER ground motion database web application, *Technical report*, Pacific Earthquake Engineering Research Center, University of California, Berkeley, California.

Peloso, S. and Pavese, A. [2008]. Secant modes superposition: A simplified method for seismic assessment of RC frames, *Proceedings of the Fourteenth World Conference on Earthquake Engineering*, Beijing, China.

Petersen, M. D., Moschetti, M. P., Powers, P. M., Mueller, C. S., Haller, K. M., Frankel, A. D., Zeng, Y., Rezaeian, S., Harmsen, S. C., Boyd, O. S., Field, N., Chen, R., Rukstales, K. S., Luco, N., Wheeler, R. L., Williams, R. A. and Olsen, A. H. [2014]. Documentation for the 2014 update of the United States national seismic hazard maps, *Technical Report 2014–1091*, U.S. Geological Survey.

Pitilakis, K., Fotopoulou, S., Argyroudis, S., Pitilakis, D., Senetakis, K., Treulopoulos, K., Kakderi, K. and Riga, E. [2011]. Physical vulnerability of elements at risk to landslides: Methodology for evaluation, fragility curves and damage states for buildings and lifelines, *Technical report*, SAFELAND Project Deliverable D2.5.

Pitilakis, K., Franchin, P., Khazai, B. and Wenzel, H. [2014]. *SYNER-G: Systemic Seismic Vulnerability and Risk Assessment of Complex Urban, Utility, Lifeline Systems and Critical Facilities: Methodology and Applications*, Springer.

Pitilakis, K. and the SYNER-G Consortium [2009–2013]. *SYNER-G: Systemic Seismic Vulnerability and Risk Analysis for Buildings, Lifeline Networks and Infrastructures Safety Gain*, Available at: www.syner-g.eu.

Poljansek, K., Bono, F. and Gutierrez, E. [2012]. Seismic risk assessment of interdependent critical infrastructure systems: the case of European gas and electricity networks, *Earthquake Engineeting and Structural Dynamics* **41**(1): 61–79.

Porter, K., Kennedy, K. and Bachman, R. [2007]. Creating fragility functions for performance-based earthquake engineering, *Earthquake Spectra* **23**(2): 471–489.

Porter, K. and Ramer, K. [2012]. Estimating earthquake-induced failure probability and downtime of critical facilities, *Journal of Business Continuity & eEergency Planning* **5**(4): 352–364.

Pousse, G., Bonilla, L. F., Cotton, F. and Margerin, L. [2006]. Non-stationary stochastic simulation of strong ground motion time-histories including natural variability: Application to the K-net Japanese database, *Bulletin of the Seismological Society of America* **96**(6): 2103–2117.

Prasad, G. G. and Banerjee, S. [2013]. The impact of flood-induced scour on seismic fragility characteristics of bridges, *Journal of Earthquake Engineering* **17**(6): 803–828.

Priestley, M. J. N. [2003]. Myths and fallacies in earthquake engineering, revisited, *The Mallet Milne Lecture*, IUSS Press, Pavia, Italy.

Priestley, M. J. N., Calvi, M. N. and Kowalsky, M. J. [2007]. *Displacement Based Seismic Design of Structures*, IUSS Press, Pavia, Italy.

Puppala, A. J., Saride, S., Archeewa, E., Hoyos, L. R. and Nazarian, S. [2009]. Recommendations for design, construction and maintenance of brdige approach slabs: synthesis report, *Technical Report FHWA/TX-09/0-6022-1*, Texas Department of Transportation, Arlington, Texas, USA.

Qi´ang, W., Ziyan, W. and Shukui, L. [2012]. Seismic fragility analysis of highway bridges considering multi-dimensional performance limit state, *Earthquake Engineering and Engineering Vibration* **11**(2): 185–193.

Richardson, E. V. and Davis, S. R. [1995]. Evaluating scour at bridges, *Technical Report FHWA-IP-90-017*, Federal Highway Administration, Washington, DC, USA.

Rohmer, J. [2013]. Uncertainty quantification: Report on uncertainty quantification and comparison for single-type risk analyses, *Technical report*, MATRIX Project Deliverable D2.2.

Rohmer, J., Douglas, J., Bertil, D., Monfort, D. and Sedan, O. [2014]. Weighing the importance of model uncertainty against parameter uncertainty in earthquake loss assessments, *Soil Dynamics and Earthquake Engineering* **58**: 1–9.

Rosenblueth, E. and Herrera, I. [1964]. On a kind of hysteretic damping, *Journal of Engineering Mechanics ASCE* **90**(4): 37–48.

Sabetta, F. and Pugliese, A. [1996]. Estimation of response spectra and simulation of non-stationary earthquake ground motions, *Bulletin of the Seismological Society of America* **86**(2): 337–352.

Sadan, O. B., Petrini, L. and Calvi, G. M. [2013]. Direct displacement-based seismic assessment procedure for multi-span reinforced concrete bridges with single-column piers, *Earthquake Engineering and Structural Dynamics* **42**(7): 1031–1051.

Saltelli, A. [2002]. Making best use of model evaluations to compute sensitivity indices, *Computer Physics Communications* **145**(2): 280–297.

Saltelli, A., Ratto, M., Andres, T., Campolongo, F., Cariboni, J., Gatelli, D., Saisana, M., and Tarantola, S. [2008]. *Global sensitivity analysis: The Primer*, Wiley, Chichester, UK.

Sarma, S. K. [1975]. Seismic stability of earth dams and embankments, *Geotechnique* **25**(4): 743–761.

Saxena, V., Deodatis, G. and Feng, M. Q. [2000]. Development of fragility curves for multi-span reinforced concrete bridges, *International Conference on Monte Carlo Simulation*, Principality of Monaco.

Saygili, G. [2008]. *A Probabilistic Approach for Evaluating Earthquake-induced Landslides*, PhD thesis, University of Texas, Austin, Texas.

Saygili, G. and Rathje, E. M. [2009]. Probabilistically based seismic landslide hazard maps: An application in Southern California, *Engineering Geology* **109**(3–4): 183–194.

Selva, J. [2013]. Long-term multi-risk assessment: Statistical treatment of interaction among risks, *Natural Hazards* **67**(2): 701–722.

Seyedi, D., Gehl, P., Douglas, J., Davenne, L., Mezher, N. and Ghavamian, S. [2010]. Development of seismic fragility surfaces for reinforced concrete buildings by means of nonlinear time-history analysis, *Earthquake Engineering and Structural Dynamics* **39**(1): 91–108.

Shinozuka, M., Feng, M. Q., Lee, J. and Naganuma, T. [2000]. Statistical analysis of fragility curves, *ASCE Journal of Engineering Mechanics* **126**(12): 1224–1231.

Silva, V., Crowley, H. and Colombi, M. [2014]. Fragility function manager tool, *SYNER-G: Typology Definition and Fragility Functions for Physical Elements at Seismic Risk*, K. Pitilakis, H. Crowley, A.M. Kaynia (Eds), Springer, pp. 385–402.

Singhal, A. and Kiremidjian, A. S. [1998]. Bayesian updating of fragilities with application to RC frames, *Journal of Structural Engineering* **124**(8): 922–929.

Siraj, T., Tesfamariam, S. and Dueñas Osorio, L. [2015]. Seismic risk assessment of high-voltage transformers using Bayesian belief networks, *Structure and Infrastructure Engineering* **11**(7): 929–943.

Song, J. and Kang, W. H. [2007]. Risk-quantification of complex systems by matrix-based system reliability method, *Special Workshop on Risk Acceptance and Risk Communication*, Standford Univerity, California.

Song, J. and Kang, W. H. [2009]. System reliability and sensitivity under statistical dependence by matrix-based system reliability method, *Structural Safety* **31**(2): 148–156.

Stewart, J. P., Douglas, J., Javanbarg, M., Bozorgnia, Y., Abrahamson, N. A., Boore, D. M., Campbell, K. W., Delavaud, E., Erdik, M. and Stafford, P. J. [2015]. Selection of ground motion prediction equations for the Global Earthquake Model, *Earthquake Spectra* **31**(1): 19–45.

Stewart, J. P., Taciroglu, E., Wallace, J. W., Ahlberg, E. R., Lemnitzer, A., Rha, C., Tehrani, P. K., Keowen, S., Nigbor, R. L. and Salamanca, A. [2007]. Full scale cyclic testing of foundation support systems for highway bridges. Part II: Abutment

backwalls, *Technical Report UCLA-SGEL 2007/02*, Structural and Geotechnical Engineering Laboratory, University of California, Los Angeles, California.

Tanasić, N., Ilić, V. and Hajdin, R. [2013]. Vulnerability Assessment of Bridges Exposed to Scour, *Transportation Research Record: Journal of the Transportation Research Board* **2360**: 36–44.

Temez, J. R. [1991]. Extended and improved rational method, *Proceedings of the Twenty-fourth IAHR World Congress*, Madrid, Spain.

The MathWorks [2013]. Matlab and statistics toolbox release 2013a, *Technical report*, The MathWorks, Inc., Natick, Massachusetts.

Thywissen, K. [2006]. Components of risk: A comparative glossary, *Technical Report UHU-EHS 2/2006*, United Nations University, Bonn, Germany.

Tien, I. and Der Kiureghian, A. [2015]. Compression and inference algorithms for Bayesian network modeling of infrastructure systems, *Proceedings of the Twelfth International Conference on Applications of Statistics and Probability in Civil Engineering*, Vancouver, Canada.

Transportation Association of Canada [2004]. *Guide to Bridge Hydraulics, Second Edition*, Thomas Telford, London, UK.

Tsionis, G. and Fardis, M. N. [2014]. Fragility functions of road and railway bridges, *SYNER-G: Typology Definition and Fragility Functions for Physical Elements at Seismic Risk*, K. Pitilakis, H. Crowley, A.M. Kaynia (Eds), Springer, pp. 259–398.

Tyagunov, S., Pittore, M., Wieland, M., Parolai, S., Bindi, D., Fleming, K. and Zschau, J. [2014]. Uncertainty and sensitivity analyses in seismic risk assessments on the example of Cologne, Germany, *Natural Hazards and Earth System Sciences* **14**(6): 1625–1640.

Vamvastikos, D. and Cornell, C. A. [2002]. Incremental dynamic analysis, *Earthquake Engineering and Structural Dynamics* **31**(3): 491–514.

Vanzi, I. [2004]. *Seismic reliability of electric power networks*, PhD thesis, Sapienza University of Rome, Rome, Italy (in Italian).

Wang, R. [2012]. *Integrated Health Prediction of Bridge Systems using Dynamic Object Oriented Bayesian Networks (DOOBNs)*, PhD thesis, Queensland University of Technology, Brisbane, Australia.

Wang, R., Ma, L., Yan, C. and Mathew, J. [2010]. Preliminary study on bridge health prediction using Dynamic Objective Oriented Bayesian Network (DOOBN), *Proceedings of the Fifth World Congress on Engineering Asset Management*, Brisbane, Australia.

Wang, Y. and Au, S. K. [2009]. Spatial distribution of water supply reliability and critical links of water supply to crucial water consumers under an earthquake, *Reliability Engineering and System Safety* **94**(2): 534–541.

Wells, D. L. and Coppersmith, K. J. [1994]. New empirical relationships among magnitude, rupture length, rupture width, rupture area, and surface displacement, *Bulletin of the Seismological Society of America* **84**(4): 974–1002.

Wen, W. [1990]. Optimal decomposition of belief networks, *Proceedings of the Sixth Conference on Uncertainty in Artificial Intelligence*, Melbourne, Australia, pp. 209–224.

Wen, Y. K., Ellingwood, B. R., Veneziano, D. and Bracci, J. [2003]. Uncertainty modeling in earthquake engineering, *Technical report*, MAE Center Project FD-2 Report.

Werner, S. D., Taylor, C. E., Cho, S., Lavoie, J. P., Huyck, C., Eitzel, C., Chung, H. and Eguchi, R. T. [2006]. REDARS 2: Methodology and software for seismic risk analysis of highway systems, *Technical Report MCEER-06-SP08*, Multidisciplinary Center for Earthquake Engineering Research, Buffalo, NY.

Werner, S. D., Taylor, C. E., Moore, J. E. and S., W. J. [2000]. A risk-based methodology for assessing the seismic performance of highway systems, *Technical Report MCEER-00-0014*, Multidisciplinary Center for Earthquake Engineering Research, Buffalo, NY.

Woessner, J., Danciu, L., Giardini, D., Crowley, H., Cotton, F., Grünthal, G., Valensise, G., Arvidsson, R., Basili, R., Demircioglu, M. N., Hiemer, S., Meletti, C., Musson, R. W., Rovida, A. N., Sesetyan, K., Stucchi, M. and the SHARE consortium [2015]. The 2013 European seismic hazard model: key components and results, *Bulletin of Earthquake Engineering* **13**(12): 3553–3596.

Woessner, J., Danciu, L., Kaestli, P. and Monelli, D. [2013]. Databases of seismogenic zones, Mmax, earthquake activity rates, ground motion attenuation relations and associated logic trees, *Technical Report SHARE Project Deliverable D6.6*.

Woo, G. [1999]. *The Mathematics of Natural Catastrophes*, Imperial College Press, London, UK.

Wu, X. Z. [2013]. Probabilistic slope stability analysis by a copula-based sampling method, *Computers and Geosciences* **17**(5): 739–755.

Wu, X. Z. [2015]. Development of fragility functions for slope instability analysis, *Landslides* **12**(1): 165–175.

Yi, J. H., Kim, S. H. and Kushiyama, S. [2007]. PDF interpolation technique, for seismic fragility analysis of bridges, *ASCE Journal of Structural Engineering* **29**(7): 1312–1322.

Yin, Y. and Konagai, K. [2001]. A simplified method for expression of the dynamic stiffness of large-scaled grouped piles in sway and rocking motions, *JSCE Journal of Applied Mechanics* **4**(9): 415–422.

Zentner, I. [2007]. Méthodes probabilistes dans les analyses sismiques : Modélisation, propagation et hiérarchisation des incertitudes, *7ème Colloque National AFPS*, Paris, France.

Zezere, J. L., Trigo, R. M., Fragoso, M., Oliveira, S. C. and Garcia, R. A. C. [2008]. Rainfall-triggered landslides in the Lisbon region over 2006 relationships with the North Atlantic Oscillation, *Natural Hazards and Earth System Science* **8**(3): 483–499.

Zhang, J., Huo, Y., Brandenberg, S. J. and Kashighandi, P. [2008]. Effects of structural characterizations on fragility functions of bridges subject to seismic shaking and lateral spreading, *Earthquake Engineering and Engineering Vibration* **7**(4): 369–382.

Zhou, X. and Taylor, J. [2014]. DTALite: A queue-based mesoscopic traffic simulator for fast model evaluation and calibration, *Cogent Engineering* **1**(1): 961345.

Zhu, W. [2008]. *An investigation into reliability-based methods to include risk of failure in life-cycle cost analysis of reinforced concrete bridge rehabilitation*, Master's thesis, RMIT University, Melbourne, Australia.

Ziv, J. and Lempel, A. [1977]. A universal algorithm for sequential data compression, *IEEE Transactions on Information Theory* **23**(3): 337–343.

Zschau, J. and the MATRIX Consortium [2010–2013]. *MATRIX: New Multi-Hazard and Multi-Risk Assessment Methods for Europe*, Available at: matrix.gpi.kit.edu.

Zuccaro, G., Cacace, F., Spence, R. J. S. and Baxter, P. J. [2008]. Impact of explosive eruption scenarios at Vesuvius, *Journal of Volcanology and Geothermal Research* **178**(3): 416–423.